LUCAS ANNUAL REPORT

Acknowledgements

This year's Lucas Annual Report is dedicated to the memory and honor of Mark Bednarski, Ph.D., Assistant Professor of Radiology, Stanford University. In his short career Mark made many contributions to medicine, chemical biology, organic chemistry, image-guided therapy, and molecular imaging. We will long be inspired by the extraordinary creativity, energy, and innovation that was Mark's trademark.

Lucas Annual Report 2006

Table of Contents

Collaborating Stanford Departments

Almost three hundred faculty, postdoctoral fellows, students and research staff from across the university are affiliated with research programs in the Department of Radiology representing the following departments:

Anesthesia
Applied Physics
Bioengineering
Cancer Biology
Cardiovascular Medicine
Chemistry
Computer Sciences
Electrical Engineering
ENT
Functional Restoration
Infectious Diseases
Materials Science
Mechanical Engineering
Medical Informatics
Medicine/Oncology

Nephrology
Neurobiology
Neurology
Neurosurgery
OB/GYN
Orthopedics/Orthopedic Surgery
Pediatrics/Neonatology
Psychiatry
Psychology
Radiation Therapy
Stanford Center for Biomedical Ethics
Stroke Center
Surgery
Urology

Outside Collaborators

Active collaborations are in place with researchers from outside Stanford representing the following institutions:

Vascular Surgery
Alza Corporation
Amgen
Brown University
Cedars Sinai, Los Angeles
Chiron Corporation
Colorado State University – Boulder
The Canary Foundation
Dana Farber Cancer Institute
Diadexus
Endius
Ethicon
FeRx, Inc.
Fred Hutch Cancer Center
Genentech, Inc.
GE Medical Systems
Glaxo Smith Kline
Intel
Intronn Inc.
Mag Design and Engineering
MediCorp Health System

Medimmune Inc.
Mellennium Pharmaceuticals
NexRay
Nova R&D Inc.
Palo Alto Veterans Administration
Pfizer
Prostrate Cancer Foundation
Riken, Saitama, Japan
RMD Inc.
Siemens Medical Systems
Smith Kettlewell Eye Institute
SRI International
University of California, Berkeley
University of California, Davis
University of California, Irvine
University of California, Los Angeles
University of California, San Francisco
University of California, San Diego
University of Texas, Austin
Varian Medical Systems

OVERVIEWS

RSL Overview

Radiological Sciences Laboratory and the Center for Advanced MR Technology

GARY H. GLOVER

DIRECTOR, RADIOLOGICAL SCIENCES LABORATORY

The Lucas Center is home to the Radiological Sciences Laboratory (RSL), a section of the Radiology Department, and in conjunction with the Electrical Engineering Department is host to the *Center for Advanced MR Technology*, an NIH-funded National Research Resource. Its state of the art imaging facilities support hundreds of on-campus and extramural researchers as a core facility. Occupation of the Lucas expansion space began in 2004 and is now complete. The new conference facility, the Radiology Learning Center, has been a wonderful asset for the department and the RSL, with daily use for resident conferences, group meetings, seminars and classes.

THE RADIOLOGICAL SCIENCES LABORATORY

For the first time in several years, the RSL has had a relatively stable census with 12 faculty, approximately 50 graduate and postdoctoral students, 33 scientific staff and 7 administrative assistants, as well as the Lucas Center/RSL Administrative Director, Donna Cronister. Dr. Daniel Fiat, a visiting scholar, continues to perform research in imaging of Oxygen-17. Drs. HsiaoWen Chung and Yi Sun, both from Taiwan, visiting Stanford and collaborating with Dr. Norbert Pelc.

The faculty serve in a wide variety of advisory roles to government and foundation agencies such as the NIH and in policy-making positions for international scientific societies such as the ISMRM and RSNA. A number of our faculty, scientific staff and students have garnered prestigious awards for their exceptional research achievements. Some of the Lab's honors of the past year are noted here with pleasure.

Rebecca Fahrig was appointed to the Editorial Board of Medical Physics, an uncommon honor for a junior faculty scientist. She also received the Sylvia Sorkin Greenfield Award for best "non-radiation therapy" publication in *Medical Physics* in 2005 (Fahrig R, Wen Z, Ganguly A, DeCrescenzo G, Rowlands JA, Stevens GM, Saunders RF, Pelc NJ. Performance of a static-anode/flat-panel x-ray fluoroscopy system in a diagnostic strength magnetic field: a truly hybrid x-ray/MR imaging system. Med Phys. 2005 Jun;32(6):1775-84). Her student **Lei Zhu**, PhD candidate,

received a Fellowship Research Trainee Prize, RSNA 2005 Physics Subcommittee.

Mike Moseley serves on four prestigious journal editorial boards, and is a standing member of the NINDS Stroke PRG-Imaging Group grant review committee. He continues to chair the Stanford IACUC IRB review panel for animal research on campus and has joined the ISMRM Dead Presidents Club as a past president of the ISMRM (joining **Bob Herfkens** and Gary Glover).

Kim Butts Pauly serves on the ISMRM Board of Trustees, an elected position that demonstrates peer recognition of her contributions to science. In addition, she is the vice chair of the Annual Meeting Program Committee, the most challenging committee of the Society. This year she was invited to be issue editor of *Topics in Magnetic Resonance Imaging*. Her grad students have done well: Jean Chen received a Bio-X student travel grant and Lena Kaye received an ISMRM poster award nomination.

Gary Glover was elected to the National Academy of Engineering and will be inducted into the Academy in October 2006. During a surprise party held in the new Light Court in the Lucas Expansion, he was further surprised and honored by a visit from Don Lucas .

Don Lucas (l) joins Gary Glazer (r) in congratulating Gary Glover (m) as Dr. Glover learns that he has been elected to the National Academy of Engineering.

Sean Mackey, a member of the fMRI group, has had numerous interviews on national television and in *Time* magazine for his pioneering work on the control of pain using fMRI-driven biofeedback, after reporting results in PNAS. Sean also received an NIH R01 to further support spinal cord fMRI in pain. **Laura Pisani** received an NIH F32 fellowship award.

Sylvia Plevritis was promoted to Associate Research Professor of Radiology. She co-authored two high impact journal papers that received widespread international media coverage. The first, which appeared in the NEJM, quantifies the impact of mammography on the U.S. breast cancer mortality rate decline and the second, which appeared in JAMA, estimates the cost-effectiveness of breast MRI screening in women who carry BRCA1/2 mutations. She is currently PI on four NCI grants that apply computational modeling to cancer biology and cancer patient outcomes; she serves as a scientific editor of a special issue of the JNCI Monograph devoted to model-based approaches for analyzing U.S. breast cancer incidence and mortality rates.

The National Center for Advanced MR Technology at Stanford (CAMRT)

The CAMRT is now in its twelfth year of operation as a Research Resource, sponsored by a grant from the NIH's National Center for Research Resources. Outstanding progress has been made in all six of the core technology development areas that include reconstruction methods (Dwight Nishimura, EE Department, core director), imaging of brain activation (Gary Glover, core director and PI), diffusion and perfusion weighted imaging methods (Mike Moseley, core director), imaging of cardiovascular structure and function (Norbert Pelc, core director and CAMRT co-PI), spectroscopic imaging development (Dan Spielman, core director) and interventional MRI technique development (Kim Butts, core director). Much of this exciting research is chronicled in the scientific reports that follow.

Lucas Center Facilities

The Center's major expansion has provided a wonderful addition to the Department, and we are grateful to the Lucas Foundation for the support. The 7T magnet has been functional since Spring 2006 and has demonstrated truly spectacular images. Many experiments are underway in using this new technology with higher resolution and alternate contrast mechanisms.

Plans for a renovation of the existing 3D lab and animal magnet space for installation of a second 3T magnet are on hold pending additional funding. A new "micro-Signa" 7T animal-sized magnet is being installed under the direction of **Mike Moseley** in the Clark Center's Small Animal Imaging Facility.

A view of the bridge as you enter the Lucas Expansion from ground level.

TH1
1.5T, 256x192, 2.0 min

TH2
3.0T, 512x512, 5.5 min

TH3
7.0T, 512x512, 5.5 min
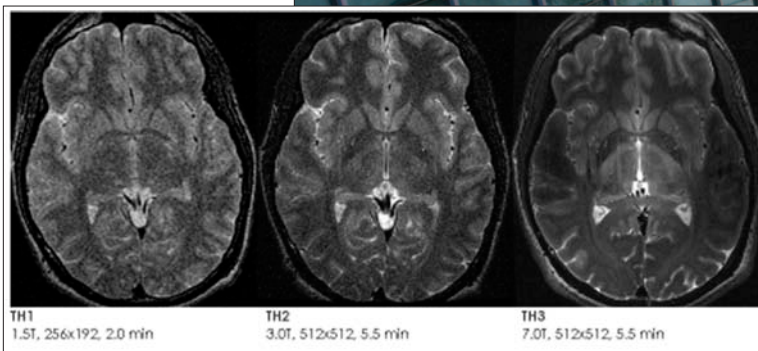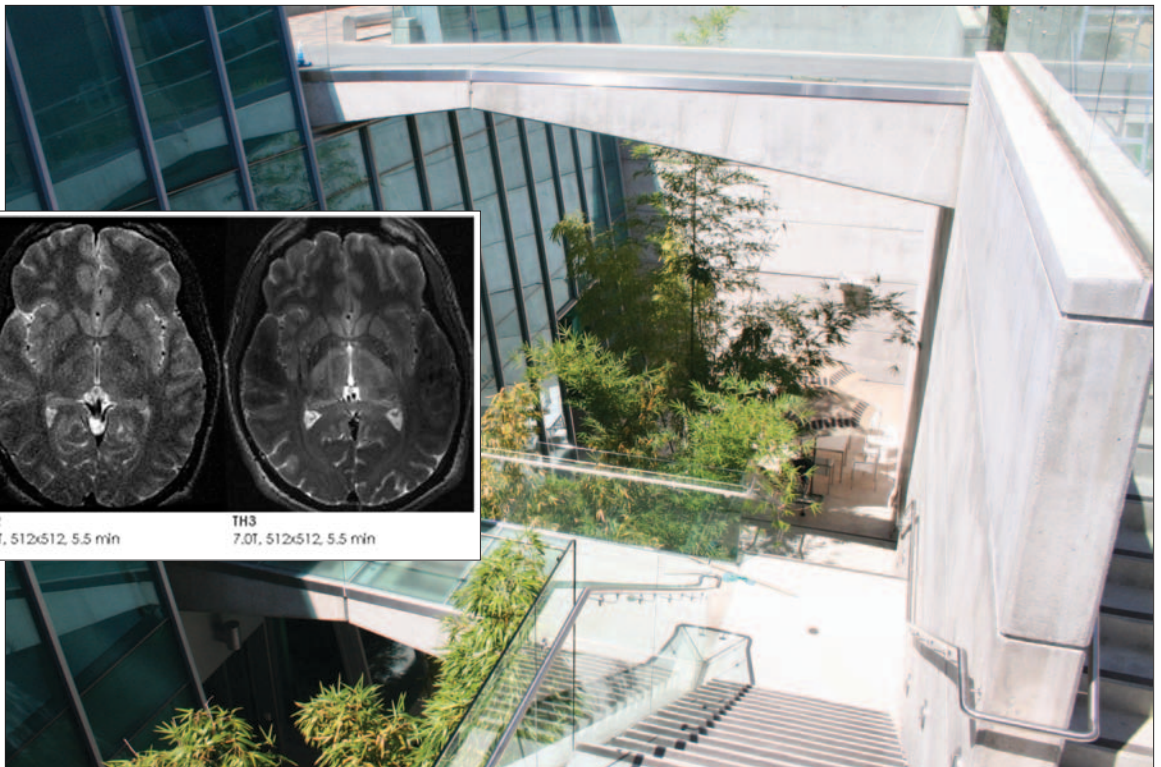
A comparison of three different magnetic field strengths (1.5T, 3.0T and 7.0T).

MIPS Overview

Molecular Imaging Program at Stanford

SANJIV SAM GAMBHIR
DIRECTOR, MIPS

The Molecular Imaging Program at Stanford (MIPS) has experienced tremendous growth this year. The faculty received a U54 nanotechnology grant and will also be awarded an R25T training grant; both grants are from the National Cancer Institute. In addition, all labs continued to grow with many new students and outstanding research staff joining the program. The second annual MIPS Retreat was held on February 17, 2006 at Pier 39 in San Francisco with over 70 MIPS faculty and students in attendance. Students each presented brief research updates, interacted with other MIPS members, and enjoyed a spectacular San Francisco Bay cruise.

Hequan Yao, Yan Zhang, Bengang Xing, and Chenjie Zu enjoy a break during the 2nd Annual MIPS Retreat earlier this year.

The National Cancer Institute (NCI) announced March 1, 2006 that it has allotted a U54 nanotechnology grant of roughly $20 million over the next five years to the Stanford Center of Cancer Nanotechnology Excellence (CCNE), which will be led by Dr. Sam Gambhir (http://mips.stanford.edu/public/grants/ccne/). The Stanford CCNE will be one of eight NCI Centers of Cancer Nanotechnology Excellence, which are research alliances of cancer centers; medical institutions; schools of engineering and physical sciences; nonprofit organizations; and private corporations. Their mission is to integrate nanotechnology into cancer research. The focus of the Stanford CCNE will be on developing nanodevices that facilitate the imaging of disease in vivo and the detection of changes in serum proteome

through ex vivo nanosensors. These efforts will then be used for future, more pinpointed evaluation of therapeutic response in cancer treatment. Co-led by Dr. Shan Wang of Materials Science and Electrical Engineering, the Stanford CCNE team will involve the scientific interaction of more than 15 separate research labs from 7 different research entities across the alliance. The experience of the Stanford CCNE team will serve as a role model for the new "team science," the way of the future for conducting broad-based medical research. Other centers involved with the Stanford CCNE include the University of California, Los Angeles; the Fred Hutchinson Cancer Research Center; Cedars Sinai Medical Center; the University of Texas at Austin; General Electric Global Research; and the Intel Corporation.

Stanford will be awarded a cancer education grant from the specialized Cancer Education and Career Development (R25T) Program (P.I., Dr. Sam Gambhir). Stanford's R25T has been named the Stanford Molecular Imaging Scholars (SMIS) program. The R25T program was developed by the NCI to support the development and implementation of curriculum-dependent, team-oriented programs to train postdoctoral candidates in cancer research team settings that are highly interdisciplinary and collaborative. The Stanford Molecular Imaging Scholars (SMIS) program will be a diverse training program bringing together more than 13 departments, predominantly from the Stanford School of Medicine, in order to train the next generation of interdisciplinary leaders in the field of molecular imaging. Oncologic molecular imaging is a rapidly growing area within the field, which combines the disciplines of chemistry, cell/molecular biology, molecular pharmacology, bioengineering, imaging sciences, and clinical medicine to advance cancer research, diagnosis, and management. The goals of SMIS are to train 15 postdoctoral fellows through mentorship by a diverse group of over 40 basic science and clinical faculty mentors representing 8 program areas; formal courses in molecular imaging, Caption for photo molecular pharmacology, cancer biology, cancer immunology, virology, and gene therapy; and a clinical component including hematology/oncology rounds. SMIS fellows will be recruited into a three-year program to audit coursework

and complete a primary focus on research with at least two complementary mentors. (http://mips.stanford.edu/smis)

Chen Lab (Molecular Imaging Probe Laboratory) Some of the molecular imaging probes developed in this lab exhibit great tumor targeting efficacy as well as favorable in vivo kinetics and are now in late-stage preclinical testing or are being translated into the clinic for initial testing in humans. Thanks to everybody's hard efforts, Dr. Chen's group is now funded through NIBIB, NCI, DOD, and MedImmune, Inc. The research work accomplished by Dr. Zhengming Xiong on the adenovirus was featured on the cover of the *Journal of Nuclear Medicine*.

Dr. Weibo Cai has been awarded the Benedict Cassen Postdoctoral Fellowship from the Society of Nuclear Medicine. The Education and Research Foundation of the Society of Nuclear Medicine has recently established the Benedict Cassen Postdoctoral Fellowship, which is awarded to recent doctoral degree (Ph.D. or Ph.D. plus M.D.) recipients who demonstrate an excellent academic record and exceptional research ability. Its purpose is to broaden the recipient's basic exposure to nuclear medicine research at an institution different from that conferring the doctoral degree.

Dr. Qizhen Cao was awarded the Stanford University Dean's Fellowship. This fellowship acknowledges scholars with an appointment in the School of Medicine and considers such factors as the scientific merit and training relevance of the research proposal as well as the number of years of the applicant's postdoctoral research training.

Gambhir Lab (Multimodality Molecular Imaging Lab) Dr. Sanjiv Sam Gambhir was awarded the Hounsfield Medal on February 23 from the Imperial College in London for his scientific achievements in biomedical imaging. The medal is awarded in memory of Sir Godfrey Hounsfield who shared the 1979 Nobel Prize for Physiology or Medicine for his invention of the CT scanner.

At the Society of Nuclear Medicine 53rd Annual Meeting in San Diego, Dr. Gambhir received the Aebersold Award for outstanding achievement in basic nuclear medicine science. The Aebersold Award is named for Paul C. Aebersold, a pioneer in the biologic and medical application of radioactive materials and the first director of the Atomic Energy Commission's Division of Isotope Development at Oak Ridge, Tennessee.

Dr. Carmel Chan has been awarded a postdoctoral fellowship from the Susan G. Komen Breast Cancer Foundation for his project entitled "Imaging the Efficacy of Heat Shock Protein 90 Inhibitors in Human Breast Cancers." The Susan G. Komen Breast Cancer Foundation has been a global leader in the fight against breast cancer through its support of innovative research and community-based outreach programs.

Ian Chen received two fellowships: the Bio-X Graduate Student Fellowship and the American Heart Association Predoctoral Fellowship. The Bio-X Graduate Student Fellowship is a generous gift of an anonymous donor who is helping Stanford to strengthen graduate training in interdisciplinary bioscience and to impel important new advances in science and engineering. The American Heart Association Predoctoral Fellowship is designed to help students initiate careers in cardiovascular research and to provide support for students conducting doctoral dissertation projects. Both fellowships will help to support Ian's research in cardiac molecular imaging.

Dr. Mohammad Namavari received the 2006 Society of Nuclear Medicine Berson-Yalow Award, for being a second author on the abstract entitled "Characterization of 131I-SKI243, a Radiolabeled EGFR-tk Binding Ligand, and Its Cross Reactivity for Iressa and Tarceva Binding Sites." The Berson-Yalow Award recognizes significant contributions to the advancement and promotion of nuclear medicine, specifically, the most significant contributions to basic or clinical radioassays.

Ricky Tong, a medical student, was awarded a Stanford Medical Scholars Research Fellowship for his research
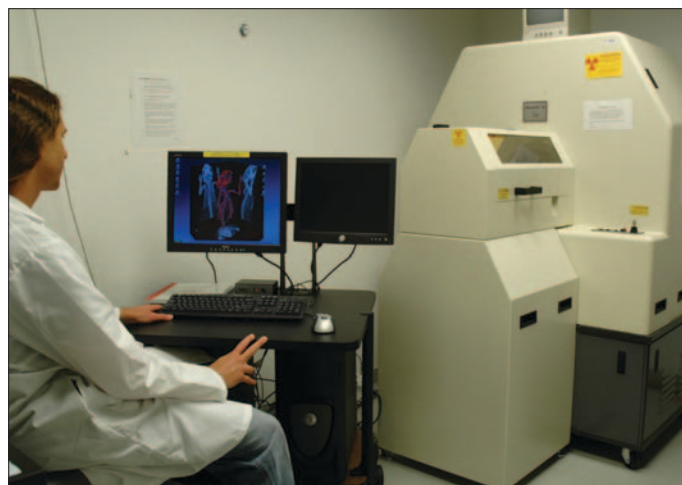
Shay Keren demonstrates the Imtek/Siemens SPECT/CT.

in tri-fusion imaging. The Stanford Medical Scholars Research Program supports medical student research, both locally and off-site. Students carry out funded research in an academic setting under the direction of faculty members here at the medical school, hospital, clinics, and throughout the University and local community.

David Yerushalmi has completed research on the potential of virtual bronchoscopy. His research is highlighted on the Aunt Minnie web site, which is the largest and most comprehensive community web site for medical imaging professionals worldwide. Three-dimensional visualization with PET/CT may soon be expanded to virtual bronchoscopy, providing a new tool for diagnosis, treatment planning, and interventional guidance. David Yerushalmi was also awarded a Bradley-Alavi Student Fellowship. This fellowship is funded by the Education and Research Fund of the Society of Nuclear Medicine (SNM) and awards students enrolled in medical, pharmacy, or graduate school as well as undergraduates who demonstrate outstanding competence in molecular and nuclear imaging research. Bradley-Alavi Fellows are named in honor of the late Stanley E. Bradley, a professor of medicine at Columbia University College of Physicians and Surgeons and a prominent researcher in the fields of renal physiology and liver disease, and Abass Alavi, M.D., professor of radiology and chief of the Division of Nuclear Medicine at the University of Pennsylvania Medical Center.

Rao Lab (Cellular and Molecular Imaging Lab) The work on the self-illuminating quantum dots by the Rao and Gambhir laboratories has been highlighted in *Nature, Nature Methods, Analytical Chemistry, Biophotonics International,* and *Foxnews.com*. A novel strategy based on a split ribozyme reporter and developed in the Rao lab for the detection of mRNA has appeared as the cover article of *ChemBioChem*. Dr. Bingang Xing, Dr. Rao's former postdoctoral fellow, has been appointed as an assistant professor at the Nanyang Technological University, Singapore. Dr. Rao has received both the Idea and Concept awards from the Department of Defense Breast Cancer

Research Program to develop novel strategies for breast cancer imaging.

Min-kyung So and Dr. Gayatri Gowrishankar have each received a Young Investigator Travel Award at the 2006 Academy of Molecular Imaging Annual Conference for their abstract submission. The award is given to selected abstracts on a competitive basis. In June, 2006, Dr. Gowrishankar also received the Ruth. L. Kirschstein National Research Service Award (NRSA) from the Cancer Biology Program at Stanford. This award is given to motivated postdoctoral fellows training for careers in cancer-related research.

Wu Lab (Cardiovascular Molecular Imaging) Joseph Wu will be awarded an ACC/GE Career Development Award Grant in Cardiovascular Imaging for $65,000 per year, for the two-year period beginning in July 2006 through June 2008. He will also receive $50,000 per year from the Stanford Cardiovascular Institute Seed Grant, from July 2006 through June 2007. Six articles have been accepted for publication in various scientific journals including the *Journal of Nuclear Medicine, Circulation, The FASEB Journal, Molecular Imaging and Biology,* and *Physiological Genomics.*

Feng Cao was awarded the Best Cardiovascular Young Investigator Award for her research in in vivo molecular imaging of human embryonic stem cell derived cardiomyocytes after transplantation into the ischemic myocardium.

Susan Shu-An Lin was named Bradley-Alavi Fellow for her research entitled "Imaging Bone Marrow Stem Cell Homing to Ischemic Myocardium." Bradley-Alavi Fellows are named in honor of the late Stanley E. Bradley, a professor of medicine at Columbia University College of Physicians and Surgeons and a prominent researcher in the fields of renal physiology and liver disease, and Abass Alavi, M.D., professor of radiology and chief of the Division of Nuclear Medicine at the University of Pennsylvania Medical Center.

Research Overview

Strategic Research Development

Norbert Pelc, Susan Kopiwoda

2006 will go on record as the most successful year of funded research for Stanford Radiology. We continue to achieve results that expand our research capabilities, discover new knowledge and directly benefit patient care. The following few pages focus on our research efforts and the successes that we have enjoyed over this past year. More importantly, we use these few pages to pay tribute to our outstanding faculty, staff, postdoctoral trainees, and graduate students. Because of their efforts as well as those of the Department leadership and the Lucas Imaging Center, many fine projects, both new and old, continue to thrive and unfold.

During this past year, we experienced the tightening of the NIH budget and felt its impact firsthand when some of our requested budgets were reduced by as much as 30%. Yet, we still managed to find success for our most carefully planned and constructed projects. Figure 1 depicts our NIH funding history with projected totals for the years 2006 and 2007.

Although the lion's share of our research is supported by NIH (82%), many of our faculty found additional funding for their projects through the Department of Defense (DOD), the State of California, private foundations, and private industry. This year, we had five projects funded by the DOD, much higher than our historic norm of one or two per year.
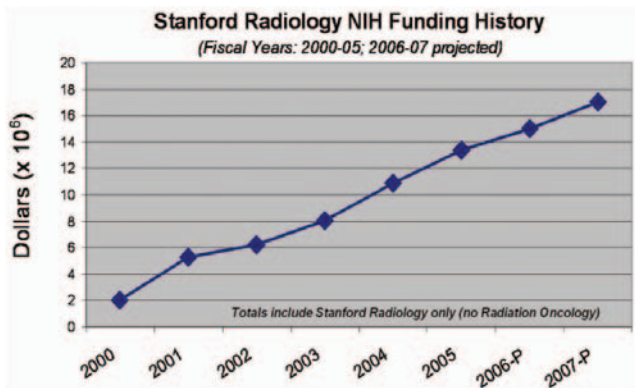

Figure 1. This chart illustrates Stanford Radiology's NIH funding history from 2000 to 2005 with projected totals for the years 2006 and 2007. These data do not include the radiation oncology.

We also had 19 clinical trials under way during the past year. The clinical trials projects provide not only an important and effective way to translate discovery to the clinic, but they also lay the foundation for new or continued collaborations with industry. The effort required to develop and maintain a clinical trials program, which is an important part of our research portfolio, is recognized and appreciated.

2005 NIH Rank and Expected 2006 Funding

We are ecstatic with the latest news from NIH. Stanford Radiology now ranks as the third highest NIH-funded radiology department among medical schools in the U.S., Figure 2, compared to our rank of 5th last year. Given that our department is much smaller (in number of faculty) than the other highly-ranked programs, our achievement is exceptional.
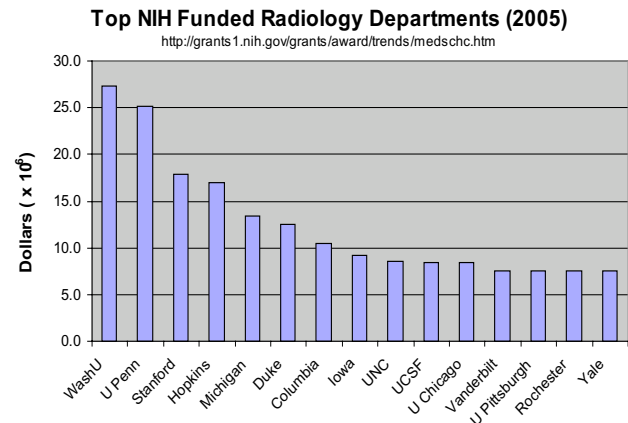

Figure 2. Data from the NIH website shows the top ranking radiology departments in the country. Totals for each school include diagnostic radiology and radiation oncology.

Stanford Radiology and the Richard M. Lucas Foundation

Research is more than just funding; we are also proud of the impact we have had in clinical practice and basic science. Our achievements, which are indebted to the generosity of the Richard M. Lucas Foundation, include virtual colonoscopy; spiral CT for CT angiography; estrogen receptor imaging for breast cancer management; the development of bilateral 3D spiral MR imaging of the breast; diffusion-weighted MR imaging for stroke imaging; image-guided techniques for thermal therapy and biopsy; and functional MRI used for understanding how the brain functions and for planning patient surgery. These projects represent only a few, select areas in which our clinicians and scientists excel and provide an example of the high level of translational research that occurs in the Richard M. Lucas Center for Imaging.

The following pages give details of existing projects led by Radiology faculty and postdoctoral trainees.

NIH Supported Research

PI	Sponsor	Title
Bammer	NIH	Improving SENSE MRI for Spiral and Echo-Planar Imaging
Beaulieu	NIH	Three-Dimensional CT Colonography
Blankenberg	NIH	Imaging Apoptosis In Vivo with Technetium 99m Annexin
Blankenberg	NIH-Univ of Wash	Membrane Binding and Imaging Applications of Annexins
Butts	NIH-Pending	iMRI Methods for Cancer Diagnosis and Treatment
Butts	NIH	MRI-Guided Focused US for Treatment of Liver and Renal Cancer
Butts	NIH	Improved Open MRI for Image-Guided Breast Procedure
Chen	NIH	MicroPET and NIR Flourescence Imaging of Tumor Angiogenesis
Chen	NIH	Imaging AVD-3 Integrin Expression
Daniel	NIH	Magnetic Resonance Imaging of Breast Cancer
Daniel	NIH	MRI-Guided Cryosurgery of Prostate Cancer
Fahrig	NIH	Improved C-Arm CT for Interventional Procedures
Fahrig	NIH-Sunnybrook	Low Cost Digital X-Ray Detectors Using Liquid Crystals
Fahrig	NIH-Ontario Cancer Inst	Image Science for the New X-Ray: Taking NEQ to Task
Gambhir	NIH	In Vivo Cellular and Molecular Imaging Center (ICMIC)
Gambhir	NIH	Reporter Imaging of Protein-Protein Interactions
Gambhir	NIH	Multimodality Imaging of Cell Mediated Gene Transfer
Gambhir	NIH	Stanford Molecular Imaging Scholars Program (SMIS)
Gambhir	NIH	Center of Cancer Nanotechnology Excellence (CCNE)
Glazer	NIH	Advanced Techniques for Cancer Imaging
Glover	NIH-UC Irvine	Functional Imaging Research in Schizophrenia Testbed
Glover	NIH	Center for Advanced Magnetic Resonance Technology (CAMRT)
Gold	NIH	Rapid MRI for Evaluation of Osteoarthritis
Gold	NIH-UCSF	Data Coordinating Center for Osetoarthritis Initiative
Gold	NIH-VAPAIRE	Biomechanical Muscle Fx Modeling after Tendon Transfer Surgery
Gold	NIH	Real-Time MRI and 3D Modeling: Development for Patellofemoral Pain
Levin	NIH-Pending	Advanced PET System Dedicated to Breast Cancer Imaging
Levin	NIH	Workshop on the Nuclear Radiology of Breast Cancer
Levin	NIH	A New Photon Sensor to Improve Molecular Cancer Imaging
Levin	NIH	New Scintillation Light Detection Concepts for PET
Moseley	NIH	Improved PWI Methodology in Acute Clinical Stroke
Napel	NIH	SIMBIOS Core-Physics-Base Simulation of Biological Structures
Napel	NIH-BioEng	Efficient Implementation of 3D Vascular Image Data
Pelc	NIH-Pending	Inverse Geometry CT for Dose-Efficient Volumetric Imaging
Pisani	NIH	Fetal Functional Magnetic Resonance Imaging
Plevritis	NIH	Cost-Effectiveness Analysis of Lung Cancer Screening
Plevritis	NIH	Breast Cancer Trend Analysis Using Stochastic Simulation
Plevritis	NIH	Computational Modeling of Cancer Biology
Rao	NIH	Unified Reporter Gene for Multi-Modality Imaging
Rubin	NIH	Improving Radiologist Detection of Lung Nodules with CAD
Sommer	NIH	Precise MRI-Directed Sonic Ablation of Prostate Cancer
Spielman	NIH-SRI	In Vivo Diffusion and Spectroscopic Brain Imaging in Alcoholism
Spielman	NIH	Magnetic Resonance Spectrosopic Neoplasm Imaging
Wu	NIH	Molecular Imaging of Cardiac Cell Transplantation

Other Government Supported Research

PI	SPONSOR	TITLE
Chen	Department of Defense	Imaging Primary Prostate Cancer and Bone Metastasis
Chen	Department of Defense	Molecular Imaging of Ovarian Carcinoma Angiogenesis
Rao	Department of Defense	Ribozyme-Mediated Imaging of p53 Expression in Breast Tumor Cells
Rao	Department of Defense	Development of Bioluminescent Nanosensors for Multiplex Imaging of MMPs
Chen	Department of Defense	Alpha-v Integrin Targeted PET Imaging of Breast Cancer Angiogenesis & Lo-Dose Metronomic Anti-Angiogenic Chemo Efficacy
Chen	Department of Defense	VEGF-Iron Oxide Conjugate for Dual MR and PET Imaging of Breast Cancer Angiogenesis
Glazer	Veterans Affairs	Solicitation Agreement
Plevritis/Kurian	California-UCOP	Cost-Effectiveness of Breast MRI Screening by Cancer Risk
Levin	California-BCRP	New Technologies to Enhance PET's Role in Breast Cancer Management

Foundation Supported Research

PI	SPONSOR	TITLE
Cai/ Chen	Society of Nuclear Medicine	PET Imaging and Therapy Targeting Tumor Angiogenesis
Cao/Gambhir	American Heart Association	Cellular Therapy for the Ischemic Myocardium: In Vivo Characterization of Biology & Physiology
Chan	The Whitaker Foundation	Optimized Four-Dimensional Magnet Resonance Flow Imaging for Congenital Heart Disease
Chen/Gambhir	American Heart Association	Multimodality Imaging of Cardiac Therapy
Gambhir	Beckman ITRP Award	Integrated Optical Bio-Sensors and Fluorescent MI Probes for Continuous Real-Time Monitoring of Stem Cells in Living Subjects
Gambhir	Doris Duke Foundation	Molecular Imaging of Cancer with a Voltage Sensor
Gambhir	Susan G. Komen Foundation	Imaging the Efficacy of Heat Shock Protein 90 Inhibitors in Human Breast Cancers
Guccione	Goldhirsh	Vascular Targeted Therapeutics for Treatment and Imaging of Diffuse Gioma
Rubin	RSNA	Fellowship in Cardiovascular Imaging
Mazin/Pelc	American Heart Association	Fast Volumetric Cardiovascular CT Scanner
Pelc	Whitaker Foundation	Department of Bioengineering-Graduate and Postdoctoral Education
Rao	The Burroughs Wellcome Fund	Career Award at the Scientific Interface
Wu	American College of Cardiology	Multi-Modality Imaging of Cardiac Stem Cell
Wu	American Heart Association	In Vivo Tracking of Stem Cells in the Ischemic Myocardium

Stanford Supported Research

PI	SPONSOR	TITLE
Do	Stanford OTL	A Novel Non-Invasive Device for Occluding Cerebral Aneurysms
Gold	BIO-X IIP Program Award	Modeling Muscles in Contact
Gold	Stanford-Wallenberg	Learning Radiology in Simulated Environments
Herfkens	Office of Technology Licensing	His-Solution Encoder for Diagnostic Radiological Imaging
Napel	BIO-X IIP Program Award	A Novel Transducer Array and Intelligent Software for Automated Detection of Asymptomatic Carotid Artery Stenosis

Industry Supported Research

PI	Sponsor	Title
Bammer/Stevens	Endius, Inc.	Multi-Center Study to Evaluate the Effect of Minimally Invasive Versus Open Posterolateral Lumbar Fusion Using High Res MRI
Chen	Med Immune, Inc.	In Vivo Imaging at Stanford
Fahrig	Siemen's Medical Solutions	Gated 3D DynaCT for Cardiac Applications
Fahrig	Varian Medical Systems	Correction Approaches for Amorphous Silicon Detector Non-Idealities
Gambhir	Alza Corporation	Delivery of Labeled FHBG to Animal Brain
Gambhir	Chiron Corporation	Assessing Tumor Response to Therapy
Gambhir	Intronn, Inc.	Molecular Imaging of mRNA through trans-splicing
Glazer	GE Med Systems	Magnetic Resonance Imaging (MRI) Systems
Glazer/Herfkens	GE Med Systems	Destination Digital Agreement
Glazer	GE Med Systems	GE PACS System
Glazer/Gambhir	GE Med Systems	Multi-Modality Molecular Imaging (preclinical)
Gold	GlaxoSmithKline	Sodium MRI at 3.0T for Drug Discovery
Guccione	Canon	Photoacoustic Tomography for Early Detection of Cancer
Hofmann	Cook Incorporated	Study of IVC Filter Retrieval without Interim Filter Manipulation Utilizing the Gunther Tulip Vena Cava Filter
Hofmann	Vivant Medical, Inc.	Feasibility Study on Microwave Ablation of Metastatic Bone Tumors for Palliation of Pain
Ikeda	U-Systems	3D Full Field Whole Breast Ultrasound: Development, Testing and Application to Breast Cancer Diagnosis
Marks	Concentric Medical, Inc.	A Multinational Controlled Registry to Evaluate the Concentric Merci Retriever System
Marks	Diversified Diagnostic Products, Inc.	Data Related to Respiratory Slowing and Apnea for Xenon-CT Imaging for the Purpose of Measuring Cerebral Blood Flow (CBF) in Patients with a Spectrum of Neurological Conditions
Marks	Micrus Corporation	Safety and Efficacy of Cerecyte Polymer Filled Coil in Patients with Intracranial Aneurysms
Napel	Siemens Corporate Research	Interventional Room of the Future
Pelc	GE Med Systems	Inverse Cone Beam CT
Rubin	Med Institute, Inc.	Zenith TX2 Thoracic TAA Endovascular Graft
Sze	Cook Incorporated	The Zilver PTX Drug Eluting Vascular Stent in the Above the Knee Femoralpopliteal Artery
Sze	Cook Incorporated	Zilver Vascular Stent in the Iliac Arteries
Sze	Cook Incorporated	Zenith TX2 Thoracic TAA Endovascular Graft
Sze	W.L. Gore & Associates	Compare the Use of the Bifurcated EXCLUDER Endoprosthesis to Open Surgical Repair in Treatment of AAA
Sze	W.L. Gore & Associates	Evaluation of GORE TAG Thoracic Endoprothesis for Treatment of Descending Thoracic Aorta
Sze	W.L. Gore & Associates	IDE for Use of GORE TAG Thoracic Endoprosthesis in Subjects with Descending Thoracic Aortic Aneurysms
Sze	W.L. Gore & Associates	Evaluation of the GORE TAG Thoracic Endoprothesis for Treatment of Descending Thoracic Aneurysms
Sze	W.L. Gore & Associates	Evaluating the Use of the Thoracic EXCLUDER Endoprosthesis in Descending Thoracic Aortic Diseases
Wu	Pfizer Pharmaceuticals	The Role of Statins in Cardiac Stem Cell

Radiology Scientific Research Personnel
Faculty, Staff, and Students

Front Row (l-r): Elizabeth Gill, Susan Kopiwoda, Jianghong Rao, Shawn Chen, David Paik, Sandy Napel, Rebecca Fahrig, Kim Butts Pauly, Gary Glazer, Gary Glover.
Row 2 (l-r): Tiffany Chung, Yi-Shan Yang, Padma Sundaram, Tejas Rakshe, Shaohua Sun, Chunlei Liu, Jongduk Baek, Sung Won Yoon, Misung Han, Kristin Granlund, Anne Marie Sawyer, Wendy Baumgarten, Sharon Pollio.
Row 3 (l-r): Shen Woo Lee, Peter Olcott, Dirk Mayer, Rexford Newbould, Markus Kukuk, Stefan Skare, Andrew Holbrook, Jean Chen, Lena Kaye, Jason Hsu, Romi Samra, Garry Chinn, Jian Zhang.
Top Row (l-r): Michelle Christierson, Suzi Kosher, Viola Rieke, Mohammed Namavari.

Radiology Scientific Research Personnel
Faculty, Staff, and Students

Lucas Center 2006

Front Row (l-r): Norbert Pelc, Sam Gambhir, Tom Brosnan, Mike Moseley, Fred Chin, Craig Levin, Susan Singh, Marc Alley, Maggie Bos.

Row 2 (l-r): Neal Bangerter, Bronislava Sigal, Maksim Pashkevich, Andrew Gentles, Julie Ruiz, Sandra Rodriguez, Lewis Chin, Jinha Park, Priti Balchandani, Sam Mazin, Donna Cronister.

Row 3 (l-r): Aiming Lu, Murat Aksoy, Tim Doyle, Carmel Chan, Michael McDonald, Marowan Zakhour, Maurice Van den Bosch, David Dick, Andrew Lamb, Sandra Horn.

Top Row (l-r): Muru Subbarayan, Betsey Sowder, Mary Bobel, Jintau Po, Samira Guccione.

Radiology Scientific Research Personnel
Faculty and Staff

FACULTY

Gary M. Glazer, M.D.

Gary H. Glover, Ph.D.

Roland Bammer, Ph.D.

Kim Butts-Pauly, Ph.D.

Xiaoyuan (Shawn) Chen, Ph.D.

Rebecca Fahrig, Ph.D.

Sam Gambhir, M.D., Ph.D.

Samira Guccione, Ph.D.

Brian Hargreaves, Ph.D.

Robert J. Herfkens, M.D.

Craig Levin, Ph.D.

Michael E. Moseley, Ph.D.

Sandy Napel, Ph.D.

David Paik, Ph.D.

Norbert J. Pelc, Sc.D.

Sylvia K. Plevritis, Ph.D.

Jianghong Rao, Ph.D.

Daniel M. Spielman, Ph.D.

ADMINISTRATIVE AND SUPPORT STAFF

Mary Bobel, M.B.A.

Maggie Bos

Nancy Bucy

Rick Carillo

Michelle Christierson

Donna Cronister

Debra Frank

Elizabeth Gill

Sofia Gonzales

Sandra Horn

Susan Kopiwoda, M.S., M.P.H.

Suzi Kosher

Marlys Lesene

Sharon Pollio

Kala Raman

John Reuling

Lanzie Rivera

Julie Ruiz, Ph.D.

Monique Schareck, M.H.A.

Susan Singh

Betsey Sowder

Susie Spielman

Lakeesha Winston

Wei Xiong

SCIENTIFIC STAFF

Marcus Alley, Ph.D.

Kristi Aruzza, B.S., R.T. (CNMT)

Neal Bangerter, Ph.D.

Wendy Baumgardner, RVT, LATg

Thomas Brosnan, Ph.D.

Danye Cheng

Zhen Cheng, Ph.D.

Frederick Chin, Ph.D.

Garry Chinn, Ph.D.

Steven Choi, B.S.

David Clayton, Ph.D.

Mangal Dandekar, M.D.

Abhijit De, Ph.D.

David Dick, Ph.D.

Tim Doyle, Ph.D.

Aihua Fu, Ph.D.

Arundhuti Ganguly, Ph.D.

Andrew Gentles, Ph.D.

Lina He, Ph.D.

William Johnsen

Keshni Kumar, R.T.

Andreas Loening, Ph.D.

Dirk Mayer, Ph.D.

Mohammed Namavari, Ph.D.

Rexford Newbould, Ph.D.

Linda Novello, R.T.

Peter Olcott, Ph.D.

Laura Pierce, M.P.A., R.T.

Paulmurgan Ramasamy, Ph.D.

Bhargav Raman

Pritha Ray, Ph.D.

Viola Rieke, Ph.D.

Sandra Rodriguez, R.T. (R)(MR)

Jarrett Rosenberg, Ph.D.

Ruminder Samra, R.T.

Anne Marie Sawyer, B.S., R.T. (R)(MR)

Meike Schipper, M.D.

Greig Scott, Ph.D.

Bronislava Sigal, Ph.D.

Stefan Skare, Ph.D.

Marc Sofilos, R.T.

Norbert Stroebel, Ph.D.

Muru Subbarayan, Ph.D.

Gopal Sundaresan

Jeffrey Tseng, M.D.

Yingyun Wang, B.S.

Lars Wigstrom, Ph.D.

Joseph Wu, M.D., Ph.D.

Yishan Yang, Ph.D.

Marowan Zakhour, M.D.

Radiology Scientific Research Personnel
Students and Visitors

POSTDOCTORAL FELLOWS

Weibo Cai, Ph.D.
Feng Cao, Ph.D.
Qizhen Cao, Ph.D.
Carmel Chan, Ph.D.
Kai Chen, Ph.D.
Nga-Wai (Tiffany) Chung, Ph.D.
Alireza Ebrahimejad, Ph.D.
Byard Edwards, M.D., Ph.D.
Daniel Ennis, Ph.D.
Tony Faranash, Ph.D.
Olivier Gheysens, Ph.D.
Gayatri Gowrishankar, Ph.D.
Frezghi Habte, Ph.D.
Gloria Huang, M.D.
Mei Huang, Ph.D.
Jung-Jin (Jason) Hsu, Ph.D.
Andrei Iagarau, M.D.
Thies Jochinsen
Shay Keren, Ph.D.
Malika Larabi, Ph.D.
Ha-Young Lee, Ph.D.
Sheen-Woo Lee, M.D.
Jelena Levi, Ph.D.
Zibo Li, Ph.D.
Zongjn Li, Ph.D.
Michael Lim, Ph.D.
Chunlei Liu, Ph.D.
Erin Liu, Ph.D.
Aiming Lu, Ph.D.
Amelie Lutz, M.D.
Michael McDonald, Ph.D.
Rex Newbold, Ph.D.
Gang Niu, Ph.D.
Jinha Park, M.D., Ph.D.
Maxim Pashkevich, Ph.D.
Laura Pisani, Ph.D.
Cesar Rodriguez, Ph.D.
Justus Roos, Ph.D.
Lewis Shin, M.D.
Bryan Smith, Ph.D.
Matus Straka, Ph.D.
Maurice VandenBosch, M.D.
Hui Wang, Ph.D.
Yingbing Wang, Ph.D.
Juergen Willmann, M.D.
Zuyong Xia, Ph.D.
Fei Xiao, Ph.D.
Xiaoyan Xie, Ph.D.
Yun Wu, Ph.D.
Zhanghong Wu, Ph.D.
Shahriar Yaghoubi, Ph.D.
Hequan Yao, Ph.D.
Yan Zhang, Ph.D.

GRADUATE STUDENTS

Arpit Aggarwall, M.S.
Murat Aksoy, M.S.
Jongduk Baek, M.S.
Priti Balchandani, M.S.
Regina Bouwer, M.S.
Jean Chen, M.S.
Ian Chen, M.D./Ph.D. student
Angela Foudray, M.S.
Kristi Granlund, M.S.
Meng Gu, M.S.
Misung Han, M.S.
Andrew Holbrook, M.S.
Yanle Hu, M.S.
Elena Kaye, M.S.
Susan Shu-An Lin, M.S.
Cyrus Jame, M.S.
Caroline Jordan, M.S.
Sonal Josan, M.S.
Ajay Joshi, M.S.
Bennie Keck, M.S.
Christine Law, M.S.
Yakir Levin, M.S.
Calvin Lew, M.S.
Pasheel Lillaney, M.S.
Susan Shu-An Lin, M.S.
Wenmiao Lu, M.S.
Sam Mazin, M.S.
Anders Nordell, M.S.
Michael Padilla, M.S.
Bini Pankhudi, M.S.
Manish Patel, M.S.
Rebecca Rakow M.D./Ph.D. student
Markus Prummer, M.S.
Tejas Rakshe, M.S.
Heiko Schmiedeskamp, M.S.
Anthony Sherbondy, M.S.
Leroy Sims, M.S.
Mi-Kyung So, Ph.D.
Gaurav Srivastra, M.S.
Jared Starman, M.S.
Ernesto Staroswiecki
Shaohua Sun, M.S.
Padma Sundaram, M.S.
Moriah Thomason, M.S.
Ricky Tong, M.S.
Chardonnay Vance, M.S.
Zachary Walls, M.S.
Yingbing Wang, M.S.
Jung Ho Won, M.S.
Yao-Hung Yang, M.S.
David Yerushalmi, M.S.
Sung-Won Yoon, M.S.
Adam dele Zerda
Jian Zheng, M.S.
Lei Zhu, M.S.

VISITING RESEARCHERS AND SCHOLARS

Hsiao-Wen Chung, Ph.D.
Daniel Fiat, Ph.D.
Min Kyung So, Ph.D.
Yi Sun, Ph.D.
Zhengming Xiong , M.D., Ph.D.
Xianzhong Zhang, Ph.D.

UNDERGRADUATES

Tom Hope

Awards and Honors

Recipient	Award
Patrick D. Barnes	Honored as senior faculty of the year 2005-2006 for outstanding contributions to resident education, compassionate patient care, and research. Department of Radiology. Stanford University Medical Center, June 2006.
Richard A. Barth	February 2006 issue of San Jose Magazine as one of the "Silicon Valley's Top Doctors" - the only pediatric radiologist listed out of 2000 entries.
Richard A. Barth	Invited to serve on the Society for Pediatric Radiology (SPR) Board of Directors, June 2006
Weibo Cai	Awarded the Benedict Cassen Postdoctoral Fellowship from the Society of Nuclear Medicine. This award recognizes an excellent academic record and exceptional research ability.
Weibo Cai	Awarded the 2006 AMI Annual Conference Travel Award.
Weibo Cai	Awarded the 2006 Gordon Research Conference travel award.
Feng Cao	Awarded the Best Cardiovascular Young Investigator Award for her research in in vivo molecular imaging of human embryonic stem cell derived cardiomyocytes after transplantation into the ischemic myocardium.
Feng Cao	Received a Best Basic Science Poster Award at the 2005 American Heart Association meeting.
Qizhen Cao	Awarded the Dean's Fellowship for her work on "Combined Integrin siRNA Therapy and Radiotherapy of Breast Cancer".
Carmel Chan	Awarded a postdoctoral fellowship from the Susan G. Komen Breast Cancer Foundation for his project entitled "Imaging the efficacy of Heat Shock Protein 90 Inhibitors in Human Breast Cancers."
Ian Chen	Awarded the Dorothy Penrose Stout Fellowship Award in recognition of being the highest ranked American Heart Association (AHA) predoctoral fellowship award recipient in the Western States Affiliate for 2006-07.
Ian Chen	Received the American Heart Association Predoctoral Fellowship which is designed to help students initiate careers in cardiovascular research and to provide support for students conducting doctoral dissertation projects.
Ian Chen	Received the Bio-X Graduate Student Fellowship, a generous gift of an anonymous donor
Jean Chen	Received a Bio-X student travel award grant.
Bao Do	Received a Trainee Research Prize at the 91st Scientific Assembly and Annual Meeting of the Radiological Society of North America (RSNA) for his work entitled: "Metabolic Profile of the Spinal Cord by Whole Body [18F]-2-deoxy-3-fluoro-d-glucose (18F-FDG) Positron Emission Tomography (PET)/CT Imaging"
Byard Edwards	2006 Roentgen Resident/Fellow Research Award from the Radiological Society of North America (RSNA)
Byard Edwards	$2000 Travel Award from the Society of Uroradiology Annual Meeting, Kauai, HI
Rebecca Fahrig	Sylvia Sorkin Greenfield Award for the best non-radiation therapy paper in Medical Physics for "Performance of a static-anode/flat-panel x-ray fluoroscopy system in a diagnostic strength magnetic field: a truly hybrid x-ray/MR imaging system."
Dominik Fleischmann	Journal of Radiology Editor's Recognition Award for reviewing with distinction for 2005.

Dominik Fleischmann	Hounsfield Award for outstanding scientific paper in cross sectional imaging. (given by SBCT/MR).
Angela Foudray	Awarded an NIH-NIBIB travel award to attend the 2005 IEEE Medical Imaging Conference in Puerto Rico.
Angela Foudray	Awarded a full scholarship to attend the 2005 Molecular Imaging Summer School in Crete September 12-17.
Cynthia Freeman	Her paper named the best paper by a Member in Training: "The advantages of "Direct" image reformatting in CT Urography" Presented at the SUR annual meeting, Kauai, Hawaii, March 2006.
Sam Gambhir	Awarded a Minnie as one of the Most Influential Radiology Researchers of 2005 by AuntMinnie.
Sam Gambhir	Received the Hounsfield Medal from Imperial College, London, for his scientific achievements in biomedical imaging. The medal is awarded in memory of Sir Godfrey Hounsfield who shared the 1979 Nobel Prize for Physiology or Medicine for his invention of the CT scanner. Medal presented February 23, 2006.
Sam Gambhir	At the Society of Nuclear Medicine 53rd Annual Meeting Dr. Sam Gambhir received the Aebersold Award for outstanding achievement in basic nuclear medicine science.
Taly Gilat	Recipient of Trainee Research Prize at the 91st Scientific Assembly & Annual Meeting of the Radiological Society of North America (RSNA) for her work entitled: "Investigation of a Prototype Table-top Inverse-geometry Volumetric CT System".
Gary M. Glazer	President, International Society of Strategic Studies in Radiology (ISSS) 2003-2005.
Gary H. Glover	Will be inducted in National Academy of Engineering, Oct. 2006. Dr. Glover is being honored and recognized for his research and engineering in the development of computed tomography and magnetic resonance imaging. His research focuses on the physics and mathematics of improving these imaging methods. He also has made significant contributions to the engineering of systems and helped develop products that have benefited millions of patients.
Garry Gold	Received the Lauterbur award for the best MRI paper in 2006 (given by SCBT-MR)
Gary Gold	Paper made the cover of Radiology "Articular Cartilage of the Knee: Rapid Three-dimensional MR Imaging at 3.0 T with IDEAL Balanced Steady-State Free Precision - Initial Experience"
Gayatri Gowrishankar	Awarded the Ruth L Kirschstein National Research Service Award (NRSA) from Cancer Biology at Stanford, 2006
Gayatri Gowrishankar	Received a Young Investigator travel award at the 2006 Academy of Molecular Imaging annual conference.
Kate Holzbauer	Received the Holzbaur American Society of Biomechanics young scientist award in 2006
Juergen	Research Fellowship Award - Swiss Foundation Fro Medical-Biological Grants (SSMBS)
Lena Kaye	Received an ISMRM poster award nomination.
Yakir Levin	Selected by Stanford and the School of Engineering as an ARCS Scholar nominee for 2006-2007.
Susan Shu-An Lin	Named a Bradley-Alavi fellow for her research entitled "Imaging Bone Marrow Stem Cell Homing to Ischemic Myocardium."
Zibo Li	Received the Dean's fellowship award from the Stanford School of Medicine

Amelie Lutz	2006 Postdoctoral Research Fellowship from the Swiss National Science Foundation
Sam Mazin	American Heart Association Pre-doctoral Fellowship for "Research on a Cardiovascular CT Scanner"
Sam Mazin	Joel Drillings Award from the American Heart Association for "Research on a Cardiovascular CT Scanner"
Mohammad Namavari	Received the 2006 Society of Nuclear Medicine Berson-Yalow Award, for the abstract "Characterization of 131I-SKI243, a radiolabeled EGFR-tk binding ligand, and its cross reactivity for Iressa and Tarceva binding sites."
Sandy Napel	Received the Hounsfield Award for outstanding scientific paper in 2006 (given by SCBT-MR)
Laura Pisani	Ruth l. Krischstein National Research Service Awards for Individual Postdoctoral Fellows (F32) Fellowship Award from National Institute of Biomedical Imaging and Bioengineering (NIBIB)
Laura Pisani	Recipient of National Institutes of Health (NIH) Pediatric Loan Repayment Program
Guillem Pratx	Named a Bradley-Alavi fellow for his research entitled "Accelerated List-Mode 3-D-OSEM".
Guillem Pratx	Awarded a 2006 NVIDIA research fellowship
Viola Rieke	Travel Award from the Deutsche Forschungsgesellschaft (DFG) = German Science Foundation.
Geoffrey D. Rubin	Presented the 33rd Annual Benjamin Felson Lecturer, University of Cincinnati
Geoffrey D. Rubin	Presented the 70th Annual Preston Hickey Lecturer, Michigan Society of Radiology
Geoffrey D. Rubin	Named one of Top 5 Candidates as " Most Influential Radiology Researcher" by AuntMinnie.com
Anne Sawyer	SMRT's Highest award, the "Society Magnetic Resonance Technologists' Honorary Membership". 2006
George M. Segall	Presented the Taplin Memorial Lecturer at the 30th Annual Western Regional at the Meeting of the Society of Nuclear Medicine, in Copper Mountain CO 9/29 - 10/2/05.
Min-kyung So	Received a Young Investigator Travel Award at the 2006 Academy of Molecular Imaging annual conference.
Daniel Mark Spielman	Received an ISMRM teaching award for his "Methods and Applications of Clinical Spectroscopy".
Jared Starman	Stanford-National Institute of Health Graduate Training Program in Biotechnology Fellowship
Ricky Tong	Received a Stanford Medical Scholars Research Fellowship for his work in tri-fusion imaging.
Joseph Wu	Received Cardiovascular Institute Seed Grant
Joseph Wu	Selected by Stanford School of Medicine as representative for the Burroughs Wellcome Fund Career Awards for Medical Scientists.
Zhengming Xiong	His work on adenovirus was featured on the cover of Journal of Nuclear Medicine.
David Yerushalmi	His research on virtual bronchoscopy is highlighted on the Aunt Minnie website
Lei Zhu	Recipient of Trainee Research Prize at the 91st Scientific Assembly & Annual Meeting of the Radiological Society of North America (RSNA) for her work entitled: "A New Scatter Correction Method for X-ray and Volumetric CT Using Primary Modulation".

RESEARCH GROUP UPDATES

RSL Group Updates

MAGNETIC RESONANCE RESEARCH

Functional Imaging - Technology Development
Gary Glover

The functional MRI group continues to develop new methods for acquisition of functional imaging data. Projects include the development of alternative fMRI contrast methods, real-time biofeedback for training brains, 3D fMRI acquisitions, localized shimming of magnetic field imperfections, calibration of fMRI using breathholding measurements, and the development of fetal fMRI methods. In addition, we continue to play an active role as chair of the calibration working group in the FIRST BIRN schizophrenia testbed funded by the NCRR. The following are a few of the highlights; see other reports for further details.

Christine Law has been examining a recently-described and controversial approach that uses an alternative to BOLD contrast, based on hypothesized changes in populations of spins with fast and slow diffusion characteristics. The advantage demonstrated by the author of the original study, Denis LeBihan, is more rapid response to neural changes because the approach does not require the intervening step of changes in brain oxygenation to generate an NMR signal. A disadvantage is substantial reduction in sensitivity. The study is controversial because other investigators have not been able to replicate the findings. Christine has found a small effect, but no evidence that the new contrast mechanism is operable. Nevertheless, investigation is continuing.

The real-time fMRI projects include collaborations with Sean Mackey (Director of the Stanford Pain Center, Anesthesiology), Allan Reiss (Director of the Center for Interdisciplinary Brain Sciences Research, Psychiatry), Ian Gotlib, (Director of the Mood and Anxiety Disorders Lab, Psychology) and Brian Knutson, Psychology. A paper published in PNAS documents that, like normal subjects, chronic pain subjects can learn to control their perception of pain using biofeedback that is developed by the processing of brain activation in the pain network during the scan. Apparently this control ability persists for months after the scanning sessions have ended. We have begun experiments in the areas of depression, learning disorders and addiction, using the same technology to see whether subjects can learn to regulate brain regions important for these disorders.

Graduate student Yanle Hu is studying the noise propagation in 3D spiral fMRI acquisitions. Theoretically, the 3D method should have improved BOLD CNR, but noise that stems from basal metabolism in the brain is greater in 3D methods than the counterpart 2D techniques. Yanle is exploring the basics of this phenomenon and has developed several methods for its implementation. Signal to noise ratio improvements of 80% have been demonstrated.

Jung Jiin (Jason) Hsu, a postdoc, has further advanced his localized shim coil approach for fMRI, that improves the homogeneity of the magnetic field in the vicinity of the frontal orbital region of the brain. Most recently, he has developed a dynamic method that changes the shim characteristics for each imaging slice, thereby reducing the signal loss over a larger region of the brain. He has developed a set of hardware and software to control this new approach and is designing new coils for the purpose.

In addition, he has developed a rapid T1 mapping method with which functional contrast has been obtained which is yet another method of fMRI that shows promise in reducing the deleterious signal dropout problem in the frontal regions of the brain.

Postdoc Laura Pisani continues her project on the use of neuronal activity measured by fMRI as a surrogate marker for fetal viability in cases of intra-uterine growth retardation (IUGR). This is a challenging project because of the issues of fetal motion and difficulty in stimulating the fetus. Preliminary results show promise for the use of an oxygen challenge to the mother as a way of observing the changes in vascular reactivity in the fetal brain. She was awarded an NIH fellowship grant application. This is a collaboration with Richard Barth, pediatric radiology section chief; OB clinicians; and Roland Bammer in the RSL.

In a related project, Chardonnay Vance is a grad student at UC-Berkeley and Stanford, who is studying aging processes as well as the biochemistry of placental membranes. Using measurements of NMR relaxation times and other parameters in vitro and in vivo, she wants to understand the various transport mechanisms in the placenta in health and IUGR.

Rebecca Rakow-Penner, a grad student in biophysics and a second-year medical student, is examining the use of functional methods to characterize breast cancer and is finishing a paper on the relation properties of breast tissue.

Moriah Thomason, grad student, has concluded a study of the use of breath holding for calibration of hemodynamic differences in subjects undergoing fMRI tasks, and the method is being adapted for use in the fBIRN. Her paper was recently published in *Human Brain Mapping*. We have started a new experiment to investigate the use of behavioral feedback to enhance the precision of the method. Meanwhile, she is finalizing her dissertation on the working memory of children and adults and will be joining the group as a postdoc, working collaboratively with Ian Gotlib on depression in children.

fMRI group (l-r) front row: Allyson Rosen, Jin Hyung Lee, Rebecca Rakow-Penner, Christine Law. Back row: Chardonnay Vance, Paul Mazaika, Joelle Barral, Sean Mackey, Laura Pisani, Yanle Hu, Jung-Jiin Hsu, Jongho Lee, GHG. Not shown: Catie Chang, Funiko Hoeft, Moriah Thomason.

Functional "Microvascular" Neuroimaging

Roland Bammer and Michael Moseley

Magnetic resonance imaging (MRI) continues to advance the state-of-the-art in adult and pediatric neuroimaging. This last year has further advanced functional MRI, which can map and measure brain tissue water diffusion rates and direction, perfusion of blood, and the brain's response to many functional activation tasks (such as vascular responses to mild reversible stresses) in a large number of diseases. We are planning to use the new 7 Tesla MRI scanner to refine new tools of high-field and high-speed MRI to focus on disease processes in "brain attacks" (cerebral stroke) using diffusion MRI (DWI), tissue perfusion mapping (PWI), as well as the new field of mapping the brain and white matter connectivity in both adults and in children (DTI). During the past year we've made significant progress in developing functional imaging technologies in several key areas under the general title of "microvascular" imaging. These include diffusion and perfusion techniques for both imaging of acute stroke and for imaging of white matter structure and integrity. By responding to the needs of our collaborators and colleagues here at Stanford and worldwide, we have found that diffusion and perfusion techniques have significantly advanced far beyond the experimental arena into everyday, routine clinical applications in a wide variety of fields where they are being actively and effectively used in numerous self-initiated and collaborative studies. The coming year will further advance our MR imaging tools and sharpen our focus on the critical clinical issues of detecting brain attacks with new experimental and clinical MR methods to predict eventual brain injury, to further map how the brain and spine are "wired," to understand the complex physiological stresses and changes that the brain experiences during stroke, and to extend these tools to better evaluate evolving therapies.

Roland Bammer is an established radiology faculty member at the Lucas Center and an assistant professor as well as imaging physicist for pediatric radiology. He has created several key collaborations with the Departments of Neurology and Pediatrics and has already initiated an active pediatric DTI program on the Lucile Packard Children's Hospital MRI scanner. Roland was a recent visiting professor at the Bosporus University, Istanbul, Turkey and is also a "University Docent" at the University of Graz, Austria, where he teaches for 3 weeks per year. Roland has two funded peer-reviewed grants from the NIH, directs one multi-center trial, and has been named as "key personnel" on ten others. Mike Moseley is the past president of the International Society of Magnetic Resonance in Medicine (ISMRM) and has had two key grants funded recently, one of which is an NCRR grant for a $2M experimental GE 7T MRI scanner. He also sits on different NIH study sections.

The neuroimaging team (shown) remains involved in white matter tensor "fiber-tracking" neuroimaging projects as well as building collaborative programs. Thies Jochimsen has just recently extended his career as a research associate at the Max Planck Institut in Leipzig. Jian Zhang is a second-year graduate student actively involved in 3D volume spiral imaging for diffusion applications. Chunlei Liu is a first-year post-doctoral scholar who has submitted a competitive-scored K00 award from the NIH on high-field applications of DWI. Scott Nagle is a clinical fellow working on cardiovascular applications in MR together with Roland. Murat Aksoy is a third-year graduate student working with Roland on the exciting applications in fiber tractography and in motion correction. Rexford Newbould is a research associate with a background in IC design and is currently involved in MR post-processing of diffusion and perfusion data together with Roland. Lanzie Rivera is our administrative associate and Clinical Coordinator. Stefan Skare is a research associate and visiting scholar from Sweden working with Roland. Stefan, together with his incoming graduate students from Sweden, is focused on multi-shot MR sequences for high-resolution diffusion and perfusion studies. In September, our group will grow further. Samantha Holdsworth from New Zealand, an expert in sodium MRI, will join us as a postdoctoral fellow. Matus Straka, from the Vienna General Hospital (Austria) and the Computer Graphics Department of the University of Vienna, will start as a new research associate focusing on parallel computing issues for image reconstruction and quantitative parameter mapping. Heiko Schmiedeskamp, a graduate student from the ETH in Zurich, will join us as a visiting researcher.
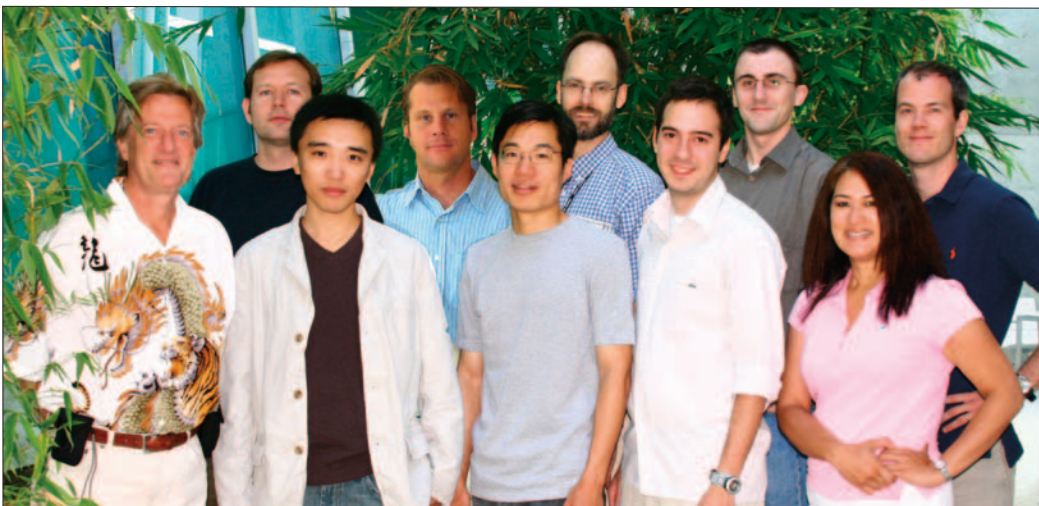
(l-r) Mike Moseley, Thies Jochimsen, Jian Zhang, Roland Bammer, Chunlei Liu, Scott Nagle, Murat Aksoy, Rexford Newbold, Lanzie Rivera, and Stefen Skare.

In Vivo Spectroscopy and Multinuclear Imaging

Daniel Spielman

We have continued our research in the development of novel magnetic resonance spectroscopy (MRS) and spectroscopic imaging (MRSI) techniques. Areas of particular focus included optimized techniques for high field (3 T) proton spectroscopy of the brain, breast, and prostate, and hyperpolarized 13C imaging and spectroscopy. We have furthered our work in parallel imaging with projects on TurboSENSE imaging, improved coil calibration methods for phase contrast SENSE, and phased-array spectroscopic imaging (MRSI).

High field MRI scanners (≥3T) offer fundamental advantages for in vivo spectroscopy including improved SNR and increased chemical shift dispersion. However, these theoretical gains can only be achieved with careful attention to the technical constraints imposed by gradient and RF system limitations. Much of our work over the past year has focused on novel RF pulse designs. New Rf pulses for proton MRSI include a matched-phase dualband spatial-spectral 90-180 pulse pair, optimized Rf pulses for robust lipid suppression, and 2D variable-density spiral RF excitation. We have also continued our collaboration with UCSF on the development and evaluation of new 1H MRSI methodologies for the assessment of developmentally-delayed children.

Our work on the development of rapid spectroscopic imaging of hyperpolarized 13C has resulted in two conference abstracts and one submitted manuscript. Hyperpolarized 13C is an exciting new technology capable of directly probing key metabolic pathways by providing an increased signal several orders of magnitude greater than previously available from 13C-
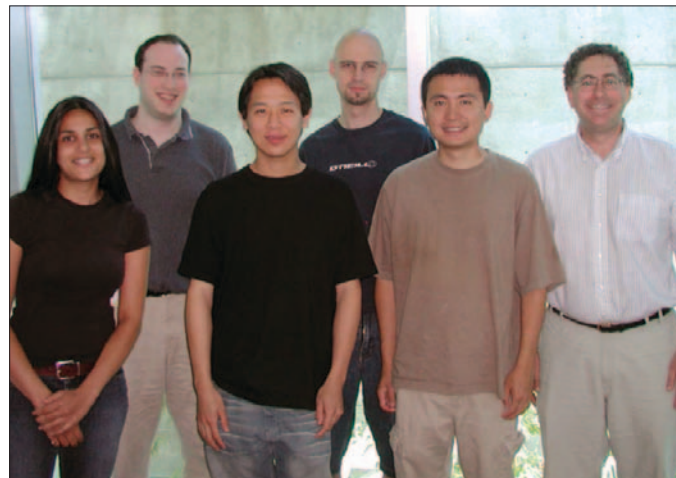
MR Spectroscopy Group (l-r) Priti Balchandani, Yakir Levin, Calvin Lew, Dirk Mayer, Meng Gu, Dan Spielman

labeled compounds injected into the body. This work is being done in collaboration with GE Healthcare.

There have been no major changes in personnel this year. However, one item of note is that Yakir Levin has received an ARCS (Achievement Rewards for College Scientists) Foundation Graduate Fellowship for 2006-2007. ARCS fellowships "recognize, honor and encourage outstanding students ... who show exceptional promise of making a significant contribution to the scientific and technological strength of the nation." Congrats Yakir!

INTERVENTIONAL AND OPEN MRI

KIM BUTTS-PAULY

A major focus of the group has been to develop interventional MRI methods for the treatment of cancer in the prostate, breast, and liver. Thermal ablation is a particularly promising method for the minimally invasive treatment of cancer. MRI is an ideal guidance modality because it can measure tissue temperature during the procedure. We have been developing improvements in the imaging methods for MR thermometry of heated and frozen tissue. We are developing methods to make MR thermometry less sensitive to tissue motion. In addition, we have been developing improved imaging methods of ultrashort T2 tissues with eddy current calibrations and novel RF pulses. Our goal has been to better image frozen tissues, but these methods are also applicable to imaging ultrashort T2 tissues such as bone, tendons, and ligaments. We have also been focused on the post-ablation assessment of tissue. Particularly interesting is the fact that thermally ablated tissue has a reduced ADC by 37%, whether it was frozen or heated. In addition, we have been correlating contrast enhanced imaging and diffusion-weighted imaging after thermal ablation with histology. With our collaborators in Electrical Engineering, we have developed innovative ultrasonic transducers based on capacitive ultrasonic transducers (CMUTs) for high intensity ultrasound treatment of liver and renal lesions. This year, we plan to team up with General Electric to develop a handheld focused ultrasound system for treating liver and renal cancers.

A second focus of the group has been to facilitate use of the open MRI system in innovative ways, such as for dynamic imaging of the knee with our collaborators in Radiology and Mechanical Engineering and for studying swallowing with our collaborators in Otolaryngology. A third focus of the group is to improve MR imaging methods around metallic devices, such as pins, screws, and total hip replacments.
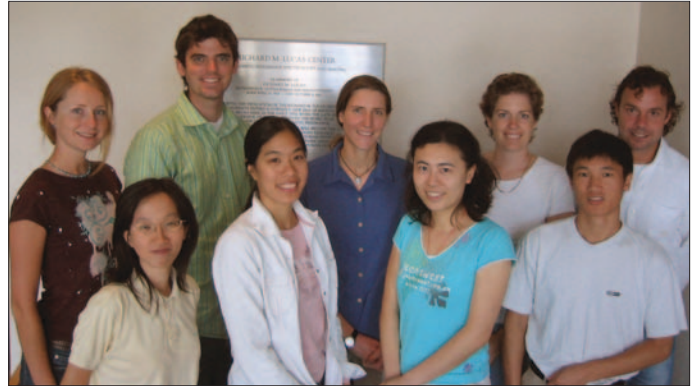
Interventional and Open MRI group: Front Row (l-r): Erin Liu, Serena Wong, Jean Chen, Aiming Lu; Back Row (l-r): Elena Kaye, Andrew Holbrook, Viola Rieke, Kim Butts Pauly, Maurice Van den Bosch.

Body MR Imaging

BRIAN A. HARGREAVES

The body MR imaging group addresses applications of MRI to body imaging. Our research includes abdominal, cardiovascular, breast, and musculoskeletal imaging. We collaborate with clinical faculty, engineering faculty, and GE's Applied Sciences Laboratory.

Wenmiao Lu has worked on rapid imaging projects such as robust multi-echo Dixon-based fat/water separation techniques that will significantly reduce scan times for body and musculoskeletal applications. This is important for breath-held scanning, where scan times currently limit the spatial resolution that can be achieved in 3D images. Misung Han has developed cartilage segmentation software and validated new contrast mechanisms for knee imaging. More recently Misung investigates parallel imaging techniques to significantly increase frame rates in dynamic contrast-enhanced breast imaging, which will result in more accurate diagnosis and classification of cancerous tumors. Anthony Faranesh is developing and validating rapid MR oximetry techniques that may be used to assess tumor hypoxia, which is an important predictor of response to chemotherapy. Ernesto Staroswiecki and Neal Bangerter are involved in developing sodium imaging of cartilage at 3.0T, in collaboration with Dr. Garry Gold. Reduced sodium levels are an important indicator of cartilage degeneration. This work will combine sodium imaging with standard proton MRI, with overlayed images providing additional information. Kristin Granlund recently joined our group and will be working on fast and motion-compensated MR techniques for imaging of the liver.

We also have collaborations with Dr. Bruce Daniel and Dr. John Pauly in breast MRI research. One of our major develop-

ments has been a fully-bilateral breast imaging protocol, which we hope becomes the standard patient protocol at the hospital. Simultaneous bilateral breast imaging will mean most patients only have to have a single MR exam, rather than the current multi-exam procedure. Anthony Faranesh is also investigating more accurate perfusion models for contrast kinetics in tumors, which will ultimately be integrated with the clinical hospital protocols. We are also working with Drs. Lewis Shin, Chris Beaulieu and Brooke Jeffrey to develop MR colonography at 3.0T. Finally, we continue to support the imaging components of numerous biomechanics projects in collaboration with Dr. Thomas Andriacchi and Dr. Nicholas Giori. These projects have a common goal of investigating the origins of osteoarthritis, for which MRI is an important diagnostic tool.
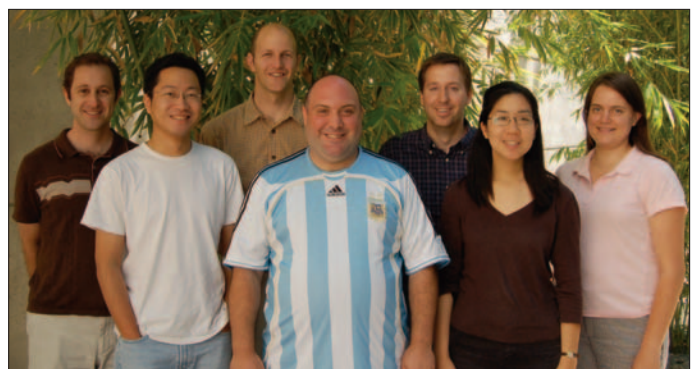
Body MR Imaging (l-r): Anthony Faranesh, Wenmiao Lu, Brian Hargreaves, Ernesto Staroswiecki, Neal Bangerter, Misung Han, Kristin Granlund.

Advanced X-Ray Techniques
X-Ray Guidance of Interventional Procedures

Rebecca Fahrig

Dr. Fahrig's research addresses x-ray guidance of interventional procedures, and x-ray system development continues in both the Axiom Lab and the Advanced X-Ray Imaging Lab.

Work continues to improve the image quality of C-arm CT images, with further developments on truncation artifact reduction (abstract by Starman) and scatter correction (abstract by Zhu). A detailed investigation of image quality issues has led to the overall improvement in low-contrast detectability, and has been investigated in depth (abstract by Strobel). We have also developed and optimized acquisition protocols for the broad spectrum of applications for which 3D imaging in the interventional suite would be useful, such as the visualization of stents in the superficial femoral artery (abstract by Ganguly) and imaging during TIPS. Our work in the area of retrospectively-gated cardiac C-arm CT, the first system to implement this approach in the U.S., also continues with new algorithms for improved temporal resolution (abstract by Pruemmer, supervisor: Dr. Joachim Hornegger, University of Erlangen) and noise reduction approaches (abstract by Wigström). The potential for 3D imaging during radiofrequency ablation of atrial fibrillation in the cardiac interventional suite is an exciting new direction of in-vestigation, and our first volunteer trial is underway. Image optimization work is funded by the NIH and benefits from a close collaboration with Siemens Medical Solutions, AX Division and with Varian Medical Systems. The cardiac C-arm CT work is a project sponsored by Siemens Medical Solutions, AX Division.

The group's work in the area of new reconstruction approaches for CT acquisitions has expanded to include the application of level-sets to reconstruction of sparse data sets, with potential application in cardiac and lung imaging (abstract by Yoon).

The X-Ray/MR project continues, focusing on applications that use the digital flat panel fluoroscopy system integrated into the bore of an interventional MR system. The work was recently awarded the Sylvia Sorkin Greenfield Award for Best Paper (non-radiation dosimetry) published in the journal *Medical Physics* in 2005. Clinical studies looking at MR imaging for cystography in infants (abstract by Vasanawala) and dual-mode imaging for hysterosalpingogram are nearing completion. With the design of a new hybrid geometry underway, this project is also moving into the area of cardiac applications.

Inverse Geometry CT and Conventional CT

Norbert Pelc

Work led by Dr. Pelc in the area of conventional and inverse geometry CT is aimed at understanding the basic limitations in current systems and the development of inverse-geometry CT (IGCT), which is an advanced CT platform that uses an inverted imaging geometry.

Our long-term aim is to push the limits in CT performance and to aid in the development of new applications. Currently our main project is to develop a system that can image an arbitrarily thick section of anatomy (e.g., an entire organ) in a single fast rotation while producing uncompromised image quality and outstanding dose efficiency. The specific approach we are pursuing employs an inverse geometry (therefore the term IGCT), with one critical aspect being a distributed x-ray source whose length is comparable to the thickness of the section being imaged. The approach presents many opportunities, and we have already demonstrated excellent spatial resolution and complete freedom from cone beam artifacts (which can plague conventional systems when they try to image a thick region in a single scan). IGCT also presents a number of problems in the image reconstruction step. One is an increased computational burden that arises from the fact that the IGCT data greatly oversamples the object. This year we explored an algorithm that greatly reduces the computational burden by first efficiently extracting the information from all the raw data to produce a much smaller data set that can then be processed using conventional algorithms (Mazin abstract). We also developed a variant of the conventional fan beam reconstruction algorithm that avoids the "rebinning" step in our standard processing (Baek abstract).

We believe we are ready to embark on research to develop a full size prototype IGCT system and submitted a proposal to the NIH, together with GE, for funding for this work. We were gratified that the proposal received an excellent score, and we expect the funding to begin at the end of 2006.
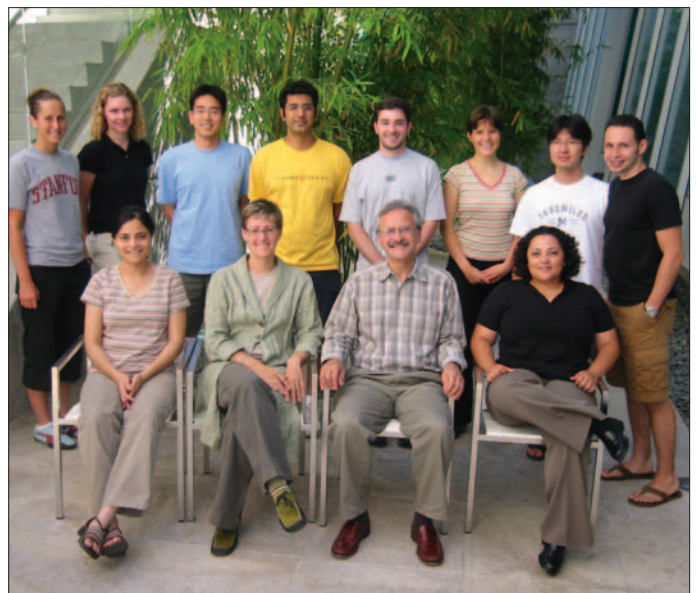
Inverse Geometry CT group, (l-r) Front row: Arun Ganguly, Rebecca Fahrig, Norbert Pelc, Marlys Lesene. Back row: Erin Girard, Caroline Jordan, Sung-Won Yoon, Persheel Lillaney, Jared Starman, , Jongduk Baek, Sam Mazin.

IMAGE ANALYSIS, BIOINFORMATICS, SYSTEMS BIOLOGY, AND PROTEOMICS
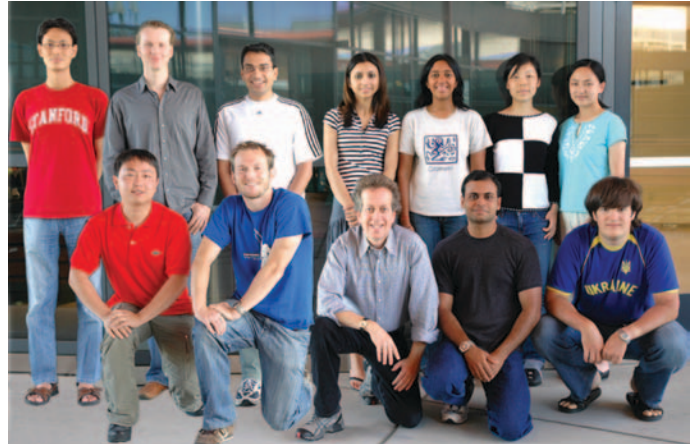
IMAGE DISPLAY AND ANALYSIS

SANDY NAPEL

Our group addresses the field of image analysis, which has become increasingly important because the number of images per patient scan has increased dramatically and now numbers in the thousands. The group focuses on volumetric visualization, structure segmentation, quantitative analysis, and computer-aided detection of lesions.

Although his group works with many colleagues both within and also outside of the Radiology Department, the members of our group are active participants in on-going funded research. Together, we have contributed many solutions to the problems of volumetric visualization, including displays for virtual colonoscopy, methods for displaying complex vascular trees in a single image, and techniques for simultaneous rendering of PET and CT data. In addition, we have published several approaches to computer-aided detection of lesions, such as colonic polyps, precursors of cancer, pulmonary nodules, and other tumors targeted with PET sensitive tracers.

We are also busy incorporating these diagnostic radiology methods into the real-time environment of the cath-angio laboratory, and have illustrated new techniques, which require less iodine contrast material, radiation, and imaging time, for navigating catheters into locations where localized therapies can be administered. We see the future of radiology as benefiting from the continuously increasing "computations/dollar" in computing technology, as we continue to refine and evaluate these techniques and apply them and their derivatives to new areas, such as automated and operator-independent determination of carotid artery stenosis using ultrasound.

Image Display and Analysis Group, (l-r) Top Row: Johann Won, Markus Kukuk, Tejas Rakshe, Bindi Pankhudi, Padma Sundaram, Shaohua Sun, Rong Shi. Bottom Row: Feng Zhuge, Anthony Sherbondy, Sandy Napel, Ajay Jayant Joshi, Gennadiy Chuyeshov and, not pictured: Bhargav Raman, Raghav Raman.

IMAGING BIOINFORMATICS

DAVID PAIK

The imaging bioinformatics lab's research interests lie at the intersection of radiology, molecular biology and informatics. We focus on developing and validating computational methodologies for extracting useful information content from anatomic, functional and molecular images, drawing upon image processing, computer vision, computer graphics, computational geometry, machine learning, biostatistics, modeling and simulation. The lab also aims to integrate image-based information with non-imaging biomedical information such as genomics and proteomics.

In the lab's first year, several new members have joined. Postdoc Jiantao Pu has developed novel algorithms for robust 3D segmentation of the lung from CT images for CAD as well as a novel lung nodule detection algorithm. He is beginning work on biologically informed modeling of pulmonary vasculature and bronchi. CS graduate student Arpit Aggarwal has developed a classification scheme for lung nodules that greatly improves detection performance through a novel shape analysis. CS graduate Shradha Budhiraja has developed sensitive methods and software for image-based quantification of tumor response to the inactivation of the RAS and MYC oncogenes. EE graduate student, Nandhini Santhanam, has worked on improvements to prior work on CAD algorithms in preparation for a multi-institutional CAD "bake-off" competition.
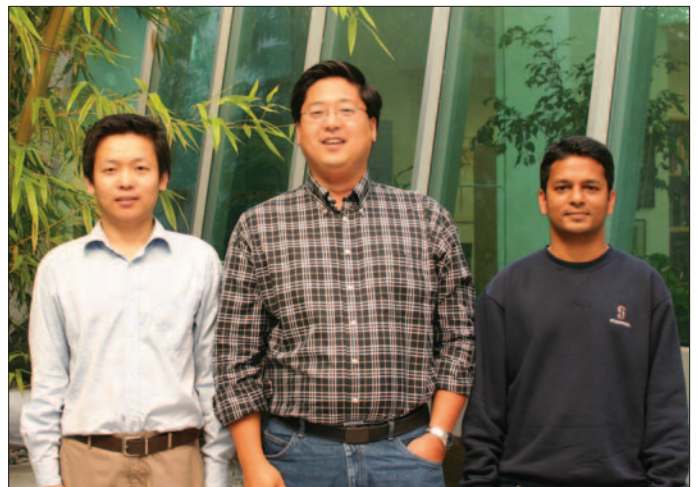
Imaging Bioinformatics Group. (l-r) Jiantao Pu, David Paik, Arpit Aggarwal.

Systems Biology of Cancer

Sylvia Plevritis

Sylvia Plevritis and her research group develop biocomputational models to better understand cancer progression. At the molecular level, they are developing computational tools to analyze high-throughput genomic and proteomic data for the purpose of identifying perturbations in molecular signaling pathways that lead to the transformation of cancer to higher grades. At the disease level, they develop mathematical models of the natural history of cancer as it progresses from non-metastatic to metastatic states. At the population level, they develop computer simulation models that estimate the long-term cancer mortality rates when asymptomatic patients are detected early with their disease by a screening test. Ultimately, their goal is to merge these three levels into a consistent understanding of cancer progression and identify targets to eradicate the disease.

For their work at the molecular level, Sylvia and her group
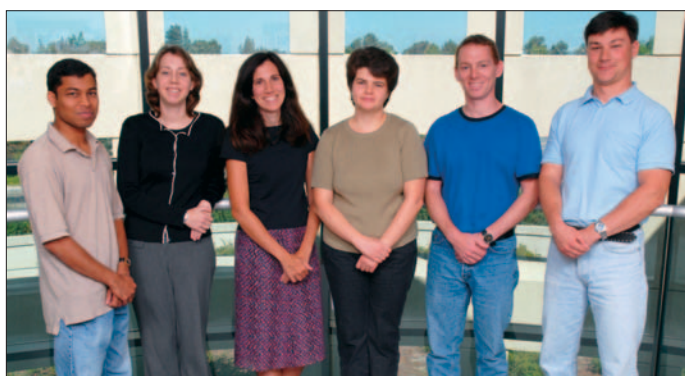
The Systems Biology of Cancer Group (l-r) Debashis Sahoo, Allison Kurian, Sylvia Plevritis, Bronislava Sigel, Andrew Gentles, Maksim Pashkevich.

have been awarded two NCI grants. The first is part of the NCI's Integrative Cancer Biology Program (ICBP), which promotes the seamless integration of experimental and computational methods to cancer biology. ICBP@Stanford involves faculty from multiple departments and aims to identify the molecular mechanism underlying neoplastic transformation in lymphoma. They are studying high throughput gene and protein expression data from tissue samples of lymphoma that has undergone transformation in both patients and mice. The second program is part of the Stanford Center of Cancer Nanotechnology Excellence focused on Therapy Response and establishes a resource Core that applies novel computational tools toward the identification of protein markers predictive of the treatment response in prostate cancer.

At the disease and population level, their work is integrated and funded under two NCI research programs. Both programs are focused on the overall goal of estimating the mortality reduction associated with cancer screening. The first program investigates the impact of mammographic screening on breast cancer mortality in the general female population and the potential impact of breast MRI as a screening test in the high risk population. The second program focuses on the impact of CT in screening for lung cancer. Both programs are affiliated with the NCI consortium Cancer Intervention and Survelliance Modeling Network (CISNET). Underlying their computational analysis of cancer screening at the population level are mathematical models that describe the progression of cancer in individual patients. These natural history models aim to predict whether or not early detection by new screening tests will have a health benefit by reducing the occurrence of advanced staged disease.

Proteomics, Biomarkers, and Nanoparticle Platforms for Imaging Therapeutics

Samira Guccione

The focus of our laboratory is translational research leading to agents for clinical use in detection, diagnosis, treatment, monitoring, and prognosis of clinical pathologies.

We take a comprehensive approach in the design of agents that span the "bench to bedside" timeline with our primary focus in development of novel agents for cancer. The research in our laboratory uses high throughput genomic and proteomic analysis on human tissue samples to identify molecular targets. Ligands that bind these molecular targets are used to develop molecular imaging and therapeutic agents. We have developed a nanoparticle-based platform for attaching these ligands; thus creating targeted imaging and/or therapeutic agents. These targeted nanoparticles are first tested in vitro and used in in-vivo animal models. We have developed probes for MRI, gamma, fluorescent, and CT imaging. Visualization and quantitative evaluation of these targeted nanoparticles in vivo will provide information on the biodistribution and accumulation of probes at the site of interest. Subsequently, we design therapeutic approaches including delivery of targeted chemo or radioactive agents or non-viral-based genes for gene therapy. This approach uses molecular imaging to identify patients who will respond to treatment prior to choosing the best treatment regiment. We have successfully used this approach to image tumor vasculature

in models of primary brain tumors, melanoma, and metastatic colon cancer. A modified form of these nanoparticles was then successfully used for an antiangiogenic therapeutic approach to the tumor vasculature.

Other research areas include tissue engineering applications in revascularization to enhance wound healing and vascularly compromised tissue; localized drug delivery systems; and biomarker development.

Proteomics group (l-r): Yi-Shan Yang, Chris Caires, Samira Guccione, Regina Bower, Steven Choi, and Michael McDonald (missing).

MIPS Group Updates

Multimodality Molecular Imaging Lab

Sam Gambhir

We are developing imaging assays to monitor fundamental cellular events in living subjects. Technologies such as micro positron emission tomography (microPET), bioluminescence optical imaging with a charge coupled-device (CCD) camera, fluorescence optical imaging, micro computerized axial tomography (microCAT) are all being actively investigated in small animal models. Our goals are to marry fundamental advances in molecular/cell biology with those in biomedical imaging to advance the field of molecular imaging. We have a particular focus on cancer biology and gene therapy. We have developed several reporter genes/reporter probes compatible with all of the above imaging modalities. These reporter genes are being used in cell trafficking models, gene therapy models, as well as in transgenic models for studying cancer biology. Assays to interrogate cells for mRNA levels, cell surface antigens, protein-protein interactions are also under active development. We are also extending many of these approaches for human clinical applications.
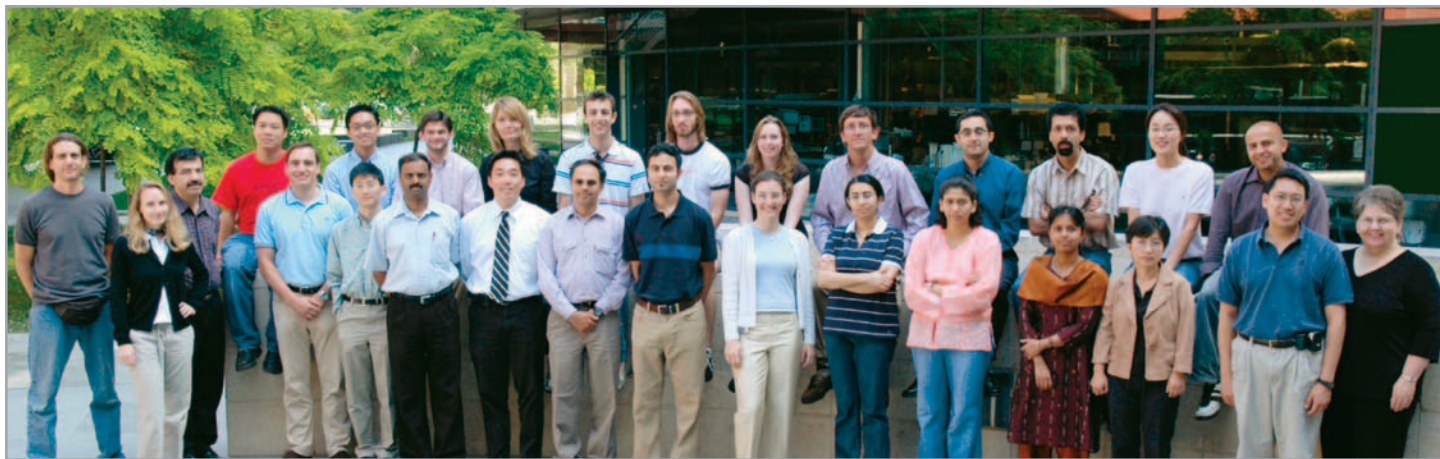
Back row (l-r): Shay Keren, Mohammad Namavari, Carmel Chan, Ricky Tong, Olivier Gheysens, Jelena Levi, Adam de la Zerda, Zac Walls, Caitlin Contag, Martin Rodriguez-Porcel, Shahriar Yaghoubi, Abhijit De, Min Kyung So, Anobel Tamruzi. Front row (l-r): Amelie Lutz, Juergen Willmann, Zhen Cheng, Sundaresan Gobalakrishnan, Jinha Park, Sam Gambhir, David Yerushalmi, Meike Schipper, Sunetra Ray, Mangal Dandekar, Pritha Ray, Wei Xiong, Jeff Tseng, Elizabeth Gill.

Cellular and Molecular Imaging Lab

Jianhong Rao

The Rao lab works at the interface of biology and chemistry, combining synthetic and physical organic chemistry and molecular biology with imaging techniques like fluorescence microscopy and whole body fluorescence/bioluminescence imaging. We work on a wide range of projects. A typical project evolves from the hands of the chemist, who synthesizes the probes into the hands of the biologist who proceeds to test the probes in cells and/or living animals. Ongoing projects include: (a) development of nanosensors for imaging and detection of tumour cells, in which a major advancement was achieved with the successful preparation of self-illuminating quantum dots, using the naturally occurring process of Bioluminescence Resonance Energy Transfer (BRET) (ref paper); (b) visualizing RNA and RNA splicing in vivo using two methods--one in which a ribozyme or RNA enzyme that catalyzes RNA splicing is linked to reporter systems and a second, more direct method, to visualize RNA localization using RNA aptamers; and (c) developing a probe for imaging β-Lactamase expression in animals.

Cellular and Molecular Imaging Lab (l-r), front row: Gayatri Gowrishankar, Tiffany Chung, Yan Chang; back row: Jianhong Rao, Hequan Yao, Fei Xiao, Zurong Xia, MinKyung So.

Molecular Imaging Instrumentation Lab

CRAIG LEVIN

Our research interests involve the development of novel instrumentation and algorithms for in vivo imaging of molecular signals in humans and small laboratory animals. These new "cameras" image radiation emissions from molecular probes designed to target specific molecular processes associated with disease in cells located deep within tissues of living subjects. The goals of the instrumentation projects are to push the detection efficiency and spatial, spectral, and temporal resolutions as far as physically possible. The algorithm goals are to understand the physical system comprising the subject tissues, radiation transport, and imaging system, and to provide the best available reconstructed image quality and quantitative accuracy. The work involves computer modeling, novel position sensitive sensors, readout electronics, data acquisition, tomographic image reconstruction, image processing, and data/image analysis algorithms, and incorporating these innovations into practical imaging devices. The ultimate goal is to introduce these new imaging tools into studies of molecular mechanisms and treatments of disease within living subjects. The research is supported by grants from the National Cancer Institute, National Institute of Biomedical Imaging and Bioengineering, California Breast Cancer Research Program, and the Whitaker Foundation.

Molecular Imaging Instrumentation Lab (l-r), top row: Marta Zanchi, Garry Chinn, Craig Levin, Angela Foudray, Lois Nisbet; bottom row: Guillem Pratx, David Aum, Peter Olcott.

Molecular Imaging Probe Lab

XIAOYUAN (SHAWN) CHEN

Shawn Chen's group is interested in developing and validating novel molecular imaging probes (monoclonal antibodies, minibodies, proteins, peptides and peptidomimetics) for the visualization and quantification of molecular targets that are aberrantly expressed during tumor growth, angiogenesis and metastasis. We are trying to combine both anatomical (microMRI and microCT) and molecular (microPET, microSPECT, and NIR fluorescence) imaging techniques to pinpoint molecular and functional information related to tumor growth and dissemination and to monitor specific molecular therapeutic efficacy. We are currently working closely with two important angiogenesis targets: integrin alpha(v)beta(3) and vascular endothelial growth factor receptor subtype-2 (VEGFR-2). Integrins expressed on endothelial cells modulate cell migration and survival during angiogenesis. Integrins expressed on carcinoma cells potentiate metastasis by facilitating invasion and movement across blood vessels. In several malignancies, tumor expression of integrin alpha(v)beta(3) correlates well with tumor progression. VEGF is a key regulator of tumor angiogenesis and is the most potent endothelial cell mitogen. Binding of VEGF to its receptor on the endothelial cell membrane stimulates the VEGF signaling pathway. VEGFR-2 (KDR/Flk-1) is the primary VEGF receptor on endothelial cells. Specific projects include multimodality (e.g., PET, SPECT, optical) imaging of tumor angiogenesis in vivo as well as tumor vessel specific delivery of gene, chemo, and radiotherapeutics.

Our research efforts are currently supported by both the federal government (NIH and DOD) and industries (MedImmune, Inc.). Dr. Weibo Cai was awarded Benedict Cassen Postdoctoral Fellowship from the Society of Nuclear Medicine. Drs. Zibo Li and Qizhen Cao were awarded Dean's Fellowships. Numerous travel awards were also received by the Chen group to attend AMI and SMI annual conferences. Collaborative work between Chen lab and Gambhir lab on chemical modification of adenoviral vectors was featured on the cover of the *Journal of Nuclear Medicine*. Overall, we are proud to say that the year of 2006 has been very busy and productive.

Molecular Imaging Probe Lab (l-r), front row: Linha He, Hui Wang, Quzhen Cao, Zhanhong Wu, Xiaoyuan (Shawn) Chen, Alireza Ebrahimnejad; back row: Gang Niu, Kai Chen, Zibo Li.

Cardiovascular Molecular Imaging Lab

Joseph Wu

Ischemic heart disease is the number one cause of morbidity and mortality in the United States. The repeated ischemic insults can lead to congestive heart failure, which is the leading cause of hospital admissions for people aged 65 years and over. With the advent of the human genome project, cardiovascular diseases will likely be targeted at the basic cellular and molecular levels.

The cardiovascular molecular imaging lab is a multidisciplinary team that combines expertise in molecular and cell biology, cardiovascular physiology, and molecular imaging. To better

understand stem cell biology in vivo, we use novel molecular markers that enable us to follow the fate of transplanted stem cells noninvasively. These include monitoring survival, proliferation, and differentiation as related to embryonic stem cells and bone marrow stem cells. The highly sensitive imaging devices we use include bioluminescence, fluorescence, positron emission tomography, and magnetic resonance scanners. We also work on gene expression profiling of stem cell markers as well as optimizing cardiac gene therapy protocols. The eventual goal is to establish molecular imaging as a platform for translational research in cellular and gene therapies for ischemic heart disease in the 21st century.

Cardiovascular Molecular Imaging (l-r): (front) Mei Huang, Esther Xie, Feng Cao, Susan Lin, (back) Amir Sadrzadeh, Koen van der Bogt, Joe Wu, Zongjin Li).

Clinical Molecular Imaging Research

Andy Quon

3D CT has been available for over 10 years and can be readily performed at many modern imaging centers. The most common viewing formats are Virtual Colonoscopy and External 3D Volume "Fly-Around."

Some issues have diminished the utility of 3D CT:
- Small and flat lesions are difficult to see/characterize
- In CT colonography, stool cannot be differentiated from polyps without very strict bowel cleansing
- Steep learning curve for radiologists

FDG PET has superior accuracy to CT for many tumors and integrated PET/CT appears to add additional value. Although fused PET/CT images for 3D volume rendering is currently undefined and undescribed, it appears to provide additional beneficial data for image interpretation and may create new

Image of the Year shows the result of PET/CT fused images.

areas of clinical application. A particularly promising avenue is usage in pre-surgical/pre-procedural planning. Future work includes: (1) further development of the 3D PET/CT software tools, (2) validation of this technique in more patients, and (3) use in tracers other than FDG.

The image, published on the cover of *Chemical & Engineering News* this year, was also the Society of Nuclear Medicine (SNM) Image of the Year at the 2005 Annual Meeting in Toronto.

Molecular Imaging of Musculoskeletal Illnesses

SANDIP BISWAL
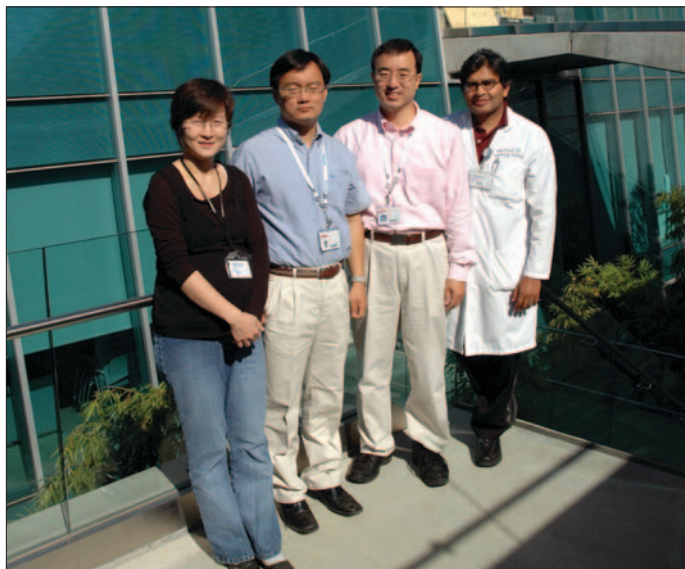
Molecular Imaging of Musculoskeletal Illnesses (l-r): Sheen-Woo Lee, Tae Joo Jeon, Sang Hoo Lee, Sandip Biswal.

Dr. Sandip Biswal, M.D. and members of the lab, Sheen-Woo Lee, M.D., Andrew Tye, Harpreet Singh, B.S., and Bao Do, M.D. are interested in using mulitimodality molecular imaging techniques to study musculoskeletal inflammation and pain. Dr. Lee has employed manganese-enhanced magnetic resonance imaging (MEMRI) to study spinal cord activation in models of peripheral inflammation and pain. She is also developing and validating the use of clinically-relevant magnetic resonance imaging and computed tomography methods for the early detection of rheumatoid arthritis. Dr. Do and Mr. Andrew Tye have made significant inroads in understanding glucose metabolism in the human and animal spinal cord. Furthermore, our lab has also been successful in building novel genetic constructs to study the expression of specific genes and to understand protein-protein interactions in vivo. We have developed methods to see estrogen receptor-mediated signaling in vivo and calmodulin folding in vitro. In the past year, we have been fortunate to receive the Research Trainee Prize for a Scientific Paper from the RSNA 2005 and the Top Scientific Abstract Award for the 2006 Academy of Molecular Imaging Meeting.

EDUCATION AND TRAINING

Education and Training

Postgraduate Education

SUSAN SPIELMAN

Stanford's Continuing Medical Education (CME) program has grown into the leading radiology CME effort in the country. In FY 2006, we welcomed over 3,300 registrants to 14 courses. Our symposia are developed to educate radiologists, technologists and scientists about impending transitions to new and emerging technologies. The Department's distinguished faculty serve as course directors and speakers for each program, and guest faculty from leading academic institutions worldwide are invited to complement our roster of presenters.

The success of our program can be attributed to the strategic focus of our efforts. We construct large courses which are tailored to serve the changing educational needs of our target. By bringing together the world experts on key topics, we are able to offer unique, high quality meetings. In 2006 we grew our program by introducing courses on PET/CT, Small Animal Imaging and the Treatment of Venous Disease. In addition, our creative new meeting formats and careful selection of hotels and timing allow us to differentiate our program from competing CME efforts.

Our International Symposium on Multidetector Row CT (MDCT), now in its eighth year, is one of our most successful programs. We had a record breaking year in 2006 with 950 attendees from 24 countries. The meeting has been ground breaking as a new model for education in radiology and its influence on the field is unmatched. This year's effort had a unique presentation format with 167 nine minute lectures and 65 speakers. We received significant press coverage highlighting the important advances presented at the meeting. The MDCT course is viewed as the best and most important CT course offered today.

This year we have also begun producing CME accredited DVD's of the lectures from our MDCT and our breast courses. These DVD's will further extend the dissemination of our advances and serve as a great resource for our registrants.

Other meetings on our calendar are co-hosted by strategic partners in Japan and Europe in order to build international relationships for our faculty and grow our international reach and reputation. We just completed a one-week program for a select group of Japanese technologists, and we are currently planning for courses in Dubrovnik, Croatia and China in 2007.

Stanford Radiology Courses

COURSE TITLE	DIRECTOR	LOCATION
Venous Disease	Hofmann/Kee	Carmel
Current Concepts–MRI	Pelc/Spielman	Monterey
Clinical High Field	Atlas/Glover/Herfkens	Las Vegas
Breast MRI	Ikeda	Las Vegas
Small Animal Imaging	Levin	Stanford
Diagnostic Imaging	Sommer	Vail
PET/CT & Molec Imaging	Gambhir/Quon	Las Vegas
CVIR	Kee	Squaw
MR – Neuro/MSK	Atlas/Beaulieu	Las Vegas
Diagnostic Imaging	Glazer	Hawaii
Breast Imaging	Ikeda	Las Vegas
MDCT	Rubin	San Francisco
Radiology Essentials	Jeffrey	Jackson Hole
State-of-the-Art Imaging	Moseley	Stanford

NCI Training Program—Advanced Techniques for Cancer Imaging
Donna Cronister

Our fourteenth year of training began on February 1, 2006. On September 10, 2006, we submitted a competing renewal and expect a response from NCI by early 2007. We have graduated 21 trainees from our program, Advanced Techniques for Cancer Imaging, thus far. A specific aim of this training program is to position our trainees for a career in academic radiology. Fifteen of the postdoctoral fellows who have completed the program are actively performing research as faculty or academic staff in major universities. Our trainees continue to be extremely productive, and we often collaborate with them in their new positions both locally and throughout the country. The following table provides a snapshot of where our trainees are in their careers and across the country.

NCI Fellow	Graduated	Mentor	Current Position	Institution
John Strang, M.D.	1995	Robert Herfkens	Assistant Professor	University of Rochester, Rochester, NY
Susan Lemieux, Ph.D.	1996	Gary Glover	Assistant Professor	Diagnostic Imaging, Western Virginia University
Ian Ch'en, M.D.	1996	King Li	Radiologist	Southwest Washington Medical Center, Vancouver, WA
Yi-Fen Yen, Ph.D.	1997	Glover	Assistant Professor	University of Western Ontario, London, Ontario
Garry Gold, M.D.	1997	Macovski	Assistant Professor	Stanford University, Department of Radiology
Bruce Daniel, M.D.	1997	Robert Herfkens	Associate Professor	Stanford University, Department of Radiology
Roger Shifrin, M.D.	1998	Norbert Pelc Robert Herfkens	Radiologist	Radiology Associates, Daytona Beach, FL
Esther Yuh, Ph.D.	1998	King Li Sandy Napel	Medical Student	Stanford University, School of Medicine
Steven G. Heiss, M.D.	1999	King Li	Radiologist	Radiology Imaging Associates, Denver, CO
Martin Blum, M.D.	2000	Brooke Jeffrey	Researcher	PET/Nuclear Medicine, Palo Alto VA Health Care
Curtis Coulam, M.D.	2001	Graham Sommer	Radiologist	Gem State Radiology Group, Boise, ID
Lawrence Chow, M.D.	2002	Graham Sommer	Assistant Professor	University of Oregon, Eugene, O
Yishan Yang, Ph.D.	2002	Mark Bednarski	Research Associate	Stanford University, Department of Radiology
Samira Guccione, Ph.D.	2002	Mark Bednarski	Assistant Professor	Stanford University, Department of Radiology
Charles Liu, M.D.	2003	Robert Herfkens Graham Sommer	Radiologist	La Jolla Radiology, La Jolla, CA
Susan Hobbs, M.D., Ph.D.	2003	Mark Bednarski	Resident	University of Minnesota
Karl Vigen, Ph.D.	2003	Kim Butts	Research Scientist	University of Wisconsin-Madison, Madison, WS
Laura Pisani, Ph.D.	2004	Gary Glover	Postdoctoral Fellow	Stanford University, Department of Radiology
Jon Levin, M.D.	2004	Robert Herfkens Graham Sommer	Radiologist	St. Luke's Medical Center & Clinic, Minneapolis, MN
Daniel Margolis, M.D.	2005	Brooke Jeffrey	Radiologist	Bay Area Imaging Consultants
Daniel Ennis, Ph.D.	2006	Norbert Pelc	Postdoctoral Fellow	Stanford University, Cardiovascular Medicine

Advanced Techniques for Cancer Imaging (T32)

PI: Gary Glazer, M.D.

The Department of Radiology at Stanford University offers qualified individuals a unique research opportunity through our Advanced Techniques for Cancer Imaging Program. The goal of our program is to provide M.D. and Ph.D. research fellows with training in cancer-related imaging research. Fellows have the opportunity to work with our world-renowned faculty who are committed to sharing their knowledge and mentoring the future leaders in radiology. Our program allows basic scientists in medical imaging (Ph.D.s) and clinical scientists (M.D.s past residency) to collaborate in an unparalleled environment that combines medical imaging sciences, clinical sciences, a strong cancer focus, and an institutional commitment to training academic radiologists and basic scientists in imaging science. The ideal candidates will be individuals who have received a Ph.D. or an M.D. degree. Ph.D. candidates must have completed their degree in physics, engineering, or an imaging-related field from an approved doctoral program within four years of acceptance to this training program. Experience in imaging is preferred. M.D. candidates must have completed at least two years in an approved radiology residency program.

In Vivo Cellular and Molecular Imaging (P50)

PI: Sam Gambhir, M.D., Ph.D.

The vision of the "In Vivo Cellular and Molecular Imaging Center at Stanford"(ICMIC@Stanford) program (NCI P50) is to bring together researchers from various disciplines to form synergistic teams that will make significant advances in the use of multimodality molecular imaging strategies for better linking pre-clinical models of cancer with the clinical management of cancer. The career development component of this P50 is designed to be as flexible as possible to attract highly qualified candidates with the passion and ability to make an impact on cancer research that will benefit patient care in terms of diagnosis, therapy, and monitoring. This overarching theme will guide the process of candidate selection and lead to successfully trained individuals who will be capable of leading their own independent research teams in the field of molecular imaging cancer research. Now in the second year of the ICMIC@Stanford we have a total of four trainees in the program. Selected candidates attend various educational activities in the Molecular Imaging Program at Stanford (MIPS) and work to bridge activities between a minimum of two laboratories. The candidates invited to join the ICMIC@Stanford program are expected to be well trained in basic science or in imaging science and to have the energy and drive to impact the growing field of molecular imaging cancer research.

Stanford Molecular Imaging Scholars (R25)

PI: Sam Gambhir, M.D., Ph.D.

The Stanford Molecular Imaging Scholars (SMIS) program is a diverse training program bringing together more than thirteen Departments, predominantly from the Stanford Schools of Medicine and Engineering, in order to train the next generation of interdisciplinary leaders in molecular imaging. Oncologic molecular imaging is a rapidly growing area within molecular imaging which combines the disciplines of chemistry, cell/molecular biology, molecular pharmacology, bioengineering, imaging sciences, and clinical medicine to advance cancer research, diagnosis and management. The goals of SMIS are to train postdoctoral fellows through a diverse group of over 40 basic science and clinical faculty mentors representing 8 program areas, incorporating formal courses in molecular imaging, molecular pharmacology, cancer biology, cancer immunology, virology, and gene therapy, with a clinical component including hematology/oncology rounds. This program is just beginning with the first students just beginning to arrive.

Systems Biology in Cancer (U56)

PI: Sylvia Plevritis, Ph.D.

The Systems Biology of Cancer Program, part of an Integrated Cancer Biology Program (ICBP) at NCI has been funded for an additional three years as a Planning Grant to create a multidisciplinary program in the systems biology of cancer. The career development component of this program is designed to attract highly qualified candidates with outstanding analytical skills and the desire to apply their skills to the study of cancer biology. Candidates are being cross-trained not only in the basic principles of cancer biology, but also in the basic mechanisms underlying novel biotechnologies, measuring genomic and proteomic signatures of molecular processes. Our goal is to produce the first generation of thought leaders who can integrate molecular biology with biocomputation. We have been and will continue to enrich our environment to train individuals who will be capable of leading their own independent research teams in biocomputational modeling of cancer biology. Over the next two years, we will extend three additional postdoctoral training fellowships in the program.

Lucas Center MR Training and Support: 1.5T,3.0T & 7.0 Whole Body Magnets

Anne Marie Sawyer, Romi Samira, Sandra Rodriguez, Kristi L. Arruza

Safety training and system instruction have been provided to 68 new researchers conducting experimental MR studies at the Lucas Center over the last twelve months. Magnet safety training is provided twice a month and is an annual requirement for all researchers assisting or conducting studies on any of the magnet systems at the Lucas Center. A magnet safety refresher course was provided to 175 researchers this past year. This ensures that all users and assistants are qualified to operate the system and satisfies Lucas Center and University requirements for safety. System and safety support is provided to the researchers 7 days a week, 24 hours a day to ensure that research endeavors are successful, generate valuable data, and, above all, are safe for the researchers, the human subjects and the MR system and its components (Figure 1). Magnet safety is an on-going concern as the MR environment can be a potentially lethal setting without continuing education and persevering support. The research environment generates many new prototype designs in RF imaging coils; imaging accessories; monitoring and response devices such as button boxes, eye trackers, and electroencephalogram (EEG) recorders; and sensory devices. Evaluation of these new devices is on-going to ensure that neither the image data, the safety of the human subject, nor the integrity of the MR system is compromised by the presence of these devices in the magnet room, in the bore of the magnet, or in the presence of an RF coil.

Figure 1. Romi, Sandra and Kristi are three of the four MR research technologists who support scanning at the Lucas Center three magnet laboratories.
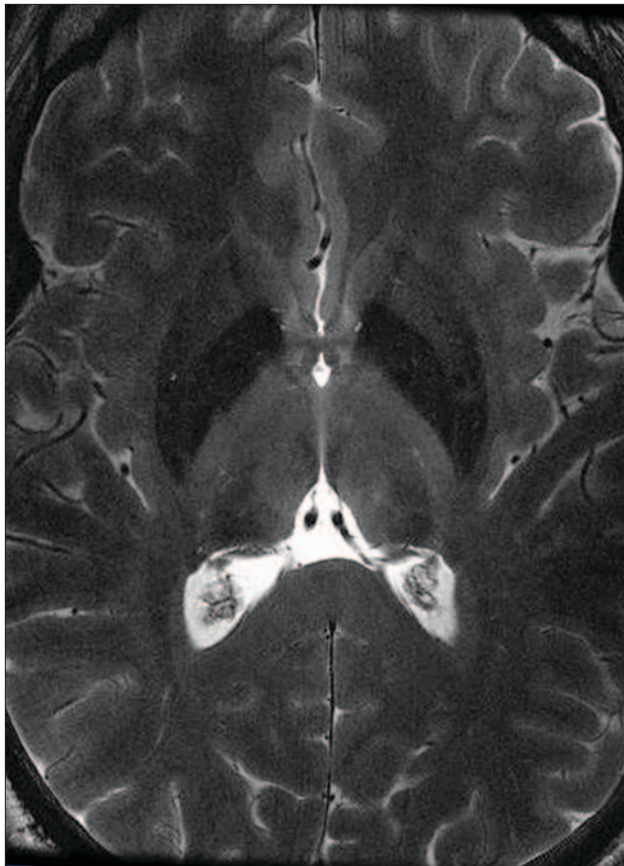
Figure left: 7T Fast Spin Echo image taken July, 2006.
Figure below: 7T GE MR imaging system.
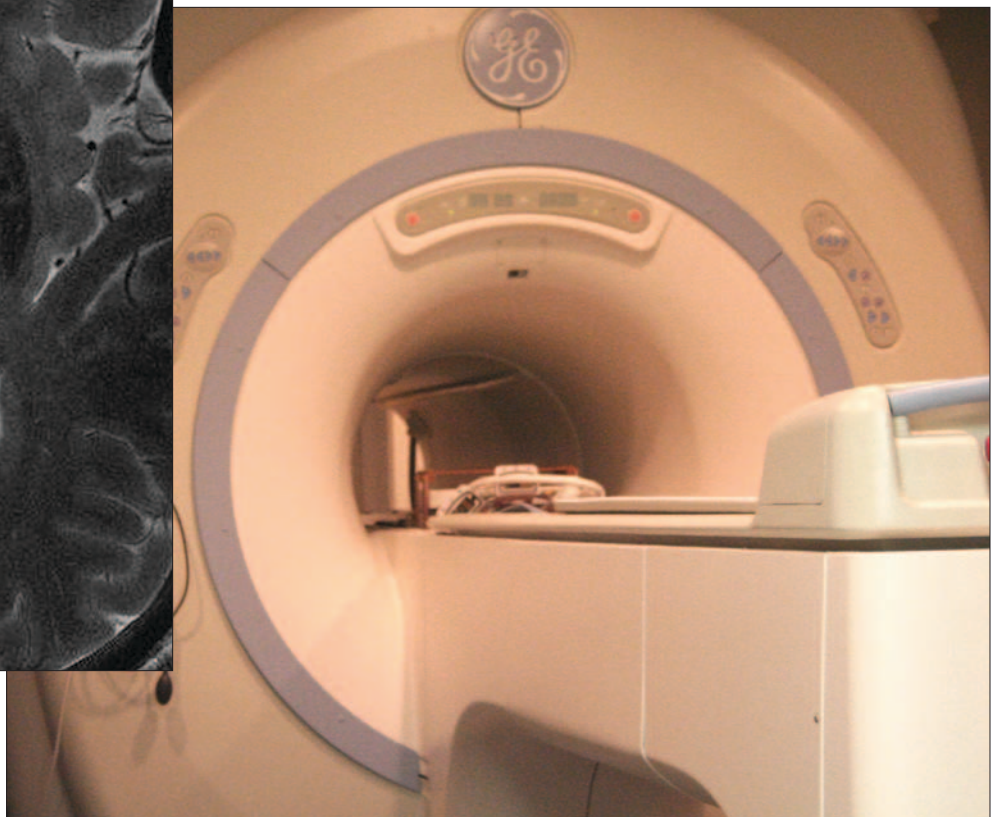
FACILITIES

Facilities Updates

3D Analysis, Clinical, and Educational Updates 2006

Laura J. Pierce, M.P.A., R.T. (CT), Sandy Napel, Ph.D. and Geoffrey D. Rubin, M.D.

Department of Radiology, Stanford University

Introduction

This year the Stanford 3D medical imaging laboratory is celebrating a decade of service to the Stanford medical community. In 1996, Geoffrey Rubin M.D. and Sandy Napel Ph.D. created the 3D Laboratory with the mission of developing and applying innovative techniques for the efficient analysis and display of medical imaging data through interdisciplinary collaboration. We continue to pursue this mission ten years later. Our clinical goal is to deliver 3D imaging advances as rapidly as possible following validation to the Stanford and worldwide healthcare communities. Our educational goal is to disseminate knowledge and duplicate our 3D services at other institutions by providing

surgery, orthopedics, and neurosurgery. Ninety percent of our referrals are from CT examinations, the remainder are from MRI studies. With rapid advances in CT and MRI scanning over the past ten years, our 3D examinations provide a larger range of coverage with better temporal and spatial resolution (see Images 1 and 2).

Education: Both 3D labs continue to be attended by a rotation of Stanford Radiology fellows, residents, and medical students who acquire skills in 3D interpretation which will be useful in their future clinical practices. Our 3D imaging specialists also train Stanford researchers from engineering and medical

Example of coronary artery plaque characterization.

Images acquired on TeraRecon Aquariusnet.

3D ANALYSIS
10 Year Celebration
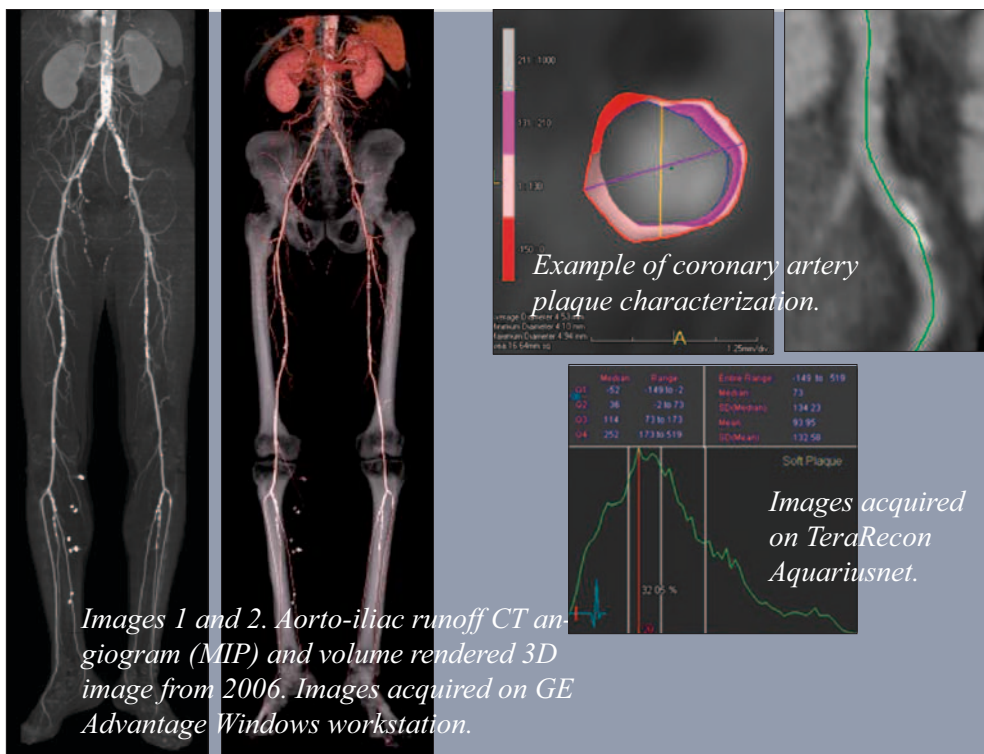
Images 1 and 2. Aorto-iliac runoff CT angiogram (MIP) and volume rendered 3D image from 2006. Images acquired on GE Advantage Windows workstation.
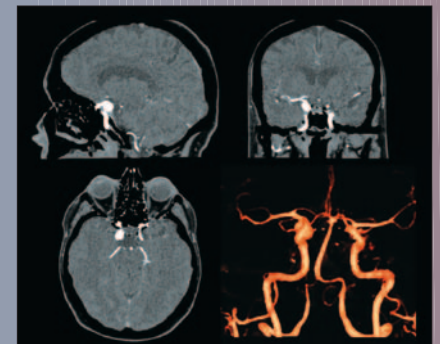
Image 6. Example of automated bone removal using subtraction method on Siemens Leonardo 3D workstation.

training for local and international physicians and technologists in the latest developments in 3D imaging.

Progress

Clinical: Over the past year, the 3D laboratory has continued its operations simultaneously in two locations: the first floor of the Lucas Center as well as the third floor of the James H. Clark Center, a building dedicated to interdisciplinary science. We have processed over 38,000 examinations since our inception in 1996, with an average annual increase of 35% (see Figure 1). We continue to provide 3D services for nearly every clinical department at the Stanford Medical Center. The majority of our referrals come from vascular surgery, cardiothoracic surgery, gastroenterology, cardiology, urology, reconstructive

departments in the latest methodology for acquiring 3D images and data for their research projects. In response to the external demand for 3D imaging training, the 3D lab has sponsored an increasing number of domestic and international visiting radiologists and technologists who have sought training through our 3D clinical fellowship program. This program provides an additional means for disseminating the imaging and management knowledge and skills we have acquired into medical communities around the world, allowing Radiology departments to offer 3D imaging to clinicians and patients in mainstream settings. This past year, we hosted approximately 50 visiting fellows from a combination of local, national, and international hospitals and medical centers. Our international fellows came from New Zealand, Japan, Hong Kong, Colombia, Canada, Thailand,

Facilities Updates

Philippines, Australia, Indonesia, South Korea, and China.

INFRASTRUCTURE

When the 3D Medical Imaging Laboratory was established in 1996, we had 300 square feet of space in the basement of the Grant building, occupied by one 3D imaging technologist (Laura Logan); one clinical GE Advantage Windows workstation; one Silicon Graphics Onyx Infinite Reality workstation; and one Silicon Grahics O2 workstation for seven engineering students, post docs, and clinical researchers. The average monthly 3D volume was 64 examinations.

Today we have 1300 square feet of space in our two labs. Our six 3D imaging technologists include: Laura Pierce, 3D lab manager (formerly Laura Logan), Marc Sofilos, Linda Novello,

development and support.

We continue our excellent relationships with corporate developers of 3D workstations (e.g., GE Healthcare, Siemens Medical Solutions, TeraRecon, and Vital Images) who site their hardware and software in the 3D lab in anticipation of our feedback. These relationships ensure that we maintain the most advanced multidimensional analytical technologies available. To facilitate the bridge between innovation and the clinical use of technology, we also serve as an imaging core lab for medical device developers. These companies use our expertise to evaluate their current and future products, in anticipation of FDA approval. Present industrial projects include evaluation of data from pulmonary vein ablation procedures (to treat atrial fibrilla-

Image 3. Overhead views of the Lucas and Clark Center 4D laboratories.

Images courtesy of Mark Riesenberger.
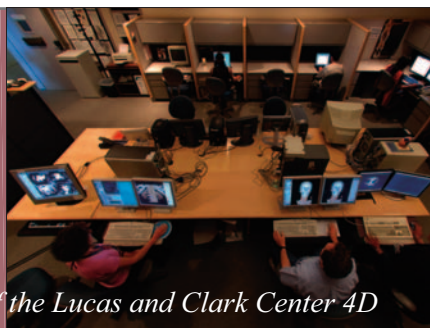
Image 4. Example of PET/CT 3D image of colorectal lesion using advanced software on GE Advantage Windows workstation.
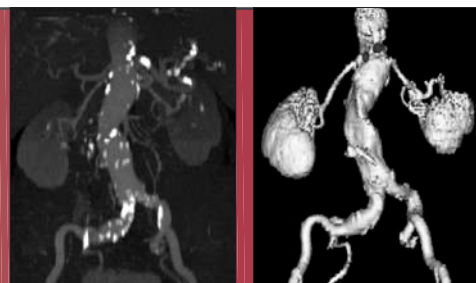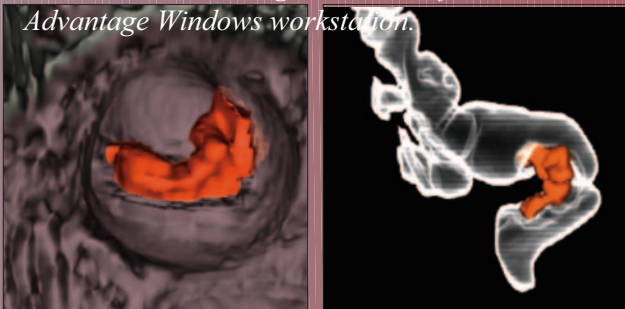
Image 5. Example of full range maximum intensity projection (MIP) and shaded surface display 3D images from 1996. 3D images acquired on GE Advantage Windows workstation.
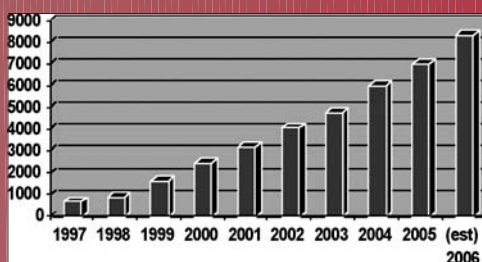
Figure 1. Annual volume of exams processed by 3D Laboratory over past ten years.

Keshni Kumar, William Johnsen, and our newest technologist Noe Hinojosa. We also employ a full-time administrative assistant (Lakeesha Winston) and a software engineer (Kala Raman). The lab retains an annual average of 12 engineering graduate students and post doctoral scholars as well as two clinical MD researchers. Our average monthly 3D volume has increased more than ten fold to 700 examinations.

Both 3D labs include a central area table that invites collaboration (see Image 3). We now have a total of ten advanced 3D workstations for processing clinical cases and for research and development. We also have three servers that provide remote 3D rendering to the Stanford medical community, and two research and development servers for image and data storage. The Lab also houses a variety of PCs, SGIs, and printers for software

tion), as well as thoracic stent-graft deployment (for treatment of thoracic aortic aneurysms).

Future clinical applications under investigation include combining CT and molecular imaging techniques to display molecular pathology in 3D anatomical models (Image 4); characterization of plaque in coronary artery disease (image 5); and improved automation of 3D visualization to improve efficiency (image 6).

CONCLUSION

The 3D Medical Imaging Lab continues to function as an international leader in clinical care, teaching, and research in medical imaging analysis. The confluence of talented, medical and engineering expertise as well as the most up-to-date equipment has been a consistent source of innovative developments in diagnostic and treatment planning approaches.

Radiology Learning Center (RLC)

John Reuling and Susie Spielman

The Radiology Learning Center was developed as part of the Lucas Center Expansion and opened in July 2005. The RLC is comprised of three distinct spaces: a conference room, an adjacent breakout room and a "hotel" space for visiting faculty. The vision for our project was to create a unique educational learning center to be used to advance radiology education and foster changes in the nature of learning, teaching and learning environments through the intelligent use of technology.

The RLC conference room is located at the entrance to Lucas II and serves as a show site for the department's achieve-

The Radiology Learning Center is a technology driven learning space with room for approximately 40 students at one time.

ments. It is a desirable teaching space for faculty and an inspiring resource which will draw talented students to Stanford for their education. It will further serve as a hub for faculty and visiting scholars.

The room was designed to support interactive, collaborative group learning. It is a technology-intensive learning space, with multiple projection and plasma displays and an audio-video routing system that allows the instructor to work with a number of computer and video "sources" in a number of different configurations. It includes technologies for remote conferencing, audience polling, and satellite TV reception. The room seats approximately 40 students in a classroom configuration, but can easily be reconfigured to facilitate various seating styles. The technological sophistication of this space is unmatched in the School of Medicine. As our faculty begin to teach in this new facility it is evident that the opportunity to create unique curriculum and new tools for teaching will provide a great advantage to our students in the years to come. Visitors from around the world are already coming to teach and do research in partnership with our faculty. Space for up to eight visiting faculty has been held to accommodate our visitors. The hotel office provides them with the essentials for a productive working environment as well as an adjacency to our research efforts and teaching facilities.

Experimental Animal Model Care Facility

Wendy Baumgardner, R.V.T., LATg, Diane Howard, R.V.T., LATg

The mission of the veterinary technical staff at the Lucas Center is to provide support to all Radiology and collaborating investigators from other departments in their research and to provide appropriate care and use of all the animals entrusted to us. Our modalities include MRI, CT, PET, MRT, fluoroscopy, and fluoroscopy/CT. We are able to study all systems of the body including such specific diseases as alcoholism, stroke, cancer of the liver, breast, and prostate, neuroimaging of the brain, and stent/graft implantation; thus, we are able to further improve the detection and treatment of disease. We are now in the planning stages of renovating our fluoroscopy suite to include a sterile surgical suite, patient preparation area, and recovery area with state-of-the-art equipment. This will vastly improve our ability to plan long-term chronic studies on animal species in an approved USDA and AALAC animal facility. As always, our goal is to diligently provide support to our animal subjects with the utmost respect, compassion and professional care, while complying with all government and university regulations and policies. All studies are carried out under IACUC approved animal use protocols that are reviewed by the APLAC panel yearly. Protocols are very explicit in terms of detailed procedures and approved personnel; deviation from a protocol is not permitted. All personnel are required to attend appropriate seminars in the use of animal subjects given by the Department of Comparative Medicine as required by Stanford University. In addition to our technical support, we have instituted a rodent use-training pro-

gram that all personnel working with rodents in the Lucas Center are required to successfully complete.

We look to the future with hope that through quality biomedical research the necessity for animal use will decrease with the increased use of computerized models or other non-living research systems. With this in mind, we realize the privilege we are granted and strive for continued excellence in all research taking place within the Department of Radiology.

Wendy Baumgardner prepares the surgical suite for a day-long procedure.

Small Animal Imaging Center

Tim Doyle, Ph.D.

Ted Graves (Radiation Oncology) evaluating a new pinhole collimator on the GEHC MicroCT.

The Stanford Center for Innovation in In Vivo Imaging (SCi3) has continued to grow over the last year, both in available instruments and users. Our facilities offer access to a wide range of systems. We have two microPET (Concorde R4 and GEHC/Suinsa eXplore Vista) systems. The GEHC eXplore Vista microPET was brought online in July and will complement the over-worked Concorde R4 system. In addition, we have two microSPECT/CT (Seimens/Imtek MicroCAT II and Gamma Medica Ideas Flex) systems. We have brought the Gamma Medica Ideas Flex system online, and it provides fast CT scans and highly sensitive SPECT images. The small animal lab also houses a dedicated GEHC eXplore Locus microCT system; four Xenogen bioluminescent systems, three of which also offer fluorescent capabilities; and two whole-animal fluorescent imaging systems (CRi Maestro and GEHC/ART eXplore Optix). The GEHC/ART eXplore Optix is online and has been upgraded to provide multi-wavelength fluorescent imaging (four lasers in the near-infrared spectrum) with the capability to image quantum dots.

Further fluorescent imaging capabilities are provided by the Mauna Kea Cellvizio fibre-based fluorescent microscope, allowing in vivo cellular imaging with minimal invasive surgery. The Visual Sonics Vevo ultrasound has been upgraded to provide micro bubble imaging capabilities. A cryomicrotome and cryomacrotome provide further tools to aid ex vivo analysis. The facility lacks only an MRI system; the 7 Tesla micro Signa magnet is ready to be installed, pending county approval of the renovations required prior to installation. We anticipate the 7T magnet will be installed by the end of the year and available to users early in 2007.

After achieving core resource status in September 2005, we now provide access to our instruments on a fee basis. We have over two hundred and forty registered users from seventy-seven laboratories; together, these users have employed our systems for over nine hundred hours per month! Core director Tim Doyle, D.Phil., and postdoctoral fellow Shay Keren, Ph.D., provide regular training sessions on each of the instruments and are available to all users to help design, interpret, and troubleshoot experiments.

Recently, the imaging facility hosted its first small animal-imaging workshop, which we hope will become an annual event. Scientists from all over the world attended seminars presented both by instrument manufacturers and MIPS faculty and viewed hands-on demonstrations by postdocs and students from Drs. Contag and Gambhir's laboratories. This educational event was a great success for all involved.

Shay inspecting the image of a fluorescent reporter in a mouse on the CRi Maestro system.

Cyclotron Suite Update

FRED CHIN, PH.D. AND DAVID DICK, PH.D.

The PET radiochemistry research and production laboratories have transformed immensely in the Cyclotron Suite over the past year. After the validation of the cyclotron and ancillary equipment, we made a tremendous effort to set up synthesis modules and analytical instrumentation for the radiochemistry within the Molecular Imaging Program at Stanford (MIPS). We had to overcome several challenges during the installation process, but we achieved our goal to provide ^{18}F-labeled PET radiotracers by early 2006, which included FDG, FHBG, FLT, and other novel compounds.

Radiochemistry Research Laboratory Update: The newly installed General Electric TRACERlab FX-FN modules #1 and #2 are typically used to carry out simple radiosynthetic methods to produce radiotracers such as FHBG and FLT, which are used in human clinical studies to monitor gene therapy and tumor proliferation, respectively. Another radiotracer, FAZA, can also be made in the FX-FN#1 and is designed to detect hypoxia using PET. In producing these radiotracers, we dedicate one of our new radiochemistry protocols to the quality control of human-use radiopharmaceuticals, while the rest are tested on a small scale (<20 mCi) in one of the five installed, shielded fume hoods. Once the radiochemistry shows proof of concept, the new synthesis procedure is applied to the FX-FN#2 for automation and optimization of the chemistry. After optimization and verification that there will not be incompatibility issues with respect to the other radiotracers, the new radiochemistry can be translated to the FX-FN#1 to reduce the demand on the FX-FN #2. Other novel radiopharmaceuticals can be more

Figure 1. A custom-made module to perform sophisticated radiochemistry while minimizing radiation exposure to the scientists.

complicated and require making an ^{18}F-radiolabeling agent (i.e., [^{18}F]fluorobenzoic acid and [^{18}F]fluoroethyl tosylate) first in the FX-FN module. Additional radiochemistry steps with the labeling agent are subsequently completed in a secondary, custom-made radiochemistry apparatus. Two custom-made modules currently being constructed consist of a pneumatic-controlled reactor, automated lab-jack lift, and switched solenoid valves used to regulate fluids and gases. These custom-made modules will allow us to perform more sophisticated radiochemistries and make improved radiotracers, while minimizing our radiation

exposure during the process.

Several analytical instruments (i.e., high performance liquid chromatography systems, dose calibration stations, gas chromatograph, radioTLC system, and bubble-test apparatus) and other instruments (i.e., Kugel-Rohr drying apparatus and Heidolph rotoevaporators) were installed to aid in our radiotracer quality control and organic chemistry efforts. Nine computer solutions that control the various analytical instruments and radiochemistry modules were mounted in the lab for ergonomic and organizational reasons.

Figure 2. Dr. Fred Chin explains state-of-the-art synthesis modules and instrumentation used to produce radiopharmaceuticals for human and animal use.

Radiochemistry Production Laboratory Update: The Comecer Dorothea dose dispensing system was installed in the Cyclotron Suite clean room in June of 2005. This piece of equipment allows for the automatic dispensing of radiopharmaceuticals from the bulk product vial into unit dose syringes. During late 2005 and early 2006, our good manufacturing practices, standard operating procedures, and equipment qualified our laboratory to produce fluorine-18 labeled fluorodeoxyglucose ([F-18]FDG). The Cyclotron Suite started producing [F-18]FDG for the Stanford Hospital on February 23, 2006. To meet the increasing clinical demand for [F-18]FDG, a General Electric TRACERlab MX-FDG system was installed in August, providing the ability to reliably produce larger quantities of the radiotracer. Work is currently ongoing to set up and validate the production of [N-13]ammonia, providing clinicians with another tool for assessing myocardial blood perfusion.

Future Plans.: Other radiotracers, such as 5-[^{18}F]fluorouracil and N-[^{11}C]methylspiperone, will be used to validate the final two radiochemistry modules (FX-FE and FX-C). Two new staff members will join our group toward the end of summer 2006 to assist in the multiple radiosyntheses performed daily. In 2007, we expect all of our commercial and custom modules to be at full operation, which will allow the research and development of PET radiopharmaceuticals to move forward significantly while providing promising radiotracers for biological evaluation at Stanford University.

Lucas Center MR Systems 1.5T, 3.0T and 7.0T Whole Body Magnets

Anne Marie Sawyer, Romi Samra, Sandra Rodrigueaz, Kristi L. Arruza

Figure 1. Sandra and Kristi, MR research technologists at the Lucas Center, conduct a cardiovascular MR examination at the 1.5T magnet.

The 1.5 Tesla (Figure 1), 3.0 Tesla and 7.0 Tesla (Figure 2) G.E. Healthcare MR systems were recently upgraded to 12.0 M5 systems revision and currently operate at a maximum slew rate of 150 milliTesla per meter per second and maximum gradient amplitudes of 50 milliTesla per meter (1.5T) and 40 milliTesla per meter (3.0T and 7.0T). The hardware currently allows the use of 8-channel phased array coils at 1.5T and 16-channel phased array coils at 3.0T and 7.0T.

New radiofrequency (RF) coils at the 3.0T magnet include: 8-channel phased array head coil from Invivo/MRI Devices, Inc. (Figure 3); 8-channel phased array neurovascular coil from G.E. Healthcare (Figure 4); 8-channel phased array vision coil from Nova Medical (Figure 5); and 8-channel phased array shoulder coil from G.E. Healthcare (Figure 6).A new Veris vital signs monitoring system from Medrad (Figure 7) was added to replace the older MR Equipment physiological monitor.

Daily support in MR system operation and screening and safety is provided to all researchers including faculty, post-doctoral fellows, graduate students, and visiting scholars in the Lucas Center and Department of Radiology; researchers from other University departments such as Psychology, Psychiatry, Neurology, Neurosurgery, and Nephrology; and service center users from outside of the University. Scan support was provided for multiple research studies including: MR Imaging of Breast Disease and Cancer; MRI/MRS of Prostate at 3.0T; MRI of Renal Anatomy and Function in Chronic Ischemia; Development of 3T Scan Protocols for the Musculoskeletal System; 3T Imaging of 3D Joint Models in Cadavers; Fat Redistribution and Metabolic Change in HIV; Diabetes Therapy to Improve Muscle Mass and Clinical Status in Cystic Fibrosis Patients with Abnormal Glucose Tolerance; Evaluate the Effect of Minimally Invasive vs. Open Posterolateral Lumbar Fusion on the Paraspinal Musculature

Using High Resolution Structural and Quantitative MR Imaging; Trial on Efficacy and Safety of Long Term Treatment with ICL670 in Comparison with Deferoxamine in B-thalassmeia Patients with Transfusional Hemosiderosis; Open Label, Safety, Tolerability Study of Deferasirox for Treatment of Transfusional Iron Overload in Low-Risk and INT-1 Myelodysplastic Patients; Women's Health Initiative Memory Study; Computer Modeling and MRI of Hemodynamic Conditions in the Aorta; In Vivo Quantification of Hemodynamic Conditions in the Human Abdominal Aorta During Lower Limb Exercise; Hemodynamic and Geometric Study of the Lower Extremity Vessels with Respect to Body Posture, External Compression, and Muscle Contraction; Hemodynamic Determinants of AAA Disease Following Spinal Cord Injury; Improving SENSE MRI for Spiral and Echoplanar Imaging; MR Characterization of Patent Foramen Ovale and Atrial Septal Aneurysm Lesions; MRI Screening and Staging of Colorectal Cancer; Apnea Positive Pressure Long-Term Efficacy Cardiovascular Outcome Research Study; Effect of Memantine on Brain Structure and Chemistry in Alzheimer's Disease; A Longitudinal Proton MRS Study of HIV-related Brain Injury; Development of Antiangiogenic Nanoparticles for Imaging and Therapy; Dual Modality Imaging Agents; Synthesis and Characterization of T1-weighted Macromolecular Contrast Agents; In Search of Tumor Stem Cells; A Model for Hypercortisolism for Major Depression; Functional MRI of the Brain; HPA Axis/Dopamine Interactions in Psychotic Depression; Cortical Processing of Visual Motion; and Physiologic Basis of Visual Cognition.

Figure 2. The 7.0T whole body MR system at the Lucas Center utilizes 16-channel receiver hardware (G.E. Healthcare, Milwaukee, Wisconsin, USA).

Figure 3. 3.0T 8-channel phased array head coil (Invivo/MRI Devices, Waukesha, Wisconsin, USA).

Figure 4. 3.0T 8-channel phased array neurovascular coil (G.E. Healthcare, Milwaukee, Wisconsin, USA).

A comparrison between 3 different magnetic field strengths (1.5T, 3.0T and 7.0T) using a 3D Timr-of-Flight angiography imaging sequence.
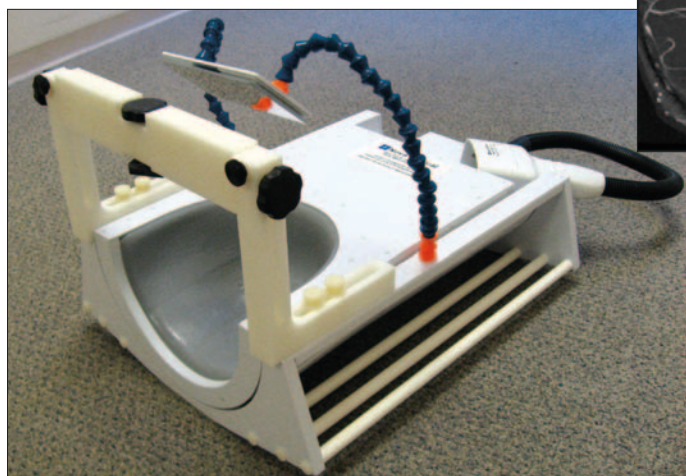
Figure 5. 3.0T 8-channel phased array vision coil (Nova Medical, Inc., Wilmington, Massachusetts, USA).

Figure 6. 3.0T 8-channel phased array shoulder coil (G.E. Healthcare, Milwaukee, Wisconsin, USA).

Figure 7. Veris, the new MR compatible physiological monitoring system (Medrad, Indianola, Pennsylvania, USA).

ABSTRACTS

The Comparisons of 3D and 2D fMRI Studies with Different Slice Thicknesses

Yanle Hu[1, 2], Gary H. Glover[2] - [1]Physics Department, [2]Department of Radiology

SNR analysis based on the thermal noise only model predicts that the 3D stack-of-spiral acquisition method should have a better SNR than the 2D multi-slice method. However, the literature reports of comparisons between 2D and 3D methods are conflicting. Thus, these results can not be explained by a thermal noise model only.

In this study, fMRI experiments were performed with the same field of view in slab-select direction (zFOV=96mm) but different slice thickness (1.5mm, 3mm, and 6mm) on five healthy volunteers using the sensory task. It clearly shows that the performance of the 3D method is better than that of the 2D method for 1.5mm slices and comparable for 3mm slices and worse for 6mm slices. The above results might be explained by the physiological noise model and the fact that the 3D method is more sensitive to the susceptibility gradient induced signal loss.

Physiological noise is a fluctuation in signal and is therefore proportional to the signal. Due to the slab excitation, the
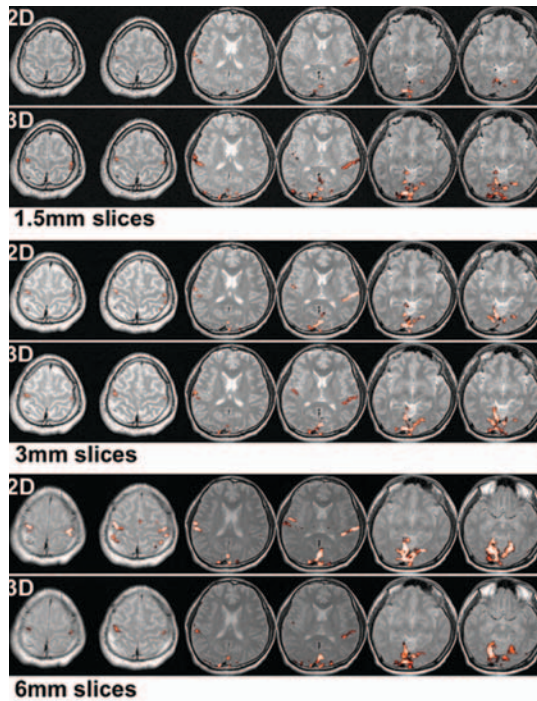
Comparisons of functional results between 2D and 3D methods.

signal, and so the physiological noise, at k-space center in the 3D method is larger than that in the 2D method. If we keep zFOV the same, then the sampling increment is always the same. For thicker slices, the k-space coverage is mainly located in the region of low frequency. Thus, it suffers more from physiological noise. In addition, the 3D method is more sensitive to the susceptibility gradient induced signal loss. Detailed analysis shows that the susceptibility gradient which is necessary to cause total signal loss in the 3D method is only half of that in the 2D method. Therefore we recommend the 3D method for high resolution fMRI experiments and the traditional 2D method for low resolution scans.

References/Funding Source
Irarrazabal P, Nishimura DG, Magn Reson Med, 1995;33(5):656-662., Yang Y, *et. al*., Magn Reson Med, 1996;36(4):620-626., Lai S, Glover GH, Magn Reson Med, 1998;39(1):68-78., Yang Y, *et. al*., Magn Reson Med, 1998;39(1):61-67.
NIH P41-09784

Feasibility of High Resolution 3D FMRI with Whole Brain Coverage

Yanle Hu[1, 2], Gary H. Glover[2] -[1]Physics Department, [2]Department of Radiology

One problem in high resolution fMRI studies is the low SNR of images. In certain cases, high resolution fMRI over the whole brain is desired which will result in a large number of slices. The 3D method, as an alternative, has the benefit of increased SNR compared to the multi-slice 2D methods especially when the number of slices is large. The temporal resolution is very poor since multi-shot spirals are used to achieve the high in-plane resolution. However, using UNFOLD technique it can be improved to a level which is equivalent to that of a single-shot spiral.

In this study, we performed a high resolution fMRI experiment
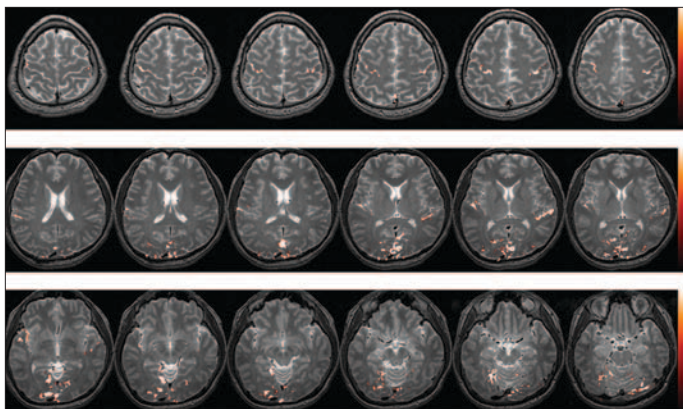
Activation maps from representative slices in motor (1st row), auditory (2nd row) and visual (3rd row) areas.

on normal volunteers using a 3 Tesla whole-body scanner (Signa, GE Medical Systems, Milwaukee, WI) with a small head coil. A 3D 2-shot stack-of-spirals trajectory was used to cover the k-space. FOV was 9.6cm×22cm×22cm and the matrix size was 64×128×128 which resulted a voxel size of 1.5mm×1.7mm×1.7mm. The TR per time frame was 5.12s when UNFOLD technique was used. A sensory task with motor, auditory and visual stimulus was used for functional scan. Functional results from representative slices in motor, auditory and visual areas are shown here.

Experiments have shown that high resolution fMRI studies over the whole brain could be done within a reasonable amount of scan time. However, the temporal resolution is still somewhat low. To improve the temporal resolution, one way is to use the conjugated spiral-in/out technique by combining the spiral in and out trajectory. Another way is to use the partial k-space method which can improve both the SNR efficiency and the temporal resolution due to the existence of physiological noise according to our recent finding. We believe that with all these technique, the high resolution fMRI study over the whole brain with reasonable temporal resolution is feasible, which not only produces activation maps with much more details, but also increases our capability to study those regions suffering from the large signal dropout due to susceptibility gradients.

References/Funding Source
Irarrazabal P, Nishimura DG. Fast three dimensional magnetic resonance imaging. Magn Reson Med 1995;33(5):656-662., Lai S, Glover GH. Three-dimensional spiral fMRI technique: a comparison with 2D spiral acquisition. Magn Reson Med 1998;39(1):68-78. NIH P41-09784

Partial K-space 3D fMRI Method

Yanle Hu[1,2], Gary H. Glover[2] - [1]Physics Department, [2]Department of Radiology

Previous studies have shown the relative importance of physiological noise and thermal noise in 2D MR images. Since physiological noise is proportional to the signal, it can be the dominant component at the center of k-space. In this study we demonstrate that the signal to noise ratio (SNR) efficiency and temporal resolution for 3D fMRI are increased by using a partial k-space acquisition method. In partial k-space methods, the high spatial frequency components are doubled in amplitude during reconstruction, resulting in twice as much noise from those components. However in sum these contributions are relatively small compared to those at the low spatial frequencies where physiological noise is dominant. Therefore the effect on the final MR images is almost negligible due to the square summation rule. Thus, using the partial k-space 3D method sacrifices much less SNR than is expected from the thermal noise model, and the SNR efficiency is increased over full-k acquisition since more time frames can be collected for the same scan time. Accordingly, the temporal resolution can be increased in 3D acquisitions since only partial coverage of k-space is nec-
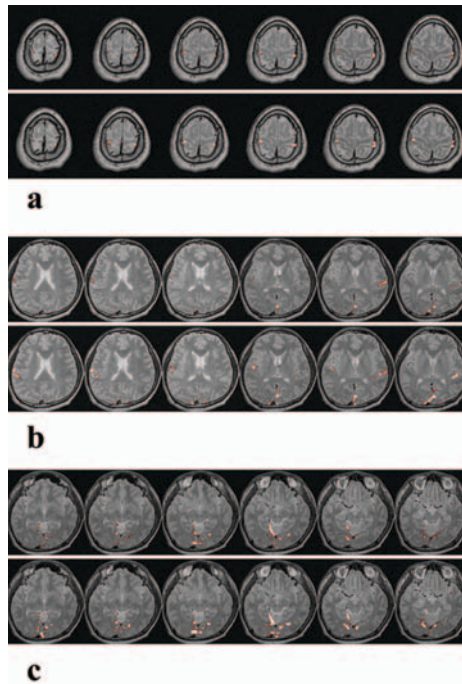
The comparisons of motor, auditory and visual activations between the full k-space method (top row) and the partial k-space method (bottom row) are shown in a, b and c respectively.

essary. Experimental results confirm that more activation with a higher average t-score is detected by this method. Low SNR and low temporal resolution are the problematic issues in the high resolution fMRI studies. The 3D method has the benefit of increased SNR compared to the multi-slices 2D method especially when the number of slices is large. Partial k-space method can further increase the SNR efficiency and the temporal resolution. Thus, the combination of two techniques may provide a possible way of doing high resolution fMRI studies over the whole brain within a reasonable amount of scan time.

Local Dynamic Shimming for Slice-wise Image Acquisition

Jung-Jiin Hsu and Gary H. Glover - Department of Radiology

The aim of this project is to develop an active shimming method to mitigate the imaging magnetic field inhomogeneity caused by local structure of smaller scale in the field of view. Such field inhomogeneity can not be corrected by the shims of the conventional clinical scanner but its correction is crucial in fMRI. Previously, we have shown that local shimming for the inferior portion of the frontal lobe (IFL) can be effectively achieved by current carrying coils held in the subject's mouth and better shimming results are obtained if the region of interest (ROI) is divided into smaller regions and each region is shimmed separately. Recently, we have developed a dynamic shimming that combines the advantage of local shimming and small ROI. The concept is that 2D MR images are usually acquired slice-wise; thus it is beneficial to shim slice by slice over shimming the entire volume. In slice-wise dynamic shimming, the shim currents are optimized for each slice and are set to the optimized values when the corresponding slice is being acquired. The shim currents are stored in a table of the control computer program in sequence matching the order of the slice acquisition. The scanner triggers the control computer by a TTL signal ~10 ms each time before a slice is selected. The control pro-
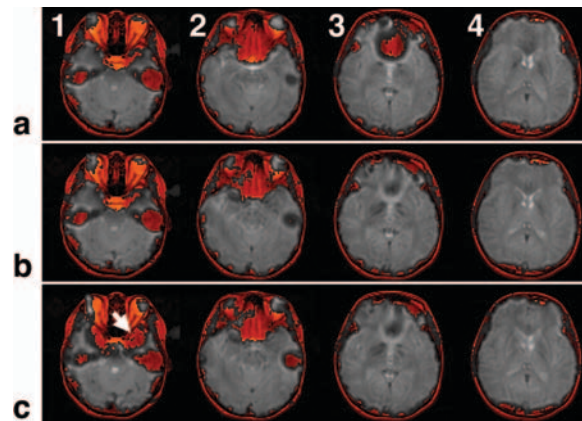
Comparison of the effect of local shimming. (a) no local shimming, (b) with local, dynamic slice-wise shimming, (c) with local, static volume shimming. The spiral images (gray; TE = 40 ms) are overlaid on fast-spin-echo anatomic images (red) for easy identification of signal recovery.

gram then retrieves the next entry in the shim table and updates the output of a multichannel shim power supply. Using an oral shim coil for shimming the IFL, we have demonstrated that slice-wise dynamic shimming can generate shim field that overall matches the desired one better than static volume shimming does (Fig. 1). By computational simulations, we have also shown that, to obtain the same shimming efficiency, slice-wise dynamic shimming is more flexible in determining the shim current distribution than static volume shimming, which greatly simplifies the shim coil design. In addition to the brain, other areas of problematic geometry may benefit as well, for example, the neck, shoulders, and breasts.

Time-Series Mapping of the Longitudinal Relaxation Time in fMRI

Jung-Jiin Hsu and Gary H. Glover - Department of Radiology

Direct longitudinal-relaxation-time (T1) mapping without a contrast agent has not been utilized in fMRI because the conventional measuring methods such as inversion recovery and saturation recovery methods require long scan time. Change of T1 related to the neuronal activity has been reported; however these results are inferred from T1-weighted scans. Recently, we develop a fast T1 mapping method

Brain activation maps of a motor-visual task by T1-based (upper row) and T2-based (BOLD; lower row) fMRI.*

that allows us to explore the utility of this important MR parameter in fMRI. Our method acquires multiple curve-fitting samples with one scan but the conventional methods can acquire only one sample at a time. Thus our method is ideal for dynamic, time-series mapping. We have applied this method to obtain the (static) T1 map of the human brain; the results are in agreement with other published values. On a phantom, the difference between our results and that of an inversion recovery method is below 2.7%. To summarize our findings over the three subjects in fMRI of a motor-visual task: (1) Our method can effectively map the T1 change in the block-designed time course. (2) The activation maps generated by the conventional T2*-based (BOLD) contrast and T1 change are consistent but not identical (Fig. 1). (3) The apparent longitudinal relaxation is faster (i.e., T1 is shorter) during activa-

tion. (4) The average T1 change is ~3.5% at 3 T. Our T1 mapping has smaller statistical t scores in comparison with T2*-based fMRI. Nevertheless, because the T1 change is closely related to the in-flow effect, we are developing T1 mapping for constructing quantitative functional perfusion maps. Regular perfusion techniques require two images (one is spin-labeled and one is control) or require repetitions for various inversion times. So in functional mapping, direct T1 mapping could be more efficient. We are also investigating how we can take advantage of the short echo-time of this method to map areas of severe field inhomogeneity.:

Precompensation of Spiral Trajectory for Reduced Temporal Fluctuation Noise in fMRI

Christine Law [1,2], Gary Glover [2] - [1]Departments of Electrical Engineering, [2] Radiology

Image quality in functional magnetic resonance imaging (fMRI) depends heavily on fidelity of the imaging trajectory actually used. Even a calibrated scanner will introduce deviation into a carefully designed trajectory. If trajectory deviates during image acquisition but reconstruction assumes the designed trajectory, aliasing artifacts will occur. We therefore propose a linear precompensation technique for generating an actual trajectory close to intended design. Image artifacts can be reduced by using this precompensated trajectory.

Between design and measured trajectories, precompensated trajectory can be calculated using linear equations. Using the precompensated trajectory as scanner input, the design trajectory is actually generated in k-space. A two-shot spiral trajectory is used to demonstrate this precompensation technique. Using precompensated trajectory in fMRI, we observed reduction in fluctuation noise caused by motion. To emphasize effects of motion, a conventional two-shot experiment was separated into two experiments, each using one interleaf. The same subject was scanned using design and precompensated trajectories. Temporal standard deviation for each pixel shows a decreased fluctuation when using precompensated trajectory. To test for reduction in artifacts, a phantom is imaged using precompensated and design trajectories (see figure). Artifacts appear as a
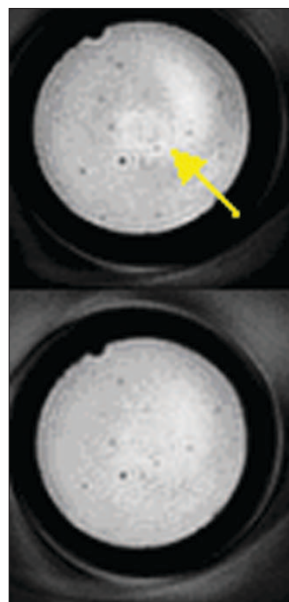
Artifact from trajectory imperfection using a 2-shot spiral is seen as a ring in image center (arrow). (top) Using design trajectory. (bottom) Artifacts reduced using pre-compensated trajectory.

circular ring at image center; reduced by precompensated trajectory.

Even with careful calibration of MRI scanners, actual imaging trajectories will always deviate from their design; in practice, images are typically acquired using imperfect trajectories. We developed a precompensation technique to minimize deviation between design and measured trajectories. We found that image aliasing artifacts from trajectory imperfection are reduced by precompensation. Fluctuation noise caused by motion can also be reduced using our technique.

A Self-navigated Spiral In & Out Pulse Sequence Design for Retrospective Motion Correction

M. Aksoy[1,2], C. Liu[1], M. Moseley[1], R. Bammer[1] - [1]Departments of Radiology and [2]Electrical Engineering

Introduction: Correction of motion artifacts still remains to be one of the most essential topics in MR. Especially in the case of uncooperative patients such as children and patients suffering from medical conditions that prevents them from staying stationary, accurate determination and correction of motion becomes a must for good image quality. Most retrospective motion correction algorithms suffer from aliasing artifacts arising because of local undersampling in k-space after rotation correction. In this study, we address this problem by using parallel imaging methods to fill in missing k-space data.

Methods and Results: In the proposed pulse sequence for this algorithm, a spiral in trajectory is used to get a fully sampled low resolution image for each interleave, and an interleaved spiral-out trajectory is used to acquired the final high resolution image. The data obtained from the scans are fed into a motion correction algorithm that uses the navigator images to accomplish co-registration and to estimate the amount of rotation and translation. After the determination of motion parameters, k-space trajectory, k-space data and the coil sensitivities are corrected accordingly by counter-rotating the k-space trajectories and applying a linear phase to k-space data. This motion correction introduces some gaps in k-space and causes aliasing in image domain. A modified version of the gener-
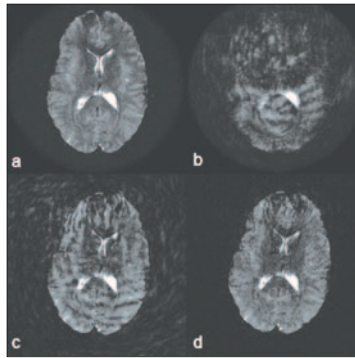
Results for the motion correction algorithm (TE/TR=90/3000 ms , Matrix Size = 256 x 256, Navigator Resolution : 32 x 32, Rotation = +- 8o, Translation = +-3 mm) (a) Reference Image (b) Image with no motion correction (c) Image obtained with motion correction and gridding (d) Final image obtained with motion correction & SENSE. The aliasing artifacts resulting from local k-space undersampling are significantly removed with parallel imaging.

alized SENSE algorithm that has a channel for each coil and for each interleaf is used to remove aliasing and reconstruct the image. This sequence has been tested on two normal volunteers using a 1.5T scanner (GE Signa LX, 11.0) with a high performance gradient system (Gmax = 50mT/m, SR = 150 mT/m/s) and an 8 channel head array (MRI Devices). The results of motion correction algorithm are shown in the figure.

Conclusion: The Spin-Echo Spiral In & Out Trajectory design used in this study for motion correction significantly reduces artifacts resulting from in-plane rigid body motion. The pulse sequence efficiently utilizes otherwise unused time prior to the formation of a spin echo to acquire low resolution navigator images. In addition to motion detection these maps can simultaneously be used to generate coil sensitivity maps. Future studies also include combining motion correction with phase correction in DTI studies

Effect of Oversampling in Multi-Shot DWI.

Chunlei Liu, Roland Bammer, Michael E. Moseley - Department of Radiology.

Multi-shot techniques, such as PROPELLER and self-navigated interleaved spirals (SNAILS), have demonstrated great utility for high resolution diffusion-weighted imaging (DWI). Recently, a conjugate gradient (CG) method that corrects for phase variation induced by physiologic motion was introduced and demonstrated to improve the image quality of multi-shot DWI dramatically. Moreover, this technique can be easily combined with the SENSE reconstruction for parallel imaging. However, little is known about how trajectory design parameters affect their navigation capabilities or how to optimize trajectories for multi-shot DWI. With the CG method we can evaluate the phase correction capability relative to different readout strategies and their trajectory design parameters in the presence of k-space undersampling and phase map errors.

Six readout trajectories were evaluated with this CG phase correction algorithm, including interleaved EPI (iEPI), conventional density spiral (α = 1) and four variable density spiral with pitch factors α of 2, 3, 4 and 5. Motion induced phase errors were added to each interleaf. Two sets of simulation were performed: one with estimation errors in phase maps and the other with k-space undersam-
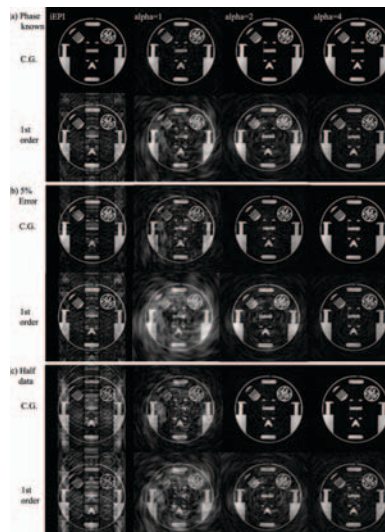
Comparison of phase correction capability of different trajectories under three conditions: (a) phase map is perfectly known; (b) phase map used for reconstruction contains 5% error; and (c) only half of the data are used, but with known phase maps. In each group, the first row shows CG reconstructed images and the second row shows images with only first-order correction. The trajectories from left to right are: iEPI, conventional spiral (α = 1), VD spiral with α = 2, and with α = 4.

pling. In the first set of simulation, true phase maps were not used for phase correction; specifically, ±5% random perturbations were introduced to the phase maps which simulate error in phase map estimation. In the second set of simulation, undersampling the k-space was achieved by skipping every other interleaf, while maintaining a perfect phase map.

In conclusion, we show that trajectories that oversample the center of k-space have more favorable properties for phase correction than critically sampled trajectories. CG phase correction achieves the best image quality in the least-square sense, while a well-balanced oversampling of the center k-space increases the tolerance for trajectory imperfection (e.g. due to eddy currents) and errors in phase map, thus offers more robustness for multi-shot DWI.

High-Resolution SNAILS DTI with a Spiral-in Navigator.

Chunlei Liu, Roland Bammer, Michael E. Moseley - Department of Radiology
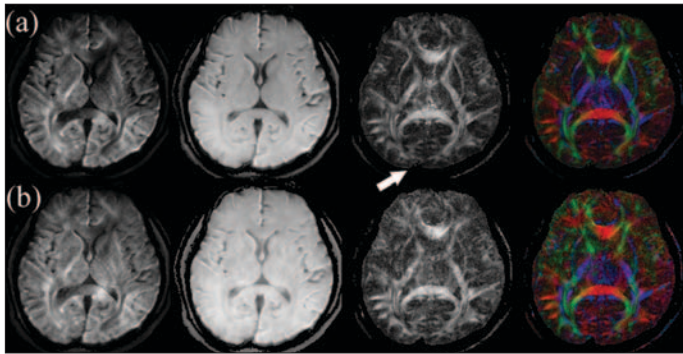
High resolution SNAILS DTI (α = 2) reconstructed (a) with spiral-in navigator; (b) without spiral-in navigator. With the navigator, images have better contrast and SNR.

Variable density (VD) spiral has been applied in SNAILS (Self-Navigated InterLeaved Spiral) for the acquisition of high-resolution diffusion weighted images. It has been shown that by oversampling the center of k-space, SNAILS provides the capability to correct for the motion-induced phase errors. Furthermore, the increased image SNR resulting from oversampling improves the tolerance for residual motion-induced phase errors. On the other hand, excessive oversampling of the center k-space increases readout time, which may increase off-resonance blurring and noise correlation. Here, a method is proposed to improve SNAILS by using a short spiral-in navigator to acquire the phase map. This extra navigator reduces the oversampling factor of the VD spiral and hence improves the acquisition efficiency, while maintaining a moderate oversampling and hence redundancy to compensate residual phase errors. In vivo high-resolution diffusion tensor imaging (DTI) are demonstrated with this improved SNAILS.

The spiral-in navigator provides more reliable phase navigation than the center k-space data alone, which results in higher SNR. The improvement is most significant for smaller pitch factors. Furthermore, the spiral-in navigator reduces the necessity to excessively oversample the center k-space. Because of this oversampling, the readout time for each interleaf of the VD spiral is typically longer for larger pitch factors. For example, with the parameters given in this abstract, each interleaf of a VD spiral has around 4486 sampling points for α = 4, and 3512 sampling points for α = 2. The spiral-in navigator enables a smaller pitch factor, which results in sharper images. On the other hand, with the readout time kept the same, the navigator can shorten the scan time of SNAILS by using a smaller pitch factor and less interleaves. Additionally, the spiral-in image can be used to co-register different interleaves.

Improved Conjugate-Gradient Phase Correction Algorithm for Multi-Shot

Jian Zhang[1,2], Chunlei Liu[1], Michael E. Moseley[1] - Lucas Center for Imaging - Departments of Radiology, [2]Electrical Engineering

Self-Navigated InterLeaved Spiral (SNAILS) image reconstruction algorithm is adapted from SENSE using conjugate gradient (CG) method, by treating the phase correction map of each interleaf as coil sensitivity. However, the system is not as well conditioned with each entry of the phase encoding matrix as a pure phase term. The computational errors from gridding could slow the convergence of CG and degrades the quality of reconstruction. Here, we present an improved CG algorithm (ICG) which converges much faster and does better reconstruction by introducing an additional phase correction stage. We evaluate the improved algorithm at various degrees of motion and a range of signal to noise ratio (SNR). Through simulation, we demonstrate that the improvement in image quality is almost independent of SNR, while the improvement in the converging speed is most significant at higher SNR.

The improvements in convergence rate can be explained in a view of system
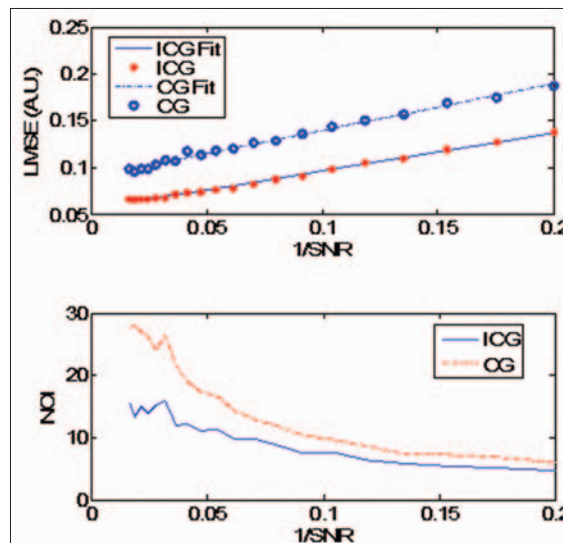
Comparison of ICG and the original CG algorithm. (a) mean square error of the reconstructed image as a function of 1/SNR. (b) Number of iterations needed at different noise levels. (More iterations are needed for high SNR to trade higher accuracy. NOI is smaller for low SNR since the residual noise error can't be further reduced after a few effective steps.)

scale. To do a SENSE reconstruction of an image, $a_{(2N)^2 \times (2N)^2}$ real system needs to be solved if the image vector is decomposed into real and imaginary parts. By forcing real updates in CG, the system size is equivalently reduced to $N^2 \times N^2$. We also tested the algorithm by reconstructing an image from samples on a conventional spiral trajectory with known motion-induced phase maps. The original CG algorithm could not eliminate the aliasing on the final image due to severe undersampling of each interleaf at the center of k-space. Whereas ICG still does a good reconstruction.

Evaluation of Conjugate-Gradient Phase Correction Algorithm Under Noisy Conditions

JIAN ZHANG[1,2], CHUNLEI LIU[2], AND MICHAEL E. MOSELEY[2] - [1]DEPARTMENTS OF ELECTRICAL ENGINEERING, [2]RADIOLOGY

SNAILS [1] is a promising new diffusion-weighted imaging method which is capable of correcting motion-induced phase errors by using variable-density (VD) spiral trajectories. However, little is known about the performance of the algorithm under noisy conditions. Although the computational algorithm is similar to the original SENSE reconstruction, the phase correction problem is not as well conditioned with each entry of the phase encoding matrix as a pure phase term. Here we show that SNAILS is not significantly affected by physiological noises by studying its performance on simulated SNAILS data with varies signal to noise ratio (SNR) and motion scales.

The SNAILS reconstruction algorithm was tested on 128x128 simulated images with additive Gaussian noises (only in image domain) and added phases by using a VD-spiral trajectory (3342x8). To study the performance quantitively, we only added linear phase maps onto the original image, which basically simulate in-plane physical motions of the subject. The algorithm was implemented in MATLAB. Average reconstruction errors and CG estimation errors were recorded at varies noise and motion (k-space shift) levels (Fig 1).
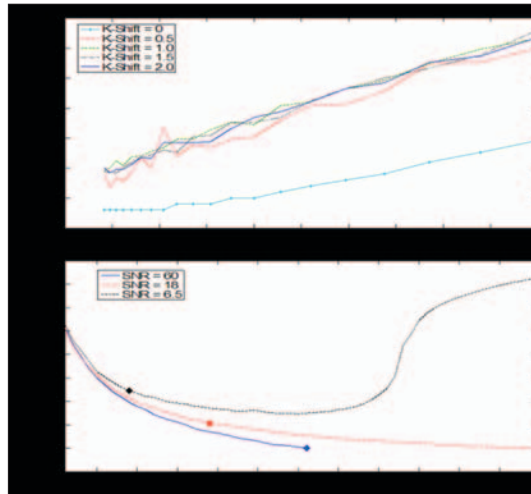
Performance of SNAILS reconstruction. (a) Reconstruction errors for various SNR and motion levels. (b) Log of CG criterion as a function of iteration count (diamonds represent the optimal termination points where the best images are obtained.)

Fig 1a shows that the reconstruction error is nearly proportional to the noise level. Motion-induced phase significantly degraded the quality of reconstruction but the error is not quite dependent on the scale of motion. Fig 1b shows that more iterations don't necessarily bring better images at higher noise levels and the algorithm even diverges when SNR is too low. However, if the algorithm is forced to terminate after only a few steps, the reconstructed image is also in reasonable quality, with a noise power comparable to that of the source image. This could be explained as CG searching errors. The redundant searches are mainly in noise directions when the inherent SNR is already reached. Empirically, we terminate the algorithm when the slope of $-\log_{10}\delta$ drops to 1/10.

Psychosurgery Revisited: Frontal Lobotomy Lesions Estimated with Diffusion Tensor Imaging.

GLENN R. FOX AND ROBERT F. DOUGHERTY - DEPARTMENT OF PSYCHOLOGY

Frontal lobotomy psychosurgery came into widespread use in the 1940's. Nearly 50,000 patients underwent some form of lobotomy in an effort to remedy various pathologies, such as schizophrenia, severe depression and OCD. The procedure took two forms: the Freeman-Watts procedure, and the Transorbital method. In the Freeman-Watts procedure, a neurosurgeon cuts White Matter (WM) pathways by entering the brain at several points along the coronal suture. Freeman later developed the transorbital lobotomy, an outpatient procedure that attempted to sever similar WM pathways by entering the brain through the eye socket. While these procedures occasionally achieved a modest reduction in symptoms, progress often came at the cost of severe cognitive and social impairments. Here we estimate the white matter pathways affected by frontal lobotomy using Diffusion Tensor Imaging and fiber tracking. Both procedures effectively severed the anterior thalamic peduncle, the inferior longitudinal fasciculus, frontal-callosal connections, the uncinate fasciculus and the cingulum. Our analysis suggests that the procedure would have severed the frontal-thalamic connections that the surgeons explicitly targeted (the anterior thalamic peduncle), but would also have severed several other major pathways, thus resulting in pervasive psychological effects. The methods developed here may also be applicable to modern psychosurgical techniques such as cingulotomy.
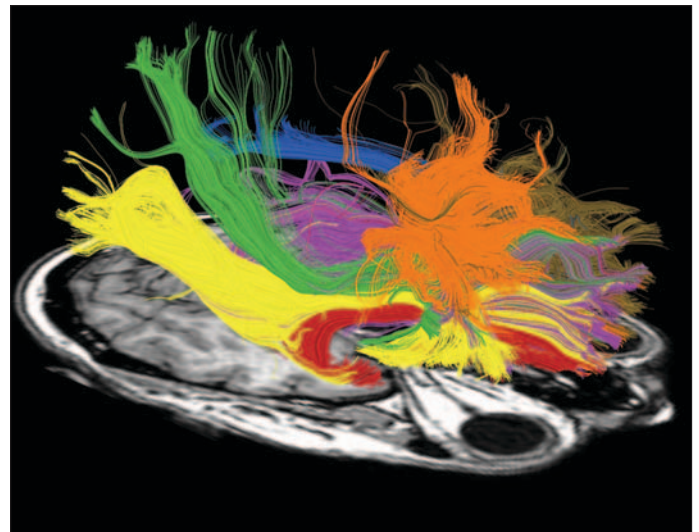
This image shows an estimation of the fibers affected by frontal lobotomy.

Isolating Linear Anisotropic Structures in Human Brain DTMRI

Daniel B. Ennis[1], Gordon Kindlmann[2], Monique Mogensen[1], Talia Vertinksy[1], Scott W. Atlas[1], Roland Bammer[1]
[1]Department of Radiology, Stanford University; [2]Laboratory of Mathematics in Imaging, Harvard University, Cambridge, MA, United States

Introduction: Diffusion tensor magnetic resonance imaging (DTMRI) is increasingly used to assess the white matter integrity of patients with a variety of pathologies. T2 images are often combined with trace and fractional anisotropy (FA) maps in the complete assessment of brain pathology. While trace and FA maps indicate the mean bulk diffusivity (magnitude of isotropy) and the level of structural organization (magnitude of anisotropy) neither map indicates the kind of underlying anisotropy (tensor mode). The mode of anisotropy characterizes the kind of anisotropy as it ranges from linear anisotropic ($\lambda1 \gg \lambda2 \cong \lambda3$) to orthotropic to planar anisotropic ($\lambda1 \cong \lambda2 \gg \lambda3$).

Methods: Without the use of TM, standard DECs highlight structures that include planar anisotropy, in which the primary eigenvector direction is only known within a plane of rotation. A comparative evaluation of DECs that incorporate TM is demonstrated. DECs that incorporate mode (DECM) are generated by encoding the components of the primary eigenvector into the red, green, and blue channels of a color
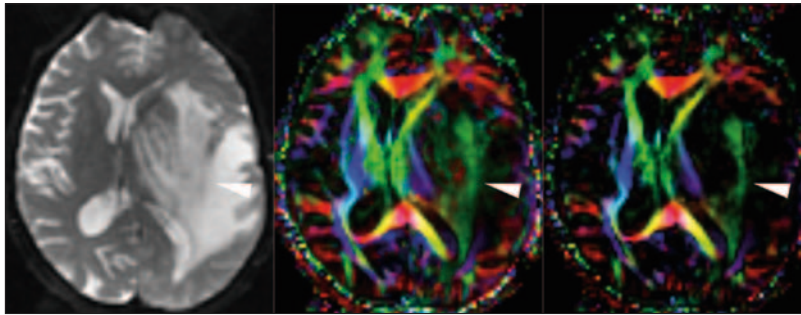
White arrows indicate regions wherein the DECM maps better characterize the underlying tissue structure.

image, then devaluating the color intensity by the product of FA and mode. The effect is to lower the brightness of planar anisotropic structures and to highlight features that are highly linear anisotropic. All colormaps are equally window-leveled.

Results: The patient in Figure 1 presented with GBM and surrounding vasogenic edema. The tissue surrounding the external capsule in Figure 1B appears as a large fibrous mass, but the DECM (Fig. 1C) clearly delineates a smaller band of linear anisotropic structure. We believe that such a map may provide important insight to surgeons during tumor resection treatment.

Callosal Segments Defined by Cortical Projection Zones Differ in Fractional Anisotropy

Arvel Hernandez[1], Robert F. Dougherty[1], Michal Ben-Shachar[1], Gayle K. Deutsch[1], Polina Potanina[1], Roland Bammer[2], Brian A. Wandell[1] - Departments of [1]Psychology, [2]Radiology

Post-mortem studies reveal systematic differences in the diameter of axonal fibers passing through various regions of the corpus callosum (CC) (Aboitiz 1992). In vivo measurements using diffusion tensor imaging show apparently similar CC differences in fractional anisotropy (FA): the splenium shows the highest FA followed by the body and then the genu (Chepuri 2002). Here we determine the cortical projection zones of the white matter pathways corresponding to the regions with these FA differences. We used DTI-based fiber tracking to segment the CC by cortical projection zone (extending Huang 2005) in 20 children aged 7-12. Mean FA was calculated for each CC segment in individual subjects. FA was highest in the inferior splenium, a region that contains fibers projecting to the occipital lobes. High FA values were also observed in the mid-splenial region, projecting to the temporal lobes. FA in both
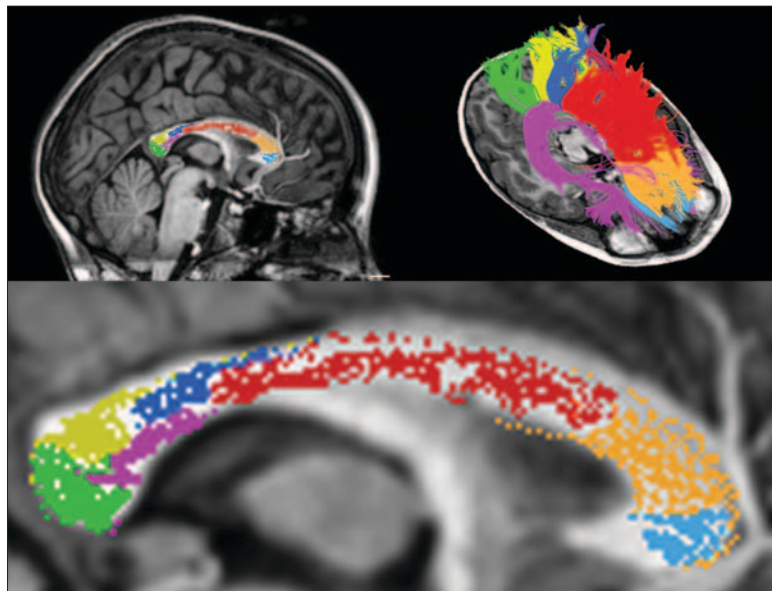
of these splenial regions was significantly higher than in all other regions. The parietal projections were comparable to those within the genu (orbital and anterior frontal projections). Such differences in FA may reflect differences in axon diameter and/or in myelin lamellae. In particular, the high FA portion of the splenium likely corresponds to the large fibers connecting visual cortical regions (especially dorsal occipital) and the temporal lobes. Damage to the mid-splenium can lead to alexia. Our results suggest that skilled reading may rely on the unique properties, measured by distinct FA values, of certain occipital and/or temporal lobe connections.

High Temporal Resolution Multi-echo DSC Perfusion Imaging using GRAPPA EPI

Rexford Newbould, Stefan Skare, Marcus Alley, Roland Bammer - Department of Radiology

Dynamic susceptibility contrast (DSC)-based perfusion-weighted imaging (PWI) is of great utility to determine "tissue-at-risk" in acute stroke patients. Together with diffusion-weighted imaging (DWI) it can help triage patients who can potentially benefit from IV tPA treatment or mechanical thrombectomy. However, the DSC-based determination of hemodynamic parameters is often frustrated by the poor image quality that results from the use of single-shot EPI. Besides the geometric distortions and poor resolution associated with EPI scans, there can be profound problems in determining an arterial input function (AIF) accurately; however, the latter is mandatory to obtain the tissue residue function by deconvolution and consequently affects the veracity of the hemodynamic parameters. Image quality issues arise mainly due to (i) strong T2*-induced blurring, (ii) susceptibility gradients emanating from the sinuses and the auditory canals adjacent to the brain, and (iii) the high concentration of contrast material in the vessels during bolus passage that causes clipping of the bolus maximum for typical echo times. Both multi-shot acquisitions and parallel imaging, such as GRAPPA and SENSE, have been demonstrated to be extremely powerful methods to reduce geometric distortions and
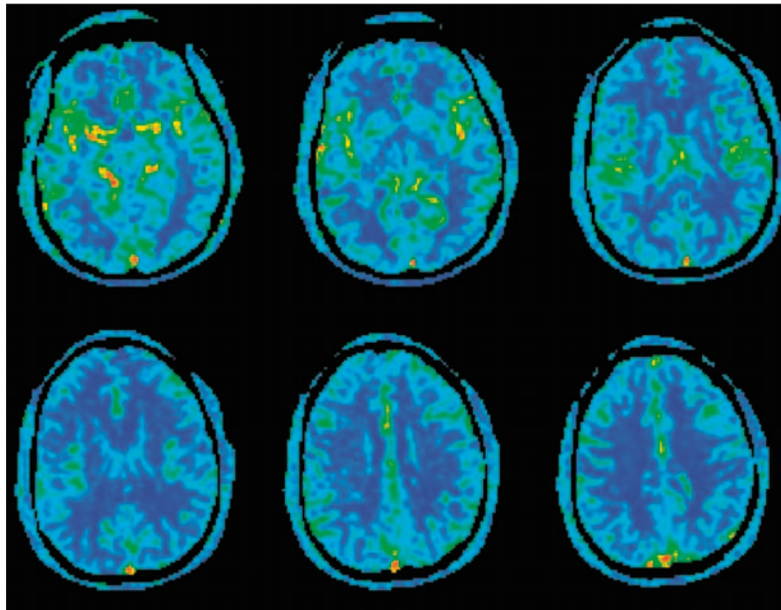
Cerebral blood flow (CBF) map created using PERMEATE. Note the lack of susceptibility artifacts in the lowest slice, where these artifacts commonly appear.

image blurring in echo planar imaging (EPI). Previous attempts at using multi-shot EPI with DSC have met with limited success due to the need for high temporal localization in the k-space acquisition, which is overcome here with a using parallel imaging for temporal localization. This study minimizes the problems associated with single-shot EPI in DSC-PWI by using multi-shot parallel imaging in combination with a multi-slice multi-echo acquisition dubbed PERMEATE (PERfusion with Multi-Echo and Accelerated Temporal Enhancement) EPI that allows both perfusion and pure T2* mapping at a very high temporal resolution.

References/Funding Source
1Ostergaard L, et al. MRM 36: 715-25, 1996. 2Griswold M, et al. MRM 47: 1202-10, 2002; 3Pruessmann K, et al. MRM 42: 952-62, 1999. 4Vonken EJ, et al. JMRI 10:109-117, 1999. 5Reishofer G, et al. 10th ISMRM, 2002; 6Bammer R, et al 12th ISMRM, 2004, p. 362. 7Skare S, et al 13th ISMRM, 2005, p. 2422.

SENSE and GRAPPA Reconstruction of Multi-Shot Multi-Echo EPI Data

D. B. Clayton, S. Skare, R. Newbould, R. Bammer - Department of Radiology

One of the most promising benefits of parallel imaging is that it can reduce distortions by shortening the read-out times of fast acquisition techniques, such as echo-planar imaging (EPI). The trade-off for this improvement is a drop in signal-to-noise ratio due to imperfect receiver geometry and fewer measurements; there is also the potential for errors due to the more complicated reconstruction algorithms that rely on estimations of additional information about the receiver coils. This additional information is typically acquired either by a separate low-resolution scan or by incorporating a segment of k-space acquired at the Nyquist sampling rate directly into the sequence of interest; both of these techniques have limitations. We have recently developed a multi-shot multi-echo EPI pulse sequence to measure PERfusion with Multiple Echoes and Temporal Enhancement (PERMEATE), described in a separate abstract herein. This sequence allows for greater reconstruction flexibility: each shot can be treated as a separate under-sampled k-space acquisition and reconstructed using either GRAPPA or SENSE with an effective reduction factor, R, equal to the number of interleaves, Ni. By

using information from the other interleaves, it is possible to generate the auto-calibration signals required for GRAPPA, or the full-FOV sensitivity maps required for SENSE. Additional flexibility is possible for acquisitions in which Ni is large enough so that shots can be collated into k-space sets with R < Ni. In this work, we explored the differences between the implementation and performance of basic GRAPPA and SENSE reconstructions of PERMEATE data with an effective reduction factor of 4. We conclude that while GRAPPA reconstruction could be treated nearly as a black-box and demonstrated extremely robust and reliable performance in the cases treated here, the SENSE reconstruction required some refinement of the details involved in transforming the data from all shots into the optimum sensitivity maps; without such refinements, noticeable artifacts could result.

References/Funding Source
ISMRM 2006, p. 2447.

A New Propeller EPI Design using Short Axis Readouts

S Skare, RD Newbould, DB Clayton, R Bammer - Lucas MRS/I Center, Department of Radiology, Stanford University

EPI suffers from various artifacts such as geometric distortions, Nyquist ghosting, T2* blurring, Maxwell effects and eddy currents (especially for DW-EPI). The magnitude of these artifacts is inversely scaled by the speed of k-space traversal along the phase encoding direction (a.k.a. pseudo bandwidth), which is determined by two factors: a) the time between two consecutive echoes in the EPI readout train and b) the phase field-of-view (FOV). For some field inhomogeneity, $\Delta B0(r)$, the local displacements (in [m]) of the object are given by:

$$d_{pe}(r) = \frac{\gamma}{2\pi} \Delta B_0(r) T_{ro} FOV_{pe} = \frac{\gamma}{2\pi} \Delta B_0(r) \Delta t_{ro} N_{ro} FOV_{pe}$$

where Δtro and Δtpe are the times between two consecutive sampling points and $Tro = Nro \Delta tro$ is the readout time for a single echo in the EPI train. Multi-shot EPI reduces the distortions in the p.e. direction since $FOVpe$, per shot, is reduced. Unfortunately, despite the use of 2D navigators, shot-to-shot phase errors may be induced by motion/diffusion gradients in DW-EPI, leading to ghosting. To cope with
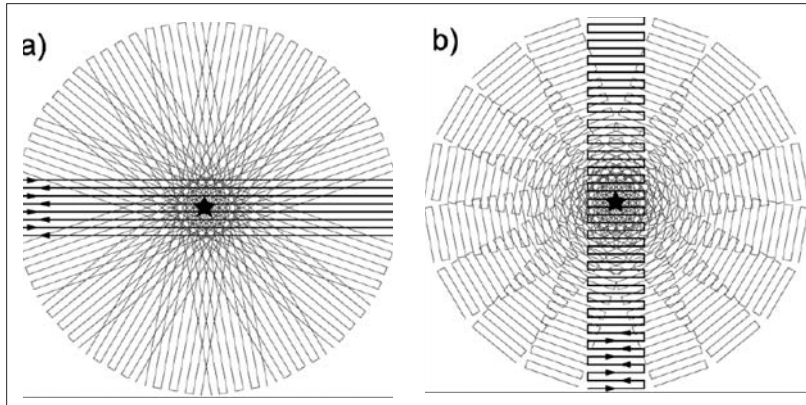
Figure 1. a) k-space trajectories for PROPELLER (1) and LAP-EPI implementations(2,3). b) k-space trajectory for the SAP-EPI sequence proposed in this work. Pentagrams denote the center

these phase errors, the RF refocused PROPELLER sequence (1,4) may be used. This has none of the geometric problems in EPI but is quite SAR intensive, which becomes primarily an issue at higher fields. Inherent navigator capabilities also exist in propeller EPI (2,3). It shares the same k-space trajectory as PROPELLER, with the readout direction along the long axis of the blades (Fig. 1a). We will refer to this propeller EPI implementation as LAP-EPI (Long Axis readout Propeller EPI) in this work for clarity. Still, the real benefit of LAP-EPI is not apparent by scrutinizing Eq. . The distortion level present in LAP-EPI is in fact identical to a standard ssEPI sequence, since readout resolution remains unchanged, but appears as a blurring effect instead of a simple displacement of the object in the phase encoding direction. In this work, the propeller EPI acquisition is redesigned in order to reduce the geometric distortions without relinquishing its advantages. We do this by decreasing the echo spacing by orienting the readout along to the short axis of each blade, hence named SAP-EPI (Short-Axis readout Propeller EPI). The new k-space trajectory SAP-EPI is shown in Fig. 1b. The low resolution in

Age Differences in Affective Working Memory: Prefrontal Contributions to the Positivity Effect in Older Adults

Joseph A. Mikels, Gregory R. Larkin, Patricia A. Reuter-Lorenz, Laura L. Carstensen - Department of Psychology

Recent research suggests that working memory may include an affective subsystem that is hypothesized to maintain a representation of emotion in the absence of its elicitor. Whereas aging is associated with well-documented decline in "cognitive" working memory, "affective" working memory appears preserved. Moreover, older adults have been shown to exhibit superior performance on an emotion maintenance task when the memoranda have positive emotional valence relative to negative, while their younger counterparts show the converse. The neural implementation of this "positivity effect" in older adults remains unknown. The larger amygdala response to positive compared to negative images that is unique to older adults may constitute one neural correlate of the positivity effect. However, recent behavioral evidence indicating that the positivity effect requires executive control suggests that the prefrontal cortex may also play a role. The current study used event-related fMRI to examine age-related changes in affective working memory for emotional responses evoked by positive versus negative pictures. We found that a lateral region of the orbitofrontal cortex was more active in younger adults than older adults during the maintenance of negative emotions, however during the maintenance of positive emotions, this OFC region was more active in the old than in the young. The roles of the prefrontal cortex and executive function in age-related emotional biases are discussed.

An Auditory Perceptual Approach to Cognitive Training in MCI

Allyson C. Rosen[1], [2], Natasha Belfor[3], Lisa Sugiura[2], Joel Kramer[3], Anthony D. Wagner[2], John D. Gabrieli[2], [4]
Departments of [1]Psychiatry and [2]Psychology, Stanford University [3]University of San Francisco;
[4]Department of Brain and Cognitive Sciences, MIT, Boston Mass.

There have been several large studies demonstrating that older adults who are involved in cognitively stimulating activities are less likely to develop Alzheimer's disease than older adults who are less active cognitively. This study represents a pilot randomized clinical trial that tested a novel cognitive training paradigm in older adults with mild cognitive impairment (MCI) using functional MRI to characterize the neural substrates of change in performance. This training program exercises auditory and language systems in ways designed to strengthen the representational salience of speech input, improve signal to noise ratios, and drive neuromodulatory systems that control learning and memory. Treatment and active control groups trained on a computer for 90 minutes/day, 5 days/week. The Repeatable Battery of Assessment of Neuropsychological Status was administered pre and post training. This measure was dissimilar to the training exercises. The treatment demonstrated a trend toward group differences on the Auditory Memory index of the RBANS (p <.072).
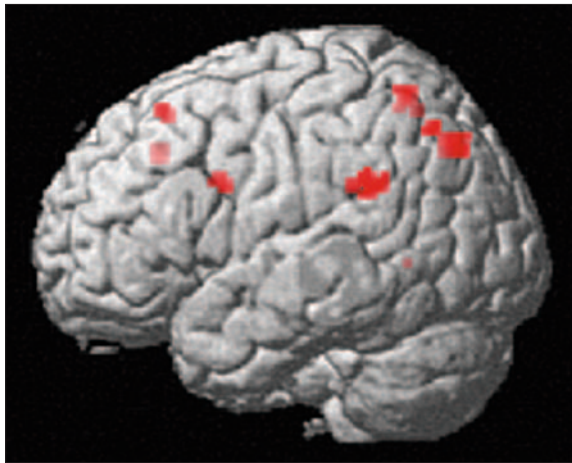
This image displays regions that declined over the 2 months during the control condition (p<.001, uncorrected, extent threshold 10 voxels). There was not a significant decline for the experimental condition.

The control group evidenced a decline in memory functioning (average change = -4 points) whereas the treatment group demonstrated a slight increase in performance (average change = +1 points). Preliminary fMRI results from 12 older adults (6 controls, 6 experimental) were notable for stability in activation in an auditory memory task comparing novel to repeated auditory words for the experimental group over the 2 month period of the training. In contrast, the control group participants demonstrated decline in regions previously demonstrated to differ among normal older adults, MCI, and patients with Alzheimer's Disease, notably parietal and frontal regions. This study is preliminary validation of an fMRI paradigm as an outcome measure for clinical trials involving cognitive training in older adults at risk for dementia.

Attention-Dependent Modulation of Medial Temporal Lobe Encoding Processes

Nicole M. Dudukovic, Alison R. Preston, Jermaine J. Archie & Anthony D. Wagner - Department of Psychology

Goal-directed attention has been shown to modulate activation in lateral cortical regions known to process faces (fusiform cortex) and scenes (parahippocampal cortex), but an open question is whether these effects propagate along the medial temporal lobe (MTL) circuit. The present study investigated how selective attention modulates stimulus-specific encoding processes in MTL cortex and the hippocampus, including how attention impacts MTL responses that predict subsequent memory. High-resolution functional magnetic resonance imaging (fMRI) of the human MTL was conducted on a 3.0 Tesla GE Signa scanner at the Lucas Center while 12 participants attended, ignored, or passively viewed face and scene stimuli. Each trial consisted of four sequentially presented images, two faces and two scenes, and participants were instructed to 1) Remember Faces and Ignore Scenes, 2) Remember Scenes and Ignore Faces, or 3) Passively View both Faces and Scenes (Gazzaley et al., 2005). After a brief delay, either a probe stimulus appeared and participants indicated whether it was in the current memory set (Remember Faces/Remember Scenes conditions), or an arrow appeared and participants indicated the direction it pointed (Passive View condition). A surprise post-scan recognition memory test revealed that participants were more accurate and had higher confidence in their memory judgments for stimuli that were attended as opposed to those that were ignored or passively viewed. Anatomical and functional region of interest (ROI) analyses differentiated between individual MTL subregions and demonstrated that goal-directed attention modulates encoding activation in perirhinal cortex (for faces) and parahippocampal cortex (for scenes) and that these effects propagate into hippocampal subfields. In addition, attention-dependent subsequent memory effects were observed within MTL subregions, suggesting that attention is critical for the encoding responses that give rise to later memory. We are currently finishing data collection and working on further analyses. The results will be presented at a scientific meeting in October and will be written up for publication in a peer-reviewed scientific journal in the fall.

Restricted Field of View Imaging for Fetal fMRI (f-fMRI).

Laura Pisani, Roland Bammer, Erika Rubesova, Richard Barth, Gary Glover - Department of Radiology

We present a restricted field of view (rFOV) sequence designed for fetal functional MRI (f-fMRI). Two-dimensional selective outer volume suppression (OVS) allows rFOV imaging without aliasing of signal from the maternal abdomen. We compare the performances of conventional spiral and rFOV pulse sequences for functional MRI (fMRI) of the fetal brain. Preliminary activation measurements from oxygen modulation are reported.

F-fMRI may be a useful component in differentiating between normal and compromised fetal well-being in pregnancies at risk for intrauterine growth restriction (IUGR). Despite the relatively small fetal head, conventional pulse sequences require long readouts for a field of view (FOV) that encompasses the maternal abdomen in order to avoid aliasing. The rFOV sequence allows tradeoffs between shortening the readout trajectory and lowering gradient slew rates for quieter scanning and increased SNR. Shortening the readout reduces artifacts arising from, fetal motion, off-resonance spins, and T2* decay in spiral imaging.

We have designed and implemented an OVS preparation module with a gradient echo (GRE) sequence so that we can restrict the readout FOV. We lower the gradient slew rate of the pulse sequence, in order to increase the signal to noise ratio and to reduce the acoustic noise. We use a 4-channel cardiac receiver-coil array on a 1.5T GE scanner, and retrospectively exclude coils from reconstruction if they introduce unsaturated signal from the maternal abdomen, and do not contribute significant signal from the fetal head. Imaging performance is compared with a conventional full FOV GRE sequence (see Figure A and B). Six subjects, between 24w and 37w pregnant, have been recruited for this study. FMRI studies were performed with a) an auditory stimulus and b) oxygen modulation. The auditory stimulus consists of 15s blocks alternating between silence and the Mozart "Wind Serenade", administered by placing headphones on the maternal abdomen. The oxygen modulation stimulus consists of 2min blocks alternating between maternal breathing of oxygen or room air through a nasal cannula. Activation maps acquired with the rFOV sequence (Figure C) show significant negative correlation with the oxygen stimulus (cc < -.2).

Future work will include f-fMRI of oxygen modulation stimulus in the liver, placenta and other extracranial sites in the fetus. We will also implement a visual stimulus alternating 20s blocks of a slowly flashing light (through the abdominal wall) or no light.

The Geometry Factor as a Cramér-Rao Bound for Magnitude and Phase

Angel R. Pineda, Calvin D. Lew, Roland Bammer - Department of Radiology

In SENSE imaging, aliased data from multiple coils is used to estimate the unaliased components of the image. Noise propagation from the aliased coil images into the complex reconstructed images is typically quantified by the geometry factor (g-factor). The geometry factor in SENSE gives the ratio of the noise of the reconstructed complex image obtained from the full acquisition over that of the accelerated acquisition. Phase estimation is important for applications like flow quantitation but the noise in the phase in parallel imaging has not been characterized in the same way as the magnitude, in part because the phase is a nonlinear parameter of the measurements. The objective of this abstract is to analyze the noise amplification for the phase and to make a connection between the g-factor and the Cramér-Rao bound (CRB). We recast SENSE in terms of the magnitude and phase. The CRB can be computed to provide the minimum variance of the magnitude and phase. We used a sensitivity map from a 4 coil acquisition
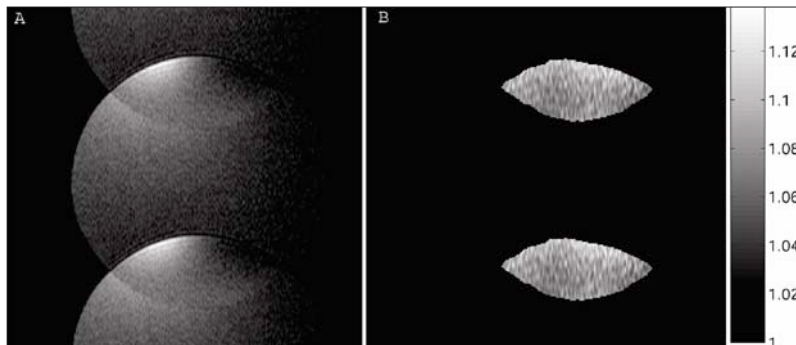
The reconstruction from a single coil showing the areas where the signal aliasing needs to be removed by SENSE. B) The normalized version of the CRB for magnitude and phase as well as the g-factor map. In our experiments, all these quantities where the same.

for a 2x acceleration acquired on a GE Signa 1.5T scanner to compute both the g-factor and the normalized CRB for the magnitude and phase. The figure shows the aliasing which is being removed by the reconstruction process, the g-factor map, and the square root of the noise efficiency for magnitude and phase. In our numerical experiments, these three quantities were the same. Hence, the minimum variance of the magnitude and phase of the reconstructed images are minimized when the geometry factor is minimized. The numerical results shown suggest an alternative interpretation of the g-factor as a normalized CRB for both magnitude and phase. An analytic solution and extension to sensitivity maps with errors are the focus of our future work.

Neural Mechanisms for Understanding Abstract Motion Stimuli

Jon Winawer, Nathan Witthoft, Lera Boroditsky - Department of Psychology

How are abstract ideas implemented in neural circuits? We address this question in the domain of visual motion. Our hypothesis is that circuits used for processing visual motion are reused for processing motion that is not physically present, but is instead either imagined, inferred from photos, or represented in words. Prior work in our lab has shown that mental imagery of motion produced a motion aftereffect on real motion test probes (such that after imagining upward motion a neutral stimulus more likely appeared to move downwards), and that the likelihood of observing the aftereffect was dependent on the level of prior activation of motion-sensitive visual areas, including hMT+. Likewise, we have shown that viewing sequences of implied motion photos (e.g., see figure) also leads to a motion aftereffect, measured behaviorally in our lab. Is this due to adaptation of direction selective circuits in hMT+? We are currently addressing this question using fMRI-adaptation. We first identify regions of interest in visual cortex sensitive to motion through the use of standard motion localizers. We then test whether there is direction selective ad-

An example of an implied motion stimulus.

aptation to implied motion in the regions of interest by comparing the amount of activation during blocks in which the direction of motion varies (left and right) versus blocks in which it is constant (left only or right only). We predict that, just as with real motion, prolonged viewing of implied motion in the same direction will lead to adaptation and thus a reduced response, whereas alternating directions of implied motion will prevent adaptation. Such a result, if obtained, would suggest that the interpretation of motion we ascribe to a picture is scaffolded, at least in part, on mechanisms also used for analyzing real motion. We thus far have obtained behavioral data on aftereffects from implied motion and are now piloting the fMRI experiments. Subsequent studies will examine whether spoken sentences that utilize motion words, whether literally or metaphorically, also activate motion-sensitive brain areas. Together we believe these results will provide an important step in explaining how conceptual knowledge is grounded in more concrete perceptual mechanisms.

High-Resolution Imaging Reveals Highly Selective Nonface Clusters in the Fusiform Face Area

Kalanit Grill-Spector[1,2], Rory Sayres[2] and David Ress[3] - [1]Dept. of Psychology, [2]Neuroscience Institute, [3]Brown University

A region in ventral human cortex (fusiform face area: FFA), thought to be important for face perception, responds strongly to faces and less to nonface objects. This pattern of response may reflect a uniform face-selective neural population or activity averaged across populations with heterogeneous selectivity. To distinguish between these hypotheses of FFA function we determined the fine-grain functional organization of the FFA using high-resolution functional magnetic resonance imaging (HR-fMRI, voxels of 1x1x1).

Five subjects were scanned in a 3T scanner at HR-fMRI with a surface coil while they viewed blocks of faces and objects (animals, cars, and abstract sculptures) that alternated with scrambled versions of these stimuli. The experiment was repeated eight times using different images and block orders. To compare HR-fMRI to previous results, subjects repeated the experiment using SR-fMRI. We defined the FFA using SR-fMRI (voxels of 3x3x3mm) and then examined the properties of this region using HR-fMRI. We found that the FFA has hetero-

geneous fine-grain structure (Fig. 1). Localized clusters in the FFA are highly selective to specific categories including nonface objects (such as cars and abstract sculptures, Fig. 1) and face-selective activations within the FFA are not spatially contiguous. Overall, we found a preponderance of face-selective responses in the FFA, but no difference in selectivity to faces compared to nonfaces.
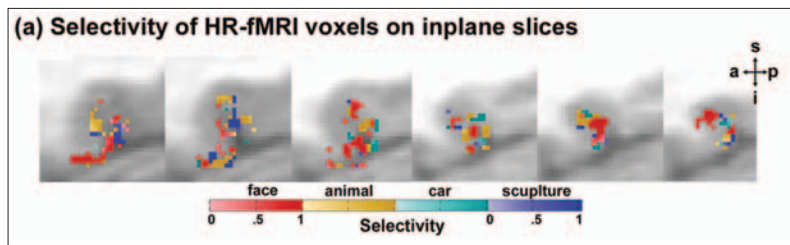
Thus, standard fMRI of the FFA reflects averaging of heterogeneous highly-selective neural populations of differing sizes, rather than higher selectivity to faces. These results challenge the notion that the FFA (as measured with standard fMRI) is a domain-specific module for processing faces. Overall, our approach provides a framework for understanding the fine-scale structure of neural representations in the human brain.

Sex Differences in Brain Activation Elicited by Humor

EIMAN AZIM[1,2], DEAN MOBBS[1,2], BOOIL JO[1,2], VINOD MENON[1,3], ALLAN L. REISS[1,2,3] - [1]DEPARTMENT OF PSYCHIATRY & BEHAVIORAL SCIENCES, [2]CENTER FOR INTERDISCIPLINARY BRAIN SCIENCES RESEARCH, AND [3]PROGRAM IN NEUROSCIENCE STANFORD UNIVERSITY SCHOOL OF MEDICINE

With recent investigation beginning to reveal the cortical and subcortical neuroanatomical correlates of humor appreciation, the present event-related functional MRI (fMRI) study was designed to elucidate sex-specific recruitment of these humor related networks. Twenty healthy subjects (10 female) underwent fMRI scanning while subjectively rating 70 verbal and nonverbal achromatic cartoons as funny or unfunny. Males and females were found to share an extensive humor-response strategy as indicated by recruitment of similar brain regions: both activate the temporal-occipital junction and temporal pole, structures implicated in semantic knowledge and juxtaposition, and the inferior frontal gyrus, likely to be involved in language processing. Females, however, activate the left prefrontal cortex more than males, suggesting a greater degree of executive processing and language based decoding. Females also exhibit greater activation of mesolimbic regions, including the nucleus accumbens, implying greater reward network response and possibly less reward expectation. These results indicate sex-specific differences in neural response to humor with implications for sex-based disparities in the integration of cognition and emotion.

In summary, this study utilizes a fundamental human characteristic to uncover overlapping and divergent neural correlates of high-order processing. Importantly, the differences in neural activity observed in this study are independent of any measured between-sex behavioral differences. Equivalent subjective amusement seems to recruit divergent processing strategies that manifest equivalent behavior, indicating either that these differences in neural processing appear without behavioral correlate, or that our behavioral assays are insensitive to more subtle dissimilarities.
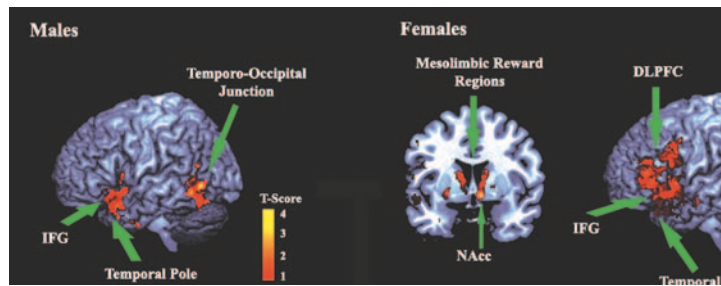
As fMRI analysis of humor progresses, examination of the role of specific brain regions can elucidate how the components of these networks interact and functionally connect, further revealing the neuroanatomical correlates of cognition, emotion, and sense of humor.

BOLD signal activation for funny-unfunny cartoons. Compared to males, females exhibit greater activation of the dorsolateral prefrontal cortex, as well as subcortical dopaminergic reward regions, including the nucleus accumbens.

Arithmetic Ability and Parietal Alterations: A Diffusion Tensor Imaging Study in Velocardiofacial Syndrome

NAAMA BARNEA-GORALY[1], STEPHAN ELIEZ[1,2], VINOD MENON[1,3], ROLAND BAMMER[4], ALLAN L. REISS[1] - [1]DEPARTMENT OF PSYCHIATRY & BEHAVIORAL SCIENCES, STANFORD UNIVERSITY SCHOOL OF MEDICINE, [2]DIV. OF CHILD AND ADOLESCENT PSYCHIATRY, GENEVA UNIVERSITY SCHOOL OF MEDICINE, [3]PROGRAM IN NEUROSCIENCE, STANFORD UNIVERSITY SCHOOL OF MEDICINE, [4]LUCAS MRS/I CENTER DEPARTMENT OF RADIOLOGY, STANFORD UNIVERSITY

Velocardiofacial syndrome (VCFS) is a congenital anomaly that causes somatic as well as cognitive and psychiatric impairments. Previous studies have found specific deficits in arithmetic abilities in subjects with VCFS. In this study, we investigated whether abnormalities in white matter pathways are correlated with reduced arithmetic ability. Nineteen individuals with VCFS aged 7 – 19 years received diffusion-weighted magnetic resonance imaging (MRI) scans. A linear regression model was used to correlate fractional anisotropy (FA) values with scores of the arithmetic subscale on a standardized cognitive assessment (WISC/WAIS) on a voxel-by-voxel basis, after co-varying for any IQ- and age-related effects. There was a statistically significant positive correlation between the arithmetic score on the WISC/WAIS and FA values in white matter tracts adjacent to the left supramarginal and angular gyri, as well as along the left intraparietal sulcus. Inferior parietal lobe white matter structural aberrations may contribute to reduced arithmetic ability in VCFS.

Our findings highlight potential cognitive implications of white matter aberrations in VCFS. Understanding biological factors underlying cognitive deficits provides potential for improving effectiveness of future assessment and intervention with children and adolescents affected by VCFS.

Voxels that showed significant correlation between FA values and the WISC/WAIS arithmetic subscale score. Sagittal view.

White Matter Development During Childhood and Adolescence: A Cross-sectional Diffusion Tensor Imaging Study

Naama Barnea-Goraly[1], Vinod Menon[1,2,3], Mark Eckert[1], Leanne Tamm[3], Roland Bammer[4], Asya Karchemskiy[1], Christopher Dant[1], Allan L. Reiss[1] - [1]Department of Psychiatry & Behavioral Sciences, [2]Program in Neuroscience, and [3]Neuroscience Institute, Stanford University School of Medicine, [3]Department of Psychology, Children's Hospital of Orange County, [4]Lucas MRS/I Center Department of Radiology, Stanford University
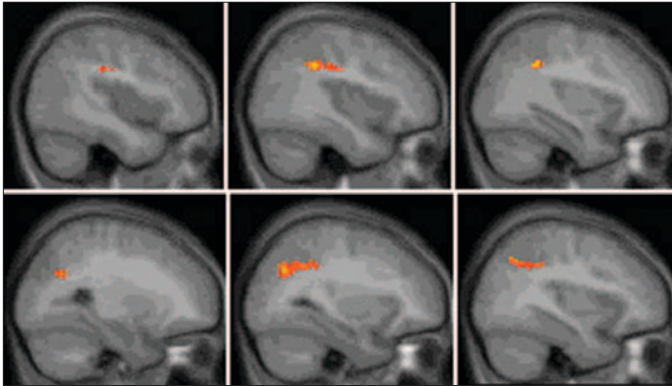
Voxels that showed significant correlation between FA values and age (axial view).

Maturation of brain white matter pathways is an important factor in cognitive, behavioral, emotional and motor development during childhood and adolescence. In this study, we investigate white matter maturation as reflected by changes in anisotropy and white matter density with age. Thirty-four children and adolescents aged 6 – 19 years received diffusion-weighted magnetic resonance imaging scans. Among these, 30 children and adolescents also received high-resolution T1-weighed anatomical scans. A linear regression model was used to correlate fractional anisotropy (FA) values with age on a voxel-by-voxel basis. Within the regions that showed significant FA changes with age, a post hoc analysis was performed to investigate white matter density changes. With increasing age, FA values increased in prefrontal regions, in the internal capsule as well as in basal ganglia and thalamic pathways, the ventral visual pathways, and the corpus callosum. The posterior limb of the internal capsule, intrathalamic connections, and the corpus callosum showed the most significant overlaps between white matter density and FA changes with age. This study demonstrates that during childhood and adolescence, white matter anisotropy changes in brain regions that are important for attention, motor skills, cognitive ability, and memory. This typical developmental trajectory may be altered in individuals with disorders of development, cognition and behavior.

This study provides new evidence of spatial and temporal development of white matter throughout childhood and adolescence. Our findings suggest that particular histological phenomena underlie this development on a regional basis. Studies such as these will be helpful in eventually delineating how typical developmental trajectory is altered in individuals with disorders of development, cognition, and behavior.

Neurofunctional Differences Associated with Arithmetic Processing in Turner Syndrome

Shelli Kesler, Vinod Menon, Allan L. Reiss - Department of Psychiatry & Behavioral Sciences

Turner syndrome (TS) is a neurogenetic disorder characterized by the absence of one X chromosome in a phenotypic female. Individuals with TS are at risk for impairments in mathematics. We investigated the neural mechanisms underlying arithmetic processing in TS. Fifteen subjects with TS and 15 age-matched typically developing controls were scanned using functional MRI while they performed easy (two-operand) and difficult (three-operand) versions of an arithmetic processing task. Both groups activated fronto-parietal regions involved in arithmetic processing during the math tasks. Compared with controls, the TS group recruited additional neural resources in frontal and parietal regions during the easier, two-operand math task. During the more difficult three-operand task, individuals with TS demonstrated significantly less activation in frontal, parietal, and subcortical regions than controls. However, the TS group's performance on both math tasks was comparable to controls. Individuals with TS demonstrate activation differences in fronto-parietal areas during arithmetic tasks compared with controls. They must recruit additional brain regions during a relatively easy task and demonstrate a potentially inefficient response to increased task difficulty compared to controls.
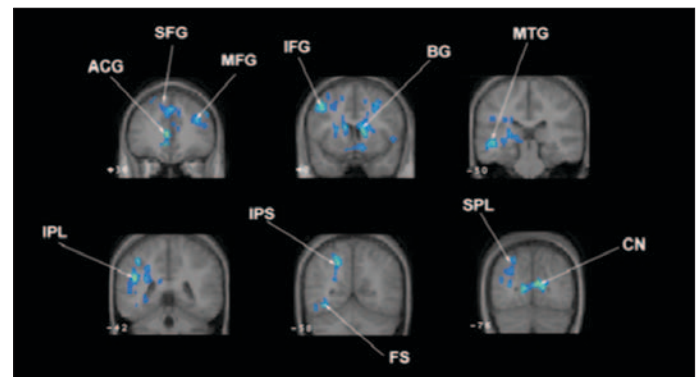
This figure shows 3-Operand Math: Between group contrast demonstrating significantly greater activation in controls compared to the TS group in left inferior parietal lobe (IPL) extending into intraparietal sulcus (IPS), superior parietal lobule (SPL), fusiform (FS) and posterior middle temporal gyrus (MTG); anterior cingulate (ACG) extending into bilateral medial superior frontal gyrus (SFG); bilateral middle (MFG) and inferior frontal (IFG) gyri; cuneus (CN) and basal ganglia (BG).

COMT Genotype Predicts Longitudinal Cognitive Decline and Psychosis in 22q11.2 Deletion Syndrome

Doron Gothelf[1,2], Stephan Eliez[3], Tracy Thompson[1], Christine Hinard[4], Lauren Penniman[1], Carl Feinstein[1], Hower Kwon[5], Shuting Jin[1], Booil Jo[1], Stylianos E. Antonarakis[6], Michael A. Moorris[4], Allan L. Reiss[1] - [1]Center for Interdisciplinary Brain Sciences Research, Stanford Univ. School of Medicine, [2]Sackler Faculty of Medicine, Tel Aviv University, [3]Department of Psychiatry, University of Geneva School of Medicine, [4]Medical Genetics Service, University Hospitals, Geneva, [5]Dept. of Psychiatry & Behavioral Sciences, University of Washington, [6]Dept. of Genetic Medicine and Development, University Medical School, Centre Medicale Universitaire, Geneva

Schizophrenia is strongly hereditary, but efforts to identify its molecular pathophysiology have yielded limited results, probably owing to the etiological heterogeneity of this symptom-defined disorder. One approach for contending with this heterogeneity is to study subjects with more homogeneous risk for psychosis. The 22q11.2 deletion syndrome (22q11.2DS) is caused by a microdeletion on chromosome 22 and occurs in about 1 of every 4,000 live births. One-third of the individuals with this condition develop schizophrenia or a related psychotic disorder, making 22q11.2DS the most commonly known risk factor for the development of psychosis and a unique model for elucidating neurodevelopmental pathways leading to psychotic disorders. The syndrome is also associated with congenital malformations and cognitive deficits.

In this study, 24 subjects with 22q11.2DS and 23 subjects with idiopathic developmental disabilities were evaluated during childhood and re-evaluated during late adolescence or early adulthood. Subjects were genotyped for several single-nucleotide polymorphisms, assessed for severity of psychiatric and cognitive functioning, and anatomical magnetic resonance images (MRI) were acquired at the Lucas Center with a GE Signa 1.5- scanner. We identified the catechol-O-methyltransferase low-activity allele (COMTL) as an important neurodevelopmental risk factor for decline in prefrontal cortical volume and cognition, as well as for the consequent development of psychotic symptoms during adolescence.

Personality Predicts Activity in Reward and Emotional Regions Associated with Humor

Dean Mobbs[1,2], Cindy Hagan[1,2], Eiman Azim[1,2], Vinod Menon[1,3], Allan L. Reiss[1,2,3] - [1]Department of Psychiatry & Behavioral Sciences, [2]Center for Interdisciplinary Brain Sciences Research, [3]Program in Neuroscience, Stanford University School of Medicine

Previous research and theory suggest that two stable personality dimensions, extroversion and neuroticism, differentially influence emotional reactivity to a variety of pleasurable phenomena. Here, we use event-related functional MRI to address the putative neural and behavioral associations between humor appreciation and the personality dimensions of introversion-extroversion and emotional stability-neuroticism. Our analysis showed extroversion to positively correlate with humor-driven blood oxygenation level-dependent (BOLD) signal in discrete regions of the right orbital frontal cortex, ventrolateral prefrontal cortex, and bilateral temporal cortices. Introversion correlated with increased activation in several regions, most prominently the bilateral amygdala. Although neuroticism did not positively correlate with any whole-brain activation, emotional stability (i.e., the inverse of neuroticism) correlated with increased activation in the mesocortical-mesolimbic reward circuitry encompassing the right orbital frontal cortex, caudate, and nuclear accumbens.

Our findings support the notion that key neurobiological structures in humor circuitry are mediated by personality. An important focus of future research will be to explore how the intriguing interaction between personality and humor exerts influence over physiological and psychological functioning.
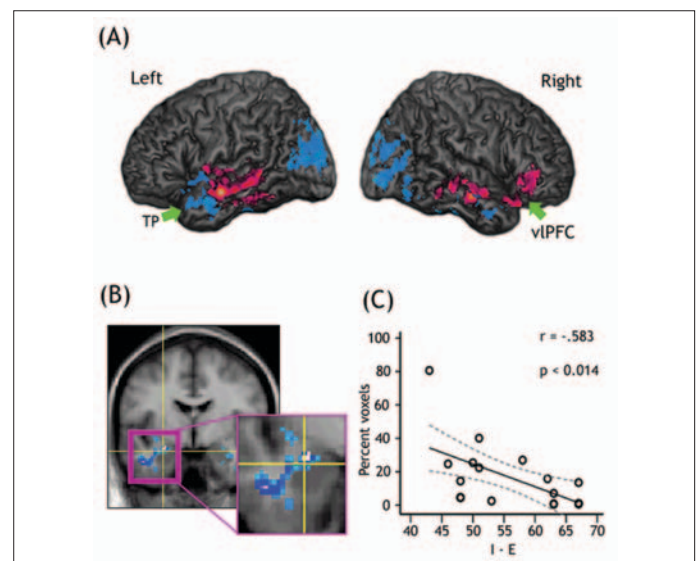
BOLD activity correlation with extroversion and introversion to humor appreciation. (A) Whole-brain BOLD signal correlations with extroversion (red) and introversion (blue) when subjectively chosen humorous cartoons were subtracted from cartoons determined nonhumorous (P < 0.05). (B) Amygdala BOLD signal correlation with introversion. (C) Scatter plot illustrating the increased amygdala activation with introversion.

Amygdala Activation in the Processing of Neutral Faces in Social Anxiety Disorder: Is Neutral Really Neutral?

Rebecca E. Cooney, Lauren Y. Atlas, Jutta Joormann, Fanny Eugène, & Ian H. Gotlib - Department of Psychology

Social Anxiety Disorder (SAD) is a prevalent and debilitating disorder characterized by intense fear of social situations that significantly impairs quality of life. Previous research has suggested that SAD is associated with a tendency to interpret ambiguous social stimuli in a threatening manner. Recently, investigators have begun to examine the neurobiological bases of the processing of social stimuli in SAD and have found that individuals with SAD exhibit elevated activation to negative faces (specifically anger and disgust) in the anterior cingulate cortex, parahippocampal gyrus, and amygdala when their responses are contrasted with activations to neutral faces. Given the results of behavioral and imaging finding indicating that SAD individuals may perceive neutral faces as threat-related, however, it is critical to assess the neural responses of SAD individuals to neutral faces alone. The present study was designed to examine whether SAD participants exhibit activation to neutral faces in areas of the brain that have been found to be associated with the processing of negative faces.

Ten participants with SAD and ten healthy control participants (CTL) viewed neutral faces from 20 actors and an oval with a crosshair in the middle in the scanner in an event-related design. Participants were instructed to use a button box to make valence ratings (negative, neutral, or positive) and to indicate 'neutral' when they saw an oval.

Analyses of activations in bilateral amygdala ROIs for the neutral face vs. oval contrasts revealed that whereas SAD participants demonstrated significantly greater activation in the right amygdala than did controls, CTL participants exhibited significantly greater activation in the left amygdala than did SAD participants. Importantly, the SAD and CTL groups did not differ significantly in the time course to ovals, suggesting that the group differences in amygdala activations in the neutral face vs. ovals contrasts are not driven by increased activation to ovals in the SAD group.

These results clearly underscore the importance of selecting adequate baseline or control conditions in studies investigating neural correlates of the processing of emotional stimuli in individuals experiencing emotional disorders.

Neural Correlates of Mood Regulation Through Mood-Incongruent Recall

Rebecca E. Cooney, Jutta Joormann, Lauren Y. Atlas, Fanny Eugene, and Ian H. Gotlib

Investigators have identified a number of strategies that people commonly use to regulate negative moods, including distraction, problem-solving, reappraisal, and spending time with other people. Only recently, however, have researchers begun to examine how and why these strategies work, whether mood-regulation strategies are uniformly successful at improving negative mood, and whether there are consistent individual differences in the use and effectiveness of these strategies. The present study was designed to use fMRI to examine the neural correlates both of the induction of a sad mood state and of the use of positive autobiographical memory to regulate that mood.

Fourteen adult females were scanned as they first recalled happy, positive memories from their high-school years that made them feel good. Next, they viewed a sad film clip and then were scanned as they elaborated their sad mood. Participants were then prompted to recall a second happy autobiographical memory. Two primary issues were addressed with the imaging data: 1) identification of brain regions involved in experiencing an induced sad mood; and 2) determination of which neural structures or regions are recruited as individuals regulate their sad mood by recalling positive autobiographical memories.

Activations during the sad mood elaboration were observed in both anteromedial and lateral sections of OFC, extending bilaterally through the inferior frontal and middle frontal gyrii (including BAs 11, 47, and 13) and into the putamen and nucleus accumbens. Activations were also found in right posterior parahippocampal gyrus (BAs 35, 36, and 38), superior temporal gyrus (BA 22), and right superior frontal gyrus (BA 8). Neural regions that were differentially active during recall of a positive memory in a sad mood state compared with recall of a positive memory in a euthymic or neutral mood state were loci in the ventromedial prefrontal cortex that included bilateral and contiguous activation extending from a region of posterior OFC to subgenual anterior cingulate (BAs 25, 32), activation along the parahippocampal gyrus extending posterior from BA 20 to BA 36, and anterior prefrontal cortical activation in left inferior frontal gyrus (BA 47).

These results suggest that the flexible recruitment of the OFC in the service of experiencing both negative and positive mood states, as well as during the regulation of those states, is a critical component of healthy emotional functioning.

The Neural Substrates of Inhibitory Dysfunction in Major Depression

FANNY EUGÈNE, JUTTA JOORMANN, REBECCA E. COONEY, LAUREN ATLAS, AND IAN H. GOTLIB - DEPARTMENT OF PSYCHOLOGY

Background: Cognitive theories of depression posit that individuals suffering from this disorder are characterized by a cognitive bias that leads them to attend selectively to negative information. An important component of this selective attention to negative information now appears to involve an inhibitory dysfunction – a reduced ability to disengage attention from task-irrelevant negative information. Importantly, this inhibitory deficit has been found in dysphoric individuals and in persons at elevated risk for depression, and has been postulated to be involved in the etiology of this disorder. To integrate these findings with a neural dysfunction formulation of depression, we used functional magnetic resonance imaging (fMRI) to examine neural correlates of inhibitory dysfunction in individuals diagnosed with Major Depressive Disorder (MDD).

Methods and Results: Ten participants diagnosed with MDD and 13 never-depressed controls completed a negative affective priming (NAP) paradigm in the scanner, in which they responded to emotional target words while attempting to ignore emotional distractor words. In the critical trials, the target words have the same valence as the distractor words that were presented in the previous trial, permitting a comparison of the neural responses of depressed and nondepressed participants to previously ignored positive or negative words. Our results indicate that, in nondepressed controls, inhibition of emotional words, regardless of valence, is associated with increased activation in anterior cingulate cortex, a structure thought to play a key role in the regulation of mood and emotion through its connections to both prefrontal cortex and other limbic structures. This increase in cingulate activation was not found in depressed participants. Interestingly, these results seem to be driven mainly by differences in neural response to inhibition of negative words. No difference was observed for positive distractors.

Conclusions: The findings of this study indicate that anterior cingulate dysfunction may underlie difficulties experienced by depressed individuals in inhibiting negative thoughts. These results underscore the importance of examining the relation between cognitive and neural functioning in depression in attempting to gain a better understanding of this debilitating disorder.

Neural Substrates of Memory Sensitivity for Negative Stimuli in Depression

J. PAUL HAMILTON AND IAN H. GOTLIB - DEPARTMENT OF PSYCHOLOGY

Background: Cognitive theories of depression posit that individuals suffering from this disorder are characterized by a cognitive bias that leads them to attend selectively to negative information. An important component of this selective attention to negative information now appears to involve an inhibitory dysfunction – a reduced ability to disengage attention from task-irrelevant negative information. Importantly, this inhibitory deficit has been found in dysphoric individuals and in persons at elevated risk for depression, and has been postulated to be involved in the etiology of this disorder. To integrate these findings with a neural dysfunction formulation of depression, we used functional magnetic resonance imaging (fMRI) to examine neural correlates of inhibitory dysfunction in individuals diagnosed with Major Depressive Disorder (MDD).

Methods and Results: Ten participants diagnosed with MDD and 13 never-depressed controls completed a negative affective priming (NAP) paradigm in the scanner, in which they responded to emotional target words while attempting to ignore emotional distractor words. In the critical trials, the target words have the same valence as the distractor words that were presented in the previous trial, permitting a comparison of the neural responses of depressed and nondepressed participants to previously ignored positive or negative words. Our results indicate that, in nondepressed controls, inhibition of emotional words, regardless of valence, is associated with increased activation in anterior cingulate cortex, a structure thought to play a key role in the regulation of mood and emotion through its connections to both prefrontal cortex and other limbic structures. This increase in cingulate activation was not found in depressed participants. Interestingly, these results seem to be driven mainly by differences in neural response to inhibition of negative words . No difference was observed for positive distractors.

Conclusions: The findings of this study indicate that anterior cingulate dysfunction may underlie difficulties experienced by depressed individuals in inhibiting negative thoughts. These results underscore the importance of examining the relation between cognitive and neural functioning in depression in attempting to gain a better understanding of this debilitating disorder.

Real-time Localized Neuromodulation in Major Depression

J. Paul Hamilton, Gary H. Glover, and Ian H. Gotlib

Background: The application of functional neuroimaging techniques to the study of major depressive disorder has been critical in helping to identifying its neural correlates as well as in informing neuroaffective models of the disorder. Two shortcomings of this approach have emerged, however. First, investigators have not distinguished neural correlates of depression from neural factors that are involved more critically in producing and sustaining depressive symptomatology. This distinction is essential in creating informative and useful neuroaffective models of depression. Second, functional neuroimaging studies of depression have had limited impact on the quality of life among those suffering from the disorder. This study was designed both to examine the use of real-time localized neurofeedback training to isolate crucial neural factors in depression, and to assess the potential effectiveness of real-time neurofeedback as a novel therapeutic procedure in the treatment of depression.

Methods and preliminary data: We have developed a software and hardware configuration capable of extracting and analyzing blood oxygen level dependent (BOLD) fMRI data in real time. Currently, this system can extract and display continuously updated BOLD signal both from a region of interest and from the whole brain. This information can be presented to participants who can then, through iterative trial and error, learn to modulate activity within a given region of interest. In addition, statistical maps reflecting contrasts of interest can be generated and displayed in real time. We have been able to isolate regions in the medial prefrontal cortex and the subgenual cingulate cortex, two structures that have been implicated in depression and that are preferentially involved in the processing of negative affect. We have been able to present indices of ongoing activity in these structures to participants. Thus far, two healthy control participants have been presented with activation indices in real time. One received information from the medial prefrontal cortex and the other from the subgenual cingulate cortex. Both participants learned to modulate neural activation across the course of a fifteen-minute training scan. We are now examining whether these training procedures can be implemented with depressed participants to determine if leaned modulation of structures that have been implicated in depressive pathology is effective in the treatment of this disorder.

Attention-Dependent Modulation of Medial Temporal Lobe Encoding Processes

Nicole M. Dudukovic, Alison R. Preston, Jermaine J. Archie & Anthony D. Wagner
Department of Psychology and Neurosciences Program

Goal-directed attention has been shown to modulate activation in lateral cortical regions known to process faces (fusiform cortex) and scenes (parahippocampal cortex), but an open question is whether these effects propagate along the medial temporal lobe (MTL) circuit. The present study investigated how selective attention modulates stimulus-specific encoding processes in MTL cortex and the hippocampus, including how attention impacts MTL responses that predict subsequent memory. High-resolution functional magnetic resonance imaging (fMRI) of the human MTL was conducted on a 3.0 Tesla GE Signa scanner at the Lucas Center while 12 participants attended, ignored, or passively viewed face and scene stimuli. Each trial consisted of four sequentially presented images, two faces and two scenes, and participants were instructed to 1) Remember Faces and Ignore Scenes, 2) Remember Scenes and Ignore Faces, or 3) Passively View both Faces and Scenes (Gazzaley et al., 2005). After a brief delay, either a probe stimulus appeared and participants indicated whether it was in the current memory set (Remember Faces/Remember Scenes conditions), or an arrow appeared and participants indicated the direction it pointed (Passive View condition). A surprise post-scan recognition memory test revealed that participants were more accurate and had higher confidence in their memory judgments for stimuli that were attended as opposed to those that were ignored or passively viewed. Anatomical and functional region of interest (ROI) analyses differentiated between individual MTL subregions and demonstrated that goal-directed attention modulates encoding activation in perirhinal cortex (for faces) and parahippocampal cortex (for scenes) and that these effects propagate into hippocampal subfields. In addition, attention-dependent subsequent memory effects were observed within MTL subregions, suggesting that attention is critical for the encoding responses that give rise to later memory. We are currently finishing data collection and working on further analyses. The results will be presented at a scientific meeting in October and will be written up for publication in a peer-reviewed scientific journal in the fall.

References/Funding Source
Dudukovic, N.M., Preston, A.R., Archie, J.J., & Wagner, A.D. (2006). Attention-Dependent Modulation of Medial Temporal Lobe Encoding Processes. Society for Neuroscience Abstracts.
National Science Foundation (BCS 0401641), NARSAD

Remembering and Forgetting During Competitive Memory Retrieval: Prefrontal and Parietal Cortical Mechanisms impact Episodic Memory Suppression

BRICE KUHL, ITAMAR KAHN, NICOLE M. DUDUKOVIC, & ANTHONY D. WAGNER
DEPT. OF PSYCHOLOGY AND NEUROSCIENCES PROGRAM, STANFORD UNIVERSITY

Episodic retrieval often involves selection of a target amidst interference from competing memories. To explore the neurobiological mechanisms recruited during retrieval in the face of competition and the mechanisms that contribute to the suppression of selected-against competitors, we used fMRI to study retrieval-induced forgetting (Anderson, Bjork, & Bjork, 1994).

Participants (n=20) initially studied cue–associate word pairs, learning multiple associates for each cue. Subsequently, participants performed retrieval practice for some of the associates of some of the cues. Finally, a cued recall test was administered for all items.

Behavioral data replicated the retrieval-induced forgetting effect: unpracticed associates of a practiced cue (competitors) were less likely to be recalled than unpracticed associates of an unpracticed cue (baseline items)—behavioral evidence for suppression of competing memories). fMRI analyses of the retrieval practice phase revealed three main findings. First, a diverse set of prefrontal and parietal regions decreased in activation as competition demands decreased (as targets were practiced repeatedly). Second, the extent to which ACC activation decreased across retrieval practice attempts was correlated with the magnitude of forgetting (suppression) of competing memories, as observed on the final test. Third, activation in a subset of prefrontal and parietal regions was correlated with both the decrease in ACC activation and the magnitude of suppression observed at test.

These data suggest a role for ACC in dynamically detecting mnemonic competition, and for select prefrontal/parietal mechanisms in implementing suppression as a means of reducing competition.

Mindfulness Meditation, Emotion Regulation, and Brain Responses in Social Phobia

PHILIPPE R. GOLDIN & JAMES J. GROSS - DEPARTMENT OF PSYCHOLOGY, STANFORD UNIVERSITY

There is a growing interest in the application of mindfulness techniques for modulating one's relationship to ongoing mental experience (cognitions, emotions, sensations). However, there is need for more detailed empirical investigations using experimental paradigms to address (a) whether mindfulness training works, (b) how it affects emotional reactivity and regulation, (c) what neural systems are modulated by training in mindfulness techniques, and (d) how these might compare to cognitive regulatory strategies.

In this talk, we consider the brain-behavior relationship of different methods of emotion regulation - mindfulness meditation, cognitive regulation, and attentional distraction - in people diagnosed with social phobia (SP), and the neural mechanisms underlying therapeutic change associated with training provided in a mindfulness meditation based stress reduction (MBSR) program.

To integrate basic and clinical literatures and empirically examine the neural mechanisms of mindfulness meditation, a multi-level assessment (psychiatric questionnaires, autonomic psychophysiology, functional magnetic resonance (fMRI) imaging of neural responses, clinical diagnostic interview) was administered before and after a 9-week mindfulness meditation based stress reduction intervention. Participants were presented with self-generated autobiographical social situation related negative self-beliefs and then cued to shift into mindful awareness of breathing, cognitive restructuring, or attentional distraction during fMRI scanning with concurrent emotion rating and autonomic physiological measurements. At baseline, SP were compared to age, gender, education, handedness matched healthy controls (HC) to examine the effect of psychiatric status. Post-MBSR, SP treatment completers were compared to their own pre-MBSR measurements to examine the effect of mindfulness training.

Initial findings at baseline indicate that SP (n=11) compared to HC (n=11) show (a) greater emotional reactivity to negative self-beliefs in emotion ratings and left amygdala, (b) less effective cognitive regulation of emotion, but (c) a statistical trend towards greater efficacy for mindful awareness of breath compared to attentional distraction in reducing emotional reactivity to social negative self-beliefs. Analyses of post-MBSR measures are underway. These results suggest (a) differential effectiveness of various emotion regulation techniques in SP and HC, and (b) highlight potential mechanisms that can be targeted in therapy.

Mechanisms of Emotion Regulation in Social Phobia

PHILIPPE R. GOLDIN & JAMES J. GROSS - DEPARTMENT OF PSYCHOLOGY, STANFORD UNIVERSITY

Clinical outcome studies have established the effectiveness of CBT for social phobia (SP). However, few systematic studies of the neurobiological mechanisms and neural dynamics of key components of the CBT (e.g., cognitive restructuring) have been conducted. Clarification of neural mechanisms of therapeutic change will provide valuable knowledge about the nature and limits of neural plasticity and the implementation of cognitive strategies for modifying distorted interpretations and hyperactive emotional responding in people suffering form social anxiety. Furthermore, increased understanding of underlying mechanisms of cognitive regulation of emotion will help clarify why CBT works and allow us to better predict which patient is most likely to benefit from CBT or another type of treatment.

To investigate emotional reactivity and cognitive regulation, we examined emotion intensity ratings and neural responses using fMRI in 11 generalized SP (diagnosed with the ADIS-IV) and 11 demographically-matched healthy controls (HC) during (a) simple viewing and (b) active implementation of pre-trained thought strategies to cognitively down-regulation emotion reactivity to critical face expressions (social threat) and violent scenes (physical threat). We expected cognitive regulation to be linked to neural signal increases in prefrontal cortical (PFC) regions implicated in cognitive control and decreases in emotion processing regions, including the amygdala (limbic) and orbitofrontal cortex (paralimbic).

Initial results suggest that SP were more emotionally reactive than HC to both social and physical threat stimuli as indexed by grater nega-tive emotion intensity ratings and neural responses in the brain regions associated with detection of emotion salience and emotion generation (i.e., amygdala, ventromedial PFC, orbitofrontal cortex, affective division of anterior cingulate). During cognitive regulation of physical threat, SP and HC did not differ on (a) degree of reduction in negative emotional intensity, and (b) distributed pattern of active brain regions implicated in top-down cognitive control. However, during cognitive regulation of critical face expressions, SP compared to HC demonstrated enhanced cognitive control activity (e.g., dorsolateral, dorsomedial PFC) without elimination of emotion reactivity related brain activity (e.g., amygdala, affective division of anterior cingulate, ventromedial PFC).

These results highlight that while social phobics can regulate nonsocial, physical threat stimuli in a manner similar to HC. However, their attempts to regulate responses to critical face expressions lead to an ineffective implementation of cognitive control that fails to "turn off" emotional reactivity to social anxiety specific stimuli. Implications for assessing the specific cognitive restructuring techniques and the relationship to severity of social anxiety will be discussed.

Taking the Observer's Perspective: Social Evaluation, Eye Gaze and Brain Responses in Social Phobia

PHILIPPE R. GOLDIN & JAMES J. GROSS - DEPARTMENT OF PSYCHOLOGY, STANFORD UNIVERSITY

Cognitive models of social phobia propose that cognitive biases and fears regarding negative evaluation by others result in preferential attention to interpersonal sources of threat. These fears may account for the hypervigilance and avoidance of eye contact commonly reported by clinicians and for the tendency to take an outside observer perspective of self in social situations as reported by social phobics.

In this talk, we examine the role of eye gaze (direct vs. averted) and social perspective (first-person vs. external observer) on evaluative judgments (like-dislike of self and other) and on neural systems underlying these psychological processes during functional magnetic resonance imaging (fMRI). Eleven adults meeting DSM-IV criteria for generalized social phobia and 11 age, education, gender, and handedness matched healthy control participants not meeting any lifetime DSM-IV criteria were recruited for this study. A block design (5 face trials, 3-seconds each) was used to present 30 direct and 30 averted eye gaze neutral face stimuli (half male, half female) twice, once under each of the two social perspectives.

Initial results indicate that compared to healthy controls, social phobics demonstrated in response to averted eye gaze increased neural signal in brain regions associated with attending to facial details (right superior temporal gyrus) and assigning emotional salience (orbitofrontal cortex), but decreased neural signal in a brain region associated with internal verbalization (left inferior frontal gyrus).

For the social perspective manipulation, social phobics failed to show the normative first-person perspective related enhanced neural response pattern evinced by healthy controls in brain regions linked to executive attention and cognitive control (dorsal anterior cingulate and medial prefrontal cortex), emotional salience (orbitofrontal cortex) and processing of face feature details (inferior temporal gyrus).

An examination of the interaction of eye gaze and social perspective showed that greater social fear (as reported in the Liebowitz Social Anxiety Scale) was associated ($r = .57$) with greater neural response in the left amygdala in social phobics, but not healthy controls, when viewing averted eye gaze and taking the external observer's perspective on self.

These data support the "distorted assumptions about self in social world" component of cognitive model of social anxiety proposed by Clark and Wells and identify a neural signature of social anxiety that may serve as a target for therapy.

fMRI Investigation of Positive Self-Referential Processing in Social Anxiety Disorder

Shabnam Hakimi, Philippe R. Goldin, & James J. Gross - Department of Psychology, Stanford University

Social phobia (SP) is characterized by fear of negative self-evaluation in social situations. Individuals with SP demonstrate a negative bias in processing of self-relevant information which results in decreased processing of positive aspects of self. We used fMRI to examine the neural substrates of positive self-referential processing of social trait adjectives in 16 individuals who met DSM-IV criteria for a primary diagnosis of generalized social anxiety disorder and 14 demographically matched healthy adults (HC). During the self-referential encoding task, participants were presented with positive social trait adjectives for which they were cued to decide if a word was self-descriptive or was presented in uppercase letters. Behavioral results indicated greater (F(1,28)=4.97, p<.05, partial eta2=.15) self-endorsement of positive words in HC (80%) than SP (62%) and no difference in the lower level control condition, where HC and SP correctly identified 99% and 97%, respectively, of uppercase words (p>.26). Neural results demonstrated greater differential BOLD response (p<.001 per voxel) in HC compared to SP for the self versus case contrast in regions implicated in self-referential (medial and dorsomedial PFC), linguistic (left inferior frontal gyrus), affective (bilateral insula, bilateral parahippocampal gyrus, anterior cingulate, oribitofrontal cortex), and visual attention (posterior cingulate) processing. These results demonstrate both behavioral and neural deficits in positive self-referential processing in individuals with SP and highlight a potentially important brain-behavior relationship that may serve as a target of treatment outcome in clinical interventions for social anxiety disorder.

The Neural Bases of Emotion Regulation: Reappraisal and Suppression of Negative Emotion

Philippe R. Goldin, Kateri McRae, Wiveka E Ramel, & James J Gross - Department of Psychology, Stanford University

Emotion regulation strategies are thought to differ in when and how they influence the emotion-generative process. However, no study has directly tested this claim by probing the neural bases of contrasting strategies. The present study used fMRI to examine reappraisal (a cognitive strategy that impacts the emotion-generative process early and effectively) and expressive suppression (a behavioral strategy that inhibits the emotion-generative process later and less effectively). Seventeen women viewed 15s neutral and negative-emotion eliciting films under four conditions – watch neutral, watch negative, reappraise negative, and suppress negative - while providing ratings of emotion experience and having their face expressions videotaped. Reappraisal resulted in early (0-4.5s) prefrontal activation with decreased negative emotion behavior and experience, and decreased amygdala and insular activations. Suppression produced late (10.5-15s) prefrontal activation with decreased negative emotion behavior and experience, but increased amygdala and insula activation. These findings demonstrate the differential efficacy of reappraisal and suppression, and highlight intriguing differences in their temporal dynamics.

VBM Analysis in Patients with Complex Regional Pain Syndrome (CRPS)

Takefumi Ueno, Deepak Soneji, [2]Kim Kaplan, [1]Fumiko Maeda, Camille Palma, Eva Patil, [2]Sean Mackey
[1]Departments of Psychiatry and [2]Anesthesia, Stanford University School of Medicine

Complex regional pain syndrome is a debilitating chronic neuropathic pain condition that is poorly understood. Recent evidence suggests that supraspinal mechanisms may play a role in the generation and maintenance of CRPS. Previous work has demonstrated volume differences in chronic back pain patients. We used VBM (voxel-based morphometry) with high-resolution anatomical MRI images to investigate volume differences in the brain's gray matter between CRPS patients and pain-free subjects.

With IRB approval, 12 healthy subjects and 9 patients who met IASP criteria for CRPS were recruited. High-resolution anatomical scans were collected on a 3T MRI scanner (T1, spin echo). SPM2 and MRIcro were used for skull stripping, normalization, segmentation, and detection of volume differences between the patients and healthy subjects. We implemented ANOVA statistics to detect volume changes between the two groups, and we then applied t-statistics to determine whether there were increases or decreases in the areas that showed a difference.

Volume changes were found in the thalamus, insular cortex, orbitofrontal cortex, anterior cingulate cortex, and cerebellum. We found volume increases in CRPS patients in the bilateral thalamus and cerebellum while the insular cortex and orbitofrontal cortex showed volume decreases.

The regions where we found volume differences have been all been previously implicated in the processing of pain. The thalamic and cerebellar volume increases might indicate that painful stimulation was repeatedly processed through these pathways and that this repetition might induce synaptic changes and gray matter volumes increases. The volume reductions in the insular cortex and frontal region might indicate that CPRS patients have a loss of inhibition to the rest of the pain processing circuits of the brain.

fMRI Investigation of Extraversion And Positive Self-Referential Processing In Social Phobia

PHILIPPE R. GOLDIN, SHABNAM HAKIMI, & JAMES J. GROSS · DEPARTMENT OF PSYCHOLOGY, STANFORD UNIVERSITY

Previous studies have shown that abnormal neural responses in individuals with mood and anxiety disorders are linked to specific personality traits. It is not yet clear, however, how extraversion interacts with social phobia (SP), which is characterized by fear of self-focused evaluation in social situations, in shaping neural responses. To examine this relationship, we assessed extraversion, and gave a positive self-referential processing task during fMRI to 16 individuals who met DSM-IV criteria for SP and 14 matched healthy controls (HC). Participants were presented with positive social trait adjectives. In the self-referential condition, they decided whether a word was self-descriptive; in the orthographic condition, they indicated whether a word was uppercase. Behaviorally, SP endorsed fewer words (63%) than HC (81%; $F_{(1,29)}=5.52$, $p<.03$); there was no difference in accuracy for uppercase (SP=97% and HC=99%; $p>.26$). There was no between-group difference in extraversion ($p>.43$). However, extraversion was positively associated with positive word endorsement in HC ($r=.57$, $p<.03$), but not in SP ($p>.30$). Neurally, within-group t-tests produced similar activations in each group in a distributed network of regions implicated in self-referential (medial, dorsomedial, and lateral PFC), emotional reactivity (amygdala, ACC, insula, caudate, NAcc), arousal (thalamus), and visual attention (lingual gyrus, cuneus). The between-group contrast showed greater BOLD response for self-referential processing in SP versus HC (voxel $p<.001$, volume=162mm3) in ventromedial PFC, rostral ACC, bilateral caudate, bilateral lentiform nucleus, and right insula, as well as right amygdala ($p<.005$). Among these regions, extraversion was positively associated with BOLD response in medial PFC ($r=.58$), right amygdala ($r=.56$), and right insula ($r=.50$) at $p<.05$ in SP only. In summary, extraversion differentiated the two groups because it was associated with self-report in HC and neural response in SP. Furthermore, elevated extraversion in SP was related to exaggerated emotional reactivity during positive self-referential processing, as evidenced by correlative relationships with affective brain regions. Greater extraversion in some SP may be explained by a mechanism whereby enhanced neural response in affective regions is upregulated in response to distorted self-view. These data highlight the importance of appreciating the role of personality in modulating neural responses in individuals with psychopathology.

Incentive Processing in the Aging Brain: Neural Responsiveness to Anticipated Gain and Loss in Younger and Older Adults

GREGORY R. LARKIN,[1] SASHA E.B. GIBBS,[1] KABIR KHANNA,[1] LISBETH NIELSEN,[2] LAURA L. CARSTENSEN,[1],[3] AND BRIAN KNUTSON[1],[4] · [1]DEPARTMENT OF PSYCHOLOGY, STANFORD UNIVERSITY; [2]NATIONAL INSTITUTE ON AGING / NATIONAL INSTITUTES OF HEALTH; [3]STANFORD CENTER ON LONGEVITY; [4]NEUROSCIENCE INSTITUTE, STANFORD UNIVERSITY

While the development of brain imaging technology has generated significant progress in characterizing the cognitive neuroscience of aging (Cabeza, Nyberg, & Park, 2005), little is known about the affective neuroscience of aging (Knight & Mather, in press). In healthy young adults, previous functional magnetic resonance imaging (FMRI) studies have implicated both ventral striatum (nucleus accumbens: NAcc) and anterior insula activation in the anticipation

of monetary rewards (Knutson, Adams, Fong, & Hommer, 2001; Knutson, Fong, Bennett, Adams, & Hommer, 2003), and caudate and anterior insula activation in the anticipation of monetary losses (Knutson, Adams, Fong, & Hommer, 2001; Knutson, Fong, Bennett, Adams, & Hommer, 2003; Kuhnen & Knutson, 2005; Paulus, Rogalsky, Simmons, Feinstein, & Stein, 2003). Prior behavioral work from our laboratory suggests that both younger and older adults report positive arousal when anticipating monetary rewards but that only younger (and not older) adults report experiencing negative arousal when anticipating monetary losses (Nielsen, Knutson, & Carstensen, in prep). Here, we used FMRI to determine whether younger and older adults differed in their neural responses to anticipated monetary gain and loss. Results revealed that while older adults show preserved ventral striatal and insular activation during gain anticipation relative to younger adults, they nonetheless show reduced activation of the caudate and anterior insula during anticipation of monetary loss. These findings have implications for understanding how aging might influence components of decision-making.
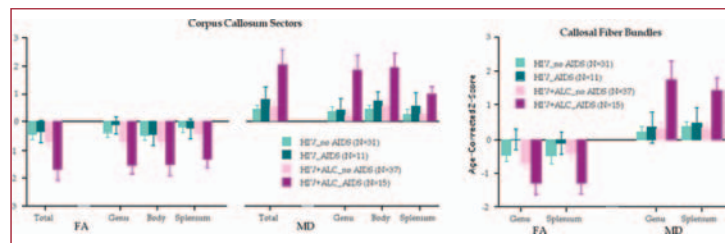
Incentive Processing in the Aging Brain: Neural Responsiveness to Anticipated Gain and Loss in Younger and Older Adults

GREGORY R. LARKIN,[1] SASHA E.B. GIBBS,[1] KABIR KHANNA,[1] LISBETH NIELSEN,[2] LAURA L. CARSTENSEN,[1,3] AND BRIAN KNUTSON[1,4] - [1]DEPARTMENT OF PSYCHOLOGY, STANFORD UNIVERSITY; [2]NATIONAL INSTITUTE ON AGING / NATIONAL INSTITUTES OF HEALTH; [3]STANFORD CENTER ON LONGEVITY; [4]NEUROSCIENCE INSTITUTE, STANFORD UNIVERSITY

While the development of brain imaging technology has generated significant progress in characterizing the cognitive neuroscience of aging (Cabeza, Nyberg, & Park, 2005), little is known about the affective neuroscience of aging (Knight & Mather, in press). In healthy young adults, previous functional magnetic resonance imaging (FMRI) studies have implicated both ventral striatum (nucleus accumbens: NAcc) and anterior insula activation in the anticipation

of monetary rewards (Knutson, Adams, Fong, & Hommer, 2001; Knutson, Fong, Bennett, Adams, & Hommer, 2003), and caudate and anterior insula activation in the anticipation of monetary losses (Knutson, Adams, Fong, & Hommer, 2001; Knutson, Fong, Bennett, Adams, & Hommer, 2003; Kuhnen & Knutson, 2005; Paulus, Rogalsky, Simmons, Feinstein, & Stein, 2003). Prior behavioral work from our laboratory suggests that both younger and older adults report positive arousal when anticipating monetary rewards but that only younger (and not older) adults report experiencing negative arousal when anticipating monetary losses (Nielsen, Knutson, & Carstensen, in prep). Here, we used FMRI to determine whether younger and older adults differed in their neural responses to anticipated monetary gain and loss. Results revealed that while older adults show preserved ventral striatal and insular activation during gain anticipation relative to younger adults, they nonetheless show reduced activation of the caudate and anterior insula during anticipation of monetary loss. These findings have implications for understanding how aging might influence components of decision-making.

DTI with Quantitative Fiber Tracking in HIV Infection and Alcoholism

ADOLF PFEFFERBAUM[1,2], MARGARET J. ROSENBLOOM[1,2] ELFAR ADALSTEINSSON[3], EDITH V. SULLIVAN[2] - [1]NEUROSCIENCE PROGRAM, SRI INTERNATIONAL, [2]DEPARTMENT OF PSYCHIATRY & BEHAVIORAL SCIENCES, STANFORD UNIVERSITY SCHOOL OF MEDICINE, [3]HARVARD-MIT DIVISION OF HEALTH SCIENCES AND TECHNOLOGY AND DEPARTMENT OF ELECTRICAL ENGINEERING AND COMPUTER SCIENCE, MIT.

Many individuals infected with human immunodeficiency virus (HIV) also abuse alcohol. Given that each condition can disrupt brain structural integrity, with a predilection for white matter, we used MR diffusion tensor imaging (DTI) and quantitative fiber tracking to examine the separate and combined effects on the microstructure of the corpus callosum. Subjects were men and women with alcoholism alone (N=87), HIV infection alone

Mean±S.E.M of age-corrected Z-scores of measures of FA and MD from each callosal region (left) and of fiber bundles at genu and splenium (right) in the four subgroups of HIV-infected patients.

(N=42), alcoholism and HIV infection comorbidity (N=52), and non-affected controls (N=88). The two alcoholism groups had similar lifetime alcohol consumption histories; the two HIV-infected groups had similar CD4+ counts and viral loads; all groups were matched in body mass index, and no participant was demented. Compared with controls, all patient groups had lower fractional anisotropy (FA) and higher mean diffusivity (MD) in callosal regions and fiber bundles coursing through the genu and splenium, effects only significant in groups with alcoholism, which exhibited .65 to 1.2 S.D. abnormalities in FA and MD. The genu of the corpus callosum was more affected than the splenium, particularly in the fiber tracks. The HIV-infected subgroup with AIDS (defined as an AIDS-defining event or low CD4+ counts <200) and alcoholism exhibited abnormalities that were more than twice the effect sizes observed in the other three HIV-infected subgroups - nearly 2 S.D. FA and MD abnormalities in the callosal sectors and fibers. Degradation of the callosal microstructure was consistently associated with alcoholism, with evidence for compounded alcoholism-HIV effects. Functional relevance of the microstructural abnormalities was supported by associations between motor deficits and low FA or high MD within the diagnostic groups. The high prevalence of alcoholism in HIV-infected individuals and the interfering effect of alcohol on HIV pharmacological response and therapy compliance underscore the need to recognize the independent and synergistic contributions of each condition to brain structure and function.

Alcoholism and HIV Effects on Ventricles and Corpus Callosum

Adolf Pfefferbaum[1,2], Margaret J. Rosenbloom[1,2] Torsten Rohlfing[1], Elfar Adalsteinsson[3], Carol A. Kemper[4], Stanley Deresinski[4], Edith V. Sullivan[2] - [1]Neuroscience Program, SRI International, [2]Department of Psychiatry & Behavioral Sciences, Stanford University School of Medicine, [3]Harvard-MIT Division of Health Sciences and Technology and Department of Electrical Engineering and Computer Science, MIT. [4]Division of Infectious Diseases, Department of Medicine, Stanford University School of Medicine and Santa Clara Valley Medical Center

Many individuals infected with human immunodeficiency virus (HIV) also abuse alcohol. Given that each condition can disrupt brain structural integrity, we used nonrigid registration and atlas-based parcellation methods (see figure) to compare the volume of the ventricular system and the cross sectional area of the midsagittal corpus callosum on brain MRIs from 272 subjects in four groups: patients with HIV infection, with and without alcoholism comorbidity, alcoholics, and controls. Prior to testing group differences in regional brain metrics, each measure was corrected by regression analysis for significant correlations with supratentorial cranial volume and age, observed in 121 normal control men and women, whose age spanned six decades. Disregarding HIV disease severity, we observed a graded pattern of modest enlargement of the total ventricular system (.28 S.D. for uncomplicated HIV, .65 S.D. for HIV comorbid with alcoholism, and .72 S.D. for the alcoholism group). The pattern of callosal thinning showed a similar but small (~.5 S.D.) graded effect. A different pattern emerged, however, when HIV severity was considered and also put in the context of alcohol-
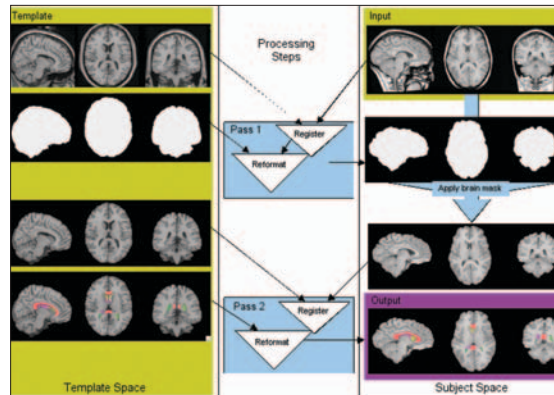
Two-pass atlas-based parcellation process: On left are images in template space. On right are images in subject coordinate space. Processing operations between the spaces are in blue boxes. Mustard-color denotes input data. Magenta denotes output parcellated image. First the unstripped template MR image is registered to the subject MR image, using a 9 degree-of-freedom affine registration followed by a nonrigid registration. The transformation is applied to the template brain mask to yield a subject-specific brain mask that is used to strip skull from subject MR image. The stripped subject image is then registered to the stripped template image. The resulting nonrigid coordinate transformation is applied to warp the template brain parcellation map into subject coordinate space, producing subject-specific brain parcellation, bottom right

ism comorbidity. Much greater volume abnormalities were present in individuals with a positive history of an AIDS-defining event or low CD4+ T cell counts (< 200 mm3) irrespective of alcoholism comorbidity, and the effect of HIV severity was disproportionately exacerbated by alcoholism comorbidity, with 1 S.D. size deficit in the genu of corpus callosum and nearly 2 S.D. greater volume of the frontal and body regions of the ventricles for the AIDS+alcohol comorbid group. The substantial effect of the alcoholism-AIDS interaction on ventricular and callosal dysmorphology and the more modest changes seen in non-AIDS, non-alcohol abusing HIV infected individuals highlight the need to consider alcohol use disorders as a major risk factor for neuropathology among HIV infected persons.
.

REFERENCES/FUNDING SOURCE
Pfefferbaum A, Rohlfing T, Deshmukh A, Sullivan EV (2006): Ventricular enlargement in HIV infection: The role of alcoholism comorbidity (abs). Supported by National Institute on Alcohol Abuse and Alcoholism (AA12999, 12388, and 05965).

Effects of Object Identity and Retinotopic Position Across Human Ventral Stream Measured with High-Resolution fMRI.

Rory Sayres[1] and Kalanit Grill-Spector1[2] - [1]Neuroscience Institute, [2]Psychology Department, Stanford University

Human object recognition is mediated by a processing hierarchy in which neurons possess increasingly large receptive fields and complex response properties. However, it is unknown whether)or at which stage of the heirarchy) visual cortex may construct object-centered representations which are invariant to stimulus transformations such as retinotopic translation. We used high resolution (1.5mm voxels, 3 Tesla) event-related fMRI to measure the response to individual objects at two retinotopic positions (centered at 4 and 9 degrees from the fovea). We scanned 5 subjects (3M/2F) on event-related and retinotopic mapping experiments, and defined a series of regions of interest (ROIs) across the ventral stream, spanning visual areas V1, V2v, V3v, V4, VO1, ventral LO, and pFus. Our results indicate a decreasing effect of position,

and an increasing category effect, for more anterior ROIs. V1 More anterior and medial ROIs such as pFus displayed both position and object effects (Position: $F_{(1,2235)}=380.03$, $p<10$-10; Object: $F_{(5,740)}=6.11$, $p<10$-5), with a larger position effect, and a significant interaction ($F=5.05$, $p=0.0001$). Conversely, ventral LO displayed a stronger object effect (Position: $F_{(1,876)}=4.25$, $p = 0.39$; Object: $F_{(5,294)}=6.79$, $p=10$-5) and an interaction between category and position. These results indicate a surprising dependence on position in ventral cortex, even in regions with complex category-selective response properties, and imply that strongly invariant object representations occur either at a small spatial scale, or well anterior to many visual cortical regions.

Longitudinal Study of Alcohol-Preferring (P) Rat: Chronic Alcohol Effects

ADOLF PFEFFERBAUM[1,8], ELFAR ADALSTEINSSON[2], ROHIT SOOD[3], DIRK MAYER[4], RICHARD BELL[5], WILLIAM McBRIDE[6], TING-KAI LI[7], EDITH V. SULLIVAN[1] - [1]DEPARTMENT OF PSYCHIATRY & BEHAVIORAL SCIENCES, STANFORD UNIVERSITY SCHOOL OF MEDICINE, [2]HARVARD-MIT DIVISION OF HEALTH SCIENCES AND TECHNOLOGY AND DEPARTMENT OF ELECTRICAL ENGINEERING AND COMPUTER SCIENCE, MIT, [3]DEPARTMENT OF NEUROLOGY, UNIVERSITY OF NEW MEXICO HEALTH CENTER, [4]DEPARTMENT OF RADIOLOGY, STANFORD UNIVERSITY SCHOOL OF MEDICINE, [5]INSTITUTE OF PSYCHIATRY, INDIANA UNIVERSITY MEDICAL CENTER, [6]DEPARTMENT OF PSYCHIATRY, INDIANA UNIVERSITY MEDICAL CENTER, [7]NATIONAL INSTITUTE ON ALCOHOL ABUSE AND ALCOHOLISM, [8]NEUROSCIENCE PROGRAM, SRI INTERNATIONAL

Tracking the dynamic course of human alcoholism brain pathology can be accomplished only through naturalistic study and without opportunity for experimental manipulation. Development of an animal model of alcohol-induced brain damage, in which animals consume large amounts of alcohol following cycles of alcohol access and deprivation and are examined regularly with neuroimaging methods, would enable hypothesis testing focused on the degree, nature, and factors resulting in alcohol-induced brain damage and the prospects for recovery or relapse. We report the results of longitudinal MRI studies of the effects of free-choice chronic alcohol intake on the brains of two cohorts of selectively bred alcohol-preferring (P) rats. In the companion paper, we described the MRI acquisition and analysis methods, delineation of brain regions, and growth patterns in total brain and selective structures of the control rats in the present study. Both cohorts were studied as adults for about one year and consumed high doses of alcohol for most of the study duration. The paradigm involved a three-bottle choice with 0%, 15% (or 20%), and 30 % (or 40%) alcohol available in several different expo-
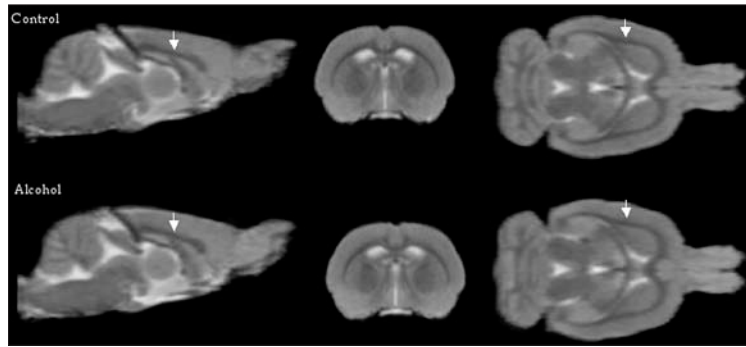
Grand average late echo images in the sagittal (left), coronal (middle), and axial (right) planes for controls (top) and alcohol exposed (bottom) animals. The white arrows on the sagittal and axial images indicate the slice position of the coronal view. The arrow on the sagittal image points to the corpus callosum.

sure schemes: continuous exposure; cycles of 2 weeks on followed by 2 weeks off alcohol; and binge drinking in the dark. Brain structures of the adult P rats in both the alcohol exposed and water control conditions showed significant growth, which was attenuated in a few measures in the alcohol-exposed groups. The region with the greatest demonstrable effect was the corpus callosum, measured on midsagittal images. The P rats showed an age-alcohol interaction different from humans, in that normal growth in selective brain regions that continues in adult rats was retarded.

Reorganization of the Somatosensory Cortex in Chronic Neuropathic Pain

UENO T[1], KAPLAN K[1], SONEJI D[1], LUCCA A[1], LUDLOW D[1], GLOVER G[2], MACKEY S[1] - [1]ANESTHESIA, STANFORD UNIVERSITY SCHOOL OF MEDICINE, [2]RADIOLOGY, STANFORD UNIVERSITY SCHOOL OF MEDICINE

Chronic neuropathic pain affects millions of people worldwide and costs society billions of dollars in direct and indirect medical expenses. While peripheral mechanisms have traditionally been studied, more recent investigations have implicated central mechanisms as a significant factor for the generation and maintenance of chronic neuropathic pain. In this study, we used fMRI to investigate neural plastic reorganization in the primary somatosensory cortex (S1) in a subset of patients with chronic neuropathic pain – those with complex regional pain syndrome (CRPS). We hypothesized that there would be significant cortical shifting of the affected hand representation in patients with CRPS compared to healthy controls.

We recruited 7 patients who met IASP criteria for CRPS and 8 healthy age and gender matched subjects. We used fMRI to map the somatotopic location of their hands in the primary somatosensory cortex with tactile stimulation of the thumb of both the affected and unaffected hands, delivered via computer-controlled pneumatic plungers embedded in a foam glove. High-resolution anatomical and functional

scans were collected on a 3T scanner. SPM2 software was used for co-registration and detection of activation areas in S1 (P<0.05 corrected).

All healthy subjects showed that tactile stimulation of the left and right thumb activated areas in S1 that were properly located at regions predicted by standard neuroanatomical (Penfield) diagrams. However, four of the patients' brain activation patterns demonstrated proper somatotopic localization of the unaffected hand but significant cephalad shifting of the affected hand. One patient had the activation area of unaffected side thumb more cephalad. Additionally, two patients underwent subsequent successful inpatient treatment and were scanned post-treatment. The fMRI results demonstrated that the affected S1 activation area relocated closer to the height of the unaffected side.
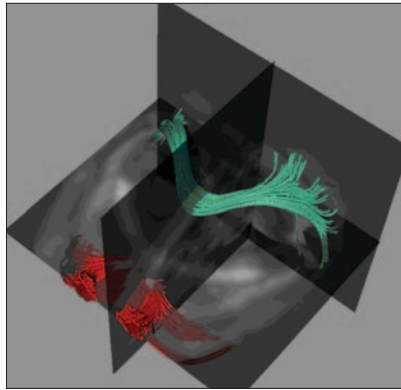
Chronic upper extremity neuropathic pain (CRPS) induces cortical reorganization in the primary somatosensory cortex, thereby validating the theory that central mechanisms play a role. This is also the first study to demonstrate that these cortical changes are reversible with appropriate therapy.

In Vivo Diffusion Tensor Imaging of Rat Brain on a 3T MR System Equipped with Insert

D. Mayer[1], E. Adalsteinsson[2,3], B.K. Rutt[4], N.M. Zahr[5], E.V. Sullivan[5], A. Pfefferbaum[5,6] - [1]Department of Radiology, Stanford University, [2]Harvard-MIT Division of Health Sciences and Technology, [3]Electrical Engineering and Computer Science, MIT, [4]Imaging Research Laboratories, Robarts Research Institute, London, Ontario, Canada, [5]Psychiatry & Behavioral Sciences, Stanford University, [6]Neuroscience Program, SRI International, Menlo Park, CA

Animal models of substance dependence can facilitate the identification of biological mechanisms underlying the predisposition, development, and maintenance of addiction. Of particular relevance to human alcohol addiction is brain white matter, which postmortem study has shown is subject to myelin and cytoskeletal degradation that may be reversible with abstinence. In vivo human diffusion tensor imaging (DTI) studies of alcohol dependence provide evidence for microstructural disruption of white matter not detectible with bulk volume measures of conventional MRI. Here, we report on the development of an in vivo echo-planar (EP) diffusion tensor imaging (DTI) protocol on a 3T human MRI system equipped with a high-strength insert gradient coil for study of rat brain.

Fiber bundles through the splenium (green) and genu (red) of the corpus callosum overlayed onto FA images

Healthy adult Wistar rats were scanned in a clinical GE 3T MR scanner equipped with a high-strength insert gradient coil (500mT/m, 1800T/m/s) and a custom quadrature birdcage coil. Imaging was accomplished with an EP DTI protocol for 0.5mm isotropic resolution. Diffusion weighting was applied for b-value=1009 s/mm2 in 6 noncollinear directions. Fractional anisotropy (FA) images had adequate signal-to-noise ratio to detect rat brain white matter structures. Fiber tracking produced pictorial fiber bundle representations similar to those seen in humans. The figure shows fibers forming posterior forceps through the splenium, and frontal cortex forceps and lateral bundles through the genu.

The high strength and speed of the insert gradient coil allowed for the strong diffusion gradients and the short readout time necessary to acquire high-resolution DTI in the rat brain on a human 3T scanner and to detect major white matter structures. The short readout time produced EP DTI data without substantial B0 field inhomogeneity distortion. The method might enable enable fiber tracking and quantitative microstructural interrogation of white matter systems following exposure to neurotoxins, such as excessive alcohol ingestion or inhalation. A major advantage of employing insert gradient technology is the use of similar pulse sequences and field strength for preclinical and clinical research, thus enhancing the translational nature of such research.

Magnetic Resonance Spectroscopic Measurement of Gamma-aminobutyric Acid Levels in Bipolar Disorders

Po W. Wang[1], Napapon Sailasuta[2], Rebecca Chandler[3], Terence A. Ketter[1] - [1]Psychiatry and Behavioral Sciences at the Bipolar Disorders Clinic, Stanford University School of Medicine. [2]Department of Medicine, University of Hawaii. [3]Department of Psychiatry, Oxford University.

Animal models of depression and psychopharmacological mechanism of activity have suggested the importance of the gamma-amino butyric acid (GABA) system in the pathophysiology of mood disorders. Mood stabilizers have common effects on GABAergic neurotransmission, and antidepressant use has been associated with alterations in GABAB receptor function. Magnetic resonance imaging provides an opportunity to noninvasively assess cerebral GABA concentrations in the anterior paralimbic brain circuits, which have been implicated in mood disorders.

In 16 bipolar disorder (9 bipolar I and 7 bipolar II disorder) and six healthy control subjects, magnetic resonance spectroscopy using a modified GABA-edited point resolved spectroscopy (PRESS) sequence (TE 68 milliseconds, TR 1500 milliseconds, 512 averages, total scan time 26 minutes) consistently yielded a 3.0 ppm GABA peak in an occipital cortex voxel. In 15 bipolar disorder (5 bipolar I, 9 bipolar II, and 1 bipolar NOS disorder) and six healthy control subjects, spectra consistently yielded a 3.0 ppm GABA peak in a medial prefrontal / anterior cingulate cortex (MPF/ACC) voxel. The concentration of GABA was referenced to creatine from an unedited spectrum. Bipolar disorder subjects tended to have higher GABA/Cr levels than healthy control subjects in the MPF/ACC. This study is the first to report GABA measurements in the anterior paralimbic brain circuit, which is important in mood disorders.
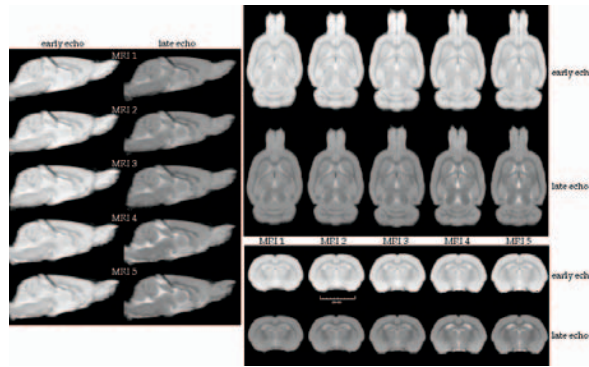
Longitudinal Brain MRI Study of the Alcohol-Preferring (P) Rat: Adult Brain Growth

[1]Edith V. Sullivan, [2]Elfar Adalsteinsson, [3]Rohit Sood, [4]Dirk Mayer, [5]Richard Bell, [6]William McBride, [7]Ting-Kai Li, [1,8]Adolf Pfefferbaum - [1]Department of Psychiatry & Behavioral Sciences, Stanford University School of Medicine, [2]Harvard-MIT Division of Health Sciences and Technology and Department of Electrical Engineering and Computer Science, MIT, [3]Department of Neurology, University of New Mexico Health Center, [4]Department of Radiology, Stanford University School of Medicine, [5]Institute of Psychiatry, Indiana University Medical Center, [6]Department of Psychiatry, Indiana University Medical Center, [7]National Institute on Alcohol Abuse and Alcoholism, [8]Neuroscience Program, SRI International.

The alcohol-preferring (P) rat, a Wistar strain selectively bred to consume large amounts of alcohol voluntarily, has been used as an animal model of human alcoholism for three decades. Heretofore, knowledge about brain morphology has been confined to postmortem examination. Quantitative neuroimaging procedures make it feasible to examine potential longitudinal effects of alcohol exposure in vivo, while controlling modifying factors, such as age, nutrition, and exercise. To date, few imaging studies have considered what morphological changes occur with age in the rodent brain, and none has systematically applied quantitative neuroimaging approaches to measure volume changes in regional brain structures over extended periods in the adult rat. We used structural MRI in a longitudinal design to examine two cohorts of adult P rats, never exposed to alcohol: Cohort A included 8 rats, 7 of which survived the entire study (578 days) and 4 MRI sessions; Cohort B included 9 rats, all of which survived the study (452 days) and 5 MRI sessions. Growth in whole brain volume reached maximal levels by about 450 days of age, whereas body weight continued its gain without asymptote. Growth was not uniform across brain structures measured. Over the initial 12 months of the study, corpus callosum area expanded 36%, cerebellum 17%, and hippocampus 10%, whereas ventricle size was unchanged. Factors affecting growth rate estimates included litter effects, MR image signal-to-noise ratio, and measurement error. Unlike longitudinal human reports of regional volume declines in aging brain tissue, several brain structures in adult rats continued growing, and some growth patterns were litter-dependent. Determining normal regional growth patterns of brain and of the substantial variance exerted by litter differences, even in selectively bred rats, is essential for establishing baselines against which normal and aberrant dynamic changes can be detected in animal models of aging and disease.

Examples of early-echo (light intensity) and late-echo (dark intensity) images aligned and averaged across the 9 rats in Cohort B and resliced in three orthogonal planes, over 5 MRI scans.

Voxel-based Morphometric Analysis of Gray Matter in Bipolar Depression

Julie C. Bonner[1], John O. Brooks III[2,1], Po W. Wang[1], Terence A. Ketter[1] - [1]Psychiatry and Behavioral Sciences at the Bipolar Disorders Clinic, Stanford University School of Medicine, [2]VA Palo Alto Health Care System.

Previous work with structural brain analysis in bipolar disorder has led to variable findings (Brambilla et al 2005). This study uses software that incorporates the latest methodological advances in voxel-based morphometry (VBM) to assess variations in gray matter density in a group of medication-free bipolar subjects.

Brain magnetic resonance imaging (MRI) scans were obtained in 33 medication-free, bipolar (12 type I, 21 type II) outpatients and 26 age- and gender-matched healthy controls. Differences in gray matter density between groups were calculated with Statistical Parametric Mapping software (SPM5).

Bipolar subjects exhibited decreased gray matter density in the right dorsal lateral perfrontal cortex (DLPFC) and bilateral subgenual prefrontal cortex (SGPFC). Bipolar subjects exhibited increased gray matter density in the right inferior frontal gyrus, left inferior and right middle temporal gyri, the left anterior cingulate/orbitofrontal cortex, and regions of the parietal cortex.

These data suggest that bipolar subjects have altered gray matter density in anterior paralimbic basal ganglia-thalamocortical circuits that have been implicated in emotional processing

Differences in Cerebellar and Striatal Metabolite Ratios in Rat Brain Detected In Vivo at 3T

D. Mayer[1], N.M. Zahr[2], E.V. Sullivan[2], A. Pfefferbaum[2,3] - [1]Departments of Radiology, [2]Psychiatry & Behavioral Sciences, [3]Neuroscience Program, Stanford University, SRI International, Menlo Park, CA

In vivo magnetic resonance spectroscopy (MRS) permits non-invasive longitudinal tracking of brain chemistry changes that can accompany aging, drug addiction, and experimental manipulations modeling such conditions. As 3T human scanners have become widely available, animal research at the same field strength with the same protocols should facilitate preclinical to clinical translational research. Constant Time PRESS (CT-PRESS) has been introduced as a method to detect coupled resonances with high signal-to-noise by using effective homonuclear decoupling. Here, we tested the feasibility of using CT-PRESS optimized for the detection of glutamate (Glu) in the rat to dissociate the biochemical profile of two brain regions affected by alcohol dependence, the cerebellum and striatum. Our aim was to establish baseline levels of principal metabolites detectable with proton MRS in different brain regions, an essential step for testing animal models of drug addiction.

Six healthy male adult Wistar rats were scanned in a clinical GE 3T MR scanner equipped with self-shielded gradients and a custom quadrature birdcage coil. The average echo time (TE) of the CT-PRESS sequence was 139 ms optimized for the detection of Glu. For each rat,
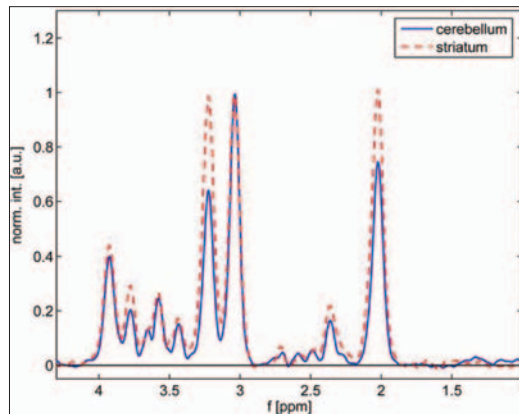
Mean CT-PRESS spectra for 6 rats from voxels in the cerebellum (solid blue) and striatum (dashed red).

spectra were acquired from two voxels: the first contained mostly the cerebellum, the second the striatum. The voxel size was 0.2 ml. The quality of the spectra allowed evaluation of signals from N-acetyl-aspartate (NAA), total creatine (tCr), choline containing compounds (Cho), Glu, Glu+glutamine (Glx), myo-inositol (mI), and taurine. Signal intensities of NAA, Cho, Glu, and Glx (relative to tCr) were significantly higher in the striatum than in the cerebellum.

This study demonstrates the feasibility of using in vivo CT-PRESS to quantitate differences in metabolite ratios between the cerebellum and the striatum of the rat brain. CT-PRESS provides the enhanced signal separation necessary to reliably measure J-coupled resonances, such as Glu and mI, in the rat brain at 3T. Establishment of absolute baseline metabolite concentrations in these brain regions in particular is necessary for animal models of chronic alcoholism, which induces changes in cerebellum and the Glu neurotransmitter system.

Cortical Population Receptive Field Estimation using fMRI

Serge O. Dumoulin, Alyssa A. Brewer, Michal Ben-Shachar, Robert F. Dougherty, Brian A. Wandel
Psychology Department

We describe a method to integrate fMRI data from a wide range of stimuli into a compact description of visual responsivity. The method estimates the population receptive field (pRF) of the neuronal population within each voxel. We used the method to estimate a pRF restricted to be a Gaussian receptive field in visual space, described by three parameters (x,y position and □ size). Convolution of a particular pRF with the stimulus sequence yields a predicted time-series; the optimal pRF parameters are estimated for each voxel by minimizing the residual sum of

Population receptive field estimates on the cortical surface. The pRF size (sigma) are plotted on the cortical surface for one subject. Using a single Gaussian pRF, the pRF size systematically increases from primary visual cortex (V1, ~0.4 deg) to lateral and ventral occipital regions (1-2 deg). Lines delineate the visual field maps of V1/2/3 and a star indicates their foveal representation.

squares between the prediction and the fMRI time-series. We estimated the pRF using several types of visual stimuli. The Gaussian pRF reconstructed many cortical visual field maps, which were in excellent

agreement with conventional estimates for all stimuli used. The pRF□size was smallest in V1 and significantly larger in lateral and ventral occipital cortex. The pRF method reconstructs the cortical visual field organization at least as accurately as conventional methods and independent of the exact stimulus configuration. Furthermore, the method integrates data from multiple types of stimuli and can thus provide new information about cortical visual field sensitivity (e.g. size) within localized portions of visual field maps and clusters.

Diffusion Tensor Imaging of Post-ictal Changes in Patients with Temporal Lobe Epilepsy

ALYSSA A. BREWER[1], DAVID CHEN[2], ANTHONY SHERBONDY[1], ROBERT F. DOUGHERTY[1], ROBERT FISHER[2], BRIAN A. WANDELL[1]
DEPARTMENTS OF PSYCHOLOGY[1] & NEUROLOGY[2], STANFORD UNIVERSITY

Introduction: Behavioral observations show that epileptic seizures have significant short term functional consequences lasting up to 24 hours following the seizure itself. Many epileptic patients suffer from a post-ictal paresis that lasts for several hours, and occasionally for a day or more. It is thought that this post-ictal state correlates with cellular changes such as edema. Thus measurements using diffusion tensor imaging (DTI) during the post-ictal period may reveal specific differences in diffusivity, which could be used to aid in the localization of seizure foci. In addition, long-term, intractable epilepsy causes neuronal death and eventual sclerosis. Since DTI can measure changes produced by such sclerotic lesions, a comparison of the changes in the fiber tracts in patients with long-term epilepsy with those of normal controls may aid in our understanding of how intractable seizures alter normal cortical organization.

Methods: We are using whole brain DTI to make measurements of white matter tract changes in epileptic patients. In this study, we have two specific aims: (1) to use DTI to measure post-ictal changes in diffusivity in focal temporal lobe epilepsy (TLE) and (2) to compare the inter-ictal DTI measurements of white matter fiber tracts in patients with long-term TLE with those of normal subjects. Thus far, we have developed basic visualization and statistical software for analyzing DTI data, and we have collected measurements on two epileptic subjects to confirm that this work is feasible.

Conclusion: This work has the potential for both clinical and biological impact. Identifying seizure loci more effectively using non-invasive methods would be a significant contribution to the treatment of epilepsy by providing both more accurate target regions for resection as well as quantitative metrics for assessing the degree of white matter deterioration. In addition, successful modeling and localization of neural pathway structures should motivate a parallel basic science effort to clarify the cellular basis of the macroscopic signals measured using DTI.
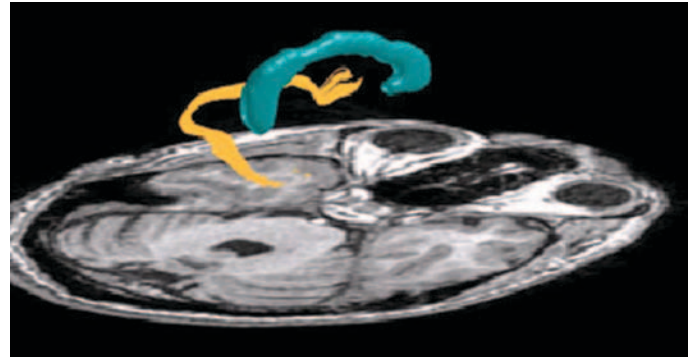
Figure 1. DTI and tractography estimate the location of white matter fiber bundles (fascicles) in individual patients. The isolated bundle (yellow) is a portion of the Circuit of Papez. The corpus callosum position is also shown (cyan).

Resting-State fMRI Distinguishes Alzheimer's Disease from Non-AD Dementias

MICHAEL D. GREICIUS[1], WILLIAM W. SEELEY[2], BRUCE L. MILLER[2], GARY H. GLOVER[1], SUDHARSHAN PARTHASARATHY[1], ALLAN L. REISS[1], VINOD MENON[1] - [1]STANFORD UNIVERSITY MEDICAL CENTER, [2] UNIVERSITY OF CALIFORNIA SAN FRANCISCO,

Background: Converging lines of evidence(Buckner et al., J Neurosci, 2005) suggest that Alzheimer's disease (AD) targets a specific network of brain regions known as the default-mode network (DMN). This network includes the posterior cingulate cortex, inferior parietal cortices, medial prefrontal cortex, and the hippocampus. We previously demonstrated that the network is deficient in AD patients compared to healthy controls (Greicius et al., PNAS, 2004) but its activity in non-AD dementias has not been investigated.

Objective: To determine if DMN activity differs between AD patients and patients with non-AD dementias.

Methods: 18 patients with probable AD, 13 healthy older controls, and 8 Pick-complex patients (3 frontotemporal dementia 2 semantic dementia, 3 corticobasal degeneration) underwent two 6-minute resting-state fMRI scans. Smoothed, normalized images were subjected to independent component analysis. An automated, spatial template-matching procedure was used to select that component from each 6-minute scan that most closely matched the standard template of the DMN (Greicius et al., PNAS, 2004). The better-fit DMN component from each subject's two scans was entered into one-sample and two-sample t-tests in SPM2.

Results: There were no significant differences in DMN activity between healthy controls and Pick-complex patients. When compared to healthy controls (Figure 1A), the AD patients showed significantly reduced DMN activity in the posterior cingulate and left inferior parietal regions. When compared to Pick-complex patients (Figure 1B), AD patients showed reduced DMN activity in the posterior cingulate.

There were no regions in which DMN activity was greater in AD patients than in the two other groups.

Conclusions: These data demonstrate that DMN activity not only distinguishes AD patients from healthy controls but also from Pick-complex patients. Ongoing work will determine if quantitative analysis of DMN activity can be applied at the single-subject level as a non-invasive biomarker of AD.
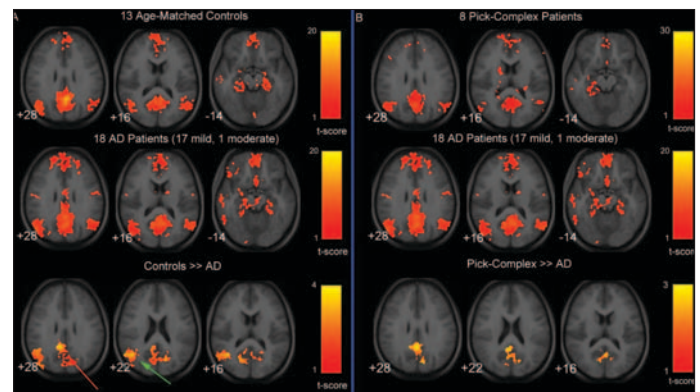

Figure 1: Group-level maps of the DMN in (A) controls vs AD and (B) Pick-complex vs AD.

Posterior Cingulate Cortex Volume Reduction and Correlation with Fear of Pain in Complex Regional Pain Syndrome (CRPS)

Takefumi Ueno[1], Meredith Barad[2], Kim Kaplan[1], Axel Lucca[1], Fumiko Hoeft[3], Deepak Soneji[1], David Muramoto[1], Cullen Aberil[1], Sean Mackey[1] -Departments of [1]Anesthesia, [2]Neurology, and [3]Psychiatry
Stanford University School of Medicine

Complex Regional Pain Syndrome(CRPS) is a debilitating neuropathic pain disorder characterized by severe burning pain, abnormal sweating, hair growth, nail growth, swelling, pathological changes in bone, and extreme sensitivity to touch. 1 McNeil and Rainwater (1998) 2 have developed the Fear of Pain Questionnaire(FPQ) that measures fears of pain. Chronic pain patients report elevated levels of fear of severe pain relative to acute pain groups, and the fear of pain uniquely predicts fear of specific events known to elicit pain and distress. We hypothesized that development of chronic pain is associated with structural changes in the brain. Recent evidence suggests that the brain functions play an important role in the chronic pain condition,3,4 however, there has been no previous investigation into volumetric changes in the brain related to CRPS. In this study, we used voxel based morphometry5 to investigate the correlation between the volume reduction and FPQ Score. 2 Nine patients (females, right handed, mean age 39.0 years, SD=9.3) meeting IASP criteria for CRPS were recruited from the Stanford University Pain Management Center.

Data Acquisition: Magnetic resonance imaging was performed on a GE 3.0 T scanner. A T1-weighted 3D structural MRI of the whole brain was acquired on each subject using a SPGR pulse sequence.

FPQ score: Fear of Pain Questionaire was completed by the patients immediately prior to the MRI scan. Voxel based morphometry compares gray matter volume by using deformation between the template of the structural MRI image and the raw image obtained from the scanner. Our method is similar to Good(2001) 6. SPM2 software were used to analyze the data and create the normalized segmented gray matter density images. The gray matter images were smoothed with 8mm Gausian kernel. Wethen performed a simple regression between Volume intensity with FPQ score for evey voxel in the gray matter.

We found area of grey matter volume reduction that correlated negatively with FPQ scores in the posterior cingulate cortex (p<0.05(corrected), R2=0.977). Apkarian et al reported that chronic back pain patients show frontal lobe volume reduction. 3 In a view of PCC function, Vogt suggested that cingulated cortex function includes the pain sensation specifically related to orientation of the pain and memory. 7 This study provides evidence that significant volume reductions in PCC grey matter may be instrumental in generating spontaneous neuronal activity that is associated with fear of pain.

References/Funding Source

Bruehl, et al., Pain 81, 147-54 (1999)., McNeil, et al., Behav Med 21, 389-410 (1998)., Apkarian, et al., J Neurosci 24, 10410-5 (2004)., Maihofner, et al., Pain 114, 93-103 (2005)., Ashburner, et al., Neuroimage 11, 805-21 (2000)., Good, et al.,Neuroimage 14, 21-36 (2001)., Vogt, Nat Rev Neurosci 6, 533-44 (2005).

Where and When the Anterior Cingulate Cortex Modulates Attentional Response: Combined fMRI and ERP Evidence

S. Crottaz-Herbette and V. Menon - Department of Psychiatry and Behavioral Sciences and Neuroscience Program

Attentional control provides top-down influences that allow task-relevant stimuli and responses to be processed preferentially. The anterior cingulate cortex (ACC) plays an important role in attentional control, but the spatiotemporal dynamics underlying this process is poorly understood. We examined the activation and connectivity of the ACC using functional magnetic resonance imaging (fMRI) along with fMRI-constrained dipole modeling of event-related potentials (ERPs) obtained from subjects who performed auditory and visual oddball attention tasks. Although attention-related responses in the ACC were similar in the two modalities, effective connectivity analyses showed modality-specific effects with increased ACC influences on the Heschl and superior temporal gyri during auditory task and on the striate cortex during visual task. Dipole modeling of ERPs based on source locations determined from fMRI activations showed that the ACC was the major generator of N2b-P3a attention-related components in both modalities, and that primary sensory regions generated a small mismatch signal about 50 msec prior to feedback from the ACC and a large signal 60 msec after feedback from the ACC. Taken together, these results provide converging neuroimaging and electrophysiological evidence for top-down attentional modulation of sensory processing by the ACC. Our findings suggest a model of attentional control based on dynamic bottom-up and top-down interactions between the ACC and primary sensory regions.

References/Funding Source

J Cogn Neurosci. 2006 May;18(5):766-80 NIH and Bio-X.

# Matched Phase Dualband Spatial-Spectral 90º-180º Pulse Pair for MRSI at 3T

P. Balchandani[1,2], J. Pauly[2], D. M. Spielman[1] - [1]Radiology, [2]Electrical Engineering

Introduction: 1H MRSI is a useful technique for obtaining spatially localized profiles of metabolites of interest in the breast, brain and prostate. However, MRSI usually suffers from: 1) Inadequate water or lipid suppression; 2) spectral shifts due to B0 inhomogeneity; 3) spatially varying phase profiles and 4) chemical shift artifacts. A pulse sequence has been designed for use at 3T that utilizes a dualband spatial-spectral matched phase 90º-180º pulse pair to excite a thin slice. The dualband spectral profile of these pulses enables complete lipid suppression and partial water suppression so that water may be used as a phase and frequency reference. Using a matched phase 90º-180º pulse pair yields a final echo with a flat phase profile and the higher spatial bandwidth of spatial-spectral compared to standard spatial pulses (3.5 kHz vs. 1.2 kHz) results in less severe chemical shift artifacts. The first set of pulses have been designed for breast MRSI, however it is not difficult to adapt the pulses to the brain or prostate.

Methods and Discussion: Initially a linear-phase 180º dualband spatial-spectral pulse that encompassed choline at 3.2 ppm and suppressed all lipid resonances was designed. The partial water band was designed to excite 1% of the water signal at 4.7 ppm. Using the Shinnar Le-Roux (SLR) algorithm for RF pulse design, each RF pulse can be described by a pair of complex polynomials ($\beta(kz,k\omega)$, $\alpha(kz,k\omega)$) or just (β, α). In order to bring the linear 180º pulse below RF peak power limits, the roots of the β polynomial that fell outside the unit circle were computed and every possible root flipped configuration was traversed to find the one that resulted in the lowest RF peak power. In order to compensate the non-linear phase profile introduced by root flipping, the β from the 180º pulse was used to create a phase matched β for the 90º pulse. The

final spectral profile had flat phase and successfully passed a 1 ppm band encompassing the metabolites present in the breast (i.e. choline at 3.2 ppm, creatine at 3 ppm) while suppressing all other resonances.

Conclusions: A matched phase 90º-180º spatial-spectral pulse pair has been developed for MRSI at 3T that makes possible flat phase profiles using just two pulses. The dualband spectral profile achieves complete lipid suppression and partial water suppression.
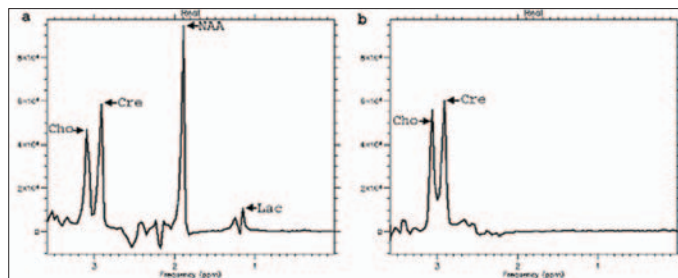
Zoomed in spectrum from a central 10 mm slice of a MRS sphere phantom acquired at 3T a: with the standard GE 3T PRESS sequence (TE/TR = 64/1500ms) and b: with the narrow-passband matched-phase 90º-180º pulse pair (TE/TR = 64/1500ms). Resonances below Cho and Cre are suppressed.

^{1}H MRS Metabolite Ratios Increase with Age in Very-Low-Birth-Weight Infants

Erin Van Brussel[3], Majid Mirmiran[2], Daniel Spielman[1], Patrick Barnes, Trenna Sutcliffe[2], Jamie Derman[3], and Ronald Ariagno[2]. - [1]Radiology, [2]Pediatrics, [3]School of Medicine

Proton magnetic resonance spectroscopy (MRS) is a noninvasive technique that quantitatively measures specific metabolites in various regions of the brain. Normal changes in metabolite ratios near term age in very low birth weight (VLBW) preterm infants may have diagnostic and prognostic value if they fail to attain term infant levels. The purpose of this retrospective study was to obtain preliminary data on normal changes in metabolite ratios between 35 and 43 postmenstrual age (PMA,weeks) in VLBW preterm infants.

Thirty-six infants scanned between 9/01-9/03 met the inclusion criteria: birth weight ≤1510g, gestational age ≤32 weeks, and scan age of 35-43 postmenstrual weeks. MRI/MRS was performed on a 1.5 T scanner. Metabolite spectra were analyzed in two regions of interest: 1) combined left and right thalamus and basal ganglia, and 2) left and right cortex. Choline (Ch), creatine and phosphocreatine (Cr), and N-acetylaspartate (NAA) peaks were integrated and the ratios of Ch/Cr, NAA/Cr, and NAA/Ch were calculated. Patients were assessed at 18-24 months by the Mental Developmental Index (MDI) and the Psychomotor Developmental Index (PDI) of the Bayley Scales of Infant Development II. From the 36 infants, 24 had a normal MDI (≥ 85) and 26 had normal PDI ((≥ 85).

Of the 24 infants with a normal MDI, metabolite ratios were calculated for 12 infants in the thalamus and basal ganglia, and 22 infants in the cortex. Of the 26 infants with a normal PDI, metabolite ratios were calculated for 14 infants in the thalamus and basal ganglia, and 24 in the cortex. MRS data acquisition was incomplete for the some infants and metabolite ratios could only be calculated for 19 infants in the thalamus and basal ganglia, and 33 infants in the cortex. A positive correlation was found between postmenstrual age and NAA/Ch in the thalamus and basal ganglia for infants with a normal MDI (r2 = 0.35, p = 0.04) and a normal PDI (r2 = 0.36, p = 0.02). No correlation was found in cortex.

The ratio of NAA/Ch in the thalamus and basal ganglia was greater at 43 postmenstrual weeks, possibly reflecting neuronal development.

Reduced Echo Time Dualband Spatial-Spectral Pulse Sequence for Brain MRSI at 3T

P. Balchandani[1,2], D. M. Spielman[1] - [1]Radiology, [2]Electrical Engineering

Introduction: 1H Magnetic resonance spectroscopic imaging (1H MRSI) is a useful technique for measuring metabolite levels in the brain. Dualband spatial-spectral (SPSP) pulses have been designed at 3T for fully exciting the metabolites of interest, partially exciting water, while suppressing lipids. However, in these sequences, the 180º SPSP pulses must have nonlinear phase (along the spectral direction) in order to stay below RF peak power limits and consequently both 180º pulses in the PRESS excitation are relatively long. This limits TE to a minimum of approximately 90 ms. In this study, the use of a PRESS sequence with only one dualband spatial-spectral linear phase 90º pulse and two standard spatial 180º pulses is proposed for brain MRSI. This sequence provides spectral selectivity while allowing significantly shorter echo times than existing SPSP PRESS sequences for the brain.

Methods and Discussion: A linear phase 90º dualband SPSP pulse was designed using twenty one linear phase subpulses that could excite a slice as thin as 5 mm. The passband for the pulse encompassed choline at 3.2 ppm to NAA at 2.0 ppm while suppressing the lipids at 1.3 ppm and below. The partial water band was designed to excite 2% of the water signal at 4.7 ppm. The final pulse duration was 24 ms resulting in TE=44 ms. An equivalent PRESS sequence with 24 ms SPSP 180's and a standard spatial 90 would result in a minimum TE = 64 ms. The dualband SPSP 90º pulse had very low ripple in the metabolite passband but considerable ripple in the partial water passband. However, since we are only using water as a frequency reference and not concerned with its magnitude, this ripple is tolerable. Phantom and in vivo studies demonstrate that the new pulse sequence achieves the targeted design parameters.

Conclusion: It can be seen from in vivo data that the linear phase dualband SPSP 90º pulse successfully suppresses fat when compared to the standard GE PRESS sequence at the same echo time.

.
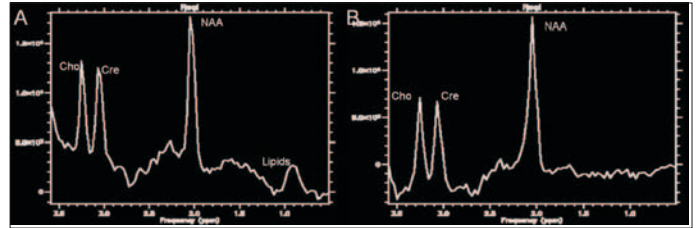
In vivo data from normal volunteer: (A) averaged spectrum using standard GE PRESS (TE/TR = 44/1500 ms) and (B) averaged spectrum using PRESS sequence with dualband SPSP 90º pulse (TE/TR = 44/1500 ms). Lipids have been significantly suppressed

^{1}H MRS at Term Age is not Predictive of Neurodevelopmental Outcome in Very-Low-Birth-Weight Infants

Erin Van Brussel[3], Majid Mirmiran[2], Daniel Spielman[1], Patrick Barnes, Trenna Sutcliffe[2], Jamie Derman[3], and Ronald Ariagno[2]. - [1]Radiology, [2]Pediatrics, [3]School of Medicine

Very low birth weight (VLBW) preterm infants are at an increased risk of neurological abnormalities, including poor cognitive function, decreased academic achievement, visual disability, hearing impairments, and cerebral palsy. 1H magnetic resonance spectroscopy (MRS), which quantitatively measures specific metabolites in various regions of the brain, has been shown to predict neurodevelopmental outcome in term, asphyxiated newborns. The purpose of this retrospective study was to evaluate near term 1H MRS in predicting neurodevelopmental outcome at 18-24 months in VLBW preterm infants.

The patient cohort was comprised of 36 infants scanned from 9/01-9/03 who met the inclusion criteria: birth weight ≤1510g, gestational age ≤32 weeks, and scan age of 35-43 postmenstrual weeks. MRI/MRS was performed on a 1.5 T scanner. Metabolite spectra were analyzed in two regions of interest: 1) the combined left and right thalamus and basal ganglia, and 2) the left and right cortex. Choline (Ch), creatine and phosphocreatine (Cr), and N-acetylaspartate (NAA) peaks were integrated and the ratios of Ch/Cr, NAA/Cr, and NAA/Ch were calculated. Patients were assessed at 18-24 months by the Mental Developmental Index (MDI) and the Psychomotor Developmental Index (PDI) of the

Bayley Scales of Infant Development II. Based on their MDI and PDI scores, patients were divided into two outcome groups for each index, normal ($\geq$ 85) and abnormal (<85). Based on the MDI and PDI, 24 (67%) and 26 (76%) infants were classified as normal and 12 (33%) and 8 (24%) as abnormal, respectively. Unpaired t-tests did not demonstrate a statistically significant difference in Ch/Cr, NAA/Cr, or NAA/Ch between infants with normal and abnormal developmental outcome.

Near term MRS did not predict neurodevelopmental outcome in VLBW preterm infants. Specifically, the ratios of Ch/Cr, NAA/Cr, and NAA/Ch were not predictive of Bayley MDI and PDI scores at 18-24 months in our patient cohort in contrast to term infants studied near birth with asphyxia. Longitudinal studies in VLBW infants are needed to assess if abnormal developmental changes in MRS are seen in infants who are at risk for later abnormal outcome.

Robust Lipid Suppression for Brain MRSI at 3T

[1]Meng Gu, [2]Daniel M. Spielman - [1]Electrical Engineering Department, Stanford University, [2] Department of Radiology, Stanford University

Brain spectroscopic imaging has been increasingly used in diagnosis and treatment of neuropathologies. Lipid suppression is critical for a successful study, and to achieve whole brain coverage, inversion recovery is often used, despite significant metabolite signal loss. At 3T, frequency selective inversion recovery technique has been implemented to avoid these signal losses. However, suppression is often incomplete due to B1 and T1 variations. To address these issues, a robust lipid suppression technique has been proposed and implemented for brain MRSI at 3T.

A 20 ms long minimum phase lipid-selective inversion pulse was designed using the Shinnar-Le Roux algorithm. To account for B1 inhomogeneity and different T1s of lipid spins, four such pulses, 10ms apart, with different flip angles were used. The four different flip angles were found by minimizing the maximum absolute value of residue longitudinal lipid magnetization at the time of excitation for three different T1s, 170/260/280 ms, and ±10 percent B1 inhomogeneity.

Simulations and experimental results showed excellent perfor-
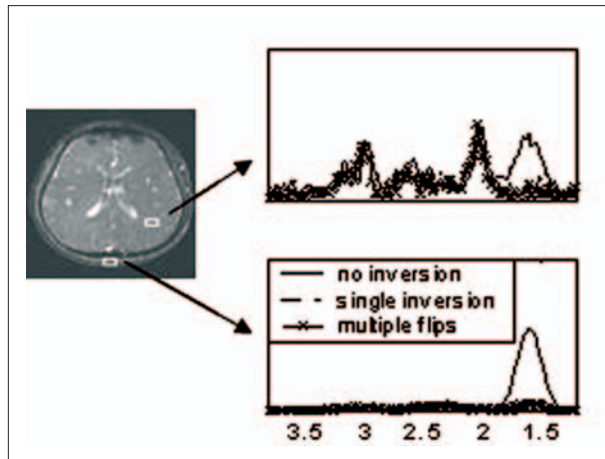
In vivo spectra of representative voxels, 2.5cc voxels, 2 minutes acquisition.

mance. The four flip angles found using the optimization algorithm are 110/74/67/162 degrees, and the use of multiple pulses clearly outperformed single pulse implementations. The multiple lipid selective pulses achieved much better lipid suppression at targeted T1s and were robust under B1 inhomogeniety. In particular, in vivo lipid suppression was on the order of 10 for a single inversion pulse and higher than 20 for multiple flip angle pulses.

We have designed and implemented a robust method to suppress lipids using frequency selective pulses for a spiral CSI scan at 3T. The effectiveness of this multiple pulse method is demonstrated on an in vivo scan. It showed improved suppression compare to single frequency selective inversion recovery and undisturbed metabolite spectra.

Quantitative 3D Brain MRSI with Phased Array Acquisition

[1]Meng Gu, [2]Donghyun Kim, [3]Daniel M. Spielman - [1]Electrical Engineering Department, Stanford University, [2] Department of Radiology, University of California at San Francisco, [3] Department of Radiology, Stanford University

Brain 1H magnetic resonance spectroscopic imaging (MRSI) has been shown to have significant diagnostic and treatment assessment value. To achieve the goals of short imaging times and robust quantification, we implemented a 3D MRSI sequence at 1.5T with dualband spectral-spatial excitation, spiral k-space readout, 8-channel phased-array acquisition, voxel-by-voxel phasing and automated quantification.

A spectral-spatial 90 degree RF pulse and two identical dualband spectral-spatial 180 degree pulses were incorporated into a PRESS sequence to form a spin echo. The 90 degree pulse is designed to fully excite both water and metabolites and the dualband 180 pulse is designed to fully excite metabolites resonances from Choline to NAA, partially excite water, while suppressing lipids signals. During readout, spirals with 4 interleaves were played out for spatial and spectral encoding. The final imaging sequence has the following characteristics: outer volume suppression, dualband spectral-spatial PRESS excitation, partial water
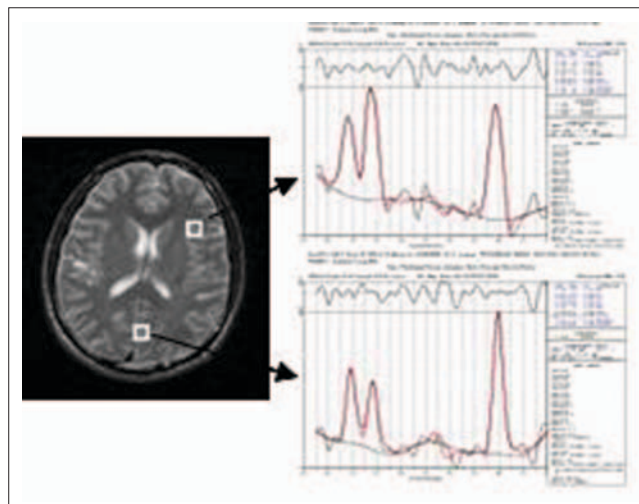
In vivo scan with spectra and their LC model fits from representative voxels

suppression, 32/32/16 matrix size, 1cc voxels, and 13 minute acquisition time at 1.5T. The signal from each of the 8 RF coils was reconstructed independently. Phased spectra for each voxel from each coil were combined according to water peak values to achieve maximum SNR. Spectra were then passed to the LCModel software package for quantification.

Phantom and in vivo data verified the excellent performance of the pulse sequence and dualband RF pulse. In vivo spectra were well phased and the standard deviation values associated with metabolite peaks indicated the reliability of the LCModel estimation and quality of spectra.

To our knowledge, this is the first demonstration of human brain 1.5T 1H MRS using spiral imaging and a phased-array coil.

Fast 3D Pediatric Brain MRSI

D. Kim[3], M, Gu[1,2], C. Cunningham[2], A. Chen[3], F. Baumer[1], O. Glenn[3], D. Vigneron[3], D. Spielman[1], J. Barkovich[3] - [1]Radiology, [2]Electrical Engineering, [3]UCSF Radiology.

Pediatric neurospectroscopy provides unique information regarding the metabolic variations during normal and abnormal brain development. Spectroscopic imaging can add to this feature by providing topologic information, but rapid scan times are needed for clinical feasible protocols. We have thus developed a 6 min 3D MRSI clinical protocol to study. The clinical goal is to understand the metabolic differences in subjects with motor dysfunction by analyzing metabolite levels in the corticospinal tract (CST).

A 3D MRSI sequence was developed using PRESS excitation in combination with a spiral based readout gradient for use at 3T. A dualband spectral spatial spin echo pulse for 3T neuro applications, designed to excite only 1% of the water signal and suppress lipids while passing the NAA, Cr, and Cho resonances was used. Data collection using a 8 channel receiver coil provided increased signal to noise ratio (SNR). Overall, the following MRSI parameters were used for data collection; 3T, TR/TE = 1500/130 ms, 32x32x8 matrix, 1cc spatial resolution, 6:24 min scan time. Quantification was performed by measuring voxels corresponding to the CST and incoporating this into the LCModel fitting procedure.
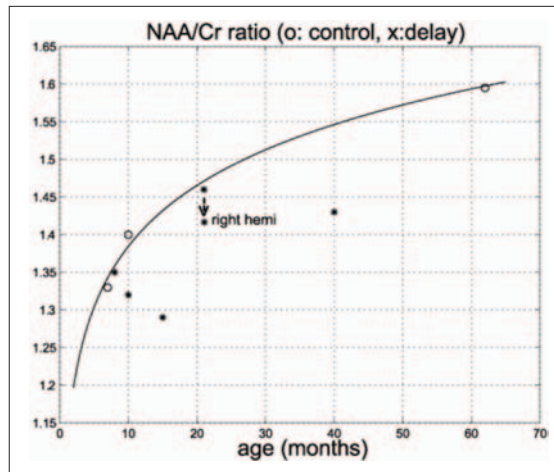
NAA/Cr ratios computed from the cortical spinal tracts of 3 controls and 5 children with motor delay.

In vivo studies demonstrated excellent results with SNRs exceeding that from adults. Metabolite values were recorded from the CST beginning at the precentral gyrus lateral to the centrum semiovale and ending at the cerebral peduncle region. NAA/Cho showed a linear trend in the change of metabolite ratios for the CST given this age range. Further data collection is needed to confirm this trend. Regardless, the ability to analyze spectra from the whole CST pathway (and other pathways) is unique using spectroscopic imaging.

We have developed a robust 3D MRSI technique for pediatric neuroim NAA/Cr ratios computed from the cortical spinal tracts of 3 controls and 5 children with motor delay.

Fast Metabolic Imaging for Systems with Sparse Spectra

D. Mayer[1], Y.S. Levin[1], R.E. Hurd[2], G.H. Glover[1], D.M. Spielman[1] - [1]Department of Radiology, Stanford University, [2]GE Healthcare, ASL, Menlo Park, CA

The development of hyperpolarized, metabolically active MRI agents presents both unprecedented opportunities as well as new technical challenges. While it theoretically permits in vivo imaging of not only the substrate, but also downstream metabolic products, the decay of the longitudinal magnetization demands fast acquisition schemes. The need for speed in combination with the sparse spectra which can occur in the application of hyperpolarized 13C metabolic imaging makes spiral chemical shift imaging (spCSI) an ideal candidate for this application.

The implemented sequence exploits sparse spectra and prior knowledge of resonance frequencies to reduce the measurement time by undersampling the data in the spectral domain. As a consequence, multiple reconstructions of a given data set have to be computed in which only components with frequencies within a certain bandwidth are reconstructed "in-focus" while other are severely blurred ("spectral tomosynthesis"). The sequence was tested at 3 T on a phantom containing solutions of alanine (Ala), lactate (Lac), and pyruvate-pyruvate hydrate C1-C2 ester (with two resonances, PPE1 and PPE2) at thermal equilibrium polarization, all enriched to 99% 13C in the C1 carbonyl positions. Spiral CSI with a single spatial interleaf (single-shot spCSI) and 3 interleaves (3-shot spCSI), respectively, were com-
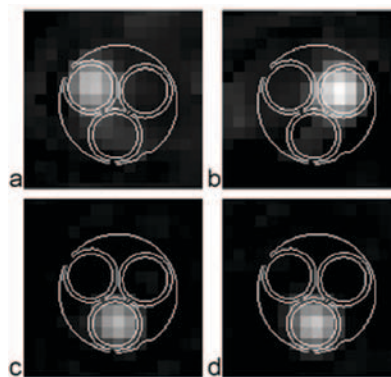
Metabolic maps of Ala (a), Lac (b), PPE1 (c), and PPE2 (d) reconstructed from single-shot

pared to phase-encoded CSI (FIDCSI). Metabolic maps of all four resonances for 3-shot spCSI and of PPE1 and PPE2 for single-shot spCSI demonstrate similar resolution and localization properties as the FIDCSI images. Metabolic maps of Ala and Lac for single-shot spCSI contain minor artifacts due to signal overlap of aliased resonances.

This work demonstrates that spectral undersampling can be used to reduce Tacq of spCSI for systems with sparse spectra. When applying this technique to hyperpolarized 13C metabolic imaging, the TR can be reduced to the minimum time necessary for excitation and data acquisition, therefore, allowing a sub-second temporal resolution. Artifacts due to the aliasing can potentially be reduced by using the prior knowledge of resonance frequencies, scalar coupling constants, and transverse relaxation times, and estimating the relative amplitudes with a minimum least-squares solution.

Least Squares Reconstruction for Hyperpolarized 13C spiral-MRSI

Levin YS[1,2], Mayer D[1], Hurd RE, Yen Y-F[3], Spielman DM[1] - Departments of [1]Radiology and [2]Electrical Engineering

Introduction: Hyperpolarized 13C enables high resolution imaging in which an injected compound and its downstream metabolites can be identified. Rapid imaging is necessary due to T1 signal decay. Although the spectral bandwidth is large, the sparse spectrum can be exploited by spectral undersampling using methods such as spiral CSI (spcsi). Conventional reconstruction (CR) involves performing a 1D FFT in kf to separate the metabolites. We propose an alternate reconstruction technique based on a least-squares (LS) algorithm.

Methods and Discussion: For a spectrum containing known peaks, spiral CSI in which a single k-space trajectory is repeated for a total of M echoes, the signal for each kx, ky point can be written in matrix form y = Am, where y is a vector corresponding to the M observations, m is a vector describing the spectral components of the point. Information about the peaks, such as chemical shifts and J-couplings are included in A. LS methods can be used to solve for y for each k-space point, and gridding performed to obtain metabolic images. Optimal TE values, subject to FOV and resolution constraints, can be obtained using the condition number of A.
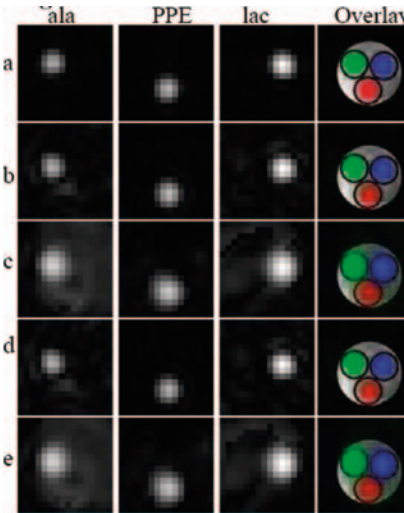
The figure depicts metabolic images from the phantom with color overlay (ala=green, PPE=red lac=blue) for each of 5 different reconstructions (a-e). a=fidcsi data with LS recon. b= spcsi, 21 echoes, LS recon. c=spcsi, 21 echoes, CR. d=spcsi, 8 echoes, LS recon. e=spcsi, 8 echoes, CR. The central region was cut out of the images for display. For the CR technique, four separate peaks are reconstructed, resulting in four separate metabolic images. Only one of the PPE peaks (-594 Hz) is

Simulations were performed for a set of peaks corresponding to 13C1 lactate, 13C1 alanine, 13C1 pyruvate and 13C bicarbonate. Phantom measurements (three tubes of 1.5M 99% enriched 13C1 ala, lac, and a pyruvate ester (PPE)) were then performed on a GE 3T MR scanner. The performance of the LS reconstruction exceeded that of conventional reconstruction as seen in lower amounts of ala detected in the lac ROI, lac detected in the ala ROI, and ala detected in the pyr ROI. Additionally, performance of the LS recon with 8 echoes was comparable to performance at 21 echoes.

Conclusion: The LS reconstruction technique allows for optimization of the acquisition parameters as well as for elimination of artifacts in reconstructed images. For the FOV and resolution used here, our results imply that metabolic images can reliably be obtained in <85 ms.

Two-Dimensional Variable-Density Spiral RF Excitation

Levin YS[1,2], Pisani LJ[1], Pauly JM[2], Spielman DM[1], - [1]Departments of Radiology, and [2]Electrical Engineering

Two-dimensional excitation pulses have found numerous uses in MR imaging. Variable-density (VD) 2-D spiral excitation has been investigated as a way to shorten the duration of excitation pulses and limit RF power deposition. This work proposes a simple method to accomplish this task.

The algorithm optimizes the excitation k-space trajectory for variable-density spirals by approximating the trajectory by concentric circles. Because a circle is radially symmetric, its Fourier transform is also radially symmetric and can be expressed one-dimensionally as a Hankel transform. The "circle approximation" was used to design a 10-turn inversion pulse with a width of 1 cm and a 15-turn an excitation (90°) pulse.

Simulations: Variable density trajectories were described by a polynomial. A global search was performed, and the polynomial coefficients yielding the minimum peak sidelobe height over all trajectories was used in designing the pulse. In order to test the accuracy of the circle approximation, the forward SLR transform was performed for each of the corresponding spiral trajectories, and the maximum sidelobe height was recorded and compared to the value obtained from the
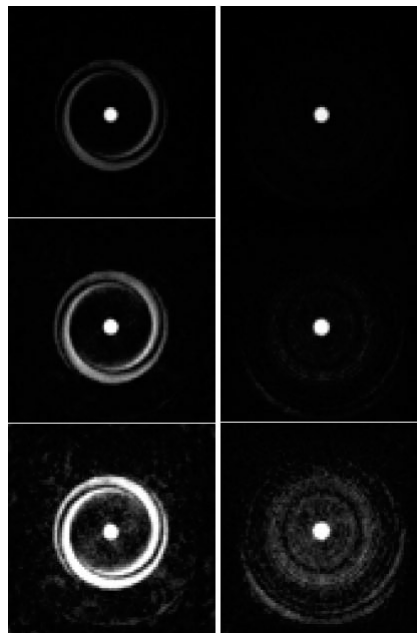
The figure depicts the images obtained from the excitation experiment, with UD on the left and VD on the right. The first row is windowed at full-scale, while the second and third rows are windowed at 2X and 5X, respectively

circle approximation.

Implementation: Inversion and excitation pulses (both uniform density (UD) and VD) were implemented on our 1.5 T GE (Signa) scanner.

(1) 10-turn inversion pulse: Cylindrical phantom of diameter 20 cm; FOV/Matrix/TR = 36cm/128X128/2; TI was set to null the mainlobe signal.

(2) 15-turn VD excitation (90°) pulse: Cylindrical phantom of diameter 26.4 cm; FOV/Matrix/TR = 36cm/128X128/2. Readouts for all images were performed with 4-interleaf spirals.

Conclusion: The "circle approximation" allows for fast and accurate optimization of the excitation k-space trajectory, with an 80% reduction in peak sidelobe height for the 1-cm inversion pulse investigated here and significant reduction of sidelobe in the excitation pulse as well. This likely makes it possible to allow the sidelobe to alias inside the field of view.

Acute Histopathological Changes in Canine Prostates Treated with High Intensity Ultrasound or Cryosurgery: Correlation with Contrast Enhanced MR Images

D. M. Bouley[1], B. Daniel[2], K. Butts Pauly[2], E. Liu[2], C. Diederich[3], W. Nau[3], G. Sommer[2]
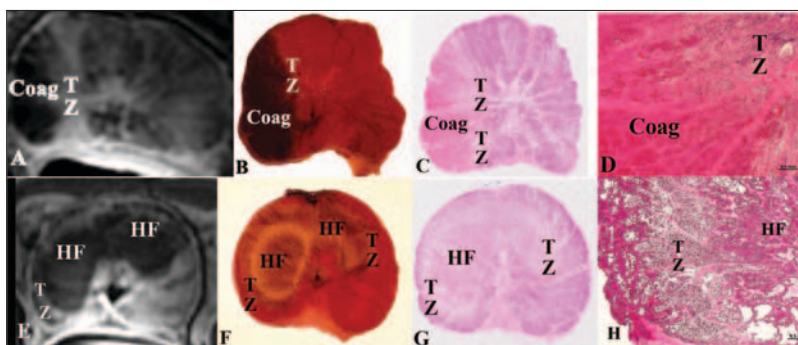Departments of [1]Comparative Medicine, and [2]Radiology, Stanford University, Stanford

Introduction: High intensity ultrasound (HIFU) and cryosurgery, both valuable treatments for prostate cancer, represent opposite ends of the minimally invasive temperature based therapies. However, in many respects, both types of thermally-induced lesions appear similar on MR images. For example, both types of thermal lesions lack contrast enhancement after injection of the contrast agent gadolinium (Fig. 1, A and E). Therefore, in order to optimize these MRI monitored treatments, this study was conducted to compare the acute histopathology of HIFU and cryosurgery-induced lesions in the dog prostate model, and to correlate patterns of tissue injury with contrast-enhanced MR imaging.

Figure 1. Images of canine prostate treated with either cryosurgery (A-D), or HIUF (E-F). The coagulated tissue (Coag) and heat fixed tissue (HF) do not enhance with gadolinium, while the transition zones (TZ) in the prostates treated with both the cryosurgery and HUS are enhanced on MR.

Methods: Studies using either transurethral or interstitial ultrasound probes (n=6) or transperineal cryoprobes (n=4) were used to ablate target regions within the prostates of 10 dogs. Following treatment, dogs were euthanized and the prostates were harvested, sliced, and stained with triphenyl tetrazolium chloride (TTC), a vital dye that stains viable tissues red. TTC-stained prostates were then fixed in 10% buffered neutral formalin, processed for routine histopathology and stained with Hematoxylin and Eosin (H&E). Oversized glass slides with complete transverse sections of prostate were scanned at 2400 dpi resolution on a flat bed-scanner for comparison with TTC-stained wet tissues and contrast-enhanced MR images. Histopathology of the lesions was analyzed at high magnification.

Results: The pathology of the prostatic lesions induced by HIFU vs cryotherapy differs in several respects. Grossly, prostates treated with HIFU develop lesions that are firm, discrete, dry, gray regions, sunken below the gland cut surface. Cryolesions are dark red, moist, soft, slightly mucinous, and do not retract beneath the cut surface. Following TTC staining, cryolesions are difficult to distinguish from the surrounding red-stained viable tissue whereas thermal lesions sharply contrast with untreated gland (Fig.1, B, and F). Thin zones of pale TTC-stained tissue, referred to as the transition zone (TZ), borders the lesions created by both treatments. These areas correlate to hyperintense lesion borders on contrast- enhanced MR images (Fig. 1, A and E).

Microscopically, both HIFU and cryo lesions have relatively distinct zones of injury characterized by severe damage surrounded by the TZ, where damage to glands and interstitial vasculature is less severe or sublethal. The TZ in turn merges irregularly with the normal, untreated glands. Prostatic glands subjected to severe cold temperatures in the center of the cryosurgery -"ice-ball" undergo total coagulation with loss of gland structure, gland remnants filled with eosinophilic coagulated cell debris, nuclear lysis, and extensive interstitial hemorrhage (Fig. 1, D). In contrast, the most intensely heated zones within the HIFU treated regions undergo heat fixation and maintain histologically "normal' appearing glands lined by epithelium that appears to be minimally altered (Fig. 1H). Irreversible cell death and vascular destruction in the coagulated cryolesions and the heat fixed zones in the HIFU lesions appear similarly as hypointense areas in the contrast-enhanced MR images. Areas of variable, sublethal or partial tissue injury to glands and blood vessels result in uptake of gadolinium on contrast enhanced MR images in the TZ of both.

Conclusions: Contrast-enhanced MR images, TTC staining and detailed histopathological analysis of HIFU and cryosurgery-induced lesions in a canine prostate model can provide a reliable means of predicting cell death in desired target areas. The implication of this work is that areas lacking contrast enhancement are lethally ablated, while the areas with partial or full contrast enhancement require further treatment. Understanding the patterns of acute tissue injury that correspond to in vivo MR images should improve clinicians' ability to accurately predict the success of these minimally invasive cancer therapies.

Improvements in Line Scan Diffusion Weighted Image Reconstruction with a Least Norm Algorithm

Jing Chen [1,2], Kim Butts Pauly[2] - [1]Departments of Electrical Engineering and [2]Radiology
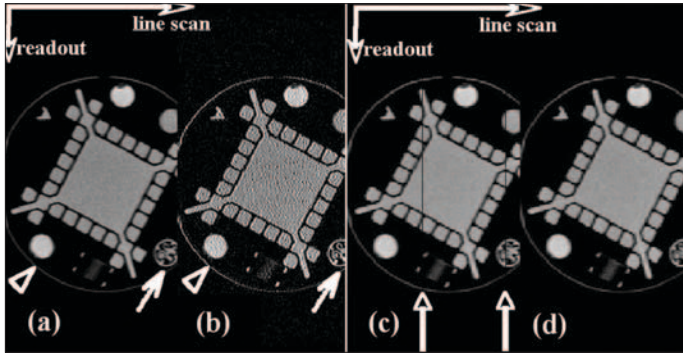
Line scan image (a) and its least norm solution (b). The image resolution was enhanced. (c) (Mi') was obtained by setting two lines in (a) to zero. The least norm solution Mln' was calculated, and the result of A×Mln' was showed in (d). The two missing lines were successfully recovered as compared to (a).

Line scan diffusion imaging (LSDI) has been shown to be relatively insensitive to motion artifacts as it is insensitive to view-to-view motion. However, the LSDI image is inherently blurred in the line scan direction due to its approximately triangular shape point spread function (PSF). In this work, we propose using a least norm (LN) algorithm to increase the resolution of line scan images without requiring ultra thin slices.

Conventional 2DFT image can be represented by a matrix Mi, each element of Mi could be approximated as the amplitude of all the magnetization within that voxel. Signal acquisition in LSDI could be viewed as several elements in one row of Mi are selected, weighted and summed to form on element in the acquired image Mlsdi. It could be simplified as one matrix operation, Mlsdi = A× Mi. A is known when imaging parameters were set, and A is a fat matrix. This condition is called underdetermined, and there are many solutions for Mi. Assuming A is full rank, one of the solutions is the least norm solution Mln = AT(AAT)-1Mlsdi. An LSDI images was acquired on the 0.5T Signa SP open MRI system, and an LN image was generated from the acquired LSDI image using the least norm method.

Improved image resolution can be appreciated around the high-resolution structures (arrow and arrow head) in the LN reconstructed image in Fig (b). One application of the LN method is to recover dropped lines. These arise from intraview motion in the presence of diffusion weighted gradients. In Fig (c), two lines are manually taken out to simulate the motion artifact. Compared to the previous example, this equation is further underdetermined. The least norm method can recover these two lines as shown in Fig (d).

In this work we present a technique using the least norm algorithm to improve the image quality of line scan diffusion imaging. The method can be used to obtain high resolution in the reconstructed image, or to remove the motion artifact in LSDI. Future work includes detailed analysis of the noise characteristics in the LN reconstructed image and in vivo applications.

Investigation of DWI to Evaluate Prostate Thermal and Cryo Lesions

Jing Chen [1,2], Bruce L. Daniel[2], Donna M. Bouley[3], Graham Sommer[2], Kim Butts Pauly[2]
Departments of [1]Electrical Engineering, [2]Radiology, and [3]Comparative Medicine

Contrast enhanced MRI (CE) is the current "gold standard" for in vivo acute lesion evaluation method in MRI. However, CE involves contrast material administration and cannot be repeated within one procedure. On the other hand, diffusion-weighted MRI (DWI) has been shown promising to evaluate the acute cryolesion in vivo. The goal of this work is to further investigate the use of DWI to estimate the cell viability immediately after thermal or cryo treatments.

All animal experiments were approved by the Administrative Panel on Laboratory Animal Care. Diffusion weighted imaging was performed in nine canine prostates with MRI-guided high intensity ultrasound thermal therapy (4 cases) or cryoablation (5 cases). All MR imaging were acquired on the 0.5T Signa SP open MRI system (GE, Milwaukee, WI). Line scan diffusion weighted images (LSDI) were acquired before the therapy and immediately after the prostates returned to body temperature. Later, the dogs were euthanized and sliced prostate samples were incubated in a 1% triphenyl tetrazolium chloride (TTC) solution. According to the TTC staining result, regions of interest (ROI) were chosen completely within the necrotic tissues and viable tissues. The ADC values of these two types of tissue were measured.

Both thermal/cryo necroses appeared as low signal intensity on the ADC trace map. The pre-treatment normal canine prostate tissue had an ADC value of (1.68±0.17) ×10-3 mm2/second. After the treatment, the ADC value of the necrotic tissue dramatically decreased to (1.02±0.09) ×10-3 mm2/second, while the post-treatment but viable tissue increased to (1.75±0.20) ×10-3 mm2/second. In general, the ADC decreased about 39% in the core of the lesions after the treatment. The difference between the viable and necrotic tissue was significant (p<0.001). There was no distant difference between thermal and cryo lesions in ADC trace value.
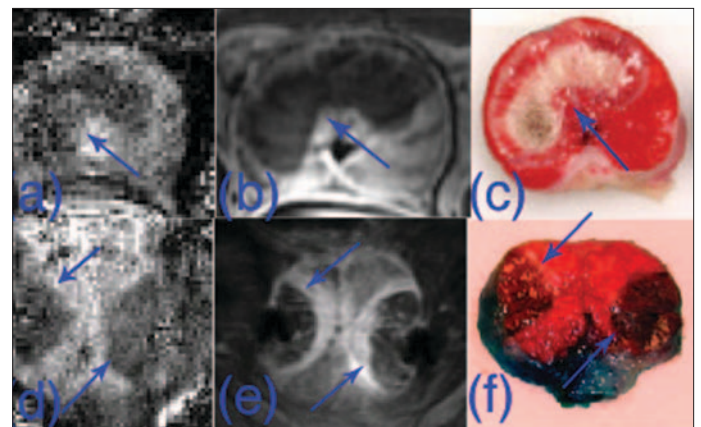
ADC trace map (a, d), contrast enhanced images (b, e) and TTC results (c, f). Corresponding thermal (a, b, c) and cryo (d, e, f) lesions could be seen in all three imaging methods, as pointed out by the arrows.

Segmentation of Costal Cartilage in CT Data using Watershed Markers

Andrew B. Holbrook[1], Kim Butts Pauly[2] - [1]Departments of Bioengineering and [2] Radiology

High Intensity Focused Ultrasound (HIFU) ablation is a promising non-invasive technique that heats a specific tumor region to fatal levels, while minimizing cell death in nearby healthy areas. For liver applications, the rib cage limits the transducer placement. A treatment plan based on CT images would segment the ribs and provide visualization of them and the tumor. A HIFU simulation of deposited heat would also require rib segmentation. Unfortunately, the ribs are difficult to segment on CT as they transition to cartilage, with CT units similar to that of the liver. The purpose of this work was to develop a rib segmentation algorithm based on CT images for HIFU treatment planning.

After an initial threshold of the CT data, rib regions were characterized based on their size, and if a region were greater than a predetermined area parameter (i.e. it consisted of rib and liver), a marker based watershed transformation separated the two regions and continued to the next inferior slice. After false positives were removed by a predetermined volume parameter, the remaining objects were reassigned high CT values.

Preliminary results from six human CT datasets indicated this segmentation method works well, successfully distinguishing the ribs from nearby organs. Of the fifty-five ribs counted in these datasets, only five contained small errors due to reconstruction shading irregularities, with four of these in one dataset. Once all costal cartilage was assigned high CT numbers, any commercially available 3D rendering software (eg Osirix) can be used to visualize the ribs and tumor.

Future work will include refining the process with more data and automating a couple of the intermediate steps in the algorithm.

Optimizing this for MR data and extending it to not only segment cartilage but also other tissue types will be next, allowing thermal dose planning to occur.
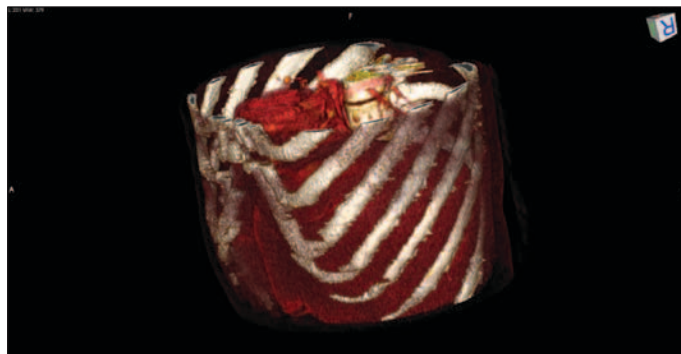
Representative volume rendering showing segmented bone and cartilage extending up to sternum.

Double Half RF for Ultrashort T2 Imaging

Sonal Josan[1,2], Aiming Lu[1], John Pauly[2], Kim Butts Pauly[1], Bruce Daniel[1]
[1]Departments of [1]Radiology, [2]Electrical Engineering

Image-guided cryoablation is a promising minimally invasive therapy for prostate cancer. MRI provides the promise of temperature mapping throughout the frozen area to better guide the procedure than the placement of discrete thermocouples. Previous studies have shown the tissue transverse relaxation rate R2* (1/T2) to be relatively linear over the temperature range of interest. In order to quantitate R2* in frozen tissue, ultrashort echo times are obtained with specialized RF pulses, called half pulses. Their slice profile is sensitive to eddy currents that make it difficult to quantitate R2*. The purpose of this work was to develop an improved RF pulse that was less sensitive to eddy currents, thereby improving MR imaging of frozen tissue.

A conventional full-sinc RF pulse is split in time and referred to here as a double half RF pulse. The proposed pulse, like the half pulse excitation, consists of two excitations with the slice-select gradient polarity inverted. Since the pulse amplitude is modulated by T2 decay, each excitation produces a half-sinc weighting in k-space for short T2, and a full-sinc weighting for long T2. A simulation of slice profile as a function of T2 shows significantly improved slice selectivity for long T2 with the double half pulse. The slice profile for short T2 is similar to the original half pulse.

Experiments were performed on a 0.5T GE Signa SP interventional MR scanner. The slice profile and free induction decay(FID) signal of a long T2 (60ms) spherical phantom were measured with both the half pulse and the double half pulse. The half pulse slice profile has tails extending far from the desired slice, while the double half RF demonstrates much better selectivity. In the presence of eddy currents, the slice selectivity of the half pulse varies over time, so that the FID demonstrates an oscillating behavior. The FID for the double half RF decays without oscillation.

Both pulses were used in an in vivo canine prostate cryoablation. Two cryoprobes were inserted into the prostate with MRI guidance, and fiberoptic temperature sensors were placed between the cryoprobes. R2* maps of the frozen region were obtained by an exponential fit of images acquired at echo times of 0.1, 0.4, 0.7, 1.0 ms. Eddy current distortions in the half pulse can contaminate the R2* maps with out of slice signal from unfrozen tissue. The double half pulse achieves a better slice profile for the warm tissue with long T2, thus improving the quality of the R2* measurements.

Consistency of MR Paremeters in Frozen Porcine Heart Muscle, Kidney, and Liver

Elena Kaye[2], Sonal Josan[2], Aiming Lu[1], Kim Butts Pauly[1], Bruce Daniel[1]. - [1]Radiology and [2]Electrical Engineering

Image-guided cryoablation is promising for the minimally invasive treatment of prostate, liver, and kidney tumors. It is also being developed for eliminating the most common cardiac arrythmias in children and adults. MRI can potentially improve the guidance of cryoablation by providing a technique for temperature mapping of the frozen tissue. Temperature dependence of transverse relaxation rate (R2*) and Signal Intensity (SI) in freshly excised porcine liver (n=4), kidney (n=4), and heart muscle (n=3) was studied in this work. In addition, the consistency of R2* and SI between tissue types was investigated. In each experiment, 10x10x25mm slabs of tissue were imaged in a clinical interventional MRI scanner (0.5T GE Signa SP). Imaging was repeated as the tissue was cooled from room temperature to -40°C in 5°C increments.

Data analysis for the three types of tissue showed that SI decreased rapidly from 0°C to about -6°C, and below -6°C it was decreasing slowly. For any given temperature between -6°C and -35°C the SI values of kidney and liver were comparable and approximately twice as low as that of the cardiac muscle. The data from cardiac muscle experiments exhibited consistency in both the slope and the intercept of the R2*(T) linear fits across the samples. Across the kidney tissue samples the R2* slopes were consistent but the intercepts had larger discrepancy. For liver tissue, a significant difference was found in the R2* intercept estimates across the samples. The difference between the slopes of the R2*(T) fits of the combined data for liver, kidney and heart tissues insignificant. However, the values of the intercept for the three models varied substantially across the three types of tissue.

In conclusion, the results of this study indicated a high degree of similarity between the MR parameters of frozen cardiac muscle, liver, and kidney tissues. Following this study similar experiments will be performed with a prostate tissue.

Improvements in R2* Mapping During In Vivo Cryoablation

Aiming Lu, Bruce L. Daniel, Kim Butts Pauly - Department of Radiology

Introduction: MR-guided cryoablation is a promising minimally invasive therapy for prostate tumors. To ensure sufficiently cold temperatures are reached throughout the tumor, temperature mapping with MRI would be desirable since it would provide information throughout the frozen area. Tissue R2* is a promising parameter to quantify temperature as it appears to be relatively linear over the temperature range of interest. Unfortunately, mapping of R2* in vivo has been sensitive to eddy currents. The purpose of this work was to optimize our R2* mapping by using radial readout, reducing the earliest echo time to 0.1 ms, and carefully measuring and compensating for eddy currents.

Materials and methods: Half-RF pulse excitation with a multiple echo radial readout is employed to achieve an ultra-short echo time for the first echo. Both B0 and linear eddy currents induced by an ideal selective gradient are measured first. Linear eddy currents are then corrected by pre-compensating the RF pulse and selective gradient. B0 eddy currents are corrected by varying the RF phase during excitation. In-vivo canine experiments were performed on a 0.5T GE Signa open scanner (GE healthcare, Milwaukee, WI). To calculate the R2*, four sets of data are acquired with TEs of 0.1 ms, 0.4 ms, 0.7 ms and 1.0 ms for the first echo at each time point.
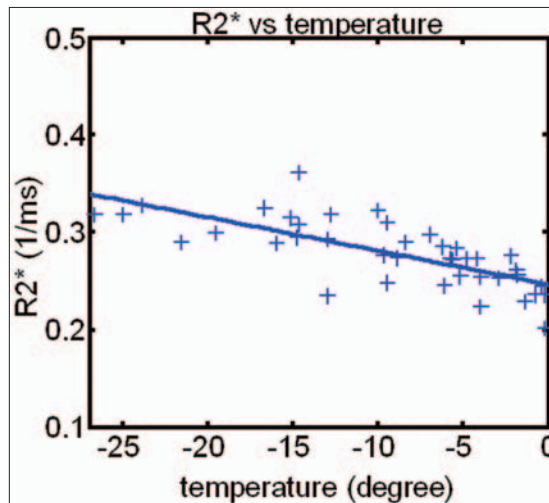
The relationship of the R2 and temperature at the location of the thermocouples are fit with a line.*

Results and discussion: The acquired images provided sufficient signal in the frozen tissue to obtain R2* maps at temperatures as low as –30°C. The multiple echo acquisition scheme increases R2* mapping efficiency, especially for tissues with relatively longer T2*. The R2* values at the thermocouple position demonstrated a monotonous decrease with temperature, as shown in the figure.

Conclusion: With an ultra short TE MRI sequence, R2* maps with improved quality have been obtained throughout the whole frozen process of in vivo experiments. The proposed technique has been shown to produce promising results for temperature monitoring during cryosurgery. Future work will further optimize the acquisition parameters.

REFERENCES/FUNDING SOURCE
Onik G, Technol Cancer Res Treat 2004; 3:p.365 2. Baust J, Cryobiology 1997; 34: p373. 3. Wong WS, Cancer 1997; 79: p.963. 4. Gage AA, Cryobiology 1998; 37: p.171. 5. Larson TR, Urology 2000; 55: p.547. 6. Wansapura J, Acad Radiology; 12: p1080. 7. Kaye E, Proc. 14th ISMRM 2006; p1423.
NIH CA092061, P41 RR009784

Dynamic Contrast Enhanced Imaging After Canine Prostate Cryoablation

E. Liu[1], D. Bouley[2], B. L. Daniel[1], K. Butts Pauly[1] - Departments of [1]Radiology and [2]Comparative Medicine

IIntroduction: MR-guided cryoablation is a promising minimally invasive therapy for prostate tumors that are solitary and unilateral. The roles of imaging are targetting, monitoring, and post-therapy evaluation. It has been shown that contrast enhanced imaging provides a beautiful depiction of the vascular damage in the cryolesion. The purpose of this work was to evaluate previously frozen prostate tissue with dynamic contrast enhanced imaging and 3D contrast enhanced imaging.

Methods: Three dogs were imaged with a phased array coil setup including an endorectal coil and an anterior surface coil in a 0.5T GE Signal MRI scanner. Two MR-compatible cryoprobes (Oncura, Israel) were placed through the anterior abdominal wall to locations on either side of the prostate. In each dog, one cryoprobe was frozen only once, while the other completed two freeze-thaw cycles. T1-weighted FSE images were obtained at the height of each freeze to delineate the iceball sizes. After complete thaw to normal body temperature, dynamic 2D SPGR images (1.9 s/image) were acquired and repeated during the injection of a gadolinium contrast agent. CE 3D SPGR images were immediately acquired. The dogs were euthanatized and sliced prostate samples were incubated in a 1% triphenyl tetrazolium chloride (TTC) solution.

Results: In all experiments, the normal prostate tissue enhanced. In the core of the cryolesion, the tissue did not enhance. An example set of images is shown in Figure 1. In all three experiments, there was a rim of hyperenhancement. Plots of the signal intensity on the dynamic contrast
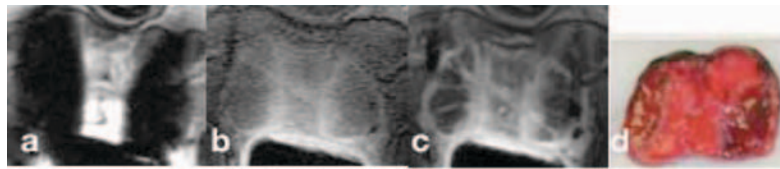

Figure 1.(a) FSE image at the height of freezing. Dynamic CE (b) and 3D SPGR (c) images demonstrate areas that do not enhance and the rim of hyperenhancement. (d) TTC image that suggests the hyperintense rim is within the pink-staining normal tissue region.
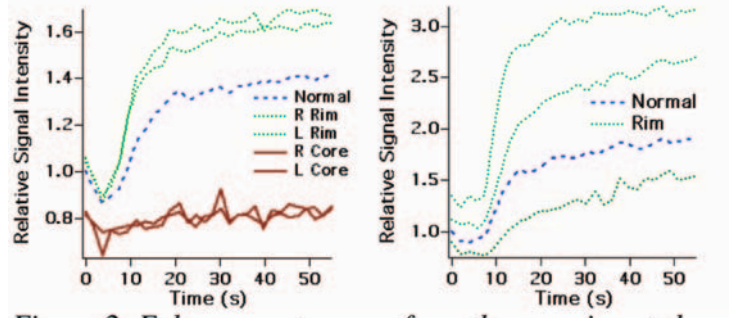

Figure 2. Enhancement curves from the experiment shown in Figure 1 (left) that demonstrate that this rim enhances more than the more normal tissue. A short time of hypointensity is also seen as the contrast agent moves through the tissue. Enhancement curves from 3 ROIs in the second experiment demonstrate variable timecourses (right)
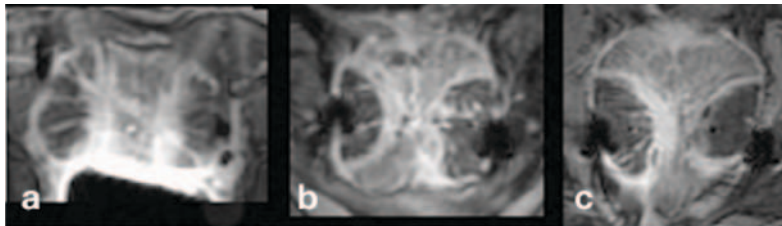

Figure 3. Hyperintense rim enhancement following cryoablation is variable in size between experiments and even within the same cryolesion

enhanced images in two experiments are provided in Figure 2. By comparison with TTC stained sections, the rim appears to lie within the normal pink staining tissue. The border of the hyperenhancing rim seemed to correspond well to the border between the hemorrhagic core of the cryolesion and the normal pink staining tissue on TTC. The size of the hyperenhancing rim varied in thickness from one experiment to another, varied in thickness from one lesion to another in the same experiment, and even varied in thickness within the same cryolesion. These variations can be seen in the images shown in Figure 3. The time course of enhancement on the rims were also variable, as shown in Figure 2.

Discussion: The results of this study suggest that the hyperintense rim seen on dynamic contrast enhanced MRI following prostate cryoablation may be within the normal staining pink area on TTC stained sections. Differences in the size and enhancement curves of the hyperenhancing rim may be due to differences in the underlying tissue structure, such as the presence of chronic prostatitis, interstitial fibrosis, and cystic hyperplasia that are scattered throughout the gland in the old dogs that were studied.

.

References/Funding Source
1. Onik G, Technol Cancer Res Treat 2004; 3:p.365 2. Gilbert J, MRI 1993;11(8): p1155.
NIH CA092061, P41 RR009784

# Referenceless PRF Thermometry with Multi-echo Processing to Monitor Prostate Ablation

Viola Rieke[1], Adam Kinsey[2], Will Nau[2], Chris Diederich[2], Graham Sommer[1], Kim Butts Pauly[1] - [1]Department of Radiology, Stanford University, [2]Department of Radiation Oncology, UCSF

MR thermometry uses the proton resonance frequency (PRF) shift with temperature to noninvasively monitor temperature during ultrasound thermal ablation of the prostate. Previously we developed a referenceless thermometry for decreased motion sensitivity. Here, we present an improvement to the method that allows temperature estimation at optimized resolution (1.7-1.9 mm) and anatomic imaging at high resolution, all in the same acquisition. The method is demonstrated during in vivo canine prostate ablation.

Referenceless thermometry measures a temperature change by estimating the background phase from a region outside the heating area, thereby eliminating the need of a baseline image. In the presence of periprostatic fat, three echoes need to be acquired to automatically determine water and fat regions which can have a constant phase offset. In this project, we acquire the three echoes with different k-space coverage. The symmetric, low resolution data is used for temperature; the asymmetric, high resolution data is reconstructed by zeropadding for anatomical images. Images were acquired during canine prostate ablation using a transurethral ultrasound transducer on a 0.5T interventional scanner. To demonstrate the robustness to tissue motion, pressure was applied to the animal's abdomen before heating started.

The referenceless method provided accurate temperature maps of the heating distribution during prostate ablation and was not affected by tissue motion. The high resolution magnitude images clearly depicted the anatomy and were used to overlay the low resolution temperature information. Collecting the three echoes in a single acquisition decreased reduced the imaging time per temperature frame by 50%.

The new pulse sequence allows for temperature monitoring during in vivo thermal ablation of the prostate with better temporal resolution, optimized temperature resolution and good visualization of underlying anatomical structures.
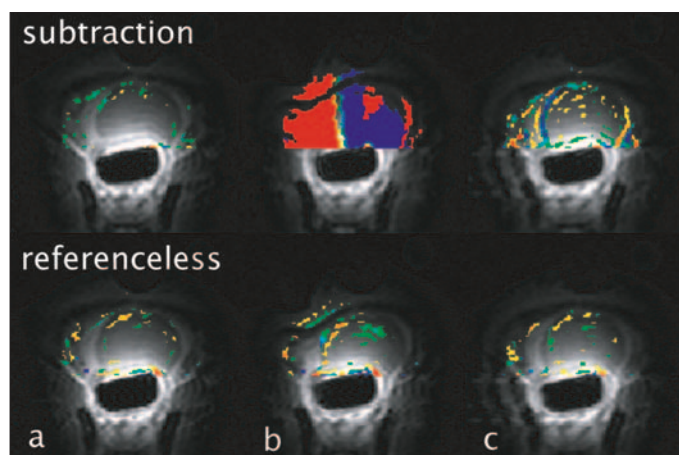
Temperature images acquired without heating and reconstructed with baseline subtraction and the referenceless method. When tissue motion occurs (b), severe errors render baseline subtraction useless.

Time Constant Sensitivity of Eddy Current Characterizing Pulse Sequence

Daniel B. Ennis, Marcus T. Alley, Brian A. Hargreaves, Norbert J. Pelc

Introduction: Eddy current compensation is important for a number of applications in magnetic resonance imaging. Eddy current induced fields impart phase on the acquired signal that can distort both magnitude images and phase estimates used to measure tissue velocities, displacements, and temperatures. Eddy current pre-emphasis provides first-order correction, but more sophisticated techniques are needed to account for a broad range of short and long time constants and spatial non-linearities. A pulse sequence was designed to measure the system's eddy current response and use this to correct the eddy current induced artifacts for an arbitrary pulse sequence using an impulse-response formalism. Herein, this pulse sequence was modeled with Bloch simulation to characterize the sensitivity and bandwidth of measured time constants (τ).

Methods: Pulse Sequence: A spin-echo pulse sequence was modified to support: 1) eddy current inducing test gradients, 2) a long τ eddy current nulling gradient, and 3) 3-D phase encoding. In order to measure phase shifts that arise from short τ eddy currents the pulse sequence was designed to acquire data (DAQ) for 62ms immediately after a gradient slew. Simulation: Simulated eddy current induced mono-exponential gradients were generated with $0.01\text{ms}<\tau<200\text{ms}$ and peak eddy current gradient strengths of $0.1\text{Gmax}/\tau$. Bloch simulation was used to simulate the signal response (time step=8μs, T1=250ms, T2=25ms) over a broad range of τ.

Results: The pulse sequence with the dummy gradients doesn't stimulate and is therefore insensitive to long τ eddy current effects, but is sensitive (phase accumulation $>\pi$) to $25\mu\text{s}<\tau<25\text{ms}$. The simulation also demonstrates that without the dummy gradients long time constant ($\tau>25\text{ms}$) eddy currents generate measurable phase accumulation during the 100ms.

Conclusions: The Bloch simulation demonstrates that the pulse sequence is maximally sensitive to short τ of ~5ms, but with good sensitivity to $25\mu\text{s}<\tau<25\text{ms}$. The fact that DAQ begins immediately after a gradient slew, combined with the high SNR of the sequence and the fact that short τ effects are not sensitive to T2 decay combine to make measurement of short τ effects possible.

Comparison of Aortic Flow Patterns in Volunteers and Ascending Aortic Aneurysms
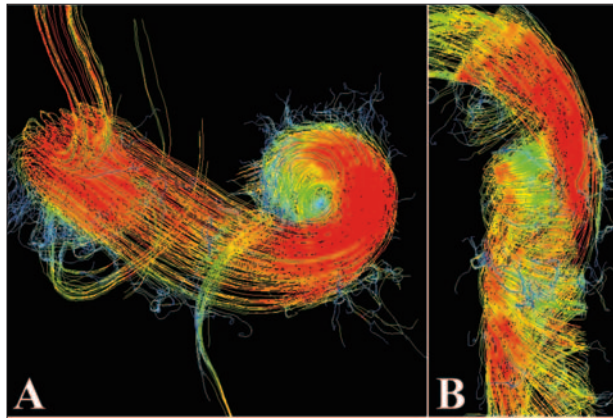
THOMAS A. HOPE[1], LARS WIGSTRÖM[1], MARCUS T. ALLEY[1], D. CRAIG MILLER[2], AND ROBERT HERFKENS[1]
[1]DEPARTMENTS OF RADIOLOGY, [2]AND CARDIOTHORACIC SURGERY.

Introduction: Time-resolved three-dimensional phase contrast magnetic resonance velocity mapping was employed to characterize the difference in flow patterns between healthy volunteers and patients with ascending aortic aneurysms.

Methods: Nineteen healthy volunteers and 13 ascending aortic aneurysm patients were scanned. Data was analyzed visually using streamlines, particle traces and vector fields. Vector fields placed on two-dimensional planes were visually graded to analyze helical flow patterns and retrograde flow along the aortic arch. Quantitative analysis of pulsatile flow was carried out on manually segmented planes extracted from the original 3D data sets.

Streamlines during mid-systole in a normal volunteer that depicts how the geometry of the aortic arch can result in left-handed helical flow in the descending aorta. A) superior view of the aortic arch with the descending aorta on the left, B) left lateral view of the descending aorta

Results: In volunteers, flow progressed as follows: an initial jet of blood skewed towards the anterior right wall of the ascending aorta is reflected posterolaterally off the wall towards the inner curvature creating opposing helices, a right-handed helix along the left wall and a left-handed helix along the right wall; retrograde flow occurred in all volunteers along the inner curvature between the location of the two helices. In ascending aortic aneurysm patients, the helices were larger and retrograde flow occurred earlier and lasted longer. In volunteers, 47% had two helices compared to 23% of the patients. Quantitative analysis showed that the average velocity fell between the ascending aorta and the transverse aorta in volunteers (47.9mm/s decrease, $p = 0.023$), while in ascending aortic aneurysm patients the velocity increased (141 mm/s increase, $p = 0.002$).

Discussion: Using time-resolved 3D PC-MRI, flow patterns in the aortic arch were characterized in healthy volunteers and in patients with ascending aortic aneurysms. Dilation of the ascending aorta skews the normal flow pattern in the ascending aorta changing retrograde and helical flow patterns. Currently we are looking at improved methods to describe helical flow patterns using automatic vortex recognition algorithms.
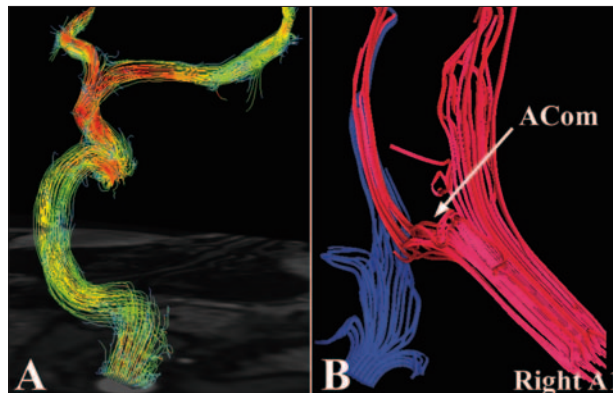
Time-Resolved 3D Quantitative Flow MRI of Intracranial Vessels Utilizing Parallel Imaging

THOMAS A. HOPE, SCOTT NAGLE, HUY DO, SCOTT ATLAS, MARCUS T. ALLEY, ROLAND BAMMER - DEPARTMENT OF RADIOLOGY

Introduction: A time-resolved three-dimensional phase-contrast MRI technique incorporating GRAPPA, a parallel imaging method, was implemented to measure the principle components of blood flow in three-dimensions at multiple instances over the cardiac cycle. The effects of magnetic field strength, parallel imaging and temporal resolution reduction factors on the data were investigated in a comparative evaluation at 1.5T and 3T.

Methods and Results: Over the past year, nine healthy volunteers were scanned on 1.5T and 3T magnets. 3D streamlines and 4D particle tracings were used to investigate dynamic blood flow properties. Data from extracted

A) streamlines in internal carotid artery during early systole depicting the increase in velocity in the carotid siphon and the bifurcation into the anterior and middle cerebral arteries; B) streamlines in midsystole with the left anterior cerebral artery in blue and the right anterior cerebral artery in red depicting an anterior communicating artery

provided a high degree of vascular conspicuity and flow visualization for even very small vessels (down to 1mm in diameter). Blood velocity measurements were in agreement with known values from transcranial Doppler ultrasound, and time-resolved streamline analysis described features that have not been reported previously for intracranial vasculature.

Discussion: We have shown that time-resolved 3D PC-MRI in combination with parallel imaging can be performed within clinically acceptable time periods and can produce high-resolution streamline data of even very small vessels. With ORFs of 2 and 3, acquisition times can be reduced from 23.1 minutes to 13.3 and 10.0 minutes given a heart

planes manually segmented were used to analyze the effect of three GRAPPA reduction factors, three temporal resolutions and the two magnetic field strengths on velocity measurements. At 3T, parallel imaging performed very well up to Outer Reduction Factors (ORFs) of 3 without any significant noise enhancement or deviations in the veracity of flow measurements. While at 1.5T, noise enhancement progressed much faster at increased reduction factors. A high temporal resolution (65ms) was required to follow dynamic processes in the intracranial vessels, such as visualization of the dicrotic notch. The 4D flow measurements rate of 70 beats per minute. We are currently enrolling patients with intracranial aneurysms to characterize changes in flow patterns that could be helpful in operative management.

Three-Dimensional Velocity Measurements in Turbulent Flows using Magnetic Resonance Imaging

Christopher Elkins[1], Marcus Alley[2], John K. Eaton[1] - Departments of [1]Mechanical Engineering and [2]Radiologyl

Fluid flow plays a major role in the function of modern technical devices. Most technological and natural flows are three-dimensional, turbulent and highly complex. This makes them nearly impossible to predict with computations, but the complexity is such that knowing the full mean velocity fields would contribute significantly to our understanding. Moreover, measurements of turbulent velocity fluctuations would enhance greatly our insight into these flows. Even the most advanced conventional laser-based measurement techniques (such as Particle Image Velocimetry (PIV)) are either too time-consuming, too expensive or simply incapable of measuring the entire flow fields for many real flows. Magnetic resonance velocimetry (MRV) presents a promising experimental alternative for use in these flows. MRV is a non-invasive technique for measuring the full three-component mean velocity field and potentially the turbulent velocity fluctuations for complex flows in and around opaque objects. MRV uses magnetic resonance imaging (MRI) techniques in conventional medical scanners. While MRV was developed for measuring blood flow in patients, we are adapting it to measure velocities in turbulent flows.
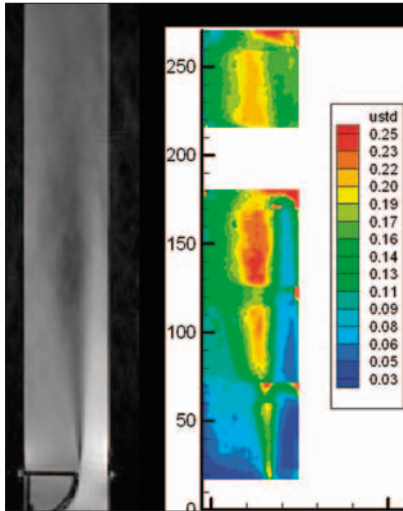

Figure 1: Contours of streamwise turbulent velocity fluctuation (u' $\equiv \sqrt{u'^2}$, units m/s) measured with PIV (right) in a turbulent backward facing step flow. The gray scale MR image of the shear layer (left) shows the qualitative features of the flow structure (dark indicates higher turbulence).

MRV is being tested in canonical three-dimensional turbulent flows such as the flow downstream of a backward facing step in order to better characterize its accuracy for different levels of turbulence. Improvements to MRV are evaluated by directly comparing MRV data to conventional measurements using PIV which are possible in this flow. The development of a robust MRV method benefits not only the engineering and physics community but also medical doctors and their patients since MRV is used increasingly in vivo for medical research and eventually for routine patient evaluation.

This work is notable because these MRV techniques are being developed to measure mean and fluctuating velocities in entire three-dimensional flow fields in turbulent flows in geometries too complex for conventional measurement systems. Currently we have good qualitative agreement between the PIV and MRV measurements although quantitatively the MRV tends to over-predict the turbulent velocity fluctuation. We are investigating these effects and hope to improve our accuracy in the near future.

Structural Basis for Regional Heterogeneity of Left Ventricular Function

Joseph Wu[1,3], Daniel B. Ennis[1], Lars Wigström[1,2], Tom Nguyen[3], Stefan Skare[1], Roland Bammer[1], Neil Ingels[3,4], D. Craig Miller[3], [1]Department of Radiology, Stanford University, [2]Center for Medical Image Science and Visualization, Linköping University, [3]Department of Cardiothoracic Surgery, Stanford University, [4]Research Institute, Palo Alto Medical Foundation

INTRODUCTION: Structure-function relationships are essential to understanding biological performance. The complex, but highly ordered arrangement of myofibers in the ventricular wall is closely related to regional myocardial function. This work tests the hypothesis that midwall myofibers are not oriented in the circumferential direction in all regions of the left ventricle and furthermore that regional gradients in myofiber orientation are heterogeneous. Regional differences of myofiber arrangement should impact regional function in addition to having implications for the interpretation of MRI tissue tagging strains.

METHODS: Mid-ventricular slices of five ex vivo ovine hearts were imaged on a 1.5T GE Signa Excite scanner using a custom diffusion tensor weighted interleaved echo-planar imaging sequence. Regional myofiber orientations were measured using a local cardiac coordinate system. Local myofiber direction was defined as the angle (α) between the primary eigenvector of the diffusion tensor and the local circumferential direction. Papillary muscles were manually masked. The left ventricular midwall was defined as 50% radial wall depth between the epicardium and endocardium. Finally, a circumferential fiber contour was defined from a b-spline fit to all locations where -5°< α <5°.

RESULTS: Contours of the circumferential fibers (α=0°) indicates that in the lateral wall there is a preponderance of negatively oriented (α<0°) epicardial fibers. In the lateral midwall (50% depth), fibers are oriented at an angle of α=-14°±8°. In comparison, septal midwall fibers average 10°±12°. The circumferential fibers are not located at the midwall, but, instead, at 43±9% wall depth in the septum and 67±11% wall depth in the lateral wall.

CONCLUSIONS: Midwall myofibers are not always oriented in the circumferential direction. When analyzing ventricular function using MRI tissue tagging or displacement imaging it is often assumed that midwall myofibers are oriented in the circumferential direction. Recent MRI tissue tagging results demonstrate a correlation between greater pre-stretch of the antero-lateral and infero-lateral wall and greater circumferential shortening[3]. This latter result implicates a hemodynamic driving force for variations in regional function. The results, herein, suggest that regional variations in myofiber arrangement may also play a role.

REFERENCES/FUNDING SOURCE
1.Ennis DB, Wigström L, Nguyen TC, Skare S, Bammer R, Ingels NB and Miller DC. Structural Basis for Regional Heterogeneity of Left Ventricular Function? ISMRM Conf. Proc. Seattle, WA, USA 2006
This work was supported by the NIH (T32 CA09695 to DBE; HL29589 to DCM), the Center of Advanced MR Technology at Stanford (P41 RR09784), The Lucas Foundation, and the Swedish Heart and Lung Foundation.

In-vivo sodium imaging of knee cartilage.

ERNESTO STAROSWIECKI, NEAL BANGERTER, BRIAN HARGREAVES, GARRY GOLD - DEPARTMENT OF RADIOLOGY

Introduction: Osteoarthritis is a highly debilitating disease afflicting tens of millions of people in the United States alone, but is difficult to detect in the early stages, making preventative treatment impractical. Early signs of osteoarthritis include changes in the matrix composition of articular cartilage, which result in reduced proteoglycan concentration. Direct quantification of sodium in cartilage has been shown to correlate with proteoglycan content [1, 2, 3]. We have begun to develop MR sequences for imaging the sodium concentration of articular cartilage in-vivo.

Methods: A 2D GRE sequence was adapted to use the broadband transmit amplifier on a 3T GE Signa system, enabling excitation of the Na+ nucleus (~33.8 MHz at 3T, instead of the ~128 MHz resonant frequency of H+ at 3T). A birdcage transmit/receive quadrature head coil tuned to the resonant frequency of sodium was employed for excitation and signal readout. The expected concentration of Na+ in healthy articular cartilage is approximately 260mM, while that in severely degenerated cartilage is approximately 40mM [4]. A set of NaCl phantoms with concentrations ranging from 50 mM to 500 mM were made for initial testing and calibration of the sequence. Initial results are shown in Figure 1.
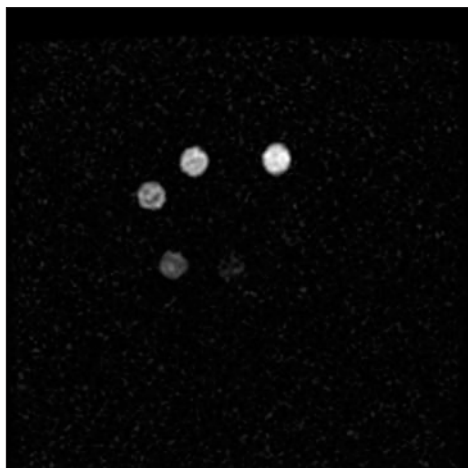
Sodium phantom images at 3T with a slice thickness of 20mm and scan time under 1min. The brightest circle corresponds to a 500mM concentration of NaCl, while the faintest distinguishable circle corresponds to 100mM.

This image was obtained with a scan time under 1 minute and a slice thickness of 20mm.

Results and Discussion: In Figure 1 we show that we can image and distinguish sodium concentrations of 500mM to 100mM (with 100mM steps), while in order to view the lowest concentration on 50mM we would require a slightly longer scan time. With this we have validated our ability to image sodium at 3T in concentrations similar to the ones expected in-vivo in human cartilage. Sodium imaging is particularly challenging given the low resolution and SNR due to low gyromagnetic ratio, the short T2, and the relatively low abundance of sodium in-vivo. We are currently working to improve these factors by building a custom knee-coil tuned to sodium, improving pulse sequences, and imaging at higher fields (7T).

REFERENCES/FUNDING SOURCE
1. Wheaton AJ, et al. Acad Radiol 2004; 11:21-28.
2. Reddy R, et al. Magn Reson Med 1998; 39:697-701.
3. Regatte RR, et al. J Magn Reson Imaging 1999; 10:961-967
4. Bashir A, et al. Magn Reson Med 1999; 41:857-865
GlaxoSmithKlein Inc., and NIH P41 RR009784 and R01 EB002524

Efficient Multi-Echo MRI of the Knee

GARRY. E. GOLD[1], SCOTT. B. REEDER[2], HUANZHOU. YU[3], J. H. BRITTAIN[4], BRIAN. A. HARGREAVES[1] - [1]RADIOLOGY, STANFORD UNIVERSITY, STANFORD, CA. [2]RADIOLOGY, UNIVERSITY OF WISCONSIN, MADISON, WI, [3]GLOBAL APPLIED SCIENCE LABORATORY, GE HEALTHCARE, MENLO PARK, CA. [4]GLOBAL APPLIED SCIENCE LABORATORY, GE HEALTHCARE, MADISON, WI.

Introduction: Three-dimensional (3D) MRI is useful to measure articular cartilage thickness and volumes, and detect cartilage lesions. It is challenging to achieve high-resolution images with fat suppression to depict cartilage. We have developed a very efficient multi-echo fat/water separation technique and validated it for knee imaging in volunteer subjects.

Methods: Six knees (four volunteers) were imaged using a GE Signa 1.5T MRI scanner and an 8-channel coil.

The standard cartilage segmentation technique, FS-SPGR was compared with multi-echo IDEAL GRE, with parameters chosen to keep scan times and total sampling time similar. All scans were 256x 256, 16 cm field-of-view, 1.5 mm section thickness, and 64 sections. Flip angles were adjusted for good cartilage to fluid contrast. Multi-echo IDEAL-GRE images were reconstructed on-line using the IDEAL method. SNR in each subject was calculated by dividing the average measured signal from 5 regions of interest in the trochlear cartilage by the standard deviation of the noise. SNR efficiency (SNR / scan time) values were compared using a student t-test.
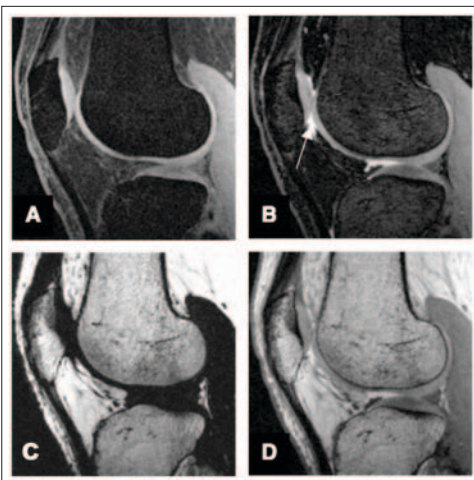
A) FS-SPGR. B) Multi-echo IDEAL-GRE water image with bright synovial fluid (arrow). C) Multi-echo IDEAL-GRE fat image. D) Multi-echo IDEAL-GRE combined image.

Results: IDEAL-GRE produced images with higher cartilage SNR (41.0 + 5.2 vs. 36.2 + 2.4; p < .01) and SNR efficiency than FS-SPGR (41.0 + 5.2 vs. 33.3 + 2.2; p < .01). All images had excellent depiction of cartilage (Shown below) The IDEAL-GRE images produced water, fat, and combined images. The multi-echo IDEAL-GRE sequence produced these images in a faster scan than FS-SPGR, and had bright signal from synovial fluid that is helpful to outline cartilage defects.

Discussion: Multi-echo IDEAL-GRE provides a faster, more SNR efficient method than FS-SPGR for examining articular cartilage at 1.5T. Multi-echo IDEAL-GRE is highly SNR efficient because it uses a large percentage of the TR for readout, and also achieves an effective signal averaging of three in one TR by using all three echoes efficiently in the water-fat decomposition.

REFERENCES/FUNDING SOURCE
G.E. Gold, S.B. Reeder, H. Yu, J. H. Brittain, B.A. Hargreaves. Multi-Echo IDEAL Water-Fat Separation for Rapid Imaging of Cartilage. Fourteenth Scientific Meeting, ISMRM May 2006, p. 632.

Bilateral Slab Modulation for Faster Breast MRI

BRIAN A. HARGREAVES[1], CHARLES H. CUNNINGHAM, AND BRUCE L. DANIEL[1], - [1]RADIOLOGY AND [2]ELECTRICAL ENGINEERING, STANFORD UNIVERSITY

Introduction: Dynamic contrast-enhanced (DCE) breast MRI is a routine clinical procedure that has very high sensitivity for detection and characterization of breast tumors [1]. Clinical outcomes are likely to improve with increased frame rates as well as higher spatial resolution. Bilateral imaging (of both breasts) normally requires more than twice the scan time, as the bilateral volume includes both breasts and the space between them. We have developed a simple, yet important method of eliminating the need to encode the volume between breasts, while maintaining the high SNR achieved from encoding the bilateral volumes simultaneously. This typically results in a 20-30% reduction in scan time, and equivalent increase in frame rates.

Methods and Results: Bilateral volumes are excited in a time-interleaved fashion, using a dual-band spectral spatial pulse which allows independent shimming of two volumes [2]. The pulse also allows independent phase modulation of volumes. When the phase is linearly modulated with phase-encode number in the left/right direction, the slab will appear shifted after 3D imaging, an extension of phase-offset multi-planar imaging [3]. By choosing the linear modulation ap-
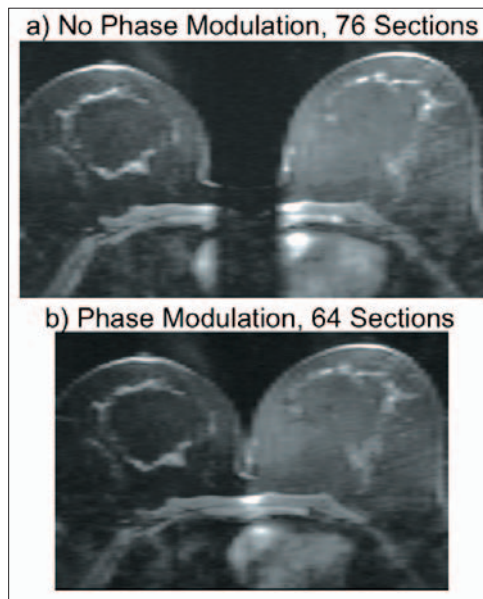
By phase-modulating the excitation, the imaged slabs are "virtually shifted" together so that the number of phase-encoding steps can be reduced

propriately for each slab, the two slabs are shifted together, and the field-of-view in the slab direction is reduced to include only the slab volumes. During reconstruction, slices can be labeled with the correct location, since the shift is known, or blank slices could be inserted between the slabs. The images below show the axial cuts through a 3D volume that was phase-encoded in the right/left direction (a) without slab modulation and (b) with slab modulation, and a reduced FOV and scan time.

Discussion: Phase-modulated slab-shifting is a simple, yet useful technique for many applications where multiple volumes are imaged simultaneously. It is compatible with different excitation schemes such as spin echo, gradient echo, spoiled gradient echo and steady state free precession, as well as acceleration schemes such as partial Fourier imaging and parallel imaging. We are already combining several of these techniques to further increase the frame rate of DCE breast imaging.

Time Constant Sensitivity of Eddy Current Characterizing Pulse Sequence

DANIEL B. ENNIS, MARCUS T. ALLEY, BRIAN A. HARGREAVES, NORBERT J. PELC - DEPARTMENT OF RADIOLOGY

Introduction: Eddy current compensation is important for a number of applications in magnetic resonance imaging. Eddy current induced fields impart phase on the acquired signal that can distort both magnitude images and phase estimates used to measure tissue velocities, displacements, and temperatures. Eddy current pre-emphasis provides first-order correction, but more sophisticated techniques are needed to account for a broad range of short and long time constants and spatial non-linearities. A pulse sequence was designed to measure the system's eddy current response and use this to correct the eddy current induced artifacts for an arbitrary pulse sequence using an impulse-response formalism. Herein, this pulse sequence was modeled with Bloch simulation to characterize the sensitivity and bandwidth of measured time constants (τ).

Methods: Pulse Sequence: A spin-echo pulse sequence was modified to support: 1) eddy current inducing test gradients, 2) a long τ eddy current nulling gradient, and 3) 3-D phase encoding. In order to measure phase shifts that arise from short τ eddy currents the pulse sequence was designed to acquire data (DAQ) for 62ms immediately after a gradient slew. Simulation: Simulated eddy current induced mono-exponential gradients were generated with 0.01ms<τ<200ms and peak eddy current

gradient strengths of 0.1Gmax/τ. Bloch simulation was used to simulate the signal response (time step=8μs, T1=250ms, T2=25ms) over a broad range of τ.

Results: The pulse sequence with the dummy gradients doesn't stimulate and is therefore insensitive to long τ eddy current effects, but is sensitive (phase accumulation >π) to 25μs<τ<25ms. The simulation also demonstrates that without the dummy gradients long time constant (τ>25ms) eddy currents generate measurable phase accumulation during the 100ms.

Conclusions: The Bloch simulation demonstrates that the pulse sequence is maximally sensitive to short τ of ~5ms, but with good sensitivity to 25μs<τ<25ms. The fact that DAQ begins immediately after a gradient slew, combined with the high SNR of the sequence and the fact that short τ effects are not sensitive to T2 decay combine to make measurement of short τ effects possible.

Flow-Independent Angiography at 3T using Phase Cycled Balanced SSFP and IDEAL

B.A. Hargreaves[1], S.B. Reeder[2], H. Yu[2], A. Shimakawa[2], J.H. Brittain[2]. - [1]Radiology, Stanford University, [2]Global Applied Science Laboratory, GE Healthcare.

Introduction: Balanced steady-state free-precession (SSFP) imaging provides excellent contrast and signal characteristics for angiography at higher field strengths (3.0T or greater), but suffers from sensitivity to off-resonance effects as well as bright fat signal. In this work, we have combined phase-cycled SSFP with IDEAL fat/water separation to overcome these difficulties. The resulting technique allows high-resolution flow-independent angiography at 3.0T with excellent contrast between arteries and veins, and is demonstrated in healthy volunteers.

Methods: A total of six images are acquired at three different echo times, both with and without alternating the SSFP excitation. For each echo time, the two images with different excitation schemes are simply combined by complex addition. Resulting images are processed using the iterative decomposition of water and fat using echo asymmetry and least squares estimation (IDEAL) algorithm. Finally, the water images are viewed using a maximum-intensity projection for angiographic images. Images used a 384x144x140 matrix over a 32x12x12 cm3 FOV for a total scan time of 8 min.
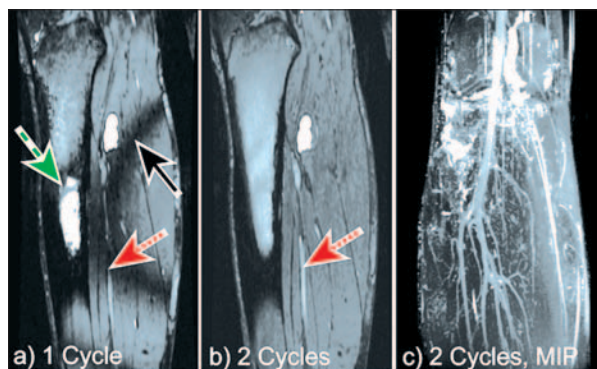
Single SSFP cycle (a) image showing dark bands (solid black arrow), fat/water swap (dashed green arrow) and vessel signal loss (dotted red arrow) compared with the dual-acquisition image (b). Coronal MIP (c) in another subject shows excellent arterial-venous vessel contrast.

Results: The images below show the water image after IDEAL separation from (a) a single RF phase and (b) the sum of signals from two RF phase cycles. The sum of phase-cycled images removes the dark signal band, and also results in correct fat/water separation. The residual bright spot in (b) is a cyst. Finally, (c) shows a coronal maximum-intensity projection in another subject, with excellent depiction of the arterial structure and suppression of veins.

Discussion: Balanced SSFP is challenging at 3.0T, due to high sensitivity to off-resonance effects. However, excellent arterial-venous separation of balanced SSFP at 3.0T with extended repetition time has been shown previously [8,9]. Further work will optimize the flip angle and slab profile to compensate for B1 variation to achieve more uniform contrast in images, and use dual leg coils as they become available.

REFERENCES/FUNDING SOURCE
B.A. Hargreaves, S.B. Reeder, H. Yu, A. Shimakawa, J.H. Brittain. Flow Independent Angiography at 3.0T with Dual-Acquisition Balanced SSFP and Multi-Echo IDEAL. Fourteenth Scientific Meeting, ISMRM May 2006, p. 1940. This work was funded by NIH 2P41-RR009784 and NIH 1R01HL075803

IDEAL Gradient-Echo Imaging for Articular Cartilage at 1.5T

Misung Han[1,2], Ann Shimakawa[3], Huanzhou Yu[3], Scott B. Reeder[4], Jean H. Brittain[3], Garry E. Gold[1], Brian A. Hargreaves[1] - [1]Department of Radiology, [2]Department of Electrical Engineering, [3]GE Healthcare, [4]University of Wisconsin, Madison

MRI is the most accurate method of cartilage assessment including diagnosing cartilage lesions and measuring articular cartilage thickness and volume. 3D fat-suppressed spoiled gradient echo (FS-SPGR) has been one of the most common clinical methods to image cartilage. Recently, Gradient Echo (GRE) imaging combined with IDEAL (Iterative Decomposition of water and fat with Echo Asymmetry and Least-squares estimation) has been proposed to enhance cartilage to fluid contrast. We optimized the flip angle of IDEAL GRE in terms of SNR and CNR and compared this sequence with FS-SPGR.

Using a GE 1.5T scanner, and an 8 channel phased-array knee coil, we scanned 6 knees from 6 healthy volunteers. 3D Ideal 3D IDEAL GRE used TR = 12.9 ms, three TE values of 4.4, 6.0, and 7.5 ms, varying flip angles from 5º to 60º, total scan time of 5:56 min (per scan). FS-SPGR used with TR/TE = 36/5 ms, 30º flip angle, total scan time of 5:35 min. All scans were acquired using 256 x 256 x 32 matrix, 16cm FOV, 3 mm slice thickness, and acquisition bandwidth of ±20.83KHz. SNR efficiency was the metric used to optimize the flip angle and compare sequences.

Figure shows mean measured SNR efficiencies for cartilage and joint
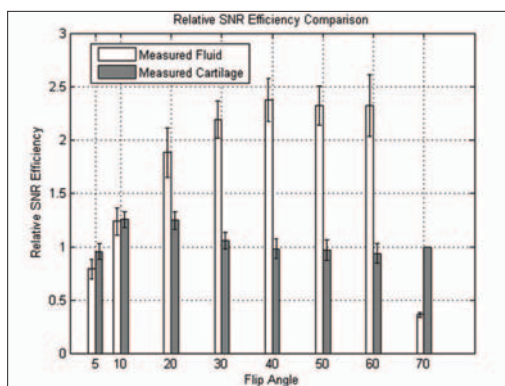
Mean values of measured relative SNR efficiency for cartilage and synovial fluid with different flip angles in IDEAL-GRE. Data from FS-SPGR are shown in the right for comparison.

fluid in IDEAL GRE with 7 different flip angles and FS-SPGR. All values shown were normalized by cartilage SNR efficiency on FS-SPGR, for the corresponding knee. Error bars represented ±1 standard deviation. The flip angle which gave the highest cartilage SNR was 10-20 º, but CNR efficiency between the cartilage and fluid increased further as the flip angles increased. With the flip angle of 30 º, IDEAL GRE gave significantly higher CNR efficiency than FS-SPGR (p < 0.002) with a slightly higher cartilage SNR efficiency (p = 0.24).

High fluid signal is useful for depicting surface irregularities, cartilage fissures, meniscal tears or subchondral edema. With high fluid signal and good cartilage SNR, IDEAL GRE is a highly promising technique for robust 3D imaging of articular cartilage. In future work, we will compare measurements of cartilage volumes and thickness with segmentation.
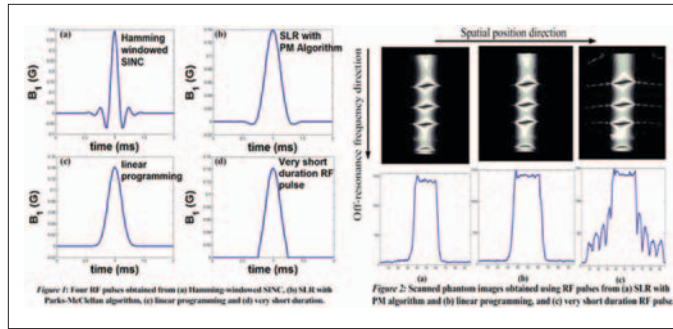
REFERENCES/FUNDING SOURCE
Scott B. Reeder, Angel R. Pineda, Zhifei Wen, Ann Shimakawa, Huanzhou Yu, Jean H. Brittain, Garry E. Gold, Christopher H. Beaulieu, Norbert J. Pelc, Iterative decomposition of water and fat with echo asymmetry and least-squares estimation (IDEAL): Application with fast spin-echo imaging 2005, 54 (3):636-644

Analysis and Suppression of Off-slice Excitation in SSFP Imaging

WENMIAO LU, BRIAN HARGREAVES - DEPARTMENT OF RADIOLOGY

Balanced steady-state free precession (SSFP) is a fast imaging sequence offering good tissue contrast and high signal-to-noise efficiency [1]. Little attention has been paid to one type of artifact often encountered in SSFP imaging – undesired steady-state excitation outside the selected slice. In practice such undesired excitation often leads to spurious imaging of objects outside the selected slice or through-slice aliasing. The goal of this project is to suppress off-slice excitation in SSFP imaging via designing RF pulses.

Figure 1: Four RF pulses obtained from (a) Hamming-windowed SINC, (b) SLR with Parks-McClellan algorithm, (c) linear programming and (d) very short duration.

Figure 2: Scanned phantom images obtained using RF pulses from (a) SLR with PM algorithm and (b) linear programming, and (c) very short duration RF pulse.

In this work we have presented RF pulses for balanced SSFP imaging, which are designed with high stop-band suppression in order to avoid off-slice excitations.

To suppress off-slice excitation, it is desirable to have a RF pulse which only excites the spins inside the selected slice. Therefore we want a RF pulse with very small stopband ripple compared with standard excitation pulses. In comparison with the Hamming-windowed SINC function shown in Figure 1(a), two other RF pulses were generated by using 1) Shinnar-Le Roux (SLR) design with PM algorithm [2] and 2) magnitude filter design with linear programming, respectively. Given the constraints on maximum allowable passband ripple δ_1, passband frequency, stopband frequency, and the filter order nf, the linear programming is able to produce the FIR filter with minimum possible stopband ripple. The RF pulses obtained from these two approaches are shown in Figure 1(b) and (c), respectively.

Using the RF pulses shown in Figure 1(b,c,d) and TR=2TE=7ms at 1.5T, and a 60º flip angle, 3D SSFP images acquired from a phantom over a 24x24x12 cm3 FOV are shown in Figure 2. The off-resonance frequencies were emulated using a local gradient shim of approximately 25 Hz/cm. Below each phantom image is shown the maximum intensity projection along off-resonance frequency direction. It can be seen that the RF pulses shown in Figure 2(b) and (c) significantly suppress the off-slice excitation.
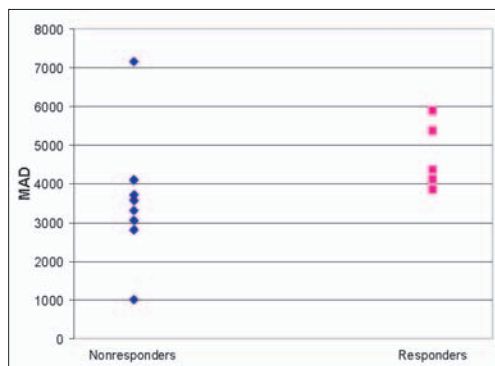
Predicting Treatment Response in Breast Cancer with Dynamic Contrast Enhanced MRI

ANTHONY FARANESH, BRIAN HARGREAVES, BRUCE DANIEL, DEPARTMENT OF RADIOLOGY

Introduction: Structure-function relationships are essential to understanding biological performance. The complex, but highly ordered arrangement of myofibers in the ventricular wall is closely related to regional myocardial function. This work tests the hypothesis that midwall myofibers are not oriented in the circumferential direction in all regions of the left ventricle and furthermore that regional gradients in myofiber orientation are heterogeneous. Regional differences of myofiber arrangement should impact regional function in addition to having implications for the interpretation of MRI tissue tagging strains.

The range in Ktrans values, calculated as MAD, is significantly lower in Noresponders than in Reponders, indicating that this parameter may help identify patients who will respond to therapy.

Methods: Mid-ventricular slices of five ex vivo ovine hearts were imaged on a 1.5T GE Signa Excite scanner using a custom diffusion tensor weighted interleaved echo-planar imaging sequence. Regional myofiber orientations were measured using a local cardiac coordinate system. Local myofiber direction was defined as the angle (θ) between the primary eigenvector of the diffusion tensor and the local circumferential direction. Papillary muscles were manually masked. The left ventricular midwall was defined as 50% radial wall depth between the epicardium and endocardium. Finally, a circumferential fiber contour was defined from a b-spline fit to all locations where $-5° < \theta < 5°$.

Results: Contours of the circumferential fibers ($\theta=0°$) indicates that in the lateral wall there is a preponderance of negatively oriented ($\theta<0°$) epicardial fibers. In the lateral midwall (50% depth), fibers are oriented at an angle of $\theta=-14°\pm8°$. In comparison, septal midwall fibers average $10°\pm12°$. The circumferential fibers are not located at the midwall, but, instead, at $43\pm9\%$ wall depth in the septum and $67\pm11\%$ wall depth in the lateral wall.

Conclusions: Midwall myofibers are not always oriented in the circumferential direction. When analyzing ventricular function using MRI tissue tagging or displacement imaging it is often assumed that midwall myofibers are oriented in the circumferential direction. Recent MRI tissue tagging results demonstrate a correlation between greater pre-stretch of the antero-lateral and infero-lateral wall and greater circumferential shortening[3]. This latter result implicates a hemodynamic driving force for variations in regional function. The results, herein, suggest that regional variations in myofiber arrangement may also play a role.

Dynamic BOLD Contrast in the Breast using Heart Saturation

Rebecca Rakow-Penner, Laura Pisani, Bruce L. Daniel, Gary H. Glover - Department of Radiology

Introduction: BOLD contrast applied to breast imaging has great potential to provide additional diagnostic information as a supplement to that collected with DCE-MRI. Recent studies (Gilad, Int. J. Cancer, 2005) indicate that while conventional DCE-MRI provides data on the permeability of a tumor, BOLD contrast reports on the tumor's vascular maturity. Thus, BOLD contrast can differentiate the healthy vessels that respond to a vasoreactive stimulus and those tumor vessels that do not. The method presented significantly improves BOLD contrast by using a new pulse sequence that selectively saturates the MRI signal of the heart and induces contrast by having the volunteer breathe pure oxygen in a time jittered approach.

Figure 1. The left image is the BOLD contrast image without heart saturation. The right image is the BOLD contrast with heart saturation..

Methods: The designed pulse sequence selectively saturates a cylinder encompassing the heart while exciting breast glandular tissue. The BOLD contrast stimulus used for this study consisted of three one-minute blocks of pure oxygen interleaved with room air for a total of seven minutes. This GRE-2D spiral sequence, was tested on the left breasts of two healthy volunteers at 1.5T with the jittered stimulus.

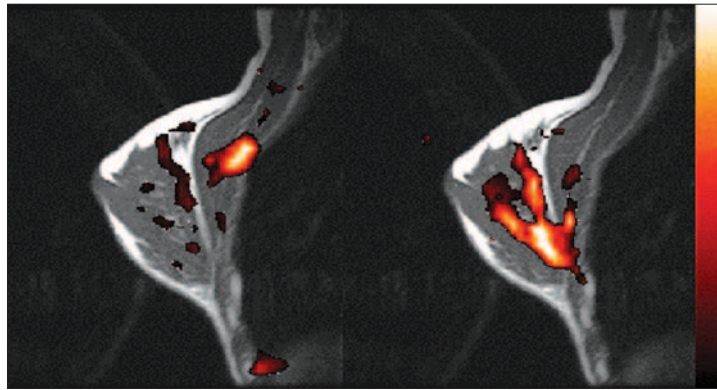Results: Saturating the signal from the heart significantly improved the measured BOLD contrast. In the figure, the left image is the BOLD signal when the heart was not saturated and the right image is the BOLD signal with heart saturation. The red mapping indicates that the jittered oxygen stimulus correlated with an increase in deoxyhemoglobin in healthy breast vasculature.

Conclusion: The method presented in this abstract allows for greater exploration of BOLD contrast in breast tissue. Saturation of signal from the heart reduces motion artifacts, enabling robust BOLD imaging. Breathing of pure oxygen is also advantageous because it does not involve stimulus-correlated motion. With an effective imaging method now in place, future studies will focus on measuring BOLD contrast in tumors.

MRI Relaxation Parameter Mapping of Human Placentas Post-Partum

Chardonnay J Vance[1,2,3], Bruce N. Ames[1,2], Richard A. Barth[3], Gary H. Glover[3] - [1]University of California at Berkeley, [2]Children's Hospital Oakland Research Institute, [3]Department of Radiology at Stanford

Although pre-eclampsia (PE) was first described more than 2000 years ago, both the cause of and a cure for this complicated and life threatening disease evade researchers and medical caregivers to this day. In the U.S., PE occurs in roughly 10% of pregnancies and is responsible for at least 20% of maternal deaths and 15% of premature births in the U.S. Several lines of evidence point towards poor placental implantation and subsequent malformation and dysfunction as a root cause of this disease. Since MR imaging is a sensitive modality with which we can study the in vivo placenta with minimal risk to the fetus, and since very little is known about the magnetic properties of the human placenta at 1.5 Tesla, our goal is to gain some knowledge of the magnetic properties of the placenta in order to improve clinical prediction and basic scientific knowledge of the human placenta and development of PE. This study of the relaxation parameters of the post partum human placenta was undertaken on seven different singleton pregnancies Placentas were collected and their T1 and T2 relaxation times calculated: two from healthy pregnancies, three from pregnancies exhibiting mild PE, and two from pregnancies exhibiting severe PE. There were no differences in the T2 times which could be linked to the pathology of PE. In contrast, average T1 times were more than two-fold higher in placentas from two severe PE pregnancies versus two normal pregnancies (averaging 1693 ms vs. 764 ms, respectively). Including the mild cases of PE, T1s do appear to correlate with the severity of PE in this small and unmatched data set. Current work includes development of a fast (< 2min) T1 mapping protocol in order to perform these measurements in the pregnant patient in vivo, and includes recruitment of a matched patient population.

High Temporal Resolution Bilateral Dynamic Contrast Enhanced Breast Imaging with TSENSE

[1,2]Misung Han, [1]Brian A. Hargreaves, [1]Bruce L. Daniel
[1]Departments of Radiology and [2]Electrical Engineering

Dynamic contrast enhanced (DCE) MRI breast imaging has shown great promise in discriminating benign and malignant breast lesions [1]. It requires fat suppression and high spatial and temporal resolution for the accurate measurement of dynamic enhancement [2]. 3D spiral combined with bilateral dual-band water-selective spectral-spatial excitation has been proposed to suppress fat robustly while obtaining high spatiotemporal resolution [3]. A further increase of temporal resolution can be achieved with parallel imaging. The TSENSE method, which incorporates the temporal filtering with spatial encoding can reduce aliasing artifacts and provide wide temporal bandwidth [4]. Here, we combined dual-band bilateral acquisition [3] with TSENSE, using acceleration in the slice-encoding direction.

Imaging was conducted with a GE 1.5T scanner, and an 8 channel phased-array breast coil. Spiral trajectories with 8 interleaves and 64 stack locations, 20 x 20 x 10 cm3 FOV over each breast, and 1.2 x 1.2 x 3 mm3 resolution, TR = 25.2 ms were used. With the acceleration factor of 2, we acquired k-space slice encoded lines in a time-interleaved fashion. With the scan time of 6.5 s for one frame, 32 temporal frames were acquired over 3.5 min.
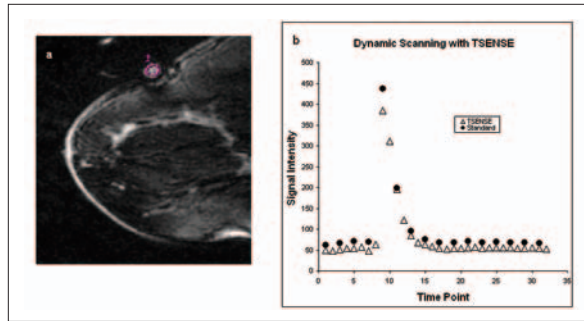

Fig.1.a) Sagittal image reconstructed with TSENSE, showing ROI used for measuring signal intensities. b) Contrast-enhancement in a tube external to the breast of a normal volunteer. When GD-DTPA is infused rapidly into the tube, signal rapidly rises, and then washes out as a slow saline infusion continues. Intensities with non-accelerated acquisition and reconstructed by TSENSE with the factor of 2 were shown.

A normal volunteer with a tube external to the breast was scanned. Gd-DTPA was injected after the 8th frame. TSENSE reconstruction was done off-line. Coil sensitivity maps were calculated from the first 7 frames to reduce the sensitivity to the rapid signal changes in the tube. Fig 1b) shows the signal intensities at each frame in the ROI drawn in Fig 1a). Signal intensities with non-accelerated imaging were also shown for the comparison. Fig.1b) demonstrates that accelerated imaging incorporating TSENSE increases temporal resolution. With shorter scan time for each frame, TSENSE also reduced the imaging artifacts resulting from rapid contrast enhancement.

Using TSENSE can increase temporal resolution in dynamic contrast enhancement imaging. For the future work, we will increase the acceleration factors and determine the highest acceleration factor that results in acceptable image quality. We will further increase imaging speed by incorporating a partial Fourier with TSENSE [5].

Capacitive Micromachined Ultrasonic Transducers for MR-guided Ultrasound Ablation of Tumors

Serena H. Wong[1], A. Sanli Ergun[1], Goksen G. Yaralioglu[1], Omer Oralkan[1], Mario Kupnik[1], R. Kim Butts[2], and B.T. Khuri-Yakub[1], [1]Departments of Electrical Engineering and [2]Radiology

We present the development of a capacitive micromachined ultrasonic transducer (CMUT) array for noninvasive focused ultrasound ablation under MR-guidance. This system would improve treatment of abdominal cancers, like metastatic colorectal cancer. Resection of these cancers increases 5-year survival from 8% to 30-35%, but only 20% of patients are suitable for resection. For 80% of patients, noninvasive treatment is needed.

We have demonstrated that current imaging CMUTs can used in high power and continuous wave mode necessary for focused ultrasound ablation. From these successful results, we have designed and developed a new generation of CMUTs specifically for ultrasound ablation. Piston CMUTs are ideal for high pressure, CW output. Using two SOI bondings, a thick silicon mass is created at the membrane center to independently control the membrane mass and elasticity. Using an axisymmetric model in ANSYS, we optimized the output pressure and frequency responses to 1Mpa and 2MHz, ideal for noninvasive surgeries. The best design has a thin 1 micron membrane with 4.5 micron thick piston. When piston widths are 75-80% of the total membrane width and the gap is 0.3 microns, the collapse voltage is optimum (100-150V) for the desired 1MPa output pressure.

These membranes are patterned into a 4 cm diameter, 16-element, annular array. Using Matlab, the power gain was calculated to be 36 at 4 cm in liver. Using the Pennes Bioheat Equation and the Cumulative Equivalent Minutes at 43 degrees, the lesion size was calculated to be 0.5 cm in diameter in the focal plane at 30 seconds. Such a lesion size and design is optimum for ablation and detection under the resolution of our current MRI temperature maps. We are currently fabricating and testing these newly optimized devices.

Optimization and Validation of MR-VCUG using the XMR System

Schreyas Vasanawala[1], Arun Ganguly[1], Bruce Daniel[1], Viola Rieke[1], Kim Butts-Pauly[1], Richard A. Barth[2], Rebecca Fahrig[1], William Kennedy[3] - Departments of [1]Radiology, [2]Pediatric Radiology and [3]Urology

This past year we have made further progress developing an MRI procedure for diagnosing and monitoring vesicoureteral reflux (VUR) with the aim of significantly reducing the radiation burden imposed on pediatric patients.

Currently a x-ray voiding cystourethrogram (VCUG) is the standard of care for the diagnosis of vesicoureteral reflux. Although highly accurate for characterizing and grading reflux, there is a considerable radiation exposure from this procedure. A standard examination includes a preliminary abdominal AP radiograph and intermittent fluoroscopy which allows detection and the characterization of the reflux based on the appearance of the calyces, pelvis, ureter and ureterovesical junction. Frequently, patients will undergo yearly x-ray VCUGs to evaluate the status of their vesicoureteral reflux, as they await spontaneous resolution.

We have developed a novel MRI-compatible x-ray fluoroscopy system, described in detail in previous reports. With this system, we are uniquely able to develop an MRI voiding cystourethrogram protocol and validate this protocol against the gold standard x-ray voiding cystourethrography during a single catheterization. Thus far, we have refined the MRI compatible x-ray fluoroscopy system for this application and we have established feasibility of obtaining MR
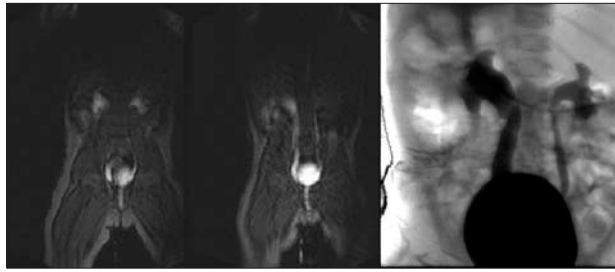
Two MR images (left) reveal dilated renal calyces, renal pelvis, and ureters bilaterally, confirmed by a concomitant x-ray image (right).

images covering the bladder, ureters, and kidneys with an MR imaging speed of 1 img/3.5 seconds, and ascertained optimal gadolinium concentrations for maximal image contrast. We have completed combined x-ray/MRI examinations on 8 patients (see figure), with two more scheduled for the near future. Grading VUR on a 4 point scale with both methods, we have thus far found an encouraging 88% agreement (95% confidence interval of 79 – 96%) between the two methods.

Currently to the best of our knowledge there is not an active national or international effort directed at the development of MR voiding cystography to aid in the detection and management of vesicoureteral reflux. We are encouraged by our initial results and are excited to continue development and validation of a non-radiation diagnostic procedure to detect VUR that could potentially have a tremendous positive effect on the healthcare of children in the local community and worldwide.
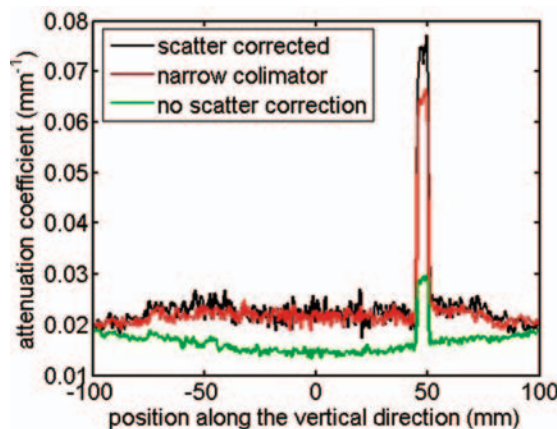
Scatter Correction for X-ray Imaging Using Primary Modulation: A Phantom Study for CBCT

Lei Zhu[1,2], N. Robert Bennett[2], Rebecca Fahrig[2], Departments of [1]Electrical Engineering and [2]Radiology

An x-ray system with a large area detector, such as cone-beam CT (CBCT), is much less immune to scatter than fan-beam CT, and the high scatter-to-primary ratios (SPR's) result in cupping/shading distortions in reconstructed CT images. Recently, we have developed a scatter correction algorithm that provides accurate scatter correction without additional patient exposure. A calibration sheet (primary modulator) with a checkerboard pattern of attenuating materials is inserted between the x-ray source and the object, so that the primary distribution of the projection image is partially modulated by a high-frequency function in the spatial domain. With the assumption that the scatter

1D profile comparison of the axial views of the reconstructed Catphan600 phantom.

is very insensitive to the x-ray source intensity spatial variation, low-frequency behavior still dominates in the scatter distribution. Filtering and demodulation techniques then suffice to extract the low-frequency components of the primary and hence obtain the scatter estimation and correction. The algorithm has been evaluated by Monte Carlo (MC) simulations. In this work, a physical primary modulator with the pattern suggested in the previous study is built using aluminum, and experiments are carried out on our bench-top CBCT system with the insertion of the modulator. A standard evaluation phantom, Catphan 600 is used

in our study. Scatter correction results using the primary modulator are compared with those without scatter correction and with scatter inherently suppressed using the slot-scan geometry. The comparisons show that the primary modulation approach reduces the relative error of the reconstructed image around the central region of interest from 31.80% to 2.30%. The reconstructions of the resolution test objects also reveal that this algorithm has no noticeable impact on the resolution of the reconstructed image, although a filtering-based technique is used. Future work includes the modulation transfer function (MTF) measurement, and a further evaluation of the algorithm performance using a primary modulator with a finer grid pattern.

# Three-dimensional Adaptive Filtering of Projection Data for Noise Reduction in Low-dose C-arm CT

Lars Wigström, Rebecca Fahrig - Department of Radiology

Recent developments of C-arm CT have enabled the acquisition of three-dimensional (3D) data in the interventional suite. With the acquisition of an increasing number of projections it is essential to minimize the radiation dose used. Adaptive anisotropic filtering has the ability to reduce the noise level in low-dose data without introducing noticeable blurring. By applying the filtering prior to 3D reconstruction, noise induced streak artifacts can also be reduced more efficiently compared to processing in the image domain.

Methods: Anisotropic filtering was used to filter the obtained stack of projection images. The orientation of structures within this 3D space (2D projections + angle) was estimated using a set of differently oriented filters. The obtained tensor representation of the local orientation was utilized to control the anisotropic filtering of the data in order to apply low-pass filtering along structures while maintaining all frequency components perpendicular to these.

For evaluation, a low-dose dataset was obtained using the Catphan® 600 phantom. An AXIOM Artis dTA system (Siemens
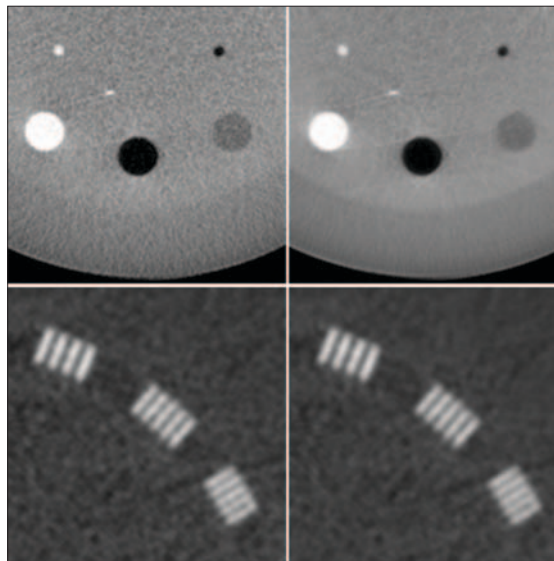
Original (left) and result after adaptive filtering (right) showing a reduction in noise level (upper) with essentially maintained spatial resolution (lower)

Medical Solutions) was used to acquire 235 projections during a 5 second sweep. The dose at the detector was 0.17 μGy/pulse. The original and filtered projection data were reconstructed using a Feldkamp reconstruction algorithm.

The noise level was measured as the standard deviation within homogenous regions in the phantom, and spatial resolution was assessed based on visual inspection of the test pattern in the high resolution module of the same phantom.

Results: Using the adaptive anisotropic filtering algorithm, the standard deviation in homogenous regions was reduced by more than 50%. Virtually no degradation of high contrast spatial resolution was seen (the resolution both before and after adaptive filtering was 8±1 line pairs per cm).

Conclusion: Adaptive anisotropic filtering has the potential to substantially reduce the radiation dose required for obtaining 3D image data using C-arm CT.

Temporal Interpolation in Retrospectively Gated Cardiac C-arm CT Reconstruction

Lars Wigström[1], Günter Lauritsch[2], Jan Boese[2], Herbert Kemeth[2], Rebecca Fahrig[1] - [1]Department of Radiology, Stanford University, Stanford, CA, [2]Siemens AG, Medical Solutions, Forchheim, Germany

We have extended the capability of C-arm CT to cardiac imaging by applying the concept of ECG gating during the acquisition of multiple rotational acquisitions. For each projection angle, the obtained raw data consists of a set of images acquired at different cardiac phases. In order to retrospectively reconstruct a 3D image volume at a specific cardiac phase, projection data corresponding to that phase has to be assembled. In this study we have compared the results from only selecting the input frames acquired closest in time to the desired cardiac phase (nearest neighbor) and interpolation in the temporal dimension using a Gaussian kernel.

Methods: Temporal interpolation of projection data was implemented using nearest neighbor or Gaussian interpolation. An in-vitro experiment was performed using a phantom with a tungsten bead moving along a trajectory similar to longitudinal cardiac motion. Projection data were acquired during four ECG synchronized sweeps with the C-arm. 165 projections were obtained during each 6 s sweep. Using the same acquisition protocol, image data were also acquired using an in-vivo porcine model.

Results: Point spread functions and modulation transfer functions
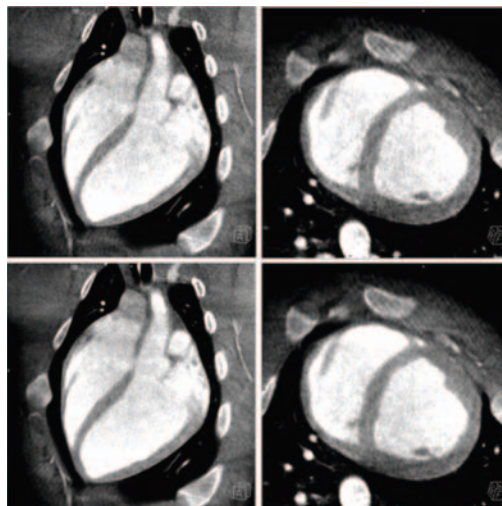
Comparison of cardiac C-arm CT data reconstructed using nearest neighbor (top) and Gaussian interpolation (bottom) in a long axis (left) and a short axis (right) view of the porcine heart.

(MFTs) calculated based on the in-vitro experiment showed only a minor drop in spatial frequency response with the Gaussian interpolation compared to nearest neighbor. A slight improvement the noise level was obtained using Gaussian interpolation. In the porcine model, Gaussian interpolation resulted in slightly reduced noise and streak artifacts, but at the expense of some blurring.

Conclusion: Interpolation in the temporal dimension can potentially improve the signal-to-noise ratio (SNR) in the resulting images, by incorporation data from multiple sweeps. However, when using a wide interpolation kernel, significant blurring can also be introduced. Consequently, the optimal interpolation will be dependent on the application and the available SNR.

In vivo 3D Stent Imaging with C-arm CT

ARUNDHUTI GANGULY[1], ALEX SCHNEIDER[2], N. ROBERT BENNETT[1], REBECCA FAHRIG[1] - [1]DEPARTMENTS OF RADIOLOGY AND [2]MECHANICAL ENGINEERING

We have developed an in vivo imaging method for 3D visualization of the superficial femoral artery (SFA) stents. These stents are used for treating atherosclerotic disease of the SFA. At 10 months after deployment, they can have as high as 37% fracture rate[1]. Fractured stents lead to increased restenosis and occlusions[2]. The exact causes for these breakages are not known. It is hypothesized that repetitive knee and hip flexions cause extensive bending, torsion and compression of the untethered SFA stent causing its fracture 2. Our imaging protocol investigated these deformations by determining the forces on the stent for different positions of the leg.

A prototype C-arm CT system (Siemens Axiom dTA, Siemens Medical Solutions AX, Forccheim, Germany) was used for imaging SFA stents in volunteers. Projection images over a 200° arc are back-projected following filtering and center-of-rotation correction to create the 3D volume image. This high resolution system (250 μm at iso-center) allows excellent imaging of high contrast objects such as stents. The imaging protocol involves: 1) placing the subject on a special table extension with the leg in a straight position (2) centering the stent in the filed of view (FOV) under flurosocopy by table adjustments (3) acquiring 494 projections during a rotation of 20s (4) repositioning the subject using a 45° and 30° wedges for hip and ankle support, respectively and as much knee flexion as allowed by the imaging geometry (5) re-centering the stent
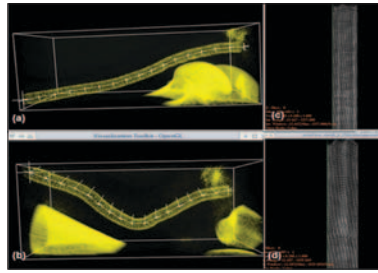

Figure 1 C-arm CT in vivo images of a stent in the a) 'straight' and b) 'bent' positions. The automatically determined centerline is shown, along with the bounding box. The corresponding 2D 'unwrapped' images are shown in c) 'straight' and d) 'bent', and the local shear resulting from the change in position can be seen.

(6) acquiring the projections. Images are acquired using automatic exposure control with a preset maximum dose. The reconstructed images are analyzed using software developed by our group that locates the stent centerline and fits ellipses perpendicular to it. This allows calculation of the changes in stent length and eccentricities of the ellipses. By unwrapping these stent images, the shear and hence the torsion is visualized.

The 10 subjects imaged (9 men and 1 woman, mean age 68±9 years) had 1, 2 or 3 overlapping stents in either left or right leg. Four of the data sets have been analyzed to date. Of these, 3 showed significant shortening and one showed lengthening of the stent from straight to bent position. The length change varied from 1.5mm to 11.5mm.

Future work will involve optimizing patient dose and image quality by selection of focal spot size and maximum exposure level. Quantification of torsional deformation using in vitro stents with known load, referenceless rigid body transformations between straight and bent leg images, vessel deformation calculations using calcification landmarks, and imaging during weight bearing will also be investigated.

Characterization of a Novel Anthropomorphic Plastinated Lung Phantom

SUNGWON YOON[1], ROBERT W. HENRY[3], DONNA M. BOULEY[3], REBECCA FAHRIG[2] - DEPARTMENTS OF [1]ELECTRICAL ENGINEERING, [2]RADIOLOGY, STANFORD UNIVERSITY, [3]UNIVERSITY OF TENNESSEE

We are interested in quantifying the anatomical and imaging characteristics of a novel anthropomorphic lung phantom constructed using plastination. In this work , we investigated whether a novel plastinated lung phantom retains the anatomical and imaging characteristics of an in-vivo lung.

For quantification, a pig's thorax was scanned in-vivo at known partial pressures on a clinical CT (Siemens Sensation 16, 120kVp, 100mAs, recon 0.54x0.54x0.75mm^3). The lungs were extracted, inflated, and fixed by intra-tracheal perfusion of 10% formalin while the pulmonary vessels were injected with Silastic E RTV silicone. The specimen was dehydrated (remove and replace tissue fluid with an organic solvent) in cold acetone and the lungs were impregnated with a curable silicone polymer via slowly decreasing pressure. Finally, the polymer was polymerized using a curing agent. The plastinated phantom was then scanned (120kVp, 200mAs, 0.43x0.43x0.75mm^3). Anatomical features, volume measurements, and CT values were compared using in-vivo and phantom clinical CT reconstructions.

The plastinated phantom is stable on the timescale of years and retains major anatomical features of the in-vivo lung. The phantom airway volume was 66% of the in-vivo measurement at inspiration but
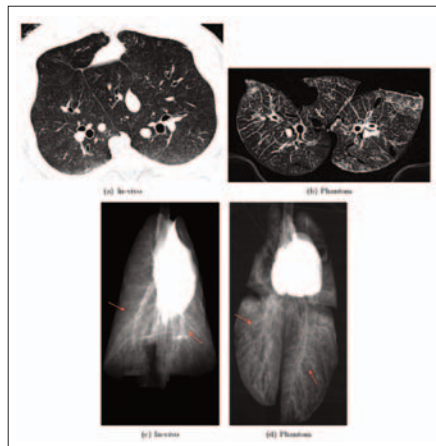
(a) Sample CT slice of a in-vivo lung. (b) Sample CT slice of the anthropomorphic phantom. (c) Simulated projection of the in-vivo acquired CT data. (d) Simulated projection of the anthropomorphic phantom CT data. The red arrows in (c) and (d) indicate pulmonary tissue regions where the anatomical complexity show resemblance such as the branching of vessels.

equal to the measurement at expiration. Vessel and lung volume comparisons were complicated by incompletely filled vessels and air pockets inside the phantom; nevertheless, lung volume measurements differed by less than 15%. Mean CT values of the cardiac tissue in the phantom (168 +/- 46) were 132 HU higher than in-vivo (36 +/- 87). Mean CT values of the pulmonary tissue were nearly equivalent for both datasets, attributed to an 11% decrease in the apparent tissue density due to over-inflation during plastination.

This work shows that the novel plastinated lung phantom retains the anatomical and imaging characteristics of an in-vivo lung. This accurate and complex lung phantom has many uses including imaging system comparisons, providing a known, stable reproducible complex background for visibility studies and will be used for our own studies in lung tomosynthesis optimization.

Level Set Reconstruction for Sparse Angularly Sampled Data

SUNGWON YOON[1], ANGEL R. PINEDA[2], REBECCA FAHRIG[2] - [1]ELECTRICAL ENGINEERING, [2]RADIOLOGY

Purpose: We are interested in the imaging of the chest area for lung nodule screening purposes. This task requires a fast, low-dose imaging system that provides improved detection compared with radiography, but lower dose and faster scanning than clinical CT. One such approach is to reconstruct iteratively from sparse angularly sampled projection data; another is to reconstruct iteratively from limited-angle projection data.

Materials and Methods: We propose a new reconstruction technique for sparse angularly sampled projections using the level set method. Sparse sampling not only provides faster acquisition but also delivers lower dose to the patients. By assuming a piece-wise constant function for the chest area where the anatomical features are relatively simple and may be modeled as consisting of a finite number of distinct materials, we incorporate this prior information into the iterative reconstruction technique. To minimize the functional that measures the inconsistency between the measured and estimated projections, we use the level set method.

Results: In this work, we applied the proposed technique using 2 level-set curves on 13 noise-free projection images of an analytical
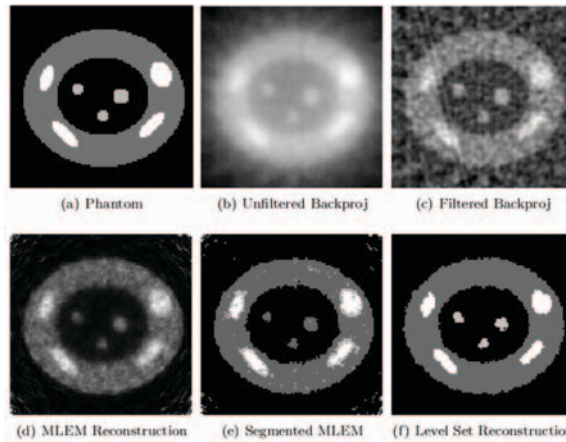
Reconstruction comparisons. (a) Original phantom used (b) Unfiltered backprojection (c) Filtered (Hann) backprojection (d) Maximum Likelihood Expectation Maximization reconstruction (e) Threshold segmentation of the MLEM reconstruction (f) Proposed level set reconstruction

piece-wise constant phantom and compared with MLEM and filtered back-projection reconstructions. We repeated the investigation with measurement noise and compared the reconstructions. We showed that the proposed technique results in better reconstructions (e.g. 2.00% mislabeled pixels compared to 13.47% for the segmented MLEM) for sparse angularly sampled noisy projections of a piece-wise constant object.

Conclusions: These encouraging preliminary results from reconstruction technique using strong prior information are the first step toward an investigation of more realistic situations where the prior assumption (piece-wise constant) does not strictly hold. We are currently developing more robust algorithm implementations for 2D and 3D data and also looking into other applications where only sparsely sampled projection data is available.

Truncation Artifact Correction in Cardiac C-Arm CT

JARED STARMAN[1], NORBERT STROBEL[2], NORBERT PELC[3], REBECCA FAHRIG[3] - [1]DEPARTMENT OF ELECTRICAL ENGINEERING, [2]SIEMENS MEDICAL SOLUTIONS, [3]DEPARTMENT OF RADIOLOGY

C-Arm CT systems suffer from artifacts due to truncated projections caused by a finite detector size. Theoretically exact reconstructions for certain specific truncation geometries have been investigated recently, but for small detectors (or large patients) it is quite easy to have a geometry that violates the minimum data needed to reconstruct a suitable, artifact-free field of view (FOV) for those algorithms. For instance, if every single projection is truncated in an acquisition, no theoretically exact reconstruction will work. Thus, only heuristic or approximate algorithms are suitable for very severely truncated acquisitions.

Preliminary investigations of the data truncation problem for the case of a 20cm detector centered on a heart, using real porcine data have been performed. Full width datasets were collected with a 40cm wide flat-panel detector, and the raw projection data was artificially truncated to 20cm. An algorithm proposed by Ohnesorge et al, referred to as symmetric mirroring, was modified to include 0th and 1st moment constraints in a similar manner as presented in [1]. An example reconstruction can be seen in Figure 1, where an average er-
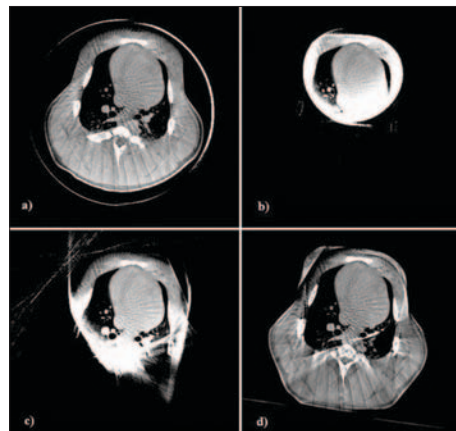
Central axial plane from volume reconstructions of a pig thorax from data taken with the C-Arm system. a) Reconstruction using the entire detector width (40 cm), b) reconstruction from projections truncated to a size equivalent to a 20 cm wide detector centered on the heart, c) reconstruction after applying a modified symmetric mirror algorithm to the truncated projections in b), and d) reconstruction from using a previous CT scan to extrapolate the simulated truncated projections. The image quality in d) is much better than b) or c), with an average gray level (GL) error of 10 GL when compared to the full reconstruction in a) for a region of interest centered on the heart.

ror in gray levels (GL) over the central 7.5cm is 93 GL. Another technique was investigated which makes use of existing CT reconstructions. After first performing the modified-symmetric mirroring technique, a 3D/3D registration between the truncated C-Arm volume and an a priori CT volume of the subject was performed. The registered CT data was forward projected to the C-Arm geometry to create digitally rendered radiographs (DRRs). The DRRs were used directly to extrapolate the truncated C-Arm projections, after appropriate scaling of the DRRs was performed. This technique gave by far the best results as seen in Figure 1, with an average error of 10 GL.

Future work will focus on improving the quality of the 3D/3D registration. For the case where a previous CT reconstruction is not available, future work will try to improve image quality through more accurate 0th and 1st moment estimates and other possible methods.
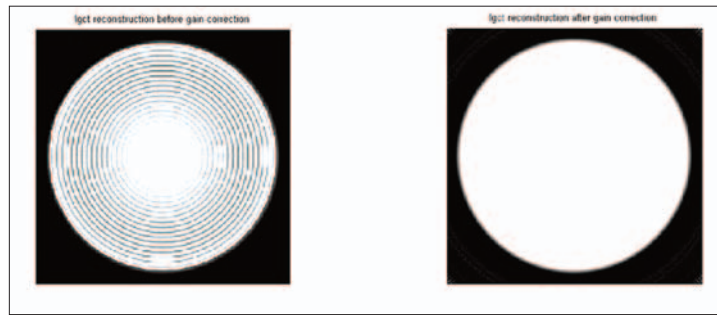
A 2D Reconstruction Algorithm for an Inverse Geometry CT System

Jongduk Baek, Norbert J. Pelc - Department of Radiology and Electrical Engineering

Introduction: This work investigates a 2D IGCT reconstruction method without gridding. Within this investigation, a new method is developed for correcting artifacts introduced by rho error.

Method and Materials: The IGCT system is composed of many equally spaced fan beam. The proposed reconstruction algorithm uses this similarity between IGCT system and fan beam system. In order to get high resolution, zeros are filled between each projection data, and reconstruction is performed from these zero-filled data set. Because of slight difference between IGCT system and fan beam system, ringing artifacts are introduced. A new method has been developed to remove these artifacts. This correction uses a pre-density weighting for IGCT system, and this pre-density weighting is calculated from matrix inversion between fan beam reconstruction image and IGCT reconstruction image. To verify the performance of the reconstruction algorithm, data was simulated using 4 detector IGCT system geometry.

Result: Simulations using the IGCT geometry show high frequency artifacts caused by rho error. These artifacts are corrected when the proposed pre-density weighting is used.

Conclusion: A 2D direct IGCT reconstruction is performed by using pre-density weighting. This method can be applied to normal IGCT geometry.

Evaluation of a Fast 3D Reconstruction Algorithm for an Inverse-geometry CT System

Samuel R. Mazin[1,2] and Norbert J. Pelc[1,2,3] - [1]Dept. of Electrical Engineering, [2]Deptartments of Radiology and [3]Bioengineering

Inverse-geometry CT (IGCT) is a new type of volumetric CT geometry. Volumetric coverage and high isotropic resolution demand a fast 3D reconstruction algorithm. IGCT employs a large array of focal spots opposite a detector array that shares the same axial extent as the source but is much smaller in the transverse direction. A single rotation is sufficient to acquire a 10 cm thick volume with isotropic resolution. Since IGCT projection data are truncated longitudinally, a standard 3D filtered backprojection algorithm requires a forward projection step after an initial reconstruction of un-truncated projections to complete the truncated projections. The method is slow due to this and the need to process so many projections. The purpose of this work is to evaluate a very fast algorithm based on Defrise's Fourier Rebinning (FORE) algorithm for PET. A 3D reconstruction algorithm was developed based on FORE. For comparison, a Feldkamp-like algorithm was developed that generates an average of Feldkamp reconstructions from each source row.
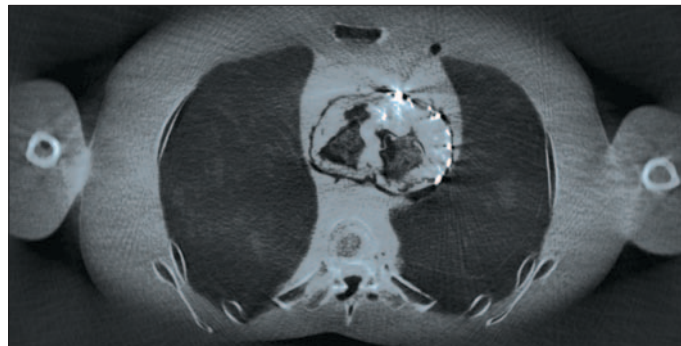
FORE reconstruction of the central slice of the anthropomorphic torso phantom.

Projection data for a numerical torso phantom and a numerical "Defrise" phantom were simulated under the IGCT geometry. To evaluate the FORE algorithm on a real data set, a prototype IGCT system was assembled involving a 100x100 scanned-anode source array and a 48x48 photon-counting detector array mounted on a C-arm system (NovaRay, Inc., Palo Alto, CA). An anthropomorphic phantom containing a real porcine heart was scanned in a step-and-shoot mode with the C-arm in a horizontal orientation. The FORE algorithm averaged 30 sec/slice while Feldkamp averaged 30 min/slice. Like Feldkamp, FORE suffers from cone-beam blurring in z, however it does not suffer from cone-beam streaking artifacts. FORE proved to be both fast and reasonably accurate.

REFERENCES/FUNDING SOURCE
S. R. Mazin, N. J. Pelc, "Evaluation of a Fast 3D Reconstruction Algorithm for an Inverse-Geometry CT System", submitted to IEEE NSS/MIC, 2006.
GE Healthcare, American Heart Association, Lucas Foundation

Motion Artifacts from an Inverse-geometry CT System with Multiple Detector Arrays

SAMUEL R. MAZIN[1,2] AND NORBERT J. PELC[1,2,3] - [1]DEPT. OF ELECTRICAL ENGINEERING, [2]DEPARTMENTS OF RADIOLOGY AND [3]BIOENGINEERING

Inverse-geometry CT (IGCT) is a promising new scanning geometry. Employing a scanned-anode x-ray source array the system is expected to provide sub-second volumetric imaging with isotropic resolution and no cone-beam effects. Three detector arrays spaced apart laterally can achieve a 50 cm in-plane field-of-view (FOV) with a 31 cm source. However, when three separate detector arrays are used, motion artifacts are expected to be different than in conventional CT and need to be assessed. The purpose of this work is to study motion artifacts across the in-plane FOV of an inverse-geometry CT (IGCT) system with multiple detector arrays. Due to the breakup of the FOV into regions that are sampled by different detector arrays, projection measurements that are adjacent in Radon space can be measured at very different points in time. This leads to concerns about the effects of motion and how the resulting artifacts compare at different points in the FOV. Simulations were performed for two objects representing slow and fast motion as well as periodic and non-periodic motion. The simulations were repeated at different points in the FOV to study motion effects in three regions: 1) the inner 15 cm region which is sampled
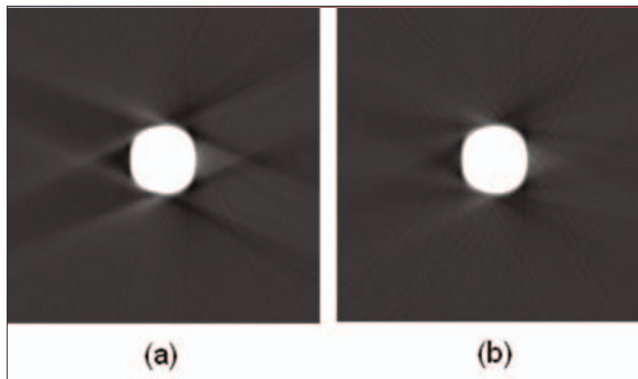
(a) Motion at 20 cm off center showing artifacts from the transition between detector arrays. (b) Same but with detector arrays spaced at 20 deg. instead of 23.6 deg. which increases the overlap region size and reduces the streaking artifact. Images are windowed to better see the motion artifacts.

only by the central detector array, 2) the transition between the inner and outer regions, and 3) the outer region which is sampled by all three detector arrays. 2D simulations assumed 125 "views" acquired in step-and-shoot mode over 360 degrees. A gridding algorithm was used to resample the data into parallel ray data which were then filtered and backprojected. Artifacts from the inner region are exactly like those that arise in a traditional CT system. The most significant artifacts caused by the multi-detector nature of the system are in the outer region, at the angles where the object sampling transitions between detector arrays. These streaking artifacts are comparable to motion artifacts in conventional CT and can be reduced by increasing the overlap region at the expense of FOV size and SNR uniformity.

Dose Efficiency Analysis for C-arm CT Imaging Systems

NORBERT STROBEL[1,2,] ROBERT DIXON[3], THOMAS PAYNE[4], RICHARD L. MORIN[5], ARUNDHUTI GANGULY[1], AND REBECCA FAHRIG[1], DEPARTMENTS OF RADIOLOGY, [1]STANFORD UNIVERSITY, [2]SIEMENS MEDICAL SOLUTIONS, [3]WAKE FOREST UNIVERSITY, [4]ABOTT NORTHWESTERN HOSPITAL, [5] MAYO CLINIC

We conducted an image quality analysis of a state-of-the-art C-arm CT imaging system (AXIOM Artis dTA, Siemens Medical Solutions, Forchheim, Germany). The Catphan 600 image quality phantom was imaged at various dose levels and tube voltages. To determine which tube voltage yields the best image quality for the dose applied, we first suggested a dose metric, then measured it, and finally conducted a perception study involving detectability profiles based on reconstructed C-arm CT slices. In our case, detectability graphs summarize how often a 0.5% nominal contrast object with a particular size was seen by an ensemble of human observers. For example, if the 10mm object contrast was seen in ten out of 13 observations, then a 77% visibility was assigned.

Since most C-arm x-ray devices, including ours, have a built-in automatic exposure control, it is difficult to specify the exact scan dose a priori. The system, however, does tell you the exact dose applied after a scan. For a meaningful comparison, detectability profiles associated with different operating points must, however, be normalized to a common reference dose. To facilitate such a comparison, we derived
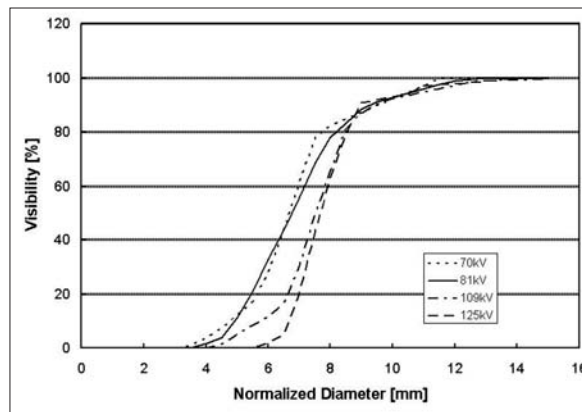
The normalized visibility charts at 70 kVp, 81 kVp, 109 kVp, and 125 kVp show that smaller objects can be better seen when data acquisition for C-arm CT is performed at lower tube voltages.

a mathematical relationship between the diameters of 'just visible' objects and their associated dose values based on Rose's threshold signal-to-noise ratio. Using this equation, we could then compare detectability profiles obtained for different dose settings.

Our perception study involving the Catphan 600 image quality phantom indicates that one can expect to see at least the 9 mm Catphan inset with 0.5% nominal contrast at the recommended head-scan dose (60 mGy) when using tube voltages ranging from 70kVp to 125kVp. When analyzing the impact of tube voltage on image quality at a fixed dose, our dose efficiency study revealed that lower tube voltages gave improved low contrast detectability for small-diameter objects.

Cardiac C-arm CT: Efficient Motion Correction for 4D-FBP

Marcus Pruemmer[1], Lars Wigstroem[2], Joachim Hornegger[1], Norbert Strobel[3] and Rebecca Fahrig[2] - [1]Institute of Pattern Recognition, FA University Erlangen-Nuremberg, Germany; [2]Department of Radiology, Stanford University, [3]Siemens AG, Medical Solutions, Stanford University.

Cardiac C-arm CT is a promising technique that enables 3D cardiac image acquisition and real-time fluoroscopy on the same system. The goal is to bring 3D imaging to the interventional suite for improved therapy planning, guiding, and monitoring. For the reconstruction of 3D cardiac image data, a complete set of projections from a specific heart phase is required. One approach to reduce motion blurring caused by the beating heart is to acquire multiple sweeps using the C-arm and retrospectively select the projections (RECG) that are closest to the desired cardiac phase [1]. In order to further improve the temporal resolution, novel image processing algorithms that utilize retrospective motion correction were investigated in this project. The main focus of this work is to extend the well established FDK algorithm to incorporate motion correction during the back-projection step using a pre-computed motion field. In our experiments we investigated the following two scenarios: (i) Can the image quality from a single sweep be improved given a known motion field? (ii) Can improved image quality be achieved using a lower number of sweeps in combination with motion correction?

Cardiac C-arm CT protocols are, among other things, constrained by the rotation speed and frame rate of the C-arm and detector, the breath hold duration, overall injected dose of contrast agent, scan synchronization with the ECG and X-ray dose. First empirical studies
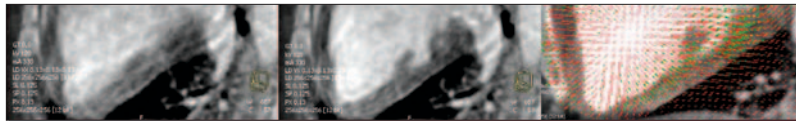

Fig. 1 (left) reconstruction from a single sweep (middle) reconstruction from a single sweep using deformation field (right) calculated from a multi-sweep reconstruction that provided 10 phases through the cardiac cycle.

show that protocols of four sweeps are reasonable for images acquired in diastoly, but temporal resolution can still be improved because of heart rate variations during the scan. We have shown that increased temporal resolution can be achieved using a first order motion estimation via 3D-3D non-rigid registration applied on a pure RECG reconstructed time series, that is blurred and has motion artifact, with correction applied in an extended FDK (FDK-4D) algorithm. For scenario (i) we showed that assuming a 4D motion field is given, the FDK-4D algorithm is able to decrease motion blurring significantly using only one single sweep for the reconstruction. For scenario (ii) we showed that even for an insufficient ECG synchronization using three and four sweeps, the reconstructed images of the diastolic and systolic phase are less blurred using FDK-4D compared to pure RECG. In conclusion, increasing temporal resolution using an estimated 4D motion field in the FDK-4D algorithm can decrease motion blurring substantially.

References/Funding Source

[1] G. Lauritsch, J. Boese, L. Wigstroem, H. Kemeth, R. Fahrig, "Towards Cardiac C-arm Computed Tomography"
IEEE Transactions on Medical Imaging, 2006, in press.

Dose Advantage of High Resolution Detectors in CT

Angel R. Pineda and Norbert J. Pelc - Department of Radiology

The advantages of smaller detector pixels in CT in terms of higher resolution reconstructions are well understood. We study the effect of the smaller pixels on the noise in the reconstructed images. The size of the detector pixel determines the amount of blurring in the x-ray projections before sampling. While the projections themselves are blurred, the noise in the projections remains uncorrelated regardless of the detector pixel size (equivalently, that there is the same amount of noise for every spatial frequency). This implies that to achieve a given resolution in the reconstructed image, a system with less detector blurring (smaller pixels) will lead to lower noise because there will be less need to undo the blurring at high frequencies. The fundamental observation we make is that even if two photon noise limited CT detectors can achieve the same resolution, the higher resolution detector will have the same or less noise for all frequencies of the reconstructed image. The difference between the low and high resolution systems will be more for small objects which have
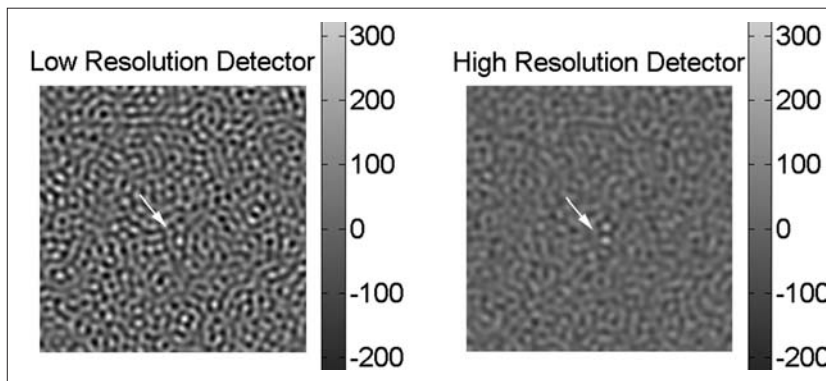
The same x-ray photons were used in the simulations for both of these CT reconstructions with the same resolution but the image using the high resolution detector (pixels half the size of the other system) lead to dramatically less noise in the reconstruction. The effect of the noise can be observed in the detectability of the object (two disks) at the center of the image.

high frequency content and less for large objects which have primarily low frequency content. Accompanying figure shows how for a small object, two systems (one with detector pixels half the size of the other) using the same dose lead to dramatically different noise in the reconstructions even though they have the same spatial resolution. The effect of this noise amplification has been studied by generating images of objects of different sizes and contrasts and quantified using mathematical observers in a two-alternative forced-choice detection task. The clinical implication of this work is that higher resolution detectors can help to reduce dose to the patient even in instances where the resolution required for a task could be obtained by a lower resolution detector.

Computer-aided Detection for Lesions in PET-CT: Clustering using Nearest Neighbor Selection
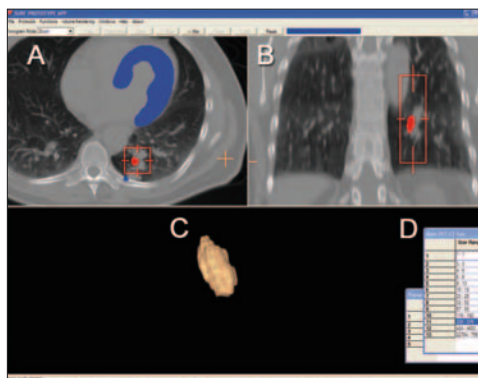
Pankhudi Pankhudi[1], Ajay Jayant Joshi[1], Sandy Napel[2], Christopher F. Beaulieu[2], Andy Quon[2] - Departments of [1]Computer Science and [2]Radiology

Purpose: To develop and evaluate algorithms for computer-aided detection (CAD) of clinically-significant, abnormal foci of FDG uptake in PET/CT.

Materials and Methods: We developed a computer aided detection algorithm that uses intensity thresholding and voxel clustering of PET data to identify foci of high glucose activity. This 3D algorithm currently detects tumor foci as well as physiological activity in normal structures. For our pilot evaluation, clusters with volumes greater than 1.0 cm3 with intensities greater than liver were considered abnormal. We applied the algorithm to 10 abnormal clinical PET/CT datasets and compared the output of the algorithm with the number of abnormal foci reported on the primarily visual clinical readings (130 total lesions, 2-32 lesions/study).

Graphical user interface showing fused PET/CT on (A) axial and (B) coronal planes with left ventricular myocardium in blue and the currently selected lung tumor, in red. (C) Volume rendering of selected lung tumor. (D) "Clickable" list of active foci sorted into size ranges.

CAD identified 24 foci of activity considered to be false positive detections (0 – 8 such foci per case, average 2.4). Foci of normal physiologic activity accounted for 4 – 13 detections per case (80 total, average 8/case). Varying the intensity and cluster size thresholds input to the CAD program demonstrated trade-offs between sensitivity and specificity.

Conclusions: This pilot project demonstrates the potential of this first of its kind CAD for PET/CT. While the current version of the algorithm is prone to both false negatives and false positives, optimal size and intensity thresholds have yet to be determined. It also demonstrated potential for identifying lesions that are missed on visual interpretation. CAD greatly reduces the time spent on analyzing PET-CT images by automatically directly the

The radiologist was provided with a graphical user interface for visualizing CT images with clusters (potential lesions) overlaid in color, a list of clusters, sorted in decreasing order of score, as well as statistics (mean, max and average intensity) for each cluster. The radiologist can examine these clusters by simply scrolling back and forth through the fused PET/CT slices, as well as by using a volumetric rendering technique.

Results: In total, the CAD program detected 91 of 130 lesions for a mean sensitivity of 70% (range 50-100%, stdev 14.6%). CAD found one additional lesion that was missed on the initial clinical interpretation.

radiologist to the most suspicious sites. On-going work in cluster shape analysis promises to automate removal of most false positives, thereby improving accuracy and efficiency of interpretation.

Transparent Rendering of Intraluminal Contrast for 3D Polyp Visualization in CT Colonography

Rong Shi[1], Sandy Napel[1], Jarrett Rosenberg[1], Lewis K. Shin[1], Cynthia B. Freeman[1], Monique B. Mogensen[1], Ajay Jayant Joshi[2], Pankhudi Pankhudi[2], Christopher F. Beaulieu[1] - [1]Departments of Radiology, [2]Computer Science.

Purpose: Patient acceptance of CT imaging for the detection of colonic polyps, precursors to colon cancer, is limited by the need for cathartic colon cleansing. Recently, oral tagging material has been introduced that would allow water and fecal material to be subtracted from the images prior to evaluation. However, this doubles the size of the dataset and may possibly introduce artifacts. To address these issues, we developed a classifier that permits transparent rendering of both tagging material and air without subtraction.

Materials and Methods: Our algorithm couples machine learning and a painting metaphor to allow interactive classification and rendering. The user initially paints a subset of image voxels (tagging material, air, and soft tissue), an iterative training algorithm classifies the volume based on intensities and gradients, and 3D subvolumes of interest in the volume are displayed. The algorithm was tested on 26 tagged CTC cases (courtesy of Dr. R. Choi, Walter Reed Army Med Ctr), containing 49 polyps: 25 adjacent to air, and 24 either completely under or coated with tagging material. Non-polyp control locations (49 total) included 25 areas against air and 24 against tagging material.
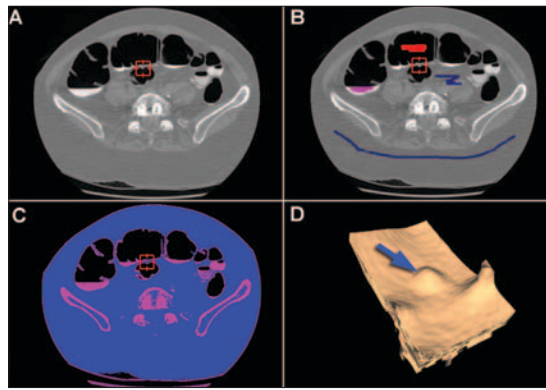
"Painting" experiment and result. A: CT image (one of several hundred in the scanned volume) with red box surrounding a polyp. B: 3 tissue types identified by painting with 3 different colors: red=air, pink=tagging material, blue=soft tissue. C: Fully classified image based on the similarity of each voxel to the painted voxels. D: Subvolume rendering including the red box showing polyp (arrow): blue (soft tissue) voxels were set to a "flesh" color and fully opaque, red (air) and pink (tagging material) voxels were set to fully transparent.

Three radiologists, without knowledge of presence of tagging material, independently viewed the 98 subvolumes for (a) presence or absence of a polyp, and (b) overall image quality.

Results: For polyp detection, readers achieved 96.6% sensitivity and 89.1% specificity (area under receiver operator characteristic curve {AUC} 0.98). Image quality ratings between polyp and control locations were not significantly different overall (p < 0.258). Image quality ratings were significantly lower overall for tagged versus untagged locations (p < 0.001) and for two readers (both p < 0.001), but not for the third reader (p < 0.272). However, readers' accuracy was equivalent between tagged (AUC = 0.99) and untagged (AUC = 0.97) locations overall (p < 0.05) and for each individual reader (p < 0.05).

Conclusions: Our method for rendering tagging material transparent resulted in a high level of polyp detection accuracy, without decreased accuracy compared to polyps in air. This new approach enables accurate 3D depiction of polyps under tagging material. Further image quality improvement could be attempted by exploring more features used in classification therefore optimizing the algorithm.

Minimally-Distorted Single Images of the Abdominal Aortic Vasculature: Method and Evaluation

Joong Ho Won[1], Geoffrey D. Rubin[2], Sandy Napel[2] - Departments of [1]Electrical Engineering and [2]Radiology

Purpose: To develop an algorithm that displays the abdominal aortic vascular tree, such as obtained from CT Angiography (CTA) or MRA, in a single image without the appearance of intersections between branches.

Materials and Methods: We compute a binary tree representation of the abdominal aortic tree from a collection of 3D centerlines. The first phase of untangling applies a projection mapping as used in stretched Curved Planar Reformatting to each node of the binary tree, and produces a 2D topology-geometry model. The second phase abstracts the projected centerline using a convex primitive. We then place these primitives in user-specified priority order, using a radial sweep line algorithm to find an available display region for placement, and then determine a suboptimal placement that minimizes the distortion of the original geometry within the region. We evaluated the method using 10 CTA datasets, and for each began with an anterior-posterior projection so as to introduce severe crossings in the renal artery region. Our metrics for distortion between the input orthographic projection of the centerlines and the output centerlines considered scaling, changes to
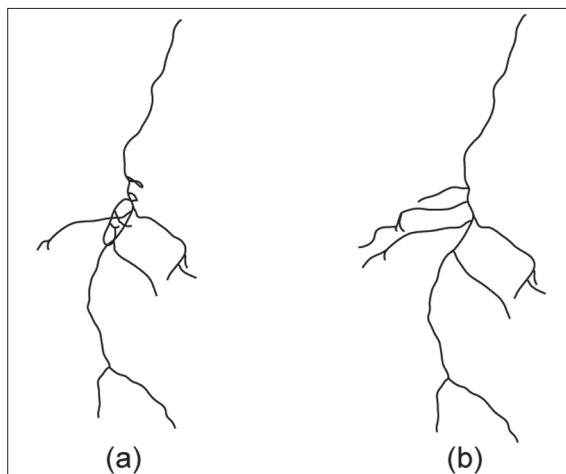
Anterior-posterior views of the abdominal aortic tree of an anonymous patient. (a) before untangling, (b) after untangling.

branch angles, and nonlinear bending.

Results: Processing of all 10 datasets resulted in a clear visualization with all false intersections removed, scale distortion close to the ideal value of 1.0 (min=0.76, max=1.05), and branch angle distortion less than 38 degrees. Bending energy was below 2.5 for 8 cases. The other 2 cases showed aggressive stretching, which occurred during the first phase of untangling, of what were originally tortuous vessels.

Conclusions: Our proposed algorithm eliminates misleading vessel crossings from conventional projections, in most cases conserves overall shape, and can form a basis for more advanced visualization techniques that provide clinical findings from cross-sectional angiographic examinations in a single 2D image. Our distortion metrics agree well with visual perception and can signal extreme behavior of the algorithm, which may possibly be used to iteratively improve visualization when it occurs.

Knowledge-based Algorithm for Automated Centerline Interpolation through Femoro-Popliteal Artery (FPA) Occlusions in Peripheral CTA

J.E. Roos[1], D. Fleischmann[1], T.Rakshe[2], M.Straka[3], M. Sofilos[1], D. Tran[1], J. Rosenberg[1], S. Napel[1] - [1]Radiology, [2]Electrical Engineering, [3]Visicom, Austrian Academy of Sciences

Purpose: Curved planar reformations (CPR) through occluded FPA provide invaluable information for treatment planning in patients with peripheral arterial occlusive disease (PAOD). Because currently available density/gradient-based algorithms fail to track the centerlines of occluded vessels, we have developed a new knowledge-based algorithm for automated centerline restoration through occluded arterial segments, and determined its accuracy compared with expert derived manual centerlines as the standard of reference.

Materials and Methods: CT angiograms (CTA) of 20 patients with PAOD (14 m/6 f; mean age 69y, range 44-88y) with 25 FPA occlusions (mean length132mm, range 16-400mm) were identified. Occlusions were categorized into 4 length groups: <50mm (n=5); 50-100mm (n=8); 100-200mm (n=6) and >200 mm (n=6). The arteries were identified using a standard density based, semiautomated vessel tracking algorithm through the patent segments. Centerlines of occluded segments were manually determined two times by each of two experts, with the mean of all 4 readings serving as the standard of reference. Each occlusion was also interpolated using a knowledge based algorithm, which uses shape information extracted from an existing vascular database (30 FPAs) using principal component analysis. Accuracy of the interpolated centerlines was quantified by the point-wise calculation of the maximum distance between the
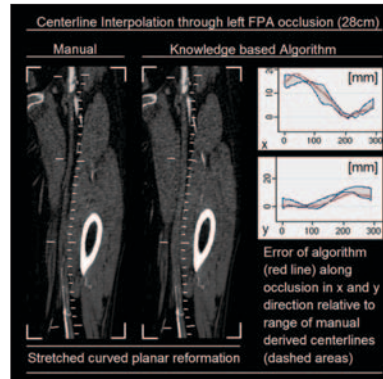

Figure shows comparison of a manual and automated centerline interpolation through left FPA occlusion. Note the non-opacified occluded artery (outlined by the course of virtual gauging tics) with its surrounding perivascular fat plane. Only subtle differences between the manual and automated derived CPR are observed.

standard of reference and the automated centerline. A reference range of error was defined as extending from the minimum expert error minus 0.5mm to the maximum expert error plus 0.5mm.

Results: The knowledge-based algorithm successfully interpolated and automatically interpolated 25 FPA occlusions. The mean of maximum error (in mm) for occlusion lengths of <50mm, 50-100mm, 100-200mm, and >200mm was 3.2, 6.5, 9.3, and 12.3 for readers and 3.2, 6.8, 10.4, and 24.2 for the algorithm. The maximum algorithm error was contained in within 0.5mm of the range of that of the readers in 18 of 25 cases (p<.022).

Conclusions: It is possible to extract vascular shape information from a database of peripheral CT angiograms and use this information to predict the course of arterial segments of the FPA that cannot be found by density and gradient based algorithms. Our initial results are encouraging having a knowledge-based algorithm that allows an accurate automated interpolation of centerlines thorough FPA occlusions up to a length of 75 mm. This may substantially accelerate the creation of CPRs in patients with PAOD in the future.

References/Funding Source
J.E. Roos, D. Fleischmann, T.Rakshe, M.Straka, M. Sofilos, D. Tran, J. Rosenberg, S. Napel. Knowledge-based Algorithm for Automated Centerline Interpolation through Femoro-Popliteal Artery (FPA) Occlusions in Peripheral CTA" 29th Annual Course of the Society of Computed Body Tomography and

Rotational Roadmapping: A New Image-Based Navigation Technique for Endovascular Interventions

Markus Kukuk[1,2], Hideki Arakawa[2], Michael Marks[2], Huy Do[2], Sandy Napel[2] - [1]Siemens Medical Solutions; [2]Department of Radiology, Stanford University

Purpose: To date, conventional 2D-roadmapping (2D-ro) is the technique of choice for instrument navigation in neuroendovascular procedures. More recently, 3D-ro, based on a 3D reconstruction of the vasculature from a prior CT angiogram (CTA) scan or from an interventional C-arm CT scan, has become popular. Both techniques may be limited by streak artifacts in the presence of indwelling metal, and sensitivity to motion during acquisition. Alternatively, we have developed a new technique, called RoRo, based on a single rotational angiographic acquisition (DSA) of any length and angular increment.

A patient undergoing treatment for a cerebral aneurysm with RoRo being used for interactive guidance.

Materials and Methods: Acquired projections are displayed as a "rotatable roadmap" linked to the current C-arm position, allowing for an interactive and intuitive selection of the best available working view. The selected projection is subtracted from the live fluoroscopic images, thus displaying any medical device within the context of the vasculature. We integrated RoRo into a Siemens Axiom Artis dBA C-arm system and used it in clinical cases.

Results: For a patient that presented with a cerebral aneurysm, a total of 128 projections (.3mm pixel size; 1k matrix) were acquired in

a 5s rotational DSA run, using 21ml of iodine. Within 70s of acquisition, RoRo was available to the interventionalist who then moved the C-arm to find the best working view to navigate a guidewire into the aneurysm. By comparison, the same projections were reconstructed into a 256x256x227 volume of .7mm voxel size for 3D-ro. For a patient that presented with a neck tumor, an acquisition of an angular range sufficient for a 3D reconstruction was not feasible due to photon starvation in the shoulder area. Instead, a short acquisition for RoRo was performed over a range of 82 degrees (55 projections), which was available within 30s and then used to embolize the tumor.

Conclusions: RoRo appears to be a simple yet powerful navigation technique that can provide guidance where 3D reconstructions are not feasible, and has the potential to show smaller vessels in a fraction of 3D-ro's processing time. This gap is increasing, as updated systems, allowing 2D acquisitions at .15mm pixel size in a 2k matrix are becoming available.

References/Funding Source
Siemens Medical Solutions, inc.

Detecting Polyps and Folds in CT Colonography: A Curvature Scale-space Approach

PADMAVATHI SUNDARAM[1,2], CHRISTOPHER BEAULIEU[1], SANDY NAPEL[1] - [1]RADIOLOGY, [2]ELECTRICAL ENGINEERING

Purpose: Although curvature has been used to detect polyps in CT Colonography (CTC), it is too local a surface descriptor and, therefore, highly affected by noise. We developed a computer-aided detection (CAD) algorithm that performs geometry-driven diffusion of curvature tensors (CTNs) to reduce these effects and improve detection of polyps (Polyp-CAD) and folds (Fold-CAD).

Materials and Methods: CTNs were computed at each vertex of a mesh representation of the colon surface. The CTN is a matrix whose eigenvalues and eigenvectors are the principal curvatures (K1, K2, |K1| >= |K2|) and principal curvature directions respectively. The CTNs were then diffused on the mesh using a Gaussian kernel of gradually increasing size, starting at 0.25 mm and increasing by 10% each time. The polyp-CAD algorithm clustered the connected peak vertices (K1 <= 0, K2 <= 0), and the fold-CAD algorithm clustered the connected saddle vertices (K1 <=0, K2 >= 0). The score assigned to each peak cluster was a product of the maximum K2 and the area-weighted integral of the Gaussian curvatures (=K1*K2), both computed over the cluster vertices. The score assigned to saddle clusters were a function of the patch area, K1 and the surface deviation of the surface points from a plane. The polyp-CAD algorithm was evaluated on 31 multi-detector row CTC datasets.
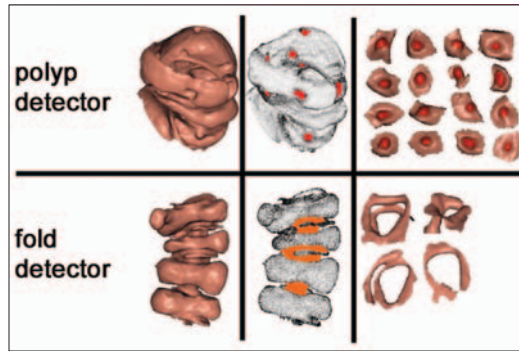
Example results on segments of patient colons. Top row: polyp-CAD. Left: surface rendering of segment. Middle: candidate detections highlighted in color. Right: automatically extracted candidates as surface patches.

There were 169 lesions in total: 60 ([0,5) mm), 85 ([5,10) mm) and 24 ((>= 10 mm) range. Comparisons to an existing algorithm (SNO), as well as to a strict fiber-optic colonoscopy (FOC) based gold standard were performed. The fold-CAD algorithm was evaluated on a segment of a patient colon with 36 salient folds. An experienced radiologist manually inspected the results and labeled them as true positives (TPs) or FPs. Folds that were missed by the algorithm were also marked.

Results: At a FP rate of 20 per dataset, the sensitivity of polyp-CAD was found to be 82% (all sizes), 65% ([0,5) mm), 89% ([5,10) mm) and 100% (>= 10 mm). At the same FP rate, the sensitivity of the SNO method was found to be 38% (all sizes), 16% ([0,5) mm), 41% ([5,10) mm), 79% (>= 10 mm). For fold-CAD, the sensitivity was found to be 90% at a FP rate of 1 and 100% at a FP rate of 9 per dataset. No salient folds were missed.

Conclusions: When further optimized, CAD of polyps may lead to greater use of CTC and aid the radiologist in diagnosis. Fold detection could help reduce FPs in CAD, and could also be used in registration of supine and prone datasets of the same patient.

Learning-Enhanced Simulated Annealing: Method, Evaluation, and Application

SHAOHUA SUN[1], FENG ZHUGE[1], GEOFFREY D. RUBIN[2], AND SANDY NAPEL[2] - [1]ELECTRICAL ENGINEERING, [2]RADIOLOGY

Purpose: Assessing the growth and composition of lung nodules appearing in Computed Tomography (CT) scans of the same patient acquired at different times is helpful for the determination of malignancy. We have developed a nodule registration system to facilitate this process. Registration consists of transforming a region in one scan into the coordinate system of the other such that some correspondence ratio is maximized. This work aims develop a new transformation method to improve robustness in the presence of nodules that change shape and composition over time.

Materials and Methods: We developed a semi-rigid (SR) transformation method that considers principal structures surrounding a given nodule and allows relative movements amongst the structures. We also introduced a new similarity metric, which evaluates image correlation and the extent of elastic deformation amongst the structures, which is maximized by a two-layered optimization method, employing a simulated annealing framework. We tested our method by simulating 5 cases that represent physiological deformation as well as different nodule shape/size changes with time. Each case was made up of a source and target scan, where the source scan consisted of a nodule-free patient CT volume into which we inserted 10 simulated lung nodules, and the
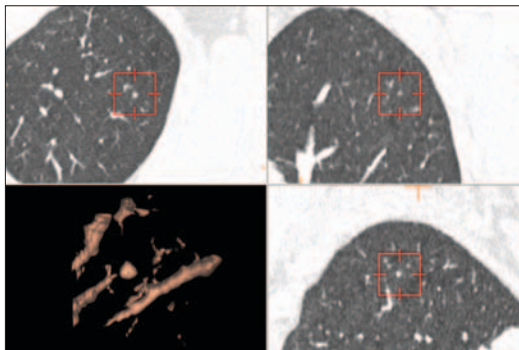

Illustration of the semi-rigid model with 3 surrounding structures, where tri and roi are defined as translation and rotation respectively. Note that the orientations and positions of each of the structures are allowed to change over time, as is the size and shape of the nodule.

target scan was the result of applying a known, physiologically-based non-rigid transformation to the nodule-free source scan, into which we inserted modified versions of the corresponding nodules at the same, known locations. Five different modification strategies were used: (1) nodules maintained size and shape, (2) nodules resolved, (3) nodules shrank uniformly by a factor of 2, (4) nodules grew uniformly by a factor of 2, and (5) nodules grew non-uniformly. We also matched 98 real nodules in pairs of scans from 12 patients and compared our registration to a radiologist's visual determination.

Results: In the simulation experiments, the mean absolute registration errors were 1.0 mm ± 0.8 mm (s.d.), 1.1 mm ± 0.7 mm (s.d.), 1.0 mm ± 0.7 mm (s.d.), 1.0 mm ± 0.6 mm (s.d.), and 1.1 mm ± 0.9 mm (s.d.), for the five cases, respectively. For the 98 nodule pairs in 12 patient scans, the mean absolute registration error was 1.5 mm ± 0.9 mm (s.d.).

Conclusions: The proposed SR model shows promise for matching nodules in a series of CT scans and is robust to size/shape change over time.
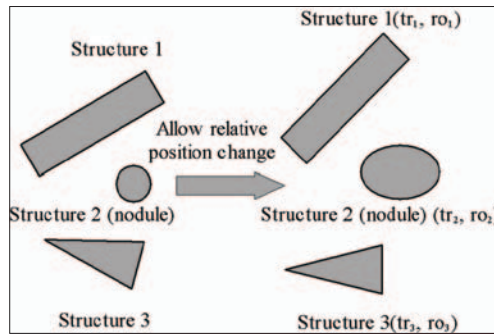
Registration of Lung Nodules Using a Semi-Rigid Model

SHAOHUA SUN[1], FENG ZHUGE[1], GEOFFREY D. RUBIN[2], SANDY NAPEL[2] - DEPARTMENTS OF [1]ELECTRICAL ENGINEERING, [2]RADIOLOGY

Purpose: Assessing the growth and composition of lung nodules appearing in Computed Tomography (CT) scans of the same patient acquired at different times is helpful for the determination of malignancy. We have developed a nodule registration system to facilitate this process. Registration consists of transforming a region in one scan into the coordinate system of the other such that some correspondence ratio is maximized. This work aims to develop a new transformation method to improve robustness in the presence of nodules that change shape and composition over time.

Materials and Methods: We developed a semi-rigid (SR) transformation method that considers principal structures surrounding a given nodule and allows relative movements amongst the structures. We also introduced a new similarity metric, which evaluates image correlation and the extent of elastic deformation amongst the structures, which is maximized by a two-layered optimization method, employing a simulated annealing framework. We tested our method by simulating 5 cases that represent physiological deformation as well as different nodule shape/size changes with time. Each case was made up of a source and target scan, where the source scan consisted of a nodule-free patient CT volume into which we inserted 10 simulated lung nodules, and the target scan was the

Illustration of the semi-rigid model with 3 surrounding structures, where tr_1 and ro_1 are defined as translation and rotation respectively. Note that the orientations and positions of each of the structures are allowed to change over time, as is the size and shape of the nodule.

result of applying a known, physiologically-based non-rigid transformation to the nodule-free source scan, into which we inserted modified versions of the corresponding nodules at the same, known locations. Five different modification strategies were used: (1) nodules maintained size and shape, (2) nodules resolved, (3) nodules shrank uniformly by a factor of 2, (4) nodules grew uniformly by a factor of 2, and (5) nodules grew non-uniformly. We also matched 98 real nodules in pairs of scans from 12 patients and compared our registration to a radiologist's visual determination.

Results: In the simulation experiments, the mean absolute registration errors were 1.0 mm ± 0.8 mm (s.d.), 1.1 mm ± 0.7 mm (s.d.), 1.0 mm ± 0.7 mm (s.d.), 1.0 mm ± 0.6 mm (s.d.), and 1.1 mm ± 0.9 mm (s.d.), for the five cases, respectively. For the 98 nodule pairs in 12 patient scans, the mean absolute registration error was 1.5 mm ± 0.9 mm (s.d.).

Conclusions: The proposed SR model shows promise for matching nodules in a series of CT scans and is robust to size/shape change over time.

Error Prediction and Performance Evaluation of a Principal Component Analysis Based Algorithm for Reconstructing Missing Segments of Vascular Centerlines in CT Angiography

TEJAS RAKSHE[1], DOMINIK FLEISCHMANN[2], JARRETT ROSENBERG[2], JUSTUS ROOS[2], DAVID TRAN[3], SANDY NAPEL[2] - DEPARTMENTS OF [1]ELECTRICAL ENGINEERING AND [2]RADIOLOGY

Purpose: To build a statistical model for error and evaluate the performance of a Principal Component Analysis (PCA) based method for reconstructing missing vascular centerlines, using a database of centerlines from other patients.

Materials and Methods: A database was constructed consisting of centerlines of femoropopliteal arteries from CT Angiography (CTA) scans of 30 subjects without peripheral arterial occlusive disease. A leave-one-out cross validation of a PCA based algorithm was performed on the database by simulating occlusions of various lengths and reconstructing them using the algorithm. Point-wise maximum departure (MD) for each case was used as the error metric. Regression analysis was performed on MD with the length and location of the occlusion, age and sex of the subject, and estimation error in the neighborhood of the occlusion (NE). The results were compared with the results obtained by a minimum mean squared error (MMSE) estimate.

Results: The 50th percentile of MD and the 95% confidence interval upper bound for each occlusion length were: (Occ. length: 50th percentile MD, 95% upper bound, all in mm) 10: 0.14, 0.15; 25: 0.40, 0.42; 50: 0.81, 0.88; 75:1.32, 1.46; 100: 1.76, 2.06. The most important effect on error was that of occlusion length (p<0.0001), with a (log-log) coefficient of 1.06 (95% Confidence Interval (CI): 1.04-1.08) (each 101 increase in length results in a 101.06 increase in MD. A simple linear regression of just log-MD on log-Occl. Length accounts for 50% of the variability in the latter. There was a smaller effect of log-NE (p<.001), with a coefficient of 0.08 (95% CI: 0.04-0.12). There was no significant effect of age or sex of the patient. The random-intercept effect of individual arteries accounted for 28% of the remaining variability. The PCA
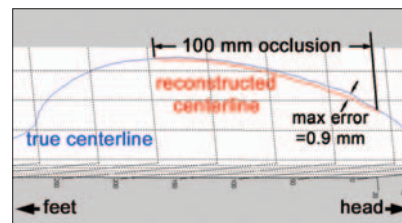
Results of reconstructing the centerline through a simulated occlusion in the femoropopliteal artery derived from a CT angiogram of a normal patient.
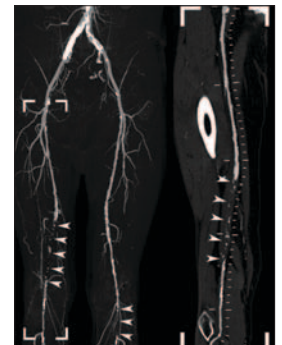
based methods produced more accurate results than MMSE method, with a Wilcoxon signed rank test of the distribution of maximum error between the two methods having a p-value <0.00001.

Conclusions: The PCA-based algorithm reconstructs missing centerlines with clinically acceptable accuracy up to 100mm OL. Longer occlusions may benefit by simple user input constraining the path to lie near a small number of user-supplied points. The expected error can be predicted to a significant level of accuracy. This method may provide efficient generation of curved planar reformations through arteries of patients with occluded segments, greatly simplifying their assessment from cross-sectional imaging.

MetroTrac: A Metropolis Algorithm for Probabilistic Tractography

ANTHONY SHERBONDY[1], MICHAL SHACHAR[2], ROBERT DOUGHERTY[2], DAVID AKERS[3], SANDY NAPEL[4], BRIAN WANDELL[2] - DEPARTMENTS OF [1]ELECTRICAL ENGINEERING, [2]PSYCHOLOGY, [3] COMPUTER SCIENCE AND [3]RADIOLOGY.

Purpose: Tractography traces white-matter connections in-vivo based on diffusion-weighted (DW) MR data. Deterministic tractography algorithms, e.g. STT, produce reliable estimates of large fiber tracts but may miss smaller ones because the algorithms do not account for the uncertainty, better modeled by probabilistic algorithms, inherent in DW data. We developed a Bayesian probabilistic framework, which incorporates both a local diffusion likelihood model as well as a fundamental fiber regularization parameter found in many deterministic algorithms, and a Metropolis algorithm (MetroTrac) that correctly samples from this distribution. Our algorithm is especially efficient at sampling pathways that connect specific regions, even when these regions are separated by major crossing pathways.

Materials and Methods: We model tractography as a sampling problem in a Bayesian framework: Let any fiber pathway be defined by the discrete position function s = $\{s_1, s_2, \ldots, s_n\}$, given a fixed distance between each point of the pathway (e.g. 1 mm). Let D represent the entire DW data set. Then, our goal is to sample the posterior distribution defined by Bayes rule as $P(s|D) = P(D|s)P(s) / P(D)$. Previous probabilistic approaches sample from the posterior in a sequential manner under the assumption $P(s|D) = P(s_1|D)P(s_2|D,s_1)\ldots P(s_n|D,s_{n-1})$. However this assumption can be violat-
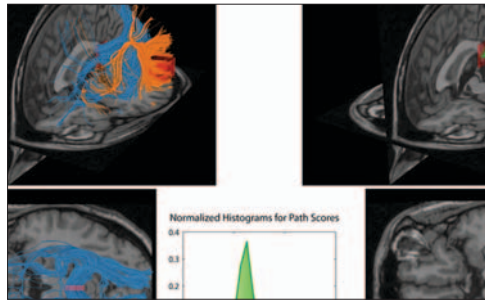
Left column shows pathways in a normal human subject computed by STT, which intersect either MT+ (orange) or Splenium (blue), but never both. Right column shows same subject, but with pathways connecting MT+ and Splenium computed by MetroTrac. The normalized histogram (center) shows that scores for the MetroTrac paths (green) are within the range of the STT paths (blue, orange).

ed with even the most straightforward models for the likelihood P(D|s) and prior P(s).

Results: We can demonstrate that MetroTrac estimates of major fasciculi agree with the most common deterministic algorithms. Second, MetroTrac has the ability to identify pathways that penetrate major structures. The Figure shows MetroTrac pathways connecting the MT+ and the splenium, crossing through the inferior longitudinal fasciculus, compared to the STT algorithm, which fails to find any connections between the same two regions even though the scores for the MetroTrac pathways are well within the range of scores for pathways computed by STT.

Conclusions: Our MetroTrac algorithm provides a straightforward mechanism for properly incorporating anatomical priors, and is able to demonstrate connections that deterministic algorithms fail to produce. MetroTrac, therefore, shows promise as a tool with which to study connectivity between various regions of the normal human brain, and perhaps to help diagnose neuronal disruption in the presence of trauma and disease.

Correcting Under-segmentation of Juxtapleural Lung Nodules in Chest CT

JIANTAO PU, GEOFF RUBIN, JUSTUS ROOS, DAVID S. PAIK - DEPARTMENT OF RADIOLOGY

When thresholding-based methods are used for lung segmentation, juxtapleural nodules are often incorrectly excluded from the segmentation. Correcting the under-segmentation of juxtapleural lung nodules is crucial for many applications such as nodule CAD. Our goal is to develop an algorithm to automatically fix this under-segmentation while minimizing any over-segmentation. To correct the under-segmentation caused by juxtapleural lung nodules, the algorithm marches along the border "bridging" juxtapleural nodules through a novel algorithm that produces a localized convex hull but leaves the border intact elsewhere. The algorithm uses a boolean OR operation so that it may only add to the

Figure 1: A correction example where juxtapleural nodules are indicated by arrows and the correction result is indicated

original segmentation. To test the algorithm, we used a total 20 chest CT scans with 330 lung nodules as determined by a consensus panel of radiologists (1.5-18 mm; mean 4.1 mm). 67 of these were juxtapleural. The results of the algorithm were reviewed and categorized by an experienced radiologist. The sensitivity of the algorithm was first tested on the axial slices that contained these juxtapleural nodules. Then, the specificity of the algorithm was tested on 500 randomly selected axial

slices from these datasets that do not contain juxtapleural nodules. 65 of 67 juxtapleural nodules were correctly fixed and added to the segmentation leading to a per-nodule sensitivity of 97%. The remaining 2 nodules (2.2 mm and 2.3 mm in diameter) were both partially fixed. Relative to the original segmentation, no undersegmention occurred. In the nodule-free images, the per-pixel oversegmentation rate was 3.8% with respect to the segmentation based on the thresholding technique. The majority of this oversegmentation was due to bronchii and hilum which, depending on the application, may be desired to be included. Figure 1 shows an example about the correction result. The contour in red indicates the lung

regions obtained by thresholding-based method, while the contour in green the lung regions with juxtapleural nodule correction.

Lung Nodule Detection by Analyzing Voxel-based Expanding Process

JIANTAO PU, GEOFF RUBIN, DAVID S. PAIK - DEPARTMENT OF RADIOLOGY

Due to the great varieties of lung nodules such as shape, location, size and intensity, it is still difficult to automatically detect nodules with a high sensitivity but few false positives. We are trying an algorithm which characterizes nodules by analyzing the principle components of a voxel-based expanding process. This algorithm is supported by three key components. The first one segments the lung region with juxtapleural nodules included. Due to the fact that lung nodules usually have a high intensity with respect to their surrounding structure, the sec-
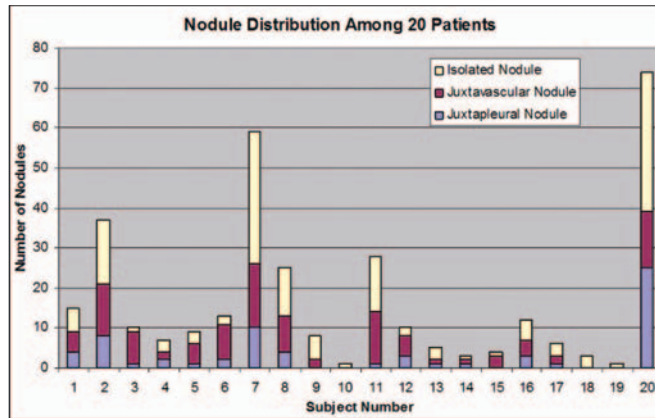

Figure 1: Nodule distribution among the 20 chest CT scans

mm; mean 4.1 mm). Figure 1 shows the nodules distributions among the 20 chest CT scans. Our preliminary experiments demonstrate that the overall sensitivity for nodule detection with this algorithm was 90.3% (298 of 330 nodules) for all nodules (1.5-18mm). For nodules 3mm and larger, the sensitivity was 94.0% (204 of 217 nodules). For nodules 3mm-6mm, the sensitivity was 93.3% (154 of 165 nodules). For nodules 6mm and larger, the sensitivity was 96.2% (50 of 52 nodules). The algorithm has some valuable properties: (1) it is not sensitive to

ond component locates all seed voxels with a local maximal intensity for the expanding process. Given a seed voxel, the third component clusters all voxels by decreasing the intensity progressively. At each expanding stage, the geometric shape of the cluster is analyzed with the help of principle component analysis. Since pulmonary nodules are approximately spherical regions, the nodule candidates are identified by comparing the three eigenvalues obtained from principle component analysis. To test the algorithm, we performed a preliminary test with a total 20 chest CT scans which contains 10,389 slices and 330 lung nodules as determined by a consensus panel of radiologists (1.5-18

nodule size; and (2) it is not sensitive to nodule locations (isolated, juxtapleural, and juxtavascular). Our future work will focus on decreasing the false positives.
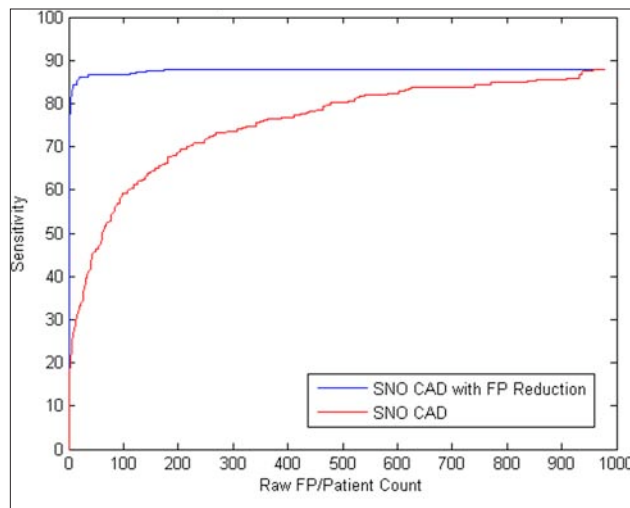
Non-Parametric Shape Analysis for Lung CAD False Positive Reduction.

A. AGGARWAL[1], G.D. RUBIN[2], D.S. PAIK[3] - DEPARTMENTS OF [1]COMPUTER SCIENCE, [2]RADIOLOGY AND [3]RADIOLOGY

Existing CAD algorithms may produce many false positives in order to achieve a high sensitivity for small lung nodules (~ 3 mm). This limits their use by radiologists. The purpose of this work is to develop an algorithm to automatically filter out as many false positive CAD detections as possible without adversely affecting the sensitivity, thus creating a composite algorithm with much improved performance for small nodules. We have built a new method for shape analysis to distinguish between lung nodules and typical CAD false positives using a non-parametric approach. Localized shape estimation is done by combining ray casting with geometric measures of isointensity contours. A statistical analysis of these

The figure shows the comparative F-ROC curves between SNO CAD and SNO CAD with FP reduction.

measures is then used to construct features for a logistic regression classifier. For evaluation, the method was given our previously published SNO CAD algorithm's detections as input. 20 chest CT scans were performed and there were a total of 329 nodules with 95 being less than 3 mm in size. 5-fold cross-validation was performed on the dataset

to assess the FP reduction algorithm. The algorithm achieves an average area under the ROC curve value of 0.985 in classifying the SNO CAD output. In particular, when combined with SNO CAD, it was able to reduce the false positive rate to 5 per patient from that of 540 per patient given by SNO CAD alone while achieving a similar sensitivity.

Our novel algorithm can considerably improve the performance of an existing CAD algorithm by successfully filtering out most of its false positives and correctly classifying almost all small lung nodules. It significantly reduces the findings radiologists have to review, without leaving out smaller nodules. In the future we hope to extend this algorithm beyond Lung CAD.

StepMiner: Extracting Digital Signals from Microarray Time Course Data

Debashis Sahoo[1], David Dill[1], Robert Tibshirani[2], Sylvia Plevritis[3] - [1]Departments of Computer Science,
[2]Health Research & Policy (Biostatistics), and [3]Radiology

StepMiner is a new method that extracts instantaneous transitions in gene expression time course data. It identifies genes with expression profiles, which appear to "turn on" and "turn off" at one or more time points. The genes are then sorted by the type of temporal behavior, and signals of the same type are ordered by the times at which on and off transitions occur. StepMiner helps to discover temporal ordering of gene expression and thereby may reveal new insight into gene regulatory networks.

StepMiner uses adaptive regression to select the best fit from a collection of curves with varying numbers and times of transitions. The binary signal extracted for each gene has a p-value which estimates the likelihood that the match would have occurred for random data, assuming a Gaussian distribution. The true false discovery rate (FDR) is estimated analyzing random permutations of the data, without making assumptions about the probability distribution of the errors, and a p-value cutoff can adjusted to obtain an acceptable FDR.

We applied StepMiner to simulated data to evaluate its signal-to-noise performance. For the artificial data, signals of each type are generated randomly, and Gaussian noise is added. The extracted results are compared with original behavior before noise was added to measure
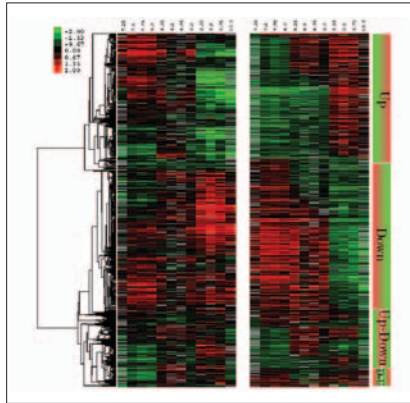
Analysis of diauxic shift on glucose limited budding yeast, a comparison of Hierarchical Clustering and StepMinter. StepMiner output is sorted according to the step positions and direc-

the accuracy of the extraction. When the step size is 5 times the standard deviation of the noise and there are 11 time points, the method finds the correct signal (p-value threshold = 0.05) over 90% of the time for each signal type.

We also evaluated StepMiner on a publicly available time course of microarrays taken at 12 time points, measuring gene expression levels in yeast that undergoes a diauxic shift when a fixed amount of glucose is depleted (see Figure). The signals are extracted from the data, then genes are grouped by the type and time of changes in their expression. These groups are then tested using GO-TermFinder to find Gene Ontology annotations that are enriched within the gene groups. Our analysis reveals groups of genes that change in similar ways and at similar times that have sig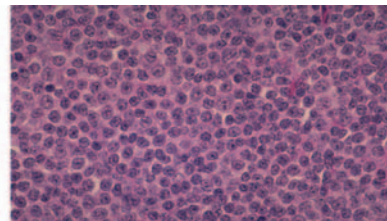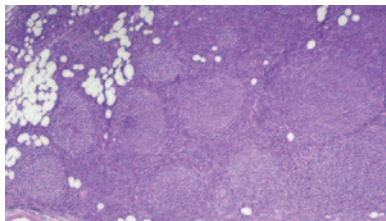nificant and relevant Gene Ontology annotations, consistent with a previous analysis of this data that was performed with traditional hierarcherial clustering and manual intervention. Furthermore, our p-values are lower than those previously published, which suggests that grouping by time-of-change may be more effective than hierarchical clustering for identifying genes with binary states.

Myc Inactivation in Mouse Lymphomas Drives a Cellular Shut-down Program

Catherine M. Shachaf[1], Andrew J. Gentles[2], Debashis Sahoo[2], Sylvia Plevritis[3], Dean W. Felsher[1]
Departments of [1]Medicine (Oncology), [2]Radiology and [3]Computer Science

In 25-60% of follicular lymphoma patients, the disease transforms to a much more aggressive form, Diffuse Large B-Cell Lymphoma, with poor prognosis and resistance to treatment. Underlying the transformation are changes in gene expression, and the Myc

FL (left) frequently transforms to DLBCL (right), with sharply decreased survival time.

oncogene has been implicated in the process. To determine genes that are directly regulated by Myc, we regulated Myc in a transgenic mouse model by titration with doxycycline, and measured gene expression changes with cDNA microarrays. We found that there is a well-defined shift in gene expression patterns at a particular Myc threshold (0.05 ng/ml doxycycline). Significantly up-regulated and down-regulated genes were determined using Significance Analysis of Microarrays on samples below and above Myc threshold. 898 genes were down-regulated and 591 genes were up-regulated, with a 5% false discovery rate (FDR). It appears that at threshold levels of Myc expression there is a change in the gene transcription profile that arrests the RNA, protein and metabolic synthesis programs of tumor cells while inducing changes in genes involved in cell signaling processes and ATP generation. We also analyzed the expression of 43 different genes known to be regulated by Myc using quantitative PCR, and a novel analysis tool (StepMiner)

to detect significant changes in mRNA abundance. Cdc25, cad1, odc, cad, cul1, elf4e and gpat follow the initial drop in Myc expression, confirming that they are indeed Myc targets. We also found an initial drop in the expression of tfrc, fkbp 53, p16ink4, dhfr, nup120, e2f1 and bap

between 0.05 to 0.06 ng/ml doxycycline. Comparison with the qtPCR results validated the measurements by microarray analysis, however the magnitude of change differs due to the greater dynamic range of qtPCR. In summary, we identified genes that change significantly at Myc threshold levels, and quantified their expression level changes. These genes may represent the group of genes that are responsible for the biological outcome of threshold Myc levels.

Cost-effectiveness of Breast MRI Screening Among BRCA1/2 Mutation Carriers

Sylvia K. Plevritis[1], Bronislava Sigal[1], Allison Kurian[2] - Departments of [1]Radiology and [2]Medicine (Oncology)

To evaluate the cost-effectiveness of screening women who carry BRCA1 or BRCA2 mutations with breast MRI when screening mammography is found to be insensitive due to extremely dense breast tissue often identified in women younger than 50 years of age. We developed a computer simulation model that generates individual life histories of the BRCA1/2 mutation carriers undergoing breast cancer screening with mammography alone or in combination with MRI. A cohort of 10 million women who were 25 years of age and breast cancer free in the year 2005 was followed. For women under age 50, mammography was assumed to have zero sensitivity to invasive tumors less than 5cm. For women above 50 years of age, the proportion of women with extremely dense breast tissue dropped to 0.33. We evaluated health benefits and cost for annual screening strategies whereby all women were screened with mammography from ages 25-69 and screened with MRI for varying ages. Published data were used on breast cancer rates among BRCA1/2 carriers, the accuracy of the mammography and breast MRI. Utilization rates and costs of diagnostic and treatment interventions were based on a combination of published literature and Medicare payments. All costs were in 2005 US dollars and cost and QALY were discounted by 3%.

Adding annual MRI to annual mammography screening yields a cost per quality-adjusted life-year gained in the range of $31,300 to $493,980, depending on the ages selected for MRI screening and the specific BRCA mutation. Screening women ages 40 to 49 years whose mammogram is extremely dense with breast MRI costs about $30,000 per QALY gained in BRCA1 mutation carriers and $80,000 per QALY gained in BRCA2 mutation carriers. The cost-effectiveness ratio of adding MRI increases when screening women in broader age ranges for both BRCA1 and BRCA2 mutation carriers. The results were most sensitive to variations in the cumulative breast cancer risk, cost of MRI and discount rate. When mammographic screening is insensitive for BRCA1/2 mutation carriers, adding breast MRI screening can be a cost-effective strategy dependent on the ages selected for MRI screening and the specific BRCA mutation.

Choosing Prophylactic Mastectomy over MRI Breast Cancer Screening Among Women at High Inherited Risk for Breast Cancer

Allison Kurian[1], Anne-Renee Hartman[2], Meredith A. Mills[1], Margo Jaffee[1], Nicolette M. Chun[1], Judy E. Garber[2], James M. Ford[1] and Sylvia K. Plevritis[3] - Departments of [1]Medicine, [2]Oncology (Harvard) and [3]Radiology

Women at high inherited risk for breast cancer consider numerous options to manage their risk, some of which are invasive and irreversible. To help these women make more informed decisions, we aim to identify the factors that influence women at high risk to choose between intensive screening (with mammography and MRI) and prophylactic mastectomy.

Women at high breast cancer risk were evaluated in cancer genetics clinics and educated about options for breast cancer risk management, including prophylactic mastectomy (PM) or screening with annual mammography plus breast MRI. After genetic counseling and testing, they were mailed an 11-item questionnaire about their intended management of their breast cancer risk, and the Revised Impact of Event Scale (RIES), a validated measure of breast-cancer related anxiety. Statistical analysis used Fisher's exact test, 2-sided for categorical variables and t-test for continuous variables.

88 women were sent a questionnaire, and 57 responded, yielding a response rate of 65%. Mean age of responders was 42 years; 47% were mutation carriers and 53% had strong family history. 21 (37%, 95% confidence interval [26-50%]) women declared a low, 23 (40%, [29-53%]) a moderate, and 13 (23% [14-35%]) a high likelihood of choosing PM. There was a non-significant trend toward increase in mean RIES score in women with high (score=23) versus moderate or low (score=20) PM likelihood groups (p=0.4); this range of scores was similar to scores

previously reported in women with high breast cancer risk. Compared to moderate and low PM likelihood groups combined, the high likelihood group had a greater proportion of patients with personal breast cancer history (77% vs. 32%, p=0.009). Low PM likelihood patients had a significantly higher mean age (47 vs. 40 years, p=0.007) than high and moderate likelihood groups combined.

In a clinic-based sample of women at high inherited breast cancer risk, younger age, personal breast cancer history, and higher breast cancer-related anxiety as measured by RIES, were more frequent among women likely to choose PM over MRI-based breast screening. Evaluation of a larger number of high-risk women is planned. Follow-up questionnaire administration for women who have chosen intensive breast screening is ongoing, which will permit identification of experiences and characteristics which predict choice of continued screening versus PM.

Modeling Mayo Lung Project to Assess Efficiency of Screening for Lung Cancer

MAKSIM PASHKEVICH, BRONISLAVA SIGAL, SYLVIA PLEVRITIS - DEPARTMENT OF RADIOLOGY

Lung cancer is the leading cause of death in the United States, and identifying medical interventions that increase the cure rate for this disease is of paramount importance. Screening for lung cancer can be beneficial to mortality reduction, since detecting the tumor at earlier stage may lead to better chances of prolonged survival or cure. Although several randomized clinical trials like the Mayo Lung Project (MLP) that were aimed at investigating the effect of x-ray screening on lung cancer did not demonstrate the statistically significant reduction of mortality, efficiency of screening is being reconsidered today. Firstly, the MLP results are still controversial, partly due to screening in the control arm. Secondly, the availability of more sensitive technologies such as computed tomography (CT) has assessing further ignited the debate on the efficiency of screening for lung cancer. To this end, our goal is to predict the impact of CT screening on lung cancer by developing a model that first simulates the outcomes of x-ray screening.

To investigate the effect of screening on lung cancer mortality, we developed a stochastic simulation model that reproduces the life and disease histories of patients at high risk, and evaluates various x-ray screening scenarios for these patients. The core of the Monte-Carlo simulation is the statistical model of the natural history of lung cancer, which is built based on the data from the Surveillance Epidemiology and End Results database. The validation of the model performance under the screening settings was performed by reproducing the MLP trial.

Our simulation model is able to closely match the incidence and mortality rates at seven years after randomization both for the control and intervention arms of the MLP within 95% confidence intervals of the observed results. For the incidence, the observed mean and 95% confidence bounds are 5.27 [4.75, 6.48] in the control arm and 5.68 [5.10 – 6.89] in the intervention; the modeled expected values are 5.16 in the control arm and 5.84 intervention in the intervention arm. The model also accurately reproduces the stage distribution and survival curves observed in the trial. While the MLP showed a 4% mortality increase in the study group, our model predicts a 3% mortality reduction due to screening, and 8% mortality reduction when compared to a hypothetical unscreened control arm. The ability to replicate this x-ray-based randomized clinical trial allows us to extend our studies to evaluate the effectiveness of CT screening for lung cancer using our mathematical model of lung cancer progression.

Stochastic Models for the Stage Progression of Breast Cancer

BRONISLAVA M. SIGAL AND SYLVIA K. PLEVRITIS - DEPARTMENT OF RADIOLOGY

Breast cancer is generally staged as local, regional or distant disease. The probability that a primary breast tumor is associated with an advanced disease stage increases with the tumor's volume at symptomatic detection. It is possible that detecting the tumor at a smaller size, in particular by screening, could result in a less advanced disease stage and improve the patient's prognosis. To quantify the health benefit of breast cancer screening programs with mammography and MRI, we model the natural progression of cancer from less to more advanced stages; in particular, we develop analyze mathematical models of tumor progression in terms of tumor growth and stage transitions.

We have fully explored two alternative stochastic models for the natural history of breast cancer stage progression. Both models are based on clinically and biologically reasonable assumptions and provide comparable fit to data obtained from the Surveillance, Epidemiology and End-Results database on tumor size and stage (local, regional, distant) at symptomatic detection. Interestingly, the models produce different predictions. For example, the models predict different distributions of tumor sizes at stage transitions. They also differ by stage at symptomatic detection for a given tumor volume doubling time. Model I predicts 83% of tumors (unde-
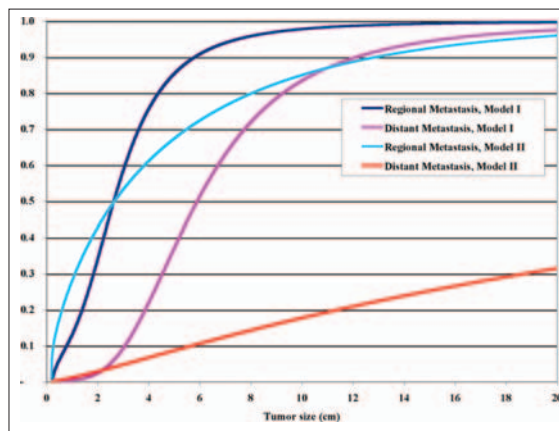
Cumulative distribution function of the tumor size at observable nodal metastasis and observable distant metastasis. Models I and II.

tected) progress to distant stages by the time tumor reaches a diameter of 10 cm whereas Model II predicts that only 18% of tumors progress to distant disease when tumor is 10 cm in diameter. Furthermore, Model I predicts that slower growing tumors are more likely to be detected in advanced stages, whereas Model II predicts that faster growing tumors are more likely to be detected in advanced stages.

This study shows that models based on reasonable assumptions and providing similar fit to the observed population level data could have widely different unobservable properties and consequently provide different predictions of the impact of screening programs. Because natural history models of cancers are increasingly being used to estimate the impact of cancer control programs on the population, the criterion for model selection should not be simply datafit, but also a careful evaluation of the model predictions

Biological Evaluation of a Novel Gene Cationic Nanoparticle for Therapeutics and Imaging of Glioblastoma Multiform (GBM) in Rat Model

MALIKA LARABI, YI-SHAN YANG, STEVEN CHOI, LEROY SIMS, MICHAEL LIM, YING WANG, SAMIRA GUCCIONE

Purpose: In this study therapeutic efficacy, volume and metabolic tumor changes, and toxicity of an anti-angiogenic $\alpha v \beta 3$-targeted gene delivery system was evaluated.

Methods: A mutant Raf-1 gene was delivered using $\alpha v \beta 3$-targeted nanoparticles. The nanoparticle size, zeta-potential, stability and electromicroscopy were determined. Intravenous injections of nanoparticle were given to rats with orthotropic intracranial RT2 tumors. For the toxicity study one single bolus injection was used. Animals were imaged with 18F-FDG-PET and T2-weighted MR. MTD, LD50, comportment, weight, blood chemistry and cell analysis and histopathology was investigated for the toxicity study.

Results: The EM pictures confirmed the small spherical shape, size and the polymerized structure of the nanoparticle. 18F-FDG-PET imaging showed increased FDG uptake in early treatment periods, followed by a continuous decrease in signal intensity that started on day 10. Signal
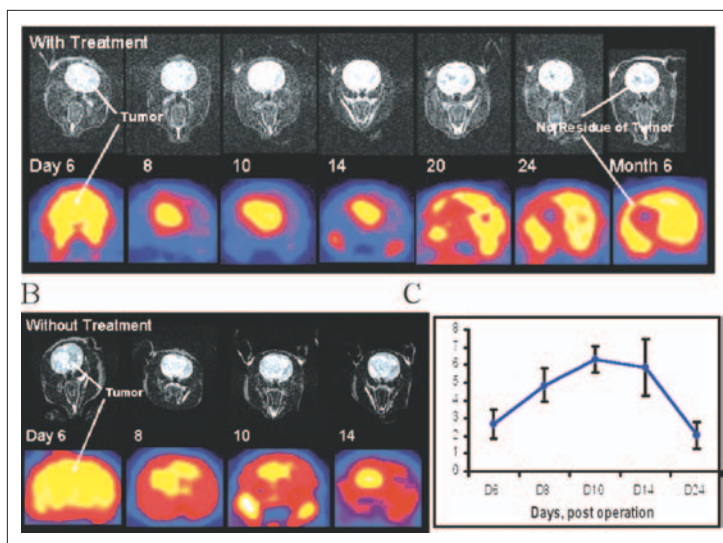
Figure 1. Representative serial T-2 weighted MR (top of A) and 18F-FDG microPET images (bottom of A) Treatments were conducted at days 6, 8, and 10 after tumor initiation. Brightness on the rim of the tumor shown on Day14 MR indicates the development of necrosis associated with a signal decrease in the corresponding PET images. Dark area in the center of the tumor on Days 20 and 24 MR images represent tumor shrinkage, observed also in the corresponding PET images. C representing the Standard Uptake Value (SUV) of 18F-FDG in rat brain tumor with treatment of NP. SUV increases up to day 10 followed by a continuous decrease till the end of the study.

decayed to background at 20 days indicating no tumor residue or recurrence (Figure 1.). T2-weighted-MR imaging showed reduction of tumor size after the treatment. The untreated rats had a continuous increase in FDG uptake and tumor volume until the animals died at 15-27 days post implantation. In toxicity study (rats without tumor) no significant difference has been observed. The blood chemistry and CBC profile of the rat treated with therapeutic and highest doses were comparable to these of control rats.

Conclusion: The targeted ability and high stability of this novel nanoparticle allows a drastic reduction of the total dose administered and the efficacy in GBM rat tumor model. Results were confirmed through in vivo imaging and immunohistochemistry. Further evaluation including biodistribution and functional imaging is necessary to better understand the mechanism of action, and the potential of this therapeutic for clinical translation.

Synthesis and Characterization of Dextran-Coated Nanoparticulate Contrast Agents

MICHAEL ALEXANDER MCDONALD - DEPARTMENT OF RADIOLOGY, LUCAS CENTER FOR MR SPECTROSCOPY AND IMAGING

Advances in instrumentation and data acquisition methods are driving the field of biomedical MRI toward the use of higher magnetic field strengths, where standard clinical MRI gadolinium (III) contrast agents exhibit poor water relaxivity. Although it is anticipated that T2/T2* agents, such as monocrystalline iron oxide nanocompounds, will play a significant role in high-field MRI, the potential use of particulate gadolinium complexes in high-field MRI and molecular imaging is still in its early stages. To date, studies involving the structural and magnetic properties of relatively few crystalline, nanometer-sized gadolinium particulate complexes have been carried out. This is in part because of the challenge of making nanoparticulate suspensions that are stable in aqueous solution. We have been able to better solubilize small particulate gadolinium oxide (SPGO), prevent particle aggregation, and investigate the physicochemical properties of dextran SPGO relevant to its use as a high-field magnetic resonance contrast agent in aqueous solution. Dextran SPGO demonstrates regular crystalline lattices and has a gadolinium oxide electron diffraction pattern consistent
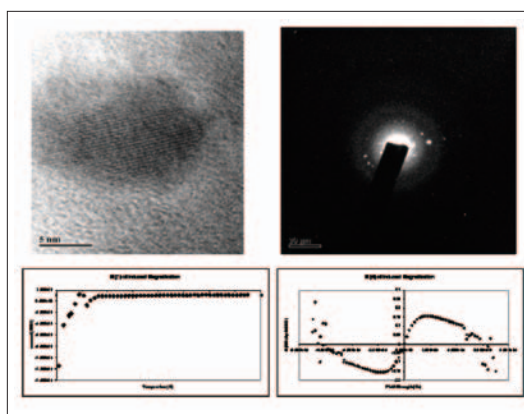
High-resolution Scanning Transmission Electron Microscopy and electron diffraction show the crystal lattice structure while Magnetic Susceptibility plots indicate the superparamagnetic nature of the nanoparticulate.

with that of published X-ray powder diffraction (XPD) patterns. The subtraction XPD pattern of dextran SPGO shows diffraction angles and intensities similar, but not identical, to that of published Gd_2O_3 diffraction patterns. High $r2/r1$ ratios and magnetic susceptibility studies indicate dextran SPGO can be classified as a superparamagnetic compound. Enhanced relaxivity is observed at high magnetic field strength; largely because of solubilization of SPGO via the surface adherent carbohydrate. Perhaps also contributing to the observed relaxivity enhancement is the ideal lattice structure of the central gadolinium oxide crystal and the effects of sonochemical preparation on nanoparticle physicochemical properties. These studies provide a basis for the development of novel nanoparticulate contrast agent platforms capable of improving contrast and sensitivity of detection for high-field MRI and molecular imaging.

REFERENCES/FUNDING SOURCE

McDonald MA, Watkin KL. Investigations into the physicochemical properties of dextran small particulate gadolinium oxide nanoparticles. Acad Radiol 2006; 13:421-427.

Acoustic Fingerprints of Photoacoustic Contrast Agents for Molecular Imaging

Michael Alexander McDonald, Samira Guccione - Department of Radiology

Photoacoustic tomography (PAT) is a multi-modality imaging technique that may play a significant role in early detection and monitoring of breast cancer. There have been few published reports on the development of contrast agents optimized for photoacoustic imaging. We hypothesized that absorbing dye-labeled protein nanospheres would respond to laser stimulation by thermoelastically generated sound production. And furthermore that manipulation of laser pulsing and nanosphere physico-chemical composition could lead to control over nanosphere oscillation and frequency of detection. The primary goals of this study are to demonstrate the utility of labeled protein nanospheres for improved photoacoustic signal generation. Towards this aim we are exploring the enhancement in signal amplitude gained by laser-driven protein nanosphere oscillation vs. that of the precursor material for nanosphere synthesis, i.e., photoacoustically active "monomers," using a phantom vessel and either ultrasound or laser stimulation. The photoacoustic contrast agent (PACA) used in the present studies, fitc-labeled nanospheres suspended in aqueous solution, were synthesized using sonochemical methods. We report the development of stable, unimodal distribution of PACA 650 nanometers in diameter capable of emitting sizable echoes in response to ultrasound stimulation and an even greater increase in signal-to-background in

Advantages: Monomers vs Nanospheres
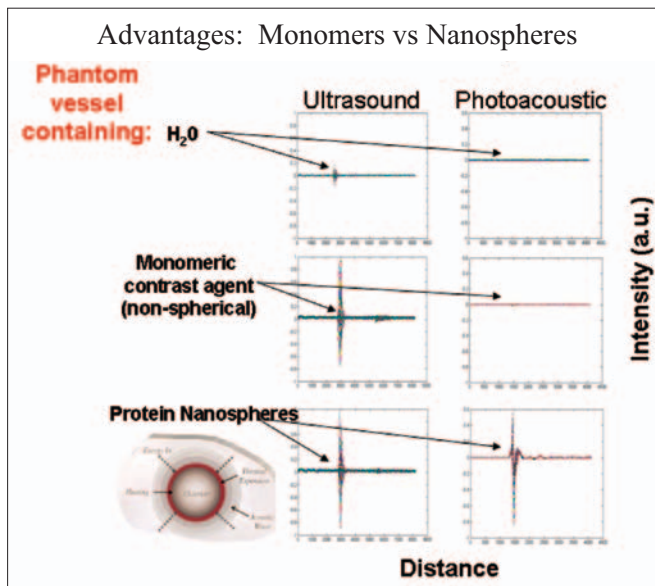
response to laser stimulation. The increase in PA signal amplitude is in part due to the low density and great compressibility of the protein nanospheres subsequent to gas and/or low density liquid incorporation. The great elasticity and strong restoring forces of the nanosphere shell likely results in a sizable relative expansion ratio and subsequent large amplitude of response to increasing driving pressure. The size range at which we are able to achieve monodisperse distribution also makes extravasation of nanospheres for imaging of tumor vasculature more likely and improves the chances of receptor targeted imaging. We are currently making smaller nanospheres (< 100 nm) with the aim of improving signaling characteristics.

REFERENCES/FUNDING SOURCE

McDonald MA, Jankovic L, Shahzad K, Burcher M, Guccione S, Li KCP. Acoustic Fingerprintes of Photoacoustic Contrast Agents for Molecular Imaging. In Press
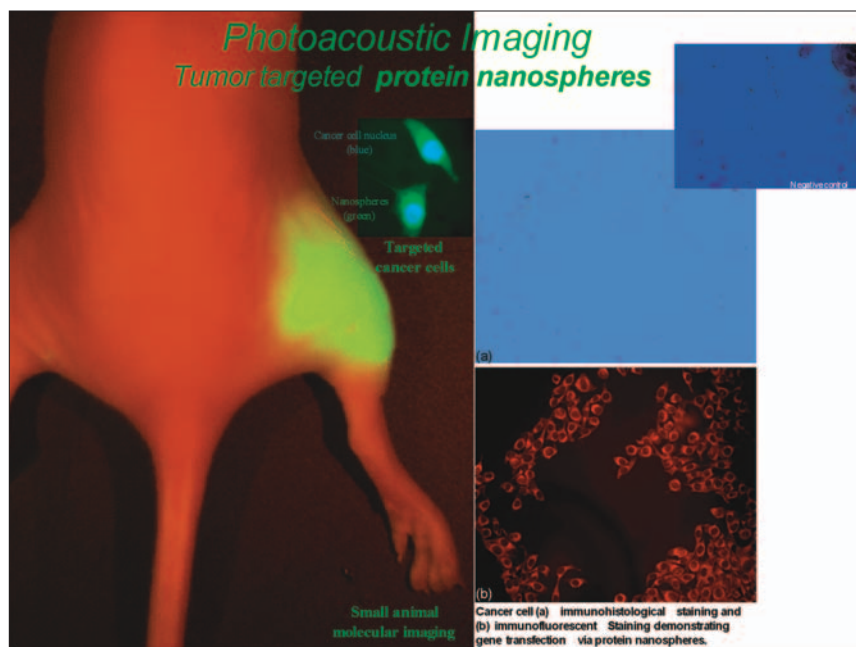
Protein Nanospheres as Photoacoustic Contrast Agents for Imaging, Molecular Targeting and Therapy using CMUT Arrays

Michael McDonald1 , Samira Guccione1 Omer Oralkan2 , Butrus T. Khuri-Yakub2

1Departments of Radiology, and 2Electrical Engineering, Stanford University

Protein nanospheres are target specific diagnostic and therapeutic agents capable of serving as a platform for imaging across several modalities; including optical, MR, CT, US and radioisotope based techniques. We have developed stable, highly absorbing protein nanospheres which emit large echoes in response to ultrasound stimulation and an even greater acoustic response to laser stimulation for photoacoustic imaging. In the present study receptor specific targeting and gene delivery are being evaluated in mammalian cells, phantom models and animal tumor models. The contrast agents used include fitc labeled protein nanospheres (fitc-NS), rhodamine labeled nanospheres (Rhd-NS), eGFP DNA loaded nanospheres (eGFP-NS) and β-galactosidase DNA loaded nanospheres (β-gal-NS). Physical characterization demonstrates negatively charged monodisperse particles. Fluorescent microscopy of fitc-NS and Rhd-NS mouse labeled melanoma cancer cells reveals NS accumulation in tumor cells proportional to NS concentration and incubation time. Fluorescent microscopy of eGFP-NS transfected mouse melanoma cancer cells show high levels of transfection in an incubation time and NS concentration dependent manner. Cancer cell immunohistological staining with anti-eGFP antibody and immunofluorescent anti-(NS) antibody demonstrates NS mediated cancer cell labeling correlates with gene transfection. Analysis of NS mediated β-gal expression via Beta-Glo transfection assay and cell viability analysis indicate NS utility in gene delivery. Agarose gel electrophoresis studies reveal β-gal DNA is associated with NS and likely intact. We demonstrate receptor-specific targeting of cancer cells using a probe synthesis technology amenable to utilization of other relevant biological molecules. The size range at which we are able to achieve mondisperse distribution makes extravasation of nanospheres for imaging of tumor vasculature more likely and improves the chances of receptor targeted imaging. In addition to optimization of photoacoustic response and imaging depth, we are currently exploring the enhancement in sensitivity, resolution, and bandwidth gained by using protein nanospheres with CMUT technology.

References/Funding Source

McDonald MA, Hunter F, Xie J, Guccione S, Li KCP. Molecular Targeting and Therapy for Cancer using Protein Nanospheres. In Press.

In Vivo Molecular Imaging of Human Embryonic Stem Cell Derived Cardiomyocytes After Transplantation Into the Ischemic Myocardium

Cao Feng[1], Ahmad Y Sheikh[2], Xiaoyan Xie[1], Shuan Lin[1], Micha Drukker[3], Sanjiv Gambhir[1], Irving Weissman[3], Robert C. Robbins[2], Joseph Wu[1, 4] - [1]Molecular Imaging Program at Stanford (MIPS) & Departments of [2]Surgery (Cardiothoracic Division) [3]Pathology and Developmental Biology, [4]Medicine and [5]Cardiology, Stanford University School of Medicine

Objective: Embryonic stem (ES) cells are self-renewing multipotent cells that constitute an unlimited cell source for regenerative medicine. In this study, we differentiated human embryonic stem cell into cardiomyocytes (hESC-CM) and tracked their survival and function in a mouse model of acute myocardial ischemia.

Methods: H9 human embryonic stem cells were stably transduced with a self-inactivating lentiviral vector carrying a double fusion (DF) reporter gene. The construct contains an ubiquitin promoter driving firefly luciferase and enhanced green fluorescent protein (LV-pUb-Fluc-egfp). The positively transduced cells were isolated by fluorescence activated cell sorting (FACS). After 10-14 days of culturing, the hESC differentiated into beating cardiomyocyte clusters which appeared in 30-40% of embryonic bodies (EB). Beating hESC-CM (1×10^6) were isolated and injected intramyocardially into SCID mice following 30 minutes of LAD ligation (n=12). Control animals received 30 µl of PBS injection instead (n=10). Longitudinal hESC-CM survival was monitored by optical bioluminescence imaging (BLI). Echocardiography was performed at 2 and 4 weeks post-transplant. Cellular engraftment was confirmed by conventional histologic analysis.

Results: FACS analysis showed 17±5% of transduced hESC were positive for green fluorescence. Their growth characteristics were not significantly different from normal untransduced hESC as assessed by cell viability and proliferation assays (P=NS). Likewise, RT-PCR showed the expression of ectodermal (Sox-2), mesodermal (Brachyury) and endodermal (AFP) differentiation markers were not affected. After hESC-CM transplantation, the cardiac BLI signals decreased progressively from $2.6\times10^6\pm2.7\times10^5$ at day 2, to $1.2\times10^6\pm2.1\times10^5$ at day 7, to $3.6\times10^5\pm5.2\times10^4$ at day 14, and $1.6\times10^5\pm1.9\times10^4$ photons/sec/cm2/steradian at day 21. After 3 weeks, the BLI signal intensity remained stable ($2.2\times10^5\pm5.6\times10^4$ at week 6 and $2.9\times10^5\pm3.0\times10^4$ at week 8), suggesting persistent engraftment of stable hESC-CM graft in the heart. Fractional shortening as measured by echo showed improvement of cardiac function following hESC-CM transplant compared to control ((29±6% vs. 24±6%, P<0.05). Finally, immunohistochemistry confirmed the expression of troponin and smooth muscle actin within the hESC-CM graft.

Conclusion: This is the first study to image the survival of human ES cell derived cardiomyocytes transplanted into ischemic host environments. Using a double fusion reporter gene, we analyzed hESC-CM in vitro by molecular and biological assays, in vivo by BLI, and ex vivo by immunohistochemistry. Furthermore, we present preliminary evidence that hESC-CM therapy can enhance cardiac function following ischemic injury. Ongoing studies will focus on elucidating the mechanisms by which such improvement might occur.
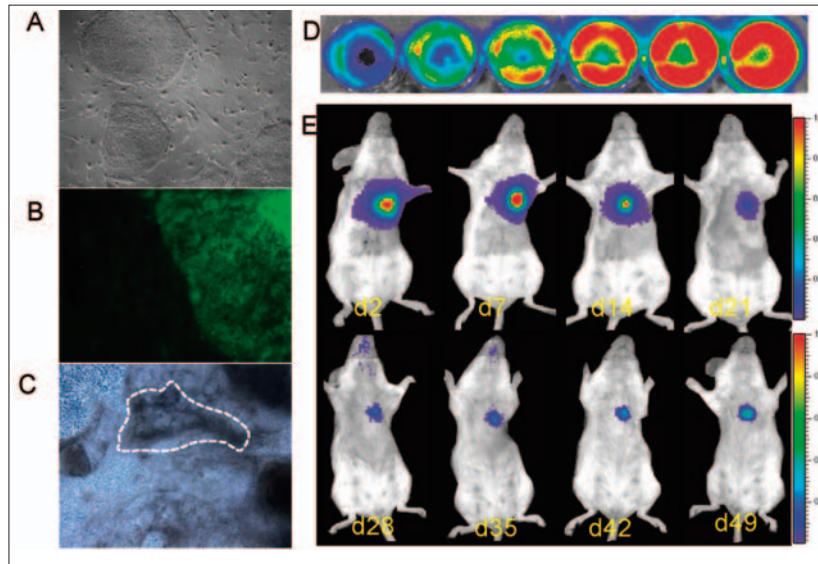
A: Bright field of hESCs (100X); B: GFP+ hESCs (400X); C: Beating area of EBs (100X); D: Bioluminescence signal increased with cell number; E: In vivo cardiac BLI imaging of hESC-CM

Transcriptional Profiling of Reporter Genes Used for Molecular Imaging of Embryonic Stem Cell Transplantation

Joseph C. Wu[1,2,3], Joshua M. Spin[1,3], Feng Cao[2], Shuan Lin[2], Xiaoyan Xie[2], Olivier Gheysens[2], Ian Y. Chen[2], Ahmad Y. Sheikh[3], Robert C. Robbins[3], Anya Tsalenko[4], Sanjiv S. Gambhir[2,] Tom Quertermous[1]

[1]Department of Medicine, Division of Cardiology, [2]Department of Radiology and Bio-X Program, [3]Department of Surgery, Stanford University School of Medicine, and [4]Agilent Technologies, Palo Alto, California

Stem cell therapy offers exciting promise for treatment of ischemic heart disease. Recent advances in molecular imaging techniques now allow investigators to monitor cell fate noninvasively and repetitively. Here we examine the effects of a triple-fusion reporter gene on embryonic stem (ES) cell transcriptional profiles. Murine ES cells were stably transfected with a self-inactivating lentiviral vector carrying a triple-fusion (TF) construct consisting of fluorescence, bioluminescence, and positron emission tomography (PET) reporter genes. Fluorescence-activated cell sorting (FACS) analysis allowed isolation of stably transfected populations. Microarray studies comparing gene expression in nontransduced control ES cells vs. stably transduced ES cells expressing triple fusion (ES-TF) revealed some increases in transcriptional variability. Annotation analysis showed that ES-TF cells downregulated cell cycling, cell death, and protein and nucleic acid metabolism genes while upregulating homeostatic and anti-apoptosis genes. Despite these transcriptional changes, expression of the TF reporter gene had no significant effects on ES cell viability, proliferation, and differentiation capability. Importantly, transplantation studies in murine myocardium demonstrated the feasibility of tracking ES-TF cells in living subjects using bioluminescence and PET imaging. Taken together, this is the first study to analyze in detail the effects of reporter genes on molecular imaging of ES cells.

# In Vivo Visualization of Embryonic Stem Cell Survival, Proliferation, and Migration After Cardiac Delivery

Feng Cao[1]; Shuan Lin[1], Xiaoyan Xie[1], Pritha Ray[1], Manishkumar Patel[1], Xianzhong Zhang[1], Micha Drukker[2], Scott J. Dylla[2], Andrew J. Connolly[2], Xiaoyuan Chen[1], Irving L. Weissman[2], Sanjiv S. Gambhir[1,3], Joseph C. Wu[1,4]

Departments of [1]Radiology, [2]Pathology and Developmental Biology, [3]Bioengineering, and [4]Medicine, Division of Cardiology

Background— Recent studies have shown that stem cell therapy can promote tissue regeneration; however, monitoring stem cells in vivo remains problematic owing to limitations of conventional histological assays and imaging modalities.

Methods and Results— Murine embryonic stem (ES) cells were stably transduced with a lentiviral vector carrying a novel triple-fusion (TF) reporter gene that consists of firefly luciferase, monomeric red fluorescence protein, and truncated thymidine kinase (fluc-mrfp-ttk). ES cell viability, proliferation, and differentiation ability were not adversely affected by either reporter genes or reporter probes compared with nontransduced control cells (P=NS). Afterward, 1x107 of ES cells carrying the TF reporter gene (ES-TF) were injected into the myocardium of adult nude rats (n=20). Control animals received nontransduced ES cells (n=6). At day 4, the bioluminescence and positron emission to-
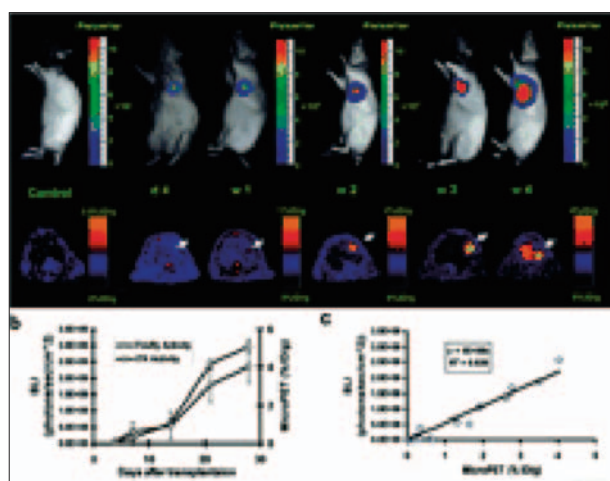
Figure 4. Molecular imaging of transplanted ES cells with bioluminescence and PET imaging. a, To assess longitudinal cell survival, animals were imaged for 4 weeks. A representative study animal injected with ES-TF cells showed significant bioluminescence (top) and PET (bottom) signals at day 4, week 1, week 2, week 3, and week 4. In contrast, control animals had background activities only. b, Quantification of imaging signals showed a drastic increase of fluc and ttk activities from week 2 to week 4. Extracardiac signals were observed during subsequent weeks. c, Quantification of cell signals showed a robust in vivo correlation between bioluminescence and PET imaging (r2=0.92). BLI indicates bioluminescence.

mography signals in study animals were $3.7 \times 10^7 \pm 5.8 \times 10^6$ photons · $s–1 · cm–2$ per steradian (sr) and 0.08±0.03% injected dose/g, respectively (P<0.05 versus control). Both signals increased progressively from week 1 to week 4, which indicated ES cell survival and proliferation in the host. Histological analysis demonstrated the formation of intracardiac and extracardiac teratomas. Finally, animals (n=4) that were treated with intraperitoneal injection of ganciclovir (50 mg/kg) did not develop teratomas when compared with control animals (n=4) treated with saline (1 mL/kg).

Conclusion— This is the first study to characterize ES cells that stably express fluorescence, bioluminescence, and positron emission tomography reporter genes and monitor the kinetics of ES cell survival, proliferation, and migration. This versatile imaging platform should have broad applications for basic research and clinical studies on stem cell therapy.

Novel Donor Mutation Enhances Sensitivity for Non-Invasive Imaging of Bioluminescence Resonance Energy Transfer Signal in Living Subjects

ABHIJIT DE, ANDREAS M. LOENING[1] AND SANJIV S. GAMBHIR[1,2]
MOLECULAR IMAGING PROGRAM AT STANFORD (MIPS) AND BIO-X PROGRAM AT STANFORD, DEPARTMENTS OF [1]RADIOLOGY AND [2]BIOENGINEERING, SCHOOL OF MEDICINE, STANFORD UNIVERSITY

Bioluminescence resonance energy transfer (BRET) is a sensitive detection assay used for studying various protein functions in vitro and in vivo. The current study demonstrates construction and validation of new improved BRET vectors by fusing novel Renilla luciferase (RLuc) mutants (donor), selected for increased quantum yield and stability to the GFP2 acceptor.

Three different mutations of RLuc, a single mutation C124A, a double mutation C124A/M185V, and a combination of eight mutations called RLuc8, were fused with GFP2 and tested in HT1080 fibro-sarcoma cells by using CCD camera based spectral imaging. The new vectors were also tested in a small animal tumor model with implanted cells at various tissue depths.

In comparison to the cells expressing GFP2-RLUC, normalized luciferase signal shows markedly significant (P<0.01) increase of 35 fold for GFP2-RLUC8 fusion, and 25 fold for GFP2-RLUCM185V, whereas BRET signal shows 80 and 40 fold increase respectively. No significant improvements are noticed with the C124A mutation. By establishing HT1080 cells constitutively over-expressing GFP2-RLUC and GFP2-RLUC8 with equal transgene expression, we determined that each GFP2-RLUC8 cell yields a BRET signal that is equivalent to approximately 30 GFP2-RLUC expressing cells. Further, we tested the sensitivity of the new BRET vector by imaging individual stable cells as well as cells at subcutaneous and deeper tissues of animals.

These new BRET vectors with improved BRET efficiency and sensitivity should accelerate the study of distance dependent processes such as protein-protein interaction and protein phosphorylation by measuring the events directly from live cells and from small animal models.

Reproducibility of 2-DEOXY2 [18F]Fluoro D Glucose (FDG) MicroPET Studies in Mice Xenografts

MANGAL S. DANDEKAR, JEFFREY R. TSENG, SANJIV S. GAMBHIR,
MOLECULAR IMAGING PROGRAM AT STANFORD (MIPS), BIO-X PROGRAM, DEPARTMENT OF RADIOLOGY

Objective: 2-deoxy-2-[18F]fluoro-D-glucose (FDG) has been used to image mouse xenograft models with microPET for therapy response. However, the reproducibility of serial scans has not been estimated. The purpose of this study was to determine the reproducibility of FDG microPET studies.

Methods: Mouse tumor xenografts were formed with murine melanoma cells, B16F10 (N=5) and human pancreatic carcinoma cells, MiaPaCa (N=3). A 10 minute microPET R4 (Concorde) scan was performed 1 hour after a 100 μCi FDG injection via the tail vein. A second microPET scan was performed 6 hours later after re-injection of FDG. Twenty-four sets of studies were performed. Mean injected dose per gram (%ID/g) values were calculated from tumor regions of interest. The coefficients of variation (COV) and differences in the mean %ID/g from studies performed on the same day were calculated to determine the reproducibility. Activity from the second scans performed after 6 hours were adjusted by subtracting the estimated residual activity from the first FDG injection.

Results: The COV for the mean %ID/g between FDG microPET scans performed on the same day 6 hours apart was 14.5±11.0%. The difference between mean %ID/g of the two scans was 0.2±1.3%. The tumor size, body temperature, and body weight did not appear to contribute to the variability of the scans.

Conclusions: FDG microPET xenograft mice studies were reproducible with moderately low variability. This level of variability is sufficient for reasonable assessments of serial changes. These results can be applied to follow tumor therapy response or for pre-clinical drug evaluation.

Proteomic Analysis of the Effects of Reporter Genes Used for Imaging Stem Cell Transplant

X Xie[1], F Cao[1], S Lin[1], S Dutta[2], M Brown[2], S Matthewson[2], N Chungfat[2], SS Gambhir[1,3], EW Wang[2], JC Wu[1,4]
[1]Departments of Radiology and Bio-X Program; [2]Stanford Proteomics and Integrative Research Facility;
[3]Bioengineering; [4]Medicine, Division of Cardiology; Stanford University School of Medicine

Objectives: Stem cell transplantation shows exciting promise for treatment of various diseases. To monitor the real-time survival of transplanted stem cells in living subjects, reporter genes are often introduced into stem cells. However, their effects on stem cell function remain poorly defined to date. To this aim, we examined the effects of a novel and versatile triple fusion (TF) reporter gene on murine embryonic stem (ES) cell function using proteomic analysis.

Methods: Murine ES cells were stably transduced with a self-inactivating lentiviral vector carrying a fluorescence (firefly luciferase; Fluc), bioluminescence (monomeric red fluorescence protein; mrfp), and positron emission tomography (mutant herpes simplex virus truncated thymidine kinase; HSV-ttk) reporter gene (ES-TF). Stably transduced populations were isolated with fluorescence activated cell sorting (FACS). Afterwards, proteins from control untransduced ES and ES-TF cells labeled with 16O and 18O isotope were analyzed and identified by combined matrix-assisted laser desorption/ionization time-of-flight (MALDI TOF) mass spectroscopy and reverse phase chromatography using Mascot search engine. The viability, proliferation, and differentiation of both control ES and ES-TF cells were also analyzed prior to subcutaneous injection into the right and left shoulders of nude mice, respectively (n=12). ES-TF cell survival in living animals was detected by bioluminescence and positron emission tomography (PET) imaging using the D-Luciferin (125 mg/kg) and 9-[4-fluoro-3-(hydroxymethyl)butyl]guanine ([18F]-FHBG) (115±27 µCi) reporter probes, respectively.

Renilla Luciferase Variants with Green Emission Peaks for Improved Imaging in Living Subjects

Andreas M. Loening[1], Anna M. Wu[3], Sanjiv S. Gambhir[1,2] - Molecular Imaging Program at Stanford (MIPS),
Departments of [1]Radiology & [2]Bioengineering, Bio-X Program, Stanford, [3]Crump Institute for Molecular Imaging,
Department of Molecular & Medical Pharmacology, UCLA School of Medicine

Renilla luciferase (RLuc) is commonly used as a reporter gene either on its own or in conjunction with firefly luciferase. Its use in bioluminescence imaging, however, has been hampered by the emission spectrum generated when it catalyzes its substrate coelenterazine (481 nm peak, 497 nm mean), as blue wavelength photons are strongly attenuated in biological tissues. To overcome this difficulty, we have explored red-shifting the emission spectrum of RLuc in order to increase its utility for small animal imaging applications.

Through the use of a homology model of RLuc and an estimate of the substrate orientation in the active pocket, residues were selected for site-directed mutagenesis. Starting from a stabilized and more active variant of RLuc (RLuc8) as the parental enzyme, a range of emission shifts were created (475-513 nm peak, 491-536 nm mean) by these single residue alterations. As these variants with active pocket mutations invariably exhibited significantly reduced enzymatic activity, further random mutagenesis and site-specific saturation mutagenesis studies were undertaken. These experiments resulted in additional RLuc variants with up to 60 nm red-shifted emission spectra (541 nm peak, 557 nm mean). More importantly, some of the identified variants showed only minimal changes in enzymatic activity. The most promising for in vivo use is a 4 mutation variant of RLuc8 that exhibits a green emission spectrum (532 nm peak, 545 nm mean) yet retains 85% of RLuc8's enzymatic activity. It is estimated that at a depth of 5 mm of liver tissue, this 4 mutant variant of RLuc8 will result in 23-fold more light escaping the tissue than RLuc, with 70% of this improved performance arising from the green peaked emission spectrum. This is a significant improvement for imaging over previous RLuc variants, and should greatly aid the use of Renilla luciferase as an in vivo reporter gene.

Evaluation of a Novel Rectangular Variable Field of View Whole Body Clinical PET System Design

Frezghi Habte, Guillem Pratx, Peter D. Olcott, Craig S. Levin - Department of Radiology

Conventional whole body PET systems have detectors arranged in a cylindrical geometry (~80 cm diameter and ~16 cm axial length). The system diameter determines the solid angle coverage, which currently limits the coincidence photon detection efficiency (a.k.a. photon sensitivity) to a few percent for existing systems. Low photon sensitivity in current systems has also restricted the detector pixel resolution to be ~4 mm for SNR considerations. Since the detectors do not provide depth-of-interaction (DOI) information, the useful field of view (FOV) is limited to ~55 cm to minimize the parallax error. There have been many recent studies describing the development of new PET detectors with DOI information. With adequate DOI resolution, a substantial enhancement of the photon sensitivity can be achieved by arranging the detector closer to the subject, providing adequate photon sensitivity for the use of higher resolution detectors to improve reconstructed spatial resolution. In this work, Monte Carlo simulation is performed using a standard block PET detector design (5.4 x 5.4 cm2 cross section area) consisting of arrays of LSO crystals of 4x4x20 cm3 coupled to PMTs

for two configurations: 1) a standard cylindrical geometry and 2) a rectangular geometry with four overlapping detector panels that can be translated with respect to each other. The rectangular geometry allows for the FOV to be adjusted specifically for the subject in consideration (e.g small adults, children, brain, breast, prostate etc). Simulation results showed slight improvement in photon sensitivity (>8 cps/kBq) for the rectangular system than for a cylindrical system (~7 cps/kBq) with the same transaxial and axial FOV (83 and 16 cm) for a line source at the center according to the NEMA NU 2-2001 standard measurement. More than twofold improvement in photon sensitivity is obtained when the same number of block detectors used in the standard cylindrical system are arranged in a rectangular geometry with smaller FOV (< 55 cm) with the detectors in close proximity to the subject. This paper will present the result of simulation study for photon sensitivity; count rate performance and reconstructed spatial resolution for the proposed rectangular PET system design compared to conventional cylindrical system.

Event Classification Techniques for List-Mode Positron Emission Tomography

Angela M K Foudray, Craig S Levin, Garry Chinn - Department of Radiology

Using the Monte Carlo package GATE, we studied a small animal detector system comprising segmented LSO scintillation crystal coupled to a position-sensitive avalanche photo-detector. The details of each Compton scatter interaction and photoelectric absorption in the scintillation crystals, for every annihilation photon, were written to a file. In the system, all Compton and photoelectric interactions from one annihilation photon which occur in one PSAPD can not resolved as separate interactions; only their center of mass (COM) position and energy are determined by the PSAPD. All subsequent positioning calculations therefore, were performed on the data after an intra-PSAPD COM calculation. A maximum likelihood approach was taken to predict the position and incident angle of an event with interactions in two or more PSAPDs due to the relatively low intrinsic energy (12%) and spatial (~2mm) resolution of this system as compared to cameras that utilize the Klein-Nishina formula for determining photon scattering angle probability. Multiple interactions that occur in only one PSAPD are not individually resolvable by the detector and look the same as a photoelectric interaction. The maximal probability in (location, angle) space was calculated from the product of the probabilities of the COM location and interaction locations and energies. These probabilities were calculated by constructing the probability density function (PDF) of the COM of an event and the PDF of the interaction locations and energies for each training incident location and angle using Bayes' equation. Using this formalism, we have developed a means to predict interaction location and incident angle for realistic data from our small animal PET detector that is capable of measuring depth of interaction. Using a maximum likelihood approach, we were able to predict incident angle to within +/- twelve degrees FWHM. This information will provide a means to reject non-true coincidences that fall outside of our incident angle resolution, beyond implementing energy and time windowing for scatter and random rejection. Other uses of this technique include utiliz-

ing single events that fall within the energy window (PET + electronically collimated SPECT).
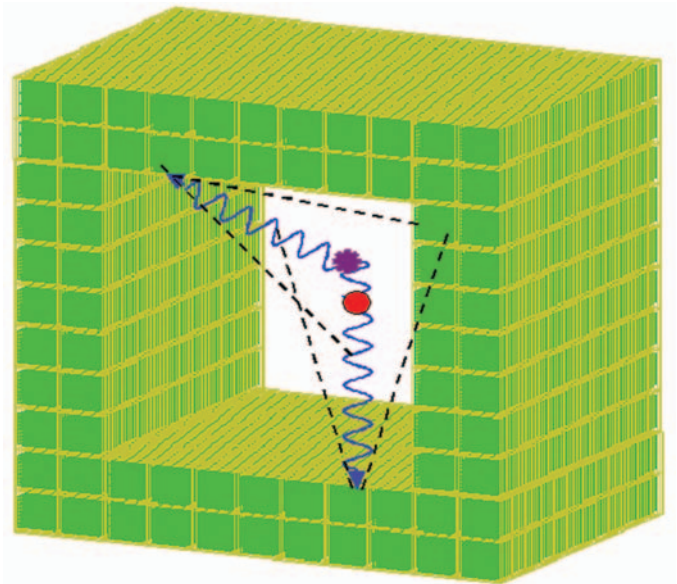
Illustration of event localization with angular information.

# Optimization of a PET Breast Imaging System Utilizing Monte Carlo Simulation

ANGELA M K FOUDRAY, FREZGHI HABTE, CRAIG S LEVIN, PETER D OLCOTT - DEPARTMENT OF RADIOLOGY

We are investigating a high-sensitivity, high-resolution positron emission tomography (PET) system for clinical use in the detection, diagnosis and staging of breast cancer. Using conventional figures of merit, design parameters were evaluated for count rate performance, module dead time, and construction complexity. The detector system modeled comprises extremely thin position-sensitive avalanche photodiodes coupled to lutetium oxy-orthosilicate scintillation crystals. We studied 10 systems with various numbers of heads, all with the same effective field of view (FOV) of 16cm. All systems acquired data without breast compression using a phantom uniformly filled with 200 µCi of 18F and water, a 16cm diameter and 12cm length. Investigations of detector geometries with Monte Carlo indicated that one of the largest impacts on sensitivity is local scintillation crystal density, even when systems had the same average scintillation crystal densities (same crystal packing fraction and system solid-angle coverage). Of the ten systems simulated, the configuration with four heads enclosing a box-shape field of view produced
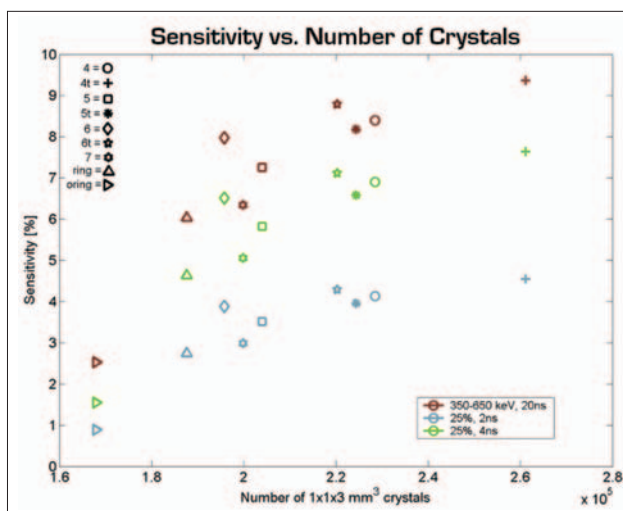
Sensitivity vs. system configuration. Nomenclature: the number specifies the number of heads in the system, the "t" designation means that the heads are translated to reduce gaps between heads. All systems have the same field of view of 16 cm.

the best overall sensitivity. This four-headed system was further investigated along with a traditional cylindrical system for scattered, random and true count rate performance for various energy and coincidence time windows. The box-shaped system had superior count rates and true counts / total counts fraction for all energy and coincidence time windows, with an optimal energy window of 24% of 511 keV and coincidence time window of 4ns. Further studies that we are currently undertaking include scintillation crystal size optimization, positioning algorithms, algorithms to determine incident annihilation photon angle, and reconstructed image quality of the considered system configurations.

Accelerated List-mode 3D-OSEM for Positron Emission Tomography on Graphics Processing Units

G PRATX[1, 2], G CHINN[1], F HABTE[1], PD OLCOTT[1], CS LEVIN[1] - DEPARTMENTS OF [1]RADIOLOGY AND [2]ELECTRICAL ENGINEERING

Advanced list-mode image reconstruction algorithms such as list-mode 3D ordered-subset expectation maximization (OSEM) are needed to leverage the potential performance of high resolution PET systems with depth-of-interaction capabilities. Such algorithms are computationally intensive. Therefore, we used graphics processing units (GPU) to accelerate list-mode 3D-OSEM by an order of magnitude with respect to CPU-based implementations. Primarily designed to deliver high-definition graphics for video games in real-time, GPUs are now increasingly being used as cost-effective high-performance co-processors for scientific computing. Parallelizable algorithms such as list-mode 3D-OSEM get drastically accelerated when the 32 programmable pipelines, clocked at 550 Mhz of the GPU are used to carry the heaviest part of the computation: the line forward projections and back-projections.

Processing time was measured for both algorithms. A single GPU (GeForce 7900 GTX, NVIDIA) performed image reconstruction 30 times faster than the CPU version of the same algorithm.

A quantitative evaluation of this novel technique was performed on Monte-Carlo simulated data and showed that the image quality was not degraded by using the GPU in place of the CPU. In addition, the GPU architecture can efficiently implement the more accurate trilinear interpolation projection technique. Doing so resulted in an improvement of the contrast recovery, noise and mean-square error over the simple Siddon's projection technique.

GPUs can make complex image reconstruction algorithms for high-resolution PET more practical for both clinical and research use.
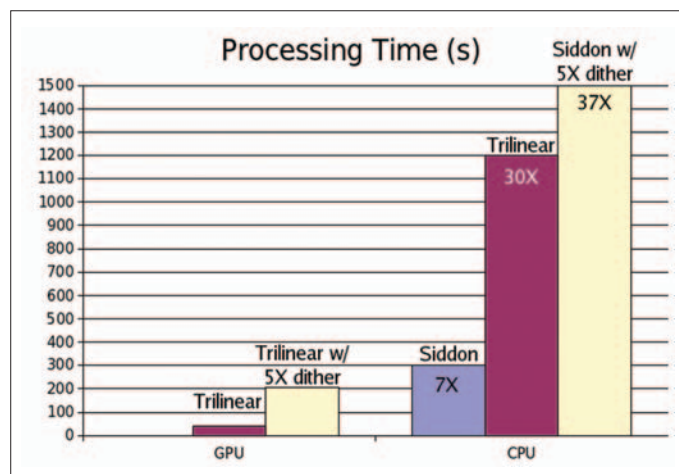
Comparison of processing time for different algorithms implemented on GPU and CPU. 1,000,000 counts were reconstructed using one iteration of list-mode OSEM.
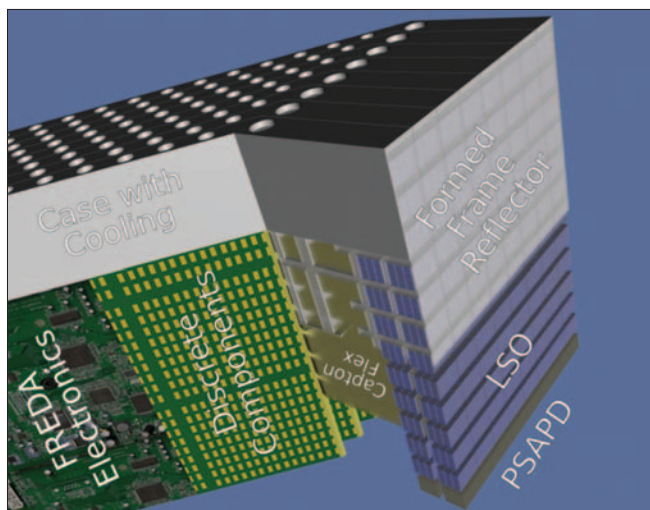
Fast Readout ASIC for Position Sensitive Avalanche Photodiodes in 1 mm resolution application specific PET systems

Peter D. Olcott[1,2], Craig S. Levin[1,2], Tumay Tumer[3], Martin Clajus[3], Victoria Cajipe[3] and S. Hayakawa[3]

Department of [1]Radiology, [2]Molecular Imaging Program, Stanford University, Stanford University, [3]Nova R&D, Inc, Riverside, CA

Position sensitive avalanche photodiodes (PSAPD) are a promising detector that may replace photomultiplier tubes in very high resolution depth-of-interaction clinical and small animal PET systems. FREDA (Fast Readout Electronics for Diode Arrays) ASIC, a 64 channel charge sensitive preamplifier, shaping amplifier, CFD trigger, and sample-hold ASIC, was designed for the low noise , high speed, and high density readout requirement of a 1 mm resolution breast-dedicated PET camera that can locate the 3-D photon interaction coordinates. A 22Na source was used to flood-irradiate two different LSO crystals placed on the 8x8mm2 PSAPD detector. For these measurements, a single channel of the FREDA front-end was connected to the PSAPD. We have characterized the front-end low noise charge sensitive pre-amplifier (LNA) and shaping amplifier of the ASIC. The front-end shaping electronics achieved 12.6%

A cut-away visualization of a 1 mm resolution breast-dedicated PET camera that uses the FREDA ASIC to readout the PSAPD detectors. The panel consists of many small position sensitive avalanche photodiodes that must be compactly readout by the data acquisition electronics.

energy resolution with an 8x8x1 mm 3 LSO sheet crystal, and 6.3% a 2x2x3 mm3 single LSO crystal at 511 keV. The FREDA ASIC-PSAPD detector needs further evaluation to determine the spatial resolution, and timing resolution of a PET detector module. The front-end electronic components of the FREDA ASIC provide performance that meets or exceeds discrete electronics. The ASIC provides the compact readout necessary for our portable PET detector.

Image Reconstruction Dual-Panel Breast-Dedicated PET System

Garry Chinn, Angela Foudray, Jin Zhang, Craig Levin - Department of Radiology

We investigated a fully 3-D list-mode ordered subset expectation maximization (OS-EM) algorithm for reconstructing images for a novel 1 mm resolution dual panel breast-dedicated positron emission tomography system with 3-D photon positioning capability. The proposed system will improve the detection of lesions in breast tissue by offering higher resolution and sensitivity than existing clinical PET systems.

The Monte Carlo package GATE was used to simulate 100x150 mm2 dual-panels comprising arrays of 1x1x3 mm3 LSO crystals coupled to novel thin position sensitive avalanche

Three planes of 2.5 mm spheres in a 5 x 5 grid were reconstructed. Shown is a single plane.

photodiodes oriented edge-on with respect to incoming photons. The simulated breast tumor phantom consisted of 125 spheres of 2.5 mm diameter in one quadrant of the FOV with a center-to-center separation of 8 mm, 18.25 mm, and 12 mm in the x, y and z directions, respectively (x is normal to the panel faces, y and z are along the 150 mm and 100 mm panel detector dimensions, respectively). Spheres were placed all the way out to the edge of the FOV in all three directions. The FOV was uniformly filled with water with 60 μCi (2.22 Mbq) of F-18 activity; the spheres were filled with a 10:1 activity concentration ratio to background (each sphere contained 8 nCi or 303 Bq). A one minute acquisi-

tion, with a 450-572 keV energy window, and a 4 ns time window, produced ~10 million counts. Limited angle tomographic images were reconstructed with a single iteration with 8 subsets of the list-mode, 3-D OS-EM algorithm with rough normalization and without attenuation correction.

We showed that for 4 cm panel separation, that a fully 3-D list-mode OS-EM algorithm could visualize 2.5 mm spheres all the way to the edge of the field of view. The sensitivity at the center of the field of view is over a thousand times greater than at the corners. We are continuing to investigate normalization and regularization strategies for addressing the wide variations in sensitivity in the dual-panel system.

Coincidence Measurements with a 1mm Resolution 3-D Positioning Scintillation Detector for PET that uses Scintillation Light Multiplexing

Frezghi Habte, Peter Olcott, Craig S. Levin - Department of Radiology

1 mm resolution PET systems are being developed for breast and small animal imaging. These PET systems consists of pixellated lutetium oxyorthosilicate (LSO) crystals coupled to position sensitive avalanche photodiodes (PSAPDs) with 8x8 mm2 active area and ~200mm thickness. The detectors are designed to provide accurate 3D photon interaction positioning with 1 mm axial/transaxial resolution and 3 mm depth-of-interaction resolution. We are studying a new crystal array that uses light multiplexing to read two layers of LSO crystals using a single PSAPD detector to reduce by a factor of two the number of PSAPDs in the system. The crystal consists of a dual-layer LSO sheet crystal (2x8x9 mm3) with slots on either side forming crystal pixels (1x1x3 mm3) in two effective layers that are offset by a half crystal pixel width with respect to each other in both directions. This paper presents the result of scanned coincidence time and spatial resolution measurements performed. A flood measurement using 22Na (511 keV) source fully resolved all crystal-pixels including the half crystal pixels (1x1x1.5 mm3) at the edge of the top layer with > 5: 1 peak to valley ratio. Due to strong optical coupling between top and bottom layers, two twin peaks have been resolved within each 3 mm long crystal pixel with an average of 2.5:1 peak to valley ratio. After crystal segmentations to a half crystal pixel (1x1x1.5 mm3) for each resolved individual crystal peak, an average energy resolution of 15% FWHM was obtained when a specular reflector was inserted in the slots. Coincidence measurements irradiating the detector system from side were performed to determine the time and intrinsic spatial resolution of the detector. A coincidence time resolution of < 5 ns was obtained after energy gating. This preliminary result provided relatively worse energy and time resolution compared to energy resolution (12%) and time resolution (2 ns) obtained for non-multiplexed single layer detector system. The energy resolution is expected to improve with optimized reflector material and configuration. We also expect an improvement of time resolution to ~ 2 ns with optimized data acquisition electronics. However, an average intrinsic spatial resolution of ~1.27±0.17 mm was obtained for both slotted layers, which is comparable to the result previously reported for a single layer non-multiplexed detector system.

Bioluminescent Quantum Dot Conjugates for Imaging in Living Subjects

Min-Kyung So, Chenjie Xu, Andreas Loening, Sanjiv S. Gambhir, Jianghong Rao - Department of Radiology

Introduction: Quantum dots (QDs) have generated wide interest because of their potential use in imaging of live biological samples. All existing QDs, however, require excitation from external illumination sources. We developed a new set of QDs that emit long wavelength (from red to infrared wavelength) light without external illumination, thus eliminating photo bleaching and high fluorescent background.

Methods: We coupled QDs that can emit a bioluminescent signal between 605 and 800nm to a mutant of the bioluminescent protein Renilla luciferase (Rluc8) which produces light in the presence of substrate coelenterazine. This method is based on the principle of bioluminescence resonance energy transfer (BRET), which is an energy transfer phenomenon between Rluc8 as the donor and QDs as the acceptor. We examined the possibility of multiplex bioluminescence imaging in vitro and in the living mouse.

Results: The efficiencies, determined by the ratio of the integrated BRET emission to the Luc8 emission, were 70 ~ 230% for the Luc8 conjugated QDs (QD605-Luc8, QD655-Luc8, QD705-Luc8, QD800-Luc8). The BRET emission from each conjugate could be selectively distinguished from the emissions of other conjugates. The three kinds of QD-conjugates injected into a mouse gave BRET emissions, and each BRET emission was distinguished with appropriate filters. According to the animal data, the long wavelength BRET emissions were more easily detected, especially in deep tissues.

Conclusion: These unique features of BRET based QD probes should open many new avenues for QD-based multiplexed imaging of living subjects, especially for imaging biological events at deep tissues in small animals.

Ribozyme-Mediated Imaging of p53 mRNA in Living Animals

Gayatri Gowrishankar, Min-Kyung So, Sumitaka Hasegawa & Jianghong Rao
Departments of Radiology and Bio-X Program, Molecular Imaging Program at Stanford,
Stanford University School of Medicine

Introduction: Group I introns of the ciliated protozoan, Tetraymena thermophila, constitute a class of catalytic RNA molecules or ribozymes, capable of catalyzing cis and trans-splicing reactions. We report here the use of the trans-splicing form of the Tetrahymena ribozyme in imaging the mRNA expression of the p53 gene in living mice.

Methods: Plasmid constructs were designed with a 200nt p53-targeting sequence, the group I intron of the Tetrahymena ribozyme and the complete ORF of the firefly luciferase reporter. COS-7 cells were transfected with plasmid constructs expressing the p53 mRNAs, and the ribozyme-luciferase reporter and cell lysates prepared for RNA analysis by RT-PCR and luciferase activity assay in vitro. For the animal imaging study, 3x106 COS-7 cells transiently transfected with the same plasmids were subcutaneously injected into nude mice (n=6) 48hrs after transfection. The mice were imaged every day in a CCD camera after D-Luciferin injections.

Results: In vitro analysis revealed that although spliced products as seen from the RT-PCR were visible as early as 24hrs after transfection, detectable differences in splicing-dependant luciferase activity were seen only at 48hrs, with the peak at 72hrs. The animal experiments substantiated the in vitro data. A 9.5±1.9 fold difference was observed between tumors with and without the p53 mRNA 24hrs following the tumor implant (72hrs after transfection).

Conclusion: We have shown here the first example of imaging ribozyme-mediated trans-splicing activity in living animals. This splicing-dependant reporter assay offers exciting opportunity to directly image endogenous mRNAs, especially over-expressed tumor-specific mRNAs in living subjects.

A Novel Thiol-Reactive 18F-Labeling Agent

Weibo Cai, Xianzhong Zhang, Yun Wu, Xiaoyuan Chen - Department of Radiology

Objective: The objective of the present work was to develop a novel thiol-reactive prosthetic group for 18F-labeling of peptides and proteins via selective conjugation with a sulfhydryl group.

Methods: A sulfhydryl group was introduced to monomeric and dimeric Arginine-Glycine-Aspartic acid (RGD) peptides (c(RGDyK) and E[c(RGDyK)]2, both potent integrin $\alpha v\beta 3$ antagonists) via N-succinimidyl S-acetylthioacetate (SATA) followed by deprotection. N-[2-(aminoethyl)maleimide]-4-[18F]fluorobenzamide ([18F]AMFB) was synthesized by coupling N-succinimidyl 4-[18F]fluorobenzoate ([18F]SFB) with N-(2-aminoethyl)-maleimide. [18F]AMFB was then reacted with the thiolated RGD peptides to yield [18F]AMFB-SRGD (RGD monomer) and [18F]AMFB-SRGD2 (RGD dimer). These two tracers were subjected to receptor binding assay, in vivo metabolic stability assessment, biodistribution and microPET imaging studies in murine xenograft models.

Results: [18F]AMFB was synthesized in 150 ± 20 min starting from [18F]F-, with decay-corrected radiochemical yield of 13.0 ± 5.1 % and specific activity of 150~200 TBq/mmol. The advantage of labeling the sulfhydryl group using [18F]AFMB over labeling the primary amino group with [18F]SFB was confirmed as conjugation of monomeric and dimeric sulfhydryl-RGD peptides with [18F]AMFB was achieved in high yields (85 ± 5 % non-decay-corrected based on [18F]AMFB). Non-invasive microPET imaging and direct tissue sampling experiments demonstrated that both tracers had integrin specific tumor uptake in subcutaneous U87MG glioma and orthotopic MDA-MB-435 breast cancer xenografts. For the monomeric tracer, U87MG and MDA-MB-435 tumor uptake were 1.27 ± 0.50 and 1.04 ± 0.28 at 60 min post-injection while for the dimeric tracer, the uptakes in the U87MG and MDA-

[18F]AMFB-SRGD2
MDA-MB-435   U87MG
3 %ID/g
0 %ID/g
2 h Post-injection
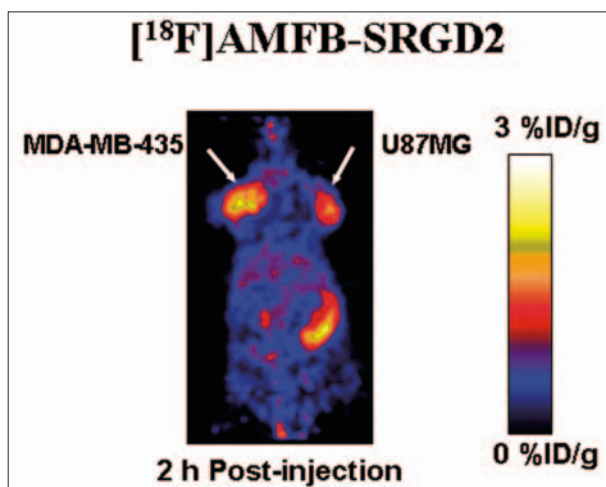
MB-435 tumor were significantly higher at 2.14 ± 0.33, 2.11 ± 0.48, respectively. Different in vivo kinetics of the two tracers was attributed to their differences in integrin affinity and lipophilicity.

Conclusion: The relatively good metabolic stability and favorable pharmacokinetics of the dimeric RGD peptide-based tracer [18F]AMFB-SRGD2 warrant further investigation in both preclinical and clinical settings for documenting tumor integrin expression. [18F]AFMB also provides a general method of labeling thiol-containing peptides, proteins, antibodies, as well as 5'-thio-functionalized oligonucleotides in high radiochemical yield and high specific activity for successful PET applications.

In Vitro and In Vivo Characterization of 64Cu-Labeled Abegrin™, a Humanized Monoclonal Antibody against Integrin αvβ3

Weibo Cai,[1] Yun Wu,[1] Kai Chen,[1] Qizhen Cao,[1] David A. Tice,[2] and Xiaoyuan Chen[1], [1]The Molecular Imaging Program at Stanford (MIPS), Department of Radiology and Bio-X Program, Stanford University School of Medicine, [2]MedImmune, Inc., Gaithersburg, Maryland

Abegrin™ (MEDI-522, or Vitaxin®), a humanized monoclonal antibody (mAb) against human integrin αvβ3, is in clinical trials for cancer therapy. In vivo imaging using Abegrin™-based probes is needed for better treatment monitoring and dose optimization. In this study we conjugated Abegrin™ with macrocyclic chelating agent DOTA at five different DOTA/Abegrin™ ratios. The conjugates were labeled with 64Cu (t1/2 = 12.7 h) and tested in three human (U87MG, MDA-MB-435, and PC-3) and one mouse (GL-26) tumor models. The in vitro and in vivo effects of these 64Cu-DOTA-Abegrin™ conjugates were evaluated. The number of DOTA per Abegrin™ varied from 1.65 ± 0.32 to 38.53 ± 5.71 and the radiolabeling yield varied from 5.20 ± 3.16 to 88.12 ± 6.98 % (based on 2 mCi 64Cu per 50 μg DOTA-Abegrin™ conjugate). No significant difference in radioimmunoreactivity was found among these conjugates (between 59.78 ± 1.33 % and 71.13 ± 2.58 %). MicroPET studies revealed that 64Cu-DOTA-Abegrin™ (1000:1) had the highest tumor activity accumulation (49.41 ± 4.54 %ID/g at 71 h post-injection for U87MG tumor). The receptor specificity of 64Cu-DOTA-Abegrin™ was confirmed by effective blocking of MDA-MB-435 tumor uptake with co-administration of non-radioactive Abegrin™. 64Cu-DOTA-IgG (isotype control) exhibited background level tumor uptake at all time points examined. Appreciable uptake at early time points in GL-26 mouse glioma (10.07 ± 2.43 %ID/g at 25h post-injec-

tion) was likely attributed to passive targeting based upon enhanced permeability and retention effect of the tumor, as evidenced by declined tumor uptake after 25h post-injection. The success of integrin αvβ3 specific tumor imaging using 64Cu-DOTA-Abegrin™ may be translated into the clinic to characterize the pharmacokinetics, tumor targeting efficacy, dose optimization and dose interval of Abegrin™ and/or Abegrin™ conjugates. Chemotherapeutics or radiotherapeutics using Abegrin™ as the delivering vehicle may also be effective in treating integrin αvβ3-positive tumors.

Positron Emission Tomography Imaging of Colorectal Cancer Using 18F-labeled Anti-CEA Diabody T84.66

Weibo Cai[1], Tove Olafsen[2], Xianzhong hang[1], Anna M. Wu[2], Xiaoyuan Chen[1], [1]Molecular Imaging Program at Stanford (MIPS) and Bio-X Program, Department of Radiology, Stanford University, [2]Crump Institute for Molecular Imaging, Department of Molecular and Medical Pharmacology, David Geffen School of Medicine at UCLA, Los Angeles

In this study we investigated the 18F-labeled anti-carcinoembryonic antigen (CEA) T84.66 diabody, a genetically engineered non-covalent dimer of scFv, for microPET imaging of CEA expression in xenograft-bearing mice.

Methods: 18F-labeling of the anti-CEA T84.66 diabody (molecular weight 55 kDa) was achieved via N-succinimidyl-4-18F-fluorobenzoate (18F-SFB). Biodistribution of 18F-FB-T84.66 diabody was evaluated in athymic nude mice bearing subcutaneous LS 174T human colon carcinoma and C6 rat glioma tumors. Serial microPET imaging studies were carried out to further evaluate in vivo targeting and pharmacokinetics.

Results: Radiolabeling required 35 ± 5 min starting from 18F-SFB and the tracer 18F-FB-T84.66 diabody was synthesized with specific activity of 1.83 ± 1.71 TBq/mmol. The decay-corrected radiochemical yield was 1.40 ± 0.16 % (n = 4) and the radiochemical purity was > 98%. Radioimmunoreactivity was 57.1 ± 2.0 %. 18F-FB-T84.66 diabody showed rapid and high tumor uptake with fast clearance from the circulation in the LS 174T xenograft model as evidenced by both microPET imaging and biodistribution studies. High-contrast microPET images were obtained as early as 1h post-injection of 18F-FB-T84.66 diabody and only background level of activity accumulation was found in CEA-negative C6 tumor. The tracer exhibited predominantly renal clearance,

with some activity in the liver and spleen at early time points.

Conclusion: 18F-labeled diabody represents a new class of tumor-specific probes for PET imaging based on targeting cell-surface antigen expression. 18F-FB-T84.66 diabody can be used for high contrast microPET imaging of CEA-positive tumor xenografts. It may be translated into the clinic for PET imaging of CEA-positive malignancies

PUBLICATIONS & PRESENTATIONS

Peer-Reviewed Presentations at Scientific Meetings

ISMRM 2006
14th Scientific Meeting
Seattle, WA, May 2006

Askoy M., C. Liu, M. E. Moseley, R. Bammer. A Self-navigated Spiral In & Out Pulse Sequence Design for Retrospective Motion Correction

Bammer R., C. Liu, M. Aksoy. Improving Rigid Head Motion Correction Using Parallel Imaging.

Bammer R., E. Rubesova, A. White, S. T. Skare, P. Beatty, A. Brau. Improving Image Quality in Fetal MRI using Autocalibrating Reconstruction for Cartesian (ARC) Sampling.

Bammer R., M. Markl. Spectrally Sensitive Imaging Using Balanced Steady State Free Precession.

Brau A.C., P. J. Beatty, S. Skare, R. Bammer. Efficient Computation of Autocalibrating Parallel Imaging Reconstructions.

Clayton D.B., S. Skare, R. Newbould, R. Bammer. SENSE and GRAPPA Reconstruction of Multi-Shot Multi-Echo EPI Data.

Conolly S.M., B.A. Hargreaves, A. Chen, L. Li. A Pyrolytic Graphite Foam for Magnetic Susceptibility Matching to Human Tissue. p. 1378.

Cukur T., N.K. Bangerter, J. DiCarlo, B.A. Hargreaves, D.G. Nishimura. Flow-Independent Hand Angiography with 3D Balanced SSFP Imaging. p. 1967.

Draper C., T.. Besier, G. Beaupre, S. Delp, G. Gold. Males have Thicker Patellofemoral Joint Cartilage than Females. p. 1236.

Ennis D.B., G. Kindlmann, M. Mogensen, T. Vertinksy, S. W. Atlas, R. Bammer. Application of Novel Directionally Encoded Colormaps for Isolating Linear Anisotropic Structures in Human Brain Diffusion Tensor Magnetic Resonance Imaging.

Ennis D.B., L. Wigström, T. Nguyen, S. Skare, R. Bammer, N. Ingels, D.C. Miller. Structural Basis for Regional Heterogeneity of Left Ventricular Function.

Ennis D.B., M.T. Alley, A. Pineda, B.A. Hargreaves, N.J. Pelc. Time Constant Sensitivity of Eddy Current Characterizing Pulse Sequence. 3544.

Gard C., A. Faranesh, G. Gold, T. Grist, S. Reeder. Sensitivity of Off-Resonance Susceptibility Separation with Superparamagnetic Iron Oxide. p. 1816.

Gold G.E., S.B. Reeder, H. Yu, J. H. Brittain, B.A. Hargreaves. Multi-Echo IDEAL Water-Fat Separation for Rapid Imaging of Cartilage. p. 632.

Gold G. E., E. Han, B. A. Hargreaves, G. A. Wright , J. H. Brittain. T1 Imaging of Articular Cartilage using a CPMG Pulse Train for Spin Locking. p. 3603.

Gurney P.T., B.A. Hargreaves, D.G. Nishimura. Three Dimensional Time Resolved Whole Heart Coronary Angiography using a 3D Cones Trajectory. p. 2156.

Hargreaves B.A., S.B. Reeder, H. Yu, A. Shimakawa, J.H. Brittain. Flow Independent Angiography at 3.0T with Dual-Acquisition Balanced SSFP and Multi-Echo IDEAL. p. 1940.

Jochimsen T.H., R. Newbould, S. Skare, D. B. Clayton, M. E. Moseley, R. Bammer,. High Resolution Dynamic-Susceptibility Contrast Perfusion Imaging Using Multi-Echo Parallel EPI.

Kim T., G. Gold, J. Pauly. Isotropic Steady-State Diffusion Weighted Imaging. p. 1051.

Lee J., C. H. Cunningham, B. A. Hargreaves, L. Vidarsson, J. M. Pauly, B. L. Daniel. High Resolution Bilateral Dynamic Contrast Enhancement Breast Imaging. p. 2871.

Lee J., P. T. Gurney, R. Dharmakumar, G.A. Wright, B.A. Hargreaves, A. Shankaranarayanan, K.L. Miller, D.G. Nishimura, J.M.Pauly. Blood Oxygenation (BOX) Level Dependent Functional Brain Imaging using Steady-State Free Precession. p. 3291.

Lee H., G. Gold, K. Nayak. High-Resolution Cartilage Imaging with Wideband SSFP. p. 207.

Liu C., R. Bammer, M. E. Moseley. Improved High-Resolution SNAILS DTI with A Spiral-in Navigator.

Liu C., R. Bammer, M. E. Moseley. Optimizing Phase Correction for Multi-Shot DWI with Conjugate Gradient Method and Oversampling.

Lu W. and B.A. Hargreaves. Analysis and Suppression of Off-Slice Excitation in SSFP Imaging. p. 2374.

Nagle S.K, D. B. Clayton, M. G. Lansberg, G. W. Albers, R. Bammer. Differentiating Perihemorrhagic Infarct from Susceptibility Artifact on DWI Images.

Nagle S.K., D. B. Clayton, M. G. Lansberg, G. W. Albers, R. Bammer. Assessment of Image Quality in a Prospective Clinical Trial of Conventional vs. SENSE DWI at 1.5T.

Newbould R., S. Skare, D. B. Clayton, M. T. Alley, G. Albers, M. Lansberg, R. Bammer. PERMEATE: High temporal resolution multi-echo/multi-slice dynamic susceptibility contrast perfusion imaging using GRAPPA EPI.

Newbould R., C. Liu, S. Ropele, R. Bammer. WIMP: Self-Navigating Magnetization Transfer Pool Mapping with Stimulated Echoes.

Newbould R., C. Liu, S. Ropele, R. Bammer. Quantitative Magnetization Transfer Bound Pool Mapping at 3T.

Newbould R., C. Liu, R. Bammer. Colored Noise and Effective Resolution: Data considerations for non-uniform k-space sampling reconstructions.

Pauly K., G. Gold. Correction of Slice Profile Distortion from Metallic Devices., p. 2380.

Pineda A.R., C. D. Lew, R. Bammer. Cramér-Rao Bound for Phase in SENSE Imaging.

Pisani L.J., R. Bammer, G. H. Glover. Reduced Field of View Imaging for Fetal fMRI (f-fMRI).

Rakow-Penner R., G. Gold, B. Daniel, J. Rosenberg, S. Mazin, J. Pauly, G. Glover. Rapid 3D Articular Cartilage Imaging with Reduction of Truncation Artifacts. p. 3608.

Reeder S.B., A. Vu, B.A. Hargreaves, A. Shimakawa, O. Wieben, C.A. McKenzie, J.A. Polzin, J.H. Brittain. Breath-held Abdominal Imaging with Multi-Echo IDEAL Water-Fat Separation. p. 2444.

Reeder S., A. Faranesh, I. Chen, C. Gard, S. Gambhir, O. Wieben, G. Gold. Off-resonance separation for Positive Contrast Imaging of Iron-Oxide Labelled Cells. p. 430.

Siepmann D., J. McGovern, G. Gold, J. Brittain, S. Reeder. High-Resolution 3D Cartilage Imaging of the Knee in Five Minutes Using IDEAL-SPGR and Parallel Imaging. p. 1251.

Skare S., R. Newbould, D. B. Clayton, R. Bammer. The Influence of Ghost Correction Accuracy on the Image Quality of GRAPPA Accelerated EPI.

Skare S., D. B. Clayton, R. Newbould, R. Bammer. A new propeller EPI design using short axis readouts.

Skare S., R. Newbould, D. B. Clayton, R. Bammer. Diffusion imaging using MinD SAP-EPI.

Skare S., D. B. Clayton, R. Newbould, M.E. Moseley, R. Bammer. A fast and robust minimum entropy based non-interactive Nyquist ghost correction algorithm.

Skare S., T.-Q. Li, D. B. Clayton, R. Newbould, R. Bammer. Diffusion weighted EPI vs. MinD SAP-EPI at 7T.

Stevens K., K. L. Griffiths, S. Bammer, T. Alamin, R. Bammer. High resolution MR imaging of paraspinal muscle injury following minimally invasive and conventional posterolateral lumbar fusion.

Ungersma S., N. Matter, R. Venook, A. Macovski, G. Scott, G. Gold, S. Conolly. Contrast-Enhanced MRI with Fat Suppression Using T1 Dispersion. p. 1696.

Venook R., N. Matter, M. Ramachandran, S. ungersma, G. Gold, N. Giori, A. Macovski, S. Conolly. Prepolarized MRI: Reducing Susceptibility Artifacts Around Metal Orthopedic Implants Without Sacrificing Image Quality. p. 1701.

Vidarsson L., C. Cunningham, P. Larson, G. Gold, J. Pauly. Design of T2 Selective Excitation Pulse Trains for Knee Imaging. p. 594.

Wigstrom L, Hope T, Draney MT, Heiberg E, Bolger A, Alley MT, Pelc NJ, Miller DC, Herfkens RJ. Segmentation and characterization of vortical flow patterns in MRI phase-contrast velocity data.

Acar B., Balci SK, Paik DS, Beaulieu CF, Napel S, "Registration of Supine and Prone CT Colonography Data Using Dynamic Time eWarping: Method and Evaluation,"

Acar B., Konukoglu E, Paik DS, Beaulieu CF, Napel S, "Polyp Enhancement Scheme for Improved Detection of Colonic Polyps in CT Colonography," Radiology 237(P):440.

Desser T., G. Gold, A. Alvarez, B. Tobin. Software Tools for Interactive Instruction in Radiologic Anatomy

Gold G., S. Fuller, A. Shimakawa, H. Yu, J. Johnson, C. Beaulieu, S. Reeder. MR Imaging of the Ankle: Comparison of FS-FSE with IDEAL-FSE., p. 311.

Lee S., D. Leaffer, J. Greve, L. Lollini, A. Manning, G. Gold, S. Biswal. Early Histologic Changes seen in a Murine Model of Rheumatoid Arthritis Can be detected with Micro-Computed Tomography and Micro-MRI. p. 223.

Reeder S.B., B.A. Hargreaves, J.W. Johnson, J.H. Brittain and G.E. Gold. Water-Fat Separation with IDEAL-GRE and IDEAL-SPGR: Comparison to FS-SPGR for Cartilage Imaging in the Knee at 3.0T. 91st

Shi R., Schraedley-Desmond P, Napel S, Margolis DJ, Yee J, Beaulieu CF, et al., "Computer Aided Polyp Detection in CT Colonograhy: Influence of 3D Viewing and Features of Polyp Candidates on Interpretation," Radiology 237(P):336.

Sundaram P., Sifakis E, Paik DS, Beaulieu CF, Napel S, "Fold Removal in CT Colonography (CTC): A Physics-based Approach," Radiology 237(P)439.

Yeluri V, Herfkens R, Lau D, Sommer G. Interpreting large volumetric and multimodality data sets in an integrated 3D-PACS environment.

Bammer R., R. Newbould, S. Skare, D. B. Clayton, M. T. Alley, G. Albers. PERMEATE: High Temporal Resolution Multiecho/Multislice Dynamic Susceptibility Contrast Perfusion Imaging Using GRAPPA EPI. 44th Annual Meeting ASNR, 2006, San Diego, CA.

Bammer R., M. Mlynash, W. Kakuda, M. Lansberg, V. Thijs, G. Albers. Inter-slice Acquisition Delay and Patient Motion can Affect the Effective Volume of Perfusion Deficit Observed with Quantitative Perfusion MR Imaging. 44th Annual Meeting ASNR, 2006, San Diego, CA.

Bammer R., M.G. Lansberg, V. Thijs, M.E. Moseley, G. Albers. Significant Artifact Reduction in Arterial Input Function Measurements of Quantitative Perfusion Imaging Using Dual-Echo Spiral-OUT-Spiral-IN Parallel MRI. AHA Stroke 2005, St. Louis, Missouri, 2005.

Besier T., G. Gold, C. Draper, S. Delp, G. Beaupre. A modeling framework to estimate patellofemoral joint cartilage stress in vivo. Proceedings of the Biomedical Engineering Society, September 2005, p. 35.

Besier T., G. Gold, S. Delp, G. Beaupre. Patellofemoral Cartilage Stress in Increased by Femoral Internal Rotation. Proceedings of the Orthopedic Research Society, March, 2006.

Draper C., A. Fiene, T. Besier, G. Gold, G. Beaupre, S. Delp. Is Patellar Cartilage Thickness Reduced in Individuals with patellofemoral Pain? Proceedings of the 29th American Society of Biomechanics, August, 2005.

Epstein N., T. Besier, J. Santos, T. McAdams, S. Delp. G. Gold. Real-time MR analysis of glenohumeral stability during overhead throwing. Proceedings of the Orthopedic Research Society, March, 2006.

Epstein N., T. Besier, C. Draper, M. Fredericson, G. Beaupre, S. Delp, G. Gold. MRI analysis of patellar and femoral rotation during upright weight bearing. Proceedings of the American Roentgen Ray Society, May 2006, p. 33.

Gold G., T. Besier, C. Draper, J. Santos, M. Fredericson, K. Butts Pauly, G. Beaupre, S. Delp. Patellofemoral Pain: Analysis with Upright Real-Time MRI and 3D Finite Element Modeling. Proceedings of the Society of Computed Body Tomography and Magnetic Resonance, April 2006.

Holzbaur K., W. Murray, G. Gold, S. Delp. Scaling of Muscle Volumes in the Upper Extremity. Proceedings of the 29th American Society of Biomechanics, August, 2005.

Hsia A.W., M. Mlynash, R. Bammer, C.A.C. Wijman. Absolute Brain Apparent Diffusion Coefficient Values and Neurologic Outcome After Cardiac Arrest, Proc. Annual Meeting of the Am Acad of Neurology 2005.

Konukoglu E., Acar B, Paik DS, Beaulieu CF, Napel S. "Heat Diffusion Based Detection of Colonic Polyps in CT Colonography," 13th Annual European Signal Processing Conference, Antalya, Turkey, Sept. 4-8, 2005. Awarded 3rd Place, Student Paper Contest.

Koo S., N. Giori, C. Dyrby, G. Gold, T. Andriacchi. 3D Laser Scan-Based Accuracy of In-Vivo Cartilage Thickness Measurement from MRI. Proceedings of the 29th American Society of Biomechanics, August, 2005.

Lansberg M.G., V. Thijs, R. Bammer, L. Wechsler, M. O'Donnell, R.A. Ohlsen, C.A.C. Wijman, S. Kemp, G. Albers. Who is most likely to benefit from tPA? The Perfusion-Diffusion and Clinical-Diffusion mismatch models disagree. AHA Stroke 2005, St. Louis, Missouri, 2005.

Lansberg M., V. Thijs, W. Kakuda, R. Bammer, L. Wechsel, S. Kemp, G. Albers. Baseline Predictors of Good Outcome in Patients Treated with IV tPA in the 3-6 Hour Time-Window. 58th Annual Meeting American Society of Neurology, 2006, San Diego, CA.

Nagle S. K., D. B. Clayton, M. G. Lansberg, G. W. Albers, R. Bammer. Differentiating Perihemorrhagic Infarct from Susceptibility Artifact on DWI Images. 44th Annual Meeting ASNR, 2006, San Diego, CA.

Pfefferbaum A, Rohlfing T, Deshmukh A, Sullivan EV. Ventricular enlargement in HIV infection: The role of alcoholism comorbidity (abs). Abstract submitted for presentation at 29th Annual Scientific Meeting of the Research Society on Alcoholism, Baltimore, MD, June 24-28, 2006.

Quon, A, Margoliss DJ, Napel S, Beaulieu CF, Gambhir S. Novel 3D rendered FDG PET-CT virtual bronchoscopy and colonography for improved lesion localization and pre-surgical evaluation. Society of Nuclear Medicine 52nd Annual Meeting, June, 2005, Toronto, Ontario, Canada.

Reeder S., A. Faranesh, I. Chen, C. Gard, G. Gold, T. Grist. Positive Contrast MR Imaging of Iron-oxide Labeled Cells by Off-Resonance Separation. Proceedings of the Society of Computed Body Tomography and Magnetic Resonance, April 2006.

Smith C.A., G.T. Stebbins, R.E. Bartt, H. Kessler, E. Martin, R. Bammer, M.E. Moseley. Gray and White Matter Reductions Associated with HIV-infection: A Voxel-based Morphometric Study. Annual Meeting of the Am Acad of Neurology 2005, Miami, FL.

Stevens K., K. Griffiths, G. Gold, T. Alamin, R. Bammer. High-Resolution MR Imaging of Paraspinal Muscle Injury following Minimally Invasive and Conventional Open Posterolateral Lumbar Fusion. Proceedings of the 12th European Society of Musculoskeletal Radiology, July 2005.

Sullivan EV, Rosenbloom MJ, Adalsteinsson E, Kemper CA, Pfefferbaum A. Effect of alcoholism and HIV comorbidity on the macrostructure and microstructure of the corpus callosum (abs). Abstract submitted for presentation at 29th Annual Scientific Meeting of the Research Society on Alcoholism, Baltimore, MD, June 24-28, 2006.

Publications

Liu C, Moseley ME, Bammer R. Simultaneous phase correction and SENSE reconstruction for navigated multi-shot DWI with non-cartesian k-space sampling. Magn Reson Med. 2005 Dec;54(6):1412-22.

Gold GE, Hargreaves BA, Stevens KJ, Beaulieu CF. Advanced magnetic resonance imaging of articular cartilage. Orthop Clin North Am. 2006 Jul;37(3):331-47.

Shi R, Schraedley-Desmond P, Napel S, Olcott EW, Jeffrey RB Jr, Yee J, Zalis ME, Margolis D, Paik DS, Sherbondy AJ, Sundaram P, Beaulieu CF. CT colonography: influence of 3D viewing and polyp candidate features on interpretation with computer-aided detection. Radiology. 2006 Jun;239(3):768-76.

Gold GE, Hargreaves BA, Vasanawala SS, Webb JD, Shimakawa AS, Brittain JH, Beaulieu CF. Articular cartilage of the knee: evaluation with fluctuating equilibrium MR imaging-initial experience in healthy volunteers. Radiology. 2006 Feb;238(2):712-8.

Na JB, Bergman AG, Oloff LM, Beaulieu CF. The flexor hallucis longus: tenographic technique and correlation of imaging findings with surgery in 39 ankles. Radiology. 2005 Sep;236(3):974-82.

Schnabel R, Lubos E, Rupprecht HJ, Espinola-Klein C, Bickel C, Lackner KJ,Cambien F, Tiret L, Munzel T, Blankenberg S. B-type natriuretic peptide and the risk of cardiovascular events and death inpatients with stable angina: results from the AtheroGene study.J Am Coll Cardiol. 2006 Feb 7;47(3):552-8. Epub 2006 Jan 18.

Lubos E, Schnabel R, Rupprecht HJ, Bickel C, Messow CM, Prigge S, Cambien F,Tiret L, Munzel T, Blankenberg S. Prognostic value of tissue inhibitor of metalloproteinase-1 for cardiovascular death among patients with cardiovascular disease: results from the Athero Gene study. Eur Heart J. 2006 Jan;27(2):150-6. Epub 2005 Oct 17.

Min JJ, Ahn Y, Moon S, Kim YS, Park JE, Kim SM, Le UN, Wu JC, Joo SY, HongMH, Yang DH, Jeong MH, Song CH, Jeong YH, Yoo KY, Kang KS, Bom HS. In vivo bioluminescence imaging of cord blood derived mesenchymal stem cell transplantation into rat myocardium. Ann Nucl Med. 2006 Apr;20(3):165-70.

Su H, Chang DS, Gambhir SS, Braun J. Monitoring the antitumor response of naive and memory CD8 T cells in RAG1-/-mice by positron-emission tomography. J Immunol. 2006 Apr 1;176(7):4459-67.

Gold GE, Reeder SB, Yu H, Kornaat P, Shimakawa AS, Johnson JW, Pelc NJ,Beaulieu CF, Brittain JH. Articular cartilage of the knee: rapid three-dimensional MR imaging at 3.0 T with IDEAL balanced steady-state free precession--initial experience. Radiology. 2006 Aug;240(2):546-51. Epub 2006 Jun 26.

Reeder SB, Hargreaves BA, Yu H, Brittain JH. Homodyne reconstruction and IDEAL water-fat decomposition. Magn Reson Med. 2005 Sep;54(3):586-93.

Wansapura JP, Daniel BL, Vigen KK, Butts K. In vivo MR thermometry of frozen tissue using R2* and signal intensity. Acad Radiol. 2005 Sep;12(9):1080-4.

Vigen KK, Jarrard J, Rieke V, Frisoli J, Daniel BL, Butts Pauly K. In vivo porcine liver radiofrequency ablation with simultaneous MR temperature imaging. J Magn Reson Imaging. 2006 Apr;23(4):578-84.

Galvan A, Hare TA, Parra CE, Penn J, Voss H, Glover G, Casey BJ. Earlier development of the accumbens relative to orbitofrontal cortex might underlie risk-taking behavior in adolescents. J Neurosci. 2006 Jun 21;26(25):6885-92.

Galvan A, Hare TA, Davidson M, Spicer J, Glover G, Casey BJ. The role of ventral frontostriatal circuitry in reward-based learning in humans. J Neurosci. 2005 Sep 21;25(38):8650-6.

Gallelli KA, Wagner CM, Karchemskiy A, Howe M, Spielman D, Reiss A, ChangKD. N-acetylaspartate levels in bipolar offspring with and at high-risk for bipolar disorder.Bipolar Disord. 2005 Dec;7(6):589-97.

Cai W, Zhang X, Wu Y, Chen X. A thiol-reactive 18F-labeling agent,N-[2-(4-18F-fluorobenzamido)ethyl]maleimide, and synthesis of RGD peptide-based tracer for PET imaging of alpha v beta 3 integrin expression. J Nucl Med. 2006 Jul;47(7):1172-80.

Wu Y, Cai W, Chen X. Near-infrared fluorescence imaging of tumor integrin alpha v beta 3 expression with Cy7-labeled RGD multimers. Mol Imaging Biol. 2006 Jul-Aug;8(4):226-36.

Wu Y, Cai W, Chen X. Near-Infrared Fluorescence Imaging of Tumor Integrin alpha(v)beta (3)Expression with Cy7-Labeled RGD Multimers. Mol Imaging Biol. 2006 May 18; [Epub ahead of print]

Yang YS, Zhang X, Xiong Z, Chen X. Comparative in vitro and in vivo evaluation of two 64Cu-labeled bombesinanalogs in a mouse model of human prostate adenocarcinoma. Nucl Med Biol. 2006 Apr;33(3):371-80. Epub 2006 Mar 9. [PubMed - in process]

Cai W, Shin DW, Chen K, Gheysens O, Cao Q, Wang SX, Gambhir SS, Chen X. Peptide-labeled near-infrared quantum dots for imaging tumor vasculature in living subjects. Nano Lett. 2006 Apr;6(4):669-76.

Zhang X, Cai W, Cao F, Schreibmann E, Wu Y, Wu JC, Xing L, Chen X. 18F-labeled bombesin analogs for targeting GRP receptor-expressing prostate cancer. J Nucl Med. 2006 Mar;47(3):492-501.

Chen X. Multimodality imaging of tumor integrin alphavbeta3 expression. Mini Rev Med Chem. 2006 Feb;6(2):227-34. Review.

Xiong Z, Cheng Z, Zhang X, Patel M, Wu JC, Gambhir SS, Chen X. Imaging Chemically Modified Adenovirus for Targeting Tumors Expressing Integrin{alpha}v{beta}3 in Living Mice with Mutant Herpes Simplex Virus Type 1 Thymidine Kinase PET Reporter Gene. J Nucl Med. 2006 Jan;47(1):130-139.

Zhang X, Xiong Z, Wu Y, Cai W, Tseng JR, Gambhir SS, Chen X. Quantitative PET Imaging of Tumor Integrin {alpha}v{beta}3 Expression with18F-FRGD2.J Nucl Med. 2006 Jan;47(1):113-21.

Cheng Z, Wu Y, Xiong Z, Gambhir SS, Chen X. Near-infrared fluorescent RGD peptides for optical imaging of integrinalphavbeta3 expression in living mice. Bioconjug Chem. 2005 Nov-Dec;16(6):1433-41.

Wu Y, Zhang X, Xiong Z, Cheng Z, Fisher DR, Liu S, Gambhir SS, Chen X. microPET imaging of glioma integrin {alpha}v{beta}3 expression using(64)Cu-labeled tetrameric RGD peptide.J Nucl Med. 2005 Oct;46(10):1707-18.

Venook RD, Matter NI, Ramachandran M, Ungersma SE, Gold GE, Giori NJ, Macovski A, Scott GC, Conolly SM. Prepolarized magnet-

ic resonance imaging around metal orthopedic implants. Magn Reson Med. 2006 Jul;56(1):177-86.

Chen X, Park R, Khankaldyyan V, Gonzales-Gomez I, Tohme M, Moats RA, BadingJR, Laug WE, Conti PS. Longitudinal microPET imaging of brain tumor growth with F-18-labeled RGD peptide. Mol Imaging Biol. 2006 Jan-Feb;8(1):9-15.

Fueger BJ, Weber WA, Quon A, Crawford TL, Allen-Auerbach MS, Halpern BS, Ratib O, Phelps ME, Czernin J. Performance of 2-deoxy-2-[F-18]fluoro-D-glucose positron emission tomography and integrated PET/CT in restaged breast cancer patients. Mol Imaging Biol. 2005 Sep-Oct;7(5):369-76.

Asakawa DS, Blemker SS, Gold GE, Delp SL. Dynamic magnetic resonance imaging of muscle function after surgery.Skeletal Radiol. 2006 Jun 30; [Epub ahead of print].

Besier TF, Gold GE, Beaupre GS, Delp SL. A modeling framework to estimate patellofemoral joint cartilage stress in vivo. Med Sci Sports Exerc. 2005 Nov;37(11):1924-30.

Alvarez A, Gold GE, Tobin B, Desser TS. Software tools for interactive instruction in radiologic anatomy. Acad Radiol. 2006 Apr;13(4):512-7.

Langer SA, Horst KC, Ikeda DM, Daniel BL, Kong CS, Dirbas FM. Pathologic correlates of false positive breast magnetic resonance imaging findings: which lesions warrant biopsy? Am J Surg. 2005 Oct;190(4):633-40.

Lauritsch G, Boese J, Wigstrom L, Kemeth H, Fahrig R. Towards cardiac C-arm computed tomography. IEEE Trans Med Imaging. 2006 Jul;25(7):922-34.

Pineda AR, Yoon S, Paik DS, Fahrig R. Optimization of a tomosynthesis system for the detection of lung nodules. Med Phys. 2006 May;33(5):1372-9.

Ganguly A, Wen Z, Daniel BL, Butts K, Kee ST, Rieke V, Do HM, Pelc NJ, Fahrig R. Truly hybrid X-ray/MR imaging: toward a streamlined clinical system. Acad Radiol. 2005 Sep;12(9):1167-77.

Berry DA, Cronin KA, Plevritis SK, Fryback DG, Clarke L, Zelen M, Mandelblatt JS, Yakovlev AY, Habbema JD, Feuer EJ; Cancer Intervention and Surveillance Modeling Network (CISNET) Collaborators. Effect of screening and adjuvant therapy on mortality from breast cancer. N Engl J Med. 2005 Oct 27;353(17):1784-92.

Sze DY, Strobel N, Fahrig R, Moore T, Busque S, Frisoli JK. Transjugular Intrahepatic Portosystemic Shunt Creation in a Polycystic LiverFacilitated by Hybrid Cross-sectional/Angiographic Imaging. J Vasc Interv Radiol. 2006 Apr;17(4):711-5.

Gaab N, Tallal P, Kim H, Lakshminarayanan K, Archie JJ, Glover GH, GabrieliJD. Neural correlates of rapid spectrotemporal processing in musicians and nonmusicians.Ann N Y Acad Sci. 2005 Dec;1060:82-8.

Quon A, Napel S, Beaulieu CF, Gambhir SS. "Flying through" and "flying around" a PET/CT scan: Pilot study and development of 3D integrated 18F-FDG PET/CT for virtual bronchoscopy and colonoscopy. J Nucl Med. 2006 Jul;47(7):1081-7.

Schipper ML, Patel MR, Gambhir SS. Evaluation of firefly luciferase

bioluminescence mediated photodynamic toxicity in cancer cells. Mol Imaging Biol. 2006 Jul-Aug;8(4):218-25.

Chen X, Gambhir SS. Significance of one-bead-one-compound combinational chemistry. Nat Chem Biol. 2006 Jul;2(7):351-2. No abstract available.

Iagaru A, Quon A, McDougall IR, Gambhir SS. Merkel cell carcinoma: Is there a role for2-deoxy-2-[f-18]fluoro-D-glucose-positron emission tomography/computed tomography? Mol Imaging Biol. 2006 Jul-Aug;8(4):212-7.

Cheng Z, Levi J, Xiong Z, Gheysens O, Keren S, Chen X, Gambhir SS. Near-infrared fluorescent deoxyglucose analogue for tumor optical imaging in cell culture and living mice. Bioconjug Chem. 2006 May-Jun;17(3):662-9.

Yaghoubi SS, Couto MA, Chen CC, Polavaram L, Cui G, Sen L, Gambhir SS. Preclinical safety evaluation of 18F-FHBG: a PET reporter probe for imaging herpes simplex virus type 1 thymidine kinase (HSV1-tk) or mutant HSV1-sr39tk'sexpression. J Nucl Med. 2006 Apr;47(4):706-15.

Penuelas I, Haberkorn U, Yaghoubi S, Gambhir SS. Gene therapy imaging in patients for oncological applications.Eur J Nucl Med Mol Imaging. 2005 Dec;32 Suppl 2:S384-403. Review.

Rodriguez-Porcel M, Gheysens O, Chen IY, Wu JC, Gambhir SS. Image-guided cardiac cell delivery using high-resolution small-animal ultrasound. Mol Ther. 2005 Dec;12(6):1142-7. Epub 2005 Aug 18.

Plevritis SK, Kurian AW, Sigal BM, Daniel BL, Ikeda DM, Stockdale FE,Garber AM. Cost-effectiveness of screening BRCA1/2 mutation carriers with breast magnetic resonance imaging. JAMA. 2006 May 24;295(20):2374-84.

Lampl Y, Lorberboym M, Blankenberg FG, Sadeh M, Gilad R. Annexin V SPECT imaging of phosphatidylserine expression in patients with dementia. Neurology. 2006 Apr 25;66(8):1253-4.

Hsu JJ, Glover GH. Rapid MRI method for mapping the longitudinal relaxation time. J Magn Reson. 2006 Jul;181(1):98-106. Epub 2006 Apr 18.

Friedman L, Glover GH. Report on a multicenter fMRI quality assurance protocol. J Magn Reson Imaging. 2006 Jun;23(6):827-39.

Thomason ME, Foland LC, Glover GH. Calibration of BOLD fMRI using breath holding reduces group variance during a cognitive task. Hum Brain Mapp. 2006 May 2; [Epub ahead of print].

Hu Y, Glover GH. Partial-k-space acquisition method for improved SNR efficiency and temporalresolution in 3D fMRI.Magn Reson Med. 2006 May;55(5):1106-13.

Li TQ, Takahashi A, Wang Y, Mathews V, Glover GH. Dual-echo spiral in/in acquisition method for reducing magnetic susceptibility artifacts in blood-oxygen-level-dependent functional magnetic resonance imaging. Magn Reson Med. 2006 Feb;55(2):325-34.

Rakow-Penner, R, Daniel B, Yu H, Sawyer-Glover A, Glover GH. Relaxation times of breast tissue at 1.5T and 3T measured using IDEAL.J Magn Reson Imaging. 2006 Jan;23(1):87-91.

Plevritis SK, Salzman P, Sigal BM, Glynn PW. A natural history model of stage progression applied to breast cancer.Stat Med. 2006 Apr 5; [Epub ahead of print].

Kornaat PR, Koo S, Andriacchi TP, Bloem JL, Gold GE. Comparison of quantitative cartilage measurements acquired on two 3.0T MRI systems from different manufacturers. J Magn Reson Imaging. 2006 May;23(5):770-3.

Pappas GP, Blemker SS, Beaulieu CF, McAdams TR, Whalen ST, Gold GE. In vivo anatomy of the Neer and Hawkins sign positions for shoulder impingement. J Shoulder Elbow Surg. 2006 Jan-Feb;15(1):40-9.

Wang C, Stebbins GT, Nyenhuis DL, Detoledo-Morrell L, Freels S, Gencheva E,Pedelty L, Sripathirathan K, Moseley ME, Turner DA, Gabrieli JD, Gorelick PB. Longitudinal changes in white matter following ischemic stroke: A three-yearfollow-up study. Neurobiol Aging. 2005 Nov 23; [Epub ahead of print]

Espinosa LA, Daniel BL, Vidarsson L, Zakhour M, Ikeda DM, Herfkens RJ. The lactating breast: contrast-enhanced MR imaging of normal tissue and cancer. Radiology. 2005 Nov;237(2):429-36.

Mariano MN, van den Bosch MA, Daniel BL, Nowels KW, Birdwell RL, Fong KJ,Desmond PS, Plevritis S, Stables LA, Zakhour M, Herfkens RJ, Ikeda DM. Contrast-enhanced MRI of ductal carcinoma in situ: characteristics of a newintensity-modulated parametric mapping technique correlated with histopathologic findings. J Magn Reson Imaging. 2005 Oct;22(4):520-6.

Lu Y, Dang H, Middleton B, Zhang Z, Washburn L, Stout DB, Campbell-Thompson M, Atkinson MA, Phelps M, Gambhir SS, Tian J, Kaufman DL. Noninvasive imaging of islet grafts using positron-emission tomography. Proc Natl Acad Sci U S A. 2006 Jul 25;103(30):11294-9.

Tsai EY, Taur A, Espinosa L, Quon A, Johnson D, Dick S, Chow S, Advani R,Warnke R, Kohler S, Hoppe RT, Kim YH. Staging accuracy in mycosis fungoides and sezary syndrome using integrated positron emission tomography and computed tomography. Arch Dermatol. 2006 May;142(5):577-84.

Street HH, Goris ML, Fisher GA, Wessels BW, Cho C, Hernandez C, Zhu HJ,Zhang Y, Nangiana JS, Shan JS, Roberts K, Knox SJ. Phase I study of 131I-chimeric(ch) TNT-1/B monoclonal antibody for the treatment of advanced colon cancer. Cancer Biother Radiopharm. 2006 Jun;21(3):243-56.

Levin CS. Primer on molecular imaging technology. Eur J Nucl Med Mol Imaging. 2005 Dec;32 Suppl 2:S325-45. Review.

Ochsner KN, Ludlow DH, Knierim K, Hanelin J, Ramachandran T, Glover GC,Mackey SC. Neural correlates of individual differences in pain-related fear and anxiety.Pain. 2006 Jan;120(1-2):69-77. Epub 2005 Dec 20.

deCharms RC, Maeda F, Glover GH, Ludlow D, Pauly JM, Soneji D, Gabrieli JD,Mackey SC. Control over brain activation and pain learned by using real-time functional MRI. Proc Natl Acad Sci U S A. 2005 Dec 20;102(51):18626-31. Epub 2005 Dec 13.

Friedman L, Glover GH, Krenz D, Magnotta V; The FIRST BIRN. Reducing inter-scanner variability of activation in a multicenter fMRI study: Role of smoothness equalization. Neuroimage. 2006 Oct 1;32(4):1656-68. Epub 2006 Jul 27.

Weigel RJ, McDougall IR. The Role of Radioactive Iodine in the Treatment of Well-differentiated Thyroid Cancer. Surg Oncol Clin N Am. 2006 Jul;15(3):625-38. No abstract available.

McDougall IR. Metastatic struma ovarii: the burden of truth. Clin Nucl Med. 2006 Jun;31(6):321-4.

Golebiewska U, Gambhir A, Hangyas-Mihalyne G, Zaitseva I, Radler J, McLaughlin S. Membrane-bound basic peptides sequester multivalent (PIP2), but not monovalent (PS), acidic lipids. Biophys J. 2006 Jul 15;91(2):588-99. Epub 2006 Apr 28.

Glover GC, Printemps C, Essemiani K, Meinhold J. Modelling of wastewater treatment plants--how far shall we go with sophisticated modelling tools? Water Sci Technol. 2006;53(3):79-89.

Jochimsen TH, Schafer A, Bammer R, Moseley ME. Efficient simulation of magnetic resonance imaging with Bloch-Torrey equations using intra-voxel magnetization gradients. J Magn Reson. 2006 May;180(1):29-38. Epub 2006 Jan 24.

Gold GE, Burstein D, Dardzinski B, Lang P, Boada F, Mosher T. MRI of articular cartilage in OA: novel pulse sequences and compositional/functional markers. Osteoarthritis Cartilage. 2006;14 Suppl A:A76-86. Epub 2006 May 23.

Robinson TE, Goris ML, Zhu HJ, Chen X, Bhise P, Sheikh F, Moss RB. Dornase alfa reduces air trapping in children with mild cystic fibrosis lung disease: a quantitative analysis. Chest. 2005 Oct;128(4):2327-35.

Schnabel R, Blankenberg S, Lubos E, Lackner KJ, Rupprecht HJ, Espinola-Klein C, Jachmann N, Post F, Peetz D, Bickel C, Cambien F, Tiret L, Munzel T. Asymmetric dimethylarginine and the risk of cardiovascular events and death in patients with coronary artery disease: results from the Athero Gene Study. Circ Res. 2005 Sep 2;97(5):e53-9. Epub 2005 Aug 11.

Zhuge F, Rubin GD, Sun S, Napel S. An abdominal aortic aneurysm segmentation method: level set with region and statistical information. Med Phys. 2006 May;33(5):1440-53.

Dayam R, Aiello F, Deng J, Wu Y, Garofalo A, Chen X, Neamati N. Discovery of small molecule integrin alpha v beta 3 antagonists as novel anticancer agents. J Med Chem. 2006 Jul 27;49(15):4526-34.

Larson PE, Gurney PT, Nayak K, Gold GE, Pauly JM, Nishimura DG. Designing long-T2 suppression pulses for ultrashort echo time imaging. Magn Reson Med. 2006 Jul;56(1):94-103.

Gurney PT, Hargreaves BA, Nishimura DG. Design and analysis of a practical 3D cones trajectory. Magn Reson Med. 2006 Mar;55(3):575-82.

Hargreaves BA, Bangerter NK, Shimakawa A, Vasanawala SS, Brittain JH, Nishimura DG. Dual-acquisition phase-sensitive fat-water separation using balanced steady-state free precession. Magn Reson Imaging. 2006 Feb;24(2):113-22. Epub 2006 Jan 10.

DiCarlo JC, Hargreaves BA, Nayak KS, Hu BS, Pauly JM, Nishimura DG. Variable-density one-shot Fourier velocity encoding. Magn Reson Med. 2005 Sep;54(3):645-55.

Carbonell P, Glover G, Fernandez JA, Ramirez M, Marin C, Castellanos G, Parrilla P. [Hereditary pancreatitis caused by a new mutation in the trypsinogen gene. Report of a family] Cir Esp. 2006 Apr;79(4):252-4. Spanish.

Lee J, Santos JM, Conolly SM, Miller KL, Hargreaves BA, Pauly JM. Respiration-induced B0 field fluctuation compensation in balanced SSFP: real-time approach for transition-band SSFP fMRI. Magn Reson Med. 2006 May;55(5):1197-201.

Vidarsson L, Gold GE, Hargreaves B, Pauly JM. Linear combination filtering for T2-selective imaging of the knee. Magn Reson Med. 2006 May;55(5):1191-6.

Santos JM, Cunningham CH, Lustig M, Hargreaves BA, Hu BS, Nishimura DG, Pauly JM. Single breath-hold whole-heart MRA using variable-density spirals at 3T. Magn Reson Med. 2006 Feb;55(2):371-9.

Chen J, Daniel BL, Pauly KB. Investigation of proton density for measuring tissue temperature. J Magn Reson Imaging. 2006 Mar;23(3):430-4.

Schmidt TG, Star-Lack J, Bennett NR, Mazin SR, Solomon EG, Fahrig R, Pelc NJ. A prototype table-top inverse-geometry volumetric CT system. Med Phys. 2006 Jun;33(6):1867-78.

Yu H, Reeder SB, McKenzie CA, Brau AC, Shimakawa A, Brittain JH, Pelc NJ. Single acquisition water-fat separation: feasibility study for dynamic imaging. Magn Reson Med. 2006 Feb;55(2):413-22.

Schmidt TG, Fahrig R, Pelc NJ. A three-dimensional reconstruction algorithm for an inverse-geometry volumetric CT system. Med Phys. 2005 Nov;32(11):3234-45.

Thornton SJ, Hochachka PW, Crocker DE, Costa DP, Leboeuf BJ, Spielman DM, Pelc NJ. Stroke volume and cardiac output in juvenile elephant seals during forced dives. J Exp Biol. 2005 Oct;208(Pt 19):3637-43.

Yu H, Reeder SB, Shimakawa A, Brittain JH, Pelc NJ. Field map estimation with a region growing scheme for iterative 3-point water-fat decomposition. Magn Reson Med. 2005 Oct;54(4):1032-9.

Reeder SB, Pineda AR, Wen Z, Shimakawa A, Yu H, Brittain JH, Gold GE, Beaulieu CH, Pelc NJ. Iterative decomposition of water and fat with echo asymmetry and least-squares estimation (IDEAL): application with fast spin-echo imaging. Magn Reson Med. 2005 Sep;54(3):636-44.

Pineda AR, Reeder SB, Wen Z, Pelc NJ. Cramer-Rao bounds for three-point decomposition of water and fat. Magn Reson Med. 2005 Sep;54(3):625-35.

Stout DB, Chatziioannou AF, Lawson TP, Silverman RW, Gambhir SS, Phelps ME. Small animal imaging center design: the facility at the UCLA Crump Institute for Molecular Imaging. Mol Imaging Biol. 2005 Nov-Dec;7(6):393-402.

Plevritis SK. Decision analysis and simulation modeling for evaluating diagnostic tests on the basis of patient outcomes. AJR Am J Roentgenol. 2005 Sep;185(3):581-90. No abstract available.

Kurian AW, Hartman AR, Mills MA, Ford JM, Daniel BL, Plevritis SK. Opinions of women with high inherited breast cancer risk about prophylactic mastectomy: an initial evaluation from a screening trial including magnetic resonance imaging and ductal lavage. Health Expect. 2005 Sep;8(3):221-33.

99: Wu JC, Spin JM, Cao F, Lin S, Xie X, Gheysens O, Chen IY, Sheikh AY, Robbins RC, Tsalenko A, Gambhir SS, Quertermous T. Transcriptional profiling of reporter genes used for molecular imaging of embryonic stem cell transplantation. Physiol Genomics. 2006 Mar 13;25(1):29-38. Epub 2006 Jan 3.

Zhang Y, So MK, Loening AM, Yao H, Gambhir SS, Rao J. HaloTag protein-mediated site-specific conjugation of bioluminescent proteins to quantum dots. Angew Chem Int Ed Engl. 2006 Jul 24;45(30):4936-40.

Xu C, Xing B, Rao J. A self-assembled quantum dot probe for detecting beta-lactamase activity. Biochem Biophys Res Commun. 2006 Jun 9;344(3):931-5. Epub 2006 Apr 19.

Hasegawa S, Gowrishankar G, Rao J. Detection of mRNA in mammalian cells with a split ribozyme reporter. Chembiochem. 2006 Jun;7(6):925-8.

Hasegawa S, Rao J. Modulating the splicing activity of Tetrahymena ribozyme via RNA self-assembly. FEBS Lett. 2006 Mar 6;580(6):1592-6. Epub 2006 Feb 3.

So MK, Xu C, Loening AM, Gambhir SS, Rao J. Self-illuminating quantum dot conjugates for in vivo imaging. Nat Biotechnol. 2006 Mar;24(3):339-43. Epub 2006 Feb 26.

Kutschka I, Kofidis T, Chen IY, von Degenfeld G, Zwierzchoniewska M, Hoyt G, Arai T, Lebl DR, Hendry SL, Sheikh AY, Cooke DT, Connolly A, Blau HM, Gambhir SS, Robbins RC. Adenoviral human BCL-2 transgene expression attenuates early donor cell death after cardiomyoblast transplantation into ischemic rat hearts. Circulation. 2006 Jul 4;114(1 Suppl):I174-80.

Kutschka I, Chen IY, Kofidis T, Arai T, von Degenfeld G, Sheikh AY, Hendry SL, Pearl J, Hoyt G, Sista R, Yang PC, Blau HM, Gambhir SS, Robbins RC. Collagen matrices enhance survival of transplanted cardiomyoblasts and contribute to functional improvement of ischemic rat hearts. Circulation. 2006 Jul 4;114(1 Suppl):I167-73.

Venkatraman R, Raman R, Raman B, Moss RB, Rubin GD, Mathers LH, Robinson TE. Fully automated system for three-dimensional bronchial morphology analysis using volumetric multidetector computed tomography of the chest. J Digit Imaging. 2006 Jun;19(2):132-9.

Brzozowski L, Ganguly A, Pop M, Wen Z, Bennett R, Fahrig R, Rowlands JA. Compatibility of interventional x-ray and magnetic resonance imaging: feasibility of a closed bore XMR (CBXMR) system. Med Phys. 2006 Aug;33(8):3033-45.

Moseley ME, Nash DJ, Williams PR, DeFrance SD, Miranda A, Ruales M. Burning down the brewery: establishing and evacuating an ancient imperial colony at Cerro Baul, Peru. Proc Natl Acad Sci U S A. 2005 Nov 29;102(48):17264-71. Epub 2005 Nov 17.

Fleischmann D, Hallett RL, Rubin GD. CT angiography of peripheral arterial disease. J Vasc Interv Radiol. 2006 Jan;17(1):3-26. Review.

Kwan SW, Partik BL, Zinck SE, Chan FP, Kee ST, Leung AN, Voracek M, Rubin GD. Primary interpretation of thoracic MDCT images using coronal reformations. AJR Am J Roentgenol. 2005 Dec;185(6):1500-8.

Roos JE, Hellinger JC, Hallet R, Fleischmann D, Zarins CK, Rubin GD. Detection of endograft fractures with multidetector row computed tomography. J Vasc Surg. 2005 Nov;42(5):1002-6.

Hiatt MD, Fleischmann D, Hellinger JC, Rubin GD. Angiographic imaging of the lower extremities with multidetector CT. Radiol Clin North Am. 2005 Nov;43(6):1119-27, ix. Review.

Chow LC, Napoli A, Klein MB, Chang J, Rubin GD. Vascular mapping of the leg with multi-detector row CT angiography prior to free-flap transplantation. Radiology. 2005 Oct;237(1):353-60. Epub 2005 Aug 11.

Fleischmann D, Rubin GD. Quantification of intravenously administered contrast medium transit through the peripheral arteries: implications for CT angiography. Radiology. 2005 Sep;236(3):1076-82. Epub 2005 Jul 6.

Schlitt A, Blankenberg S, Weise K, Gartner BC, Mehrer T, Peetz D, Meyer J, Darius H, Rupprecht HJ. Herpesvirus DNA (Epstein-Barr virus, herpes simplex virus, cytomegalovirus) in circulating monocytes of patients with coronary artery disease. Acta Cardiol. 2005 Dec;60(6):605-10.

Isoda H, Hirano M, Takeda H, Kosugi T, Alley MT, Markl M, Pelc NJ, Sakahara H. Visualization of hemodynamics in a silicon aneurysm model using time-resolved, 3D, phase-contrast MRI. AJNR Am J Neuroradiol. 2006 May;27(5):1119-22.

Sommer G, Olcott EW, Chow LC, Saket RR, Schraedley-Desmond P. Measurement of renal extraction fraction with contrast-enhanced CT. Radiology. 2005 Sep;236(3):1029-33. Epub 2005 Jul 14.

Venook RD, Hargreaves BA, Gold GE, Conolly SM, Scott GC. Automatic tuning of flexible interventional RF receiver coils. Magn Reson Med. 2005 Oct;54(4):983-93.

Rubin GD, Bradley WG Jr, Foley WD, Herold CJ, Jaramillo D, Seeger LL. Image Interpretation Session: Sunday, November 27, 2005. Radiographics. 2005 Sep-Oct;25(5):1437-47.

Mayer D, Levin YS, Hurd RE, Glover GH, Spielman DM. Fast metabolic imaging of systems with sparse spectra: Application for hyperpolarized (13)C imaging. Magn Reson Med. 2006 Aug 29; [Epub ahead of print]

Kim DH, Spielman DM. Reducing gradient imperfections for spiral magnetic resonance spectroscopic imaging. Magn Reson Med. 2006 Jul;56(1):198-203.

Mayer D, Kim DH, Adalsteinsson E, Spielman DM. Fast CT-PRESS-based spiral chemical shift imaging at 3 Tesla. Magn Reson Med. 2006 May;55(5):974-8.

Medina D, DeToledo-Morrell L, Urresta F, Gabrieli JD, Moseley M, Fleischman D, Bennett DA, Leurgans S, Turner DA, Stebbins GT. White matter changes in mild cognitive impairment and AD: A diffusion tensor imaging study. Neurobiol Aging. 2006 May;27(5):663-72. Epub 2005 Jul 7.

Greve JM, Les AS, Tang BT, Draney Blomme MT, Wilson NM, Dalman RL, Pelc NJ, Taylor CA. Allometric scaling of wall shear stress from mice to humans: quantification using cine phase-contrast MRI and computational fluid dynamics. Am J Physiol Heart Circ Physiol. 2006 Oct;291(4):H1700-8. Epub 2006 May 19.

Tang BT, Cheng CP, Draney MT, Wilson NM, Tsao PS, Herfkens RJ, Taylor CA. Abdominal aortic hemodynamics in young healthy adults at rest and during lower limb exercise: quantification using image-based computer modeling. Am J Physiol Heart Circ Physiol. 2006 Aug;291(2):H668-76. Epub 2006 Apr 7.

Cheng CP, Wilson NM, Hallett RL, Herfkens RJ, Taylor CA. In vivo MR angiographic quantification of axial and twisting deformations of the superficial femoral artery resulting from maximum hip and knee flexion. J Vasc Interv Radiol. 2006 Jun;17(6):979-87.

Kobayashi C, Glover GH, Temple E. Cultural and linguistic influence on neural bases of 'Theory of Mind': an fMRI study with Japanese bilinguals. Brain Lang. 2006 Aug;98(2):210-20. Epub 2006 Jun 5.

Blankenberg S, Godefroy T, Poirier O, Rupprecht HJ, Barbaux S, Bickel C, Nicaud V, Schnabel R, Kee F, Morrison C, Evans A, Lackner KJ, Cambien F, Munzel T, Tiret L; AtheroGene Investigators. Haplotypes of the caspase-1 gene, plasma caspase-1 levels, and cardiovascular risk. Circ Res. 2006 Jul 7;99(1):102-8. Epub 2006 Jun 15.

Padmanabhan P, Otero J, Ray P, Paulmurugan R, Hoffman AR, Gambhir SS, Biswal S, Ulaner GA. Visualization of Telomerase Reverse Transcriptase (hTERT) Promoter Activity Using a Trimodality Fusion Reporter Construct. J Nucl Med. 2006 Feb;47(2):270-277.

Ghosh M, Gambhir SS, De A, Nowels K, Goris M, Wapnir I. Bioluminescent monitoring of NIS-mediated (131)I ablative effects in MCF-7 xenografts. Mol Imaging. 2006 Apr-Jun;5(2):76-84.

Shu CJ, Guo S, Kim YJ, Shelly SM, Nijagal A, Ray P, Gambhir SS, Radu CG, Witte ON. Visualization of a primary anti-tumor immune response by positron emission tomography. Proc Natl Acad Sci U S A. 2005 Nov 29;102(48):17412-7. Epub 2005 Nov 17.

Illes J, Kirschen MP, Edwards E, Stanford LR, Bandettini P, Cho MK, Ford PJ, Glover GH, Kulynych J, Macklin R, Michael DB, Wolf SM; Working Group on Incidental Findings in Brain Imaging Research. Ethics. Incidental findings in brain imaging research. Science. 2006 Feb 10;311(5762):783-4. No abstract available.

Chang GY, Xie X, Wu JC. Overview of stem cells and imaging modalities for cardiovascular diseases. J Nucl Cardiol. 2006 Jul;13(4):554-69. Review.

Gheysens O, Lin S, Cao F, Wang D, Chen IY, Rodriguez-Porcel M, Min JJ, Gambhir SS, Wu JC. Noninvasive evaluation of immunosuppressive drug efficacy on acute donor cell survival. Mol Imaging Biol. 2006 May-Jun;8(3):163-70.

Sheikh AY, Wu JC. Molecular imaging of cardiac stem cell transplantation. Curr Cardiol Rep. 2006 Mar;8(2):147-54.

Cao F, Lin S, Xie X, Ray P, Patel M, Zhang X, Drukker M, Dylla SJ, Connolly AJ, Chen X, Weissman IL, Gambhir SS, Wu JC. In vivo visualization of embryonic stem cell survival, proliferation, and migration after cardiac delivery. Circulation. 2006 Feb 21;113(7):1005-14. Epub 2006 Feb 13.

Krishnan M, Park JM, Cao F, Wang D, Paulmurugan R, Tseng JR, Gonzalgo ML, Gambhir SS, Wu JC. Effects of epigenetic modulation on reporter gene expression: implications for stem cell imaging. FASEB J. 2006 Jan;20(1):106-8. Epub 2005 Oct 24.

Iyer M, Sato M, Johnson M, Gambhir SS, Wu L. Applications of molecular imaging in cancer gene therapy. Curr Gene Ther. 2005 Dec;5(6):607-18. Review.

Johnson M, Sato M, Burton J, Gambhir SS, Carey M, Wu L. Micro-PET/CT monitoring of herpes thymidine kinase suicide gene therapy in a prostate cancer xenograft: the advantage of a cell-specific transcrip-

tional targeting approach. Mol Imaging. 2005 Oct-Dec;4(4):463-72.

Blankenberg FG, Kalinyak J, Liu L, Koike M, Cheng D, Goris ML, Green A, Vanderheyden JL, Tong DC, Yenari MA. 99mTc-HYNIC-annexin V SPECT imaging of acute stroke and its response to neuroprotective therapy with anti-Fas ligand antibody. Eur J Nucl Med Mol Imaging. 2006 May;33(5):566-74. Epub 2006 Feb 14.

Wu JC, Yla-Herttuala S. Human gene therapy and imaging: cardiology. Eur J Nucl Med Mol Imaging. 2005 Dec;32 Suppl 2:S346-57. Review.

Blankenberg S, McQueen MJ, Smieja M, Pogue J, Balion C, Lonn E, Rupprecht HJ, Bickel C, Tiret L, Cambien F, Gerstein H, Munzel T, Yusuf S. HOPE Study Investigators. Comparative impact of multiple biomarkers and N-Terminal pro-brain natriuretic peptide in the context of conventional risk factors for the prediction of recurrent cardiovascular events in the Heart Outcomes Prevention Evaluation (HOPE) Study. Circulation. 2006 Jul 18;114(3):201-8. Epub 2006 Jul 10.

Cao F, Sheikh AY, Xie X, Lin S, Drukker M, Gambhir SS, Weissman I, Robbins RC, Wu JC. In vivo molecular imaging of human embryonic stem cell derived cardiomyocytes after transplantation into the ischemic myocardium. J Nucl Med 2006;47(1):2P

Kang KW, Min JJ, Chen X, Gambhir SS. Comparison of [14C]FMAU, [3H]FEAU, [14C]FIAU, and [3H]PCV for monitoring reporter gene expression of wild type and mutant herpes simplex virus type 1 thymidine kinase in cell culture. Mol Imaging Biol. 2005 Jul-Aug;7(4):296-303.